The Synthesis and Characterization of Post Sulfonated Poly (Arylene Ether Sulfone)s Utilizing Chlorosulfonic Acid and it's Silyl Derivative

Natalie Y. Arnett*, W. L. Harrison, K. O'Connor, and J.E. McGrath
Virginia Polytechnic Institute and State University
Department of Chemistry, Center for High Performance Polymeric Adhesives and Composites
Blacksburg, VA
*Department of Chemistry, Grambling State University, Grambling, LA

ABSTRACT

The proton electrolyte membrane (PEM) is an integral component of a fuel cell.[1,2] Sulfonated poly (arylene ether sulfone)s, which are potential candidates for PEM, are prepared via nucleophilic aromatic substitution and post- sulfonation. Chlorosulfonic acid was used as the sulfonating agent and chlorotrimethylsilane is also used as a protecting agent against cleavage of the isopropylidene group. In this research, sulfonation of three types of poly (arylene ether sulfone)s monomers derived from bisphenol A, 6F bisphenol and biphenol were carried out. The polymers were chosen on the basis of morphology, thermal considerations, and hydrophobicity. Transparent, ductile films of the sulfonated polymers were solution cast from dimethylacetamide (DMAc) or N-methyl-2-pyrrolidinone (NMP) and characterized using FTIR, thermogravimetric analysis (TGA), differential scanning calorimetry (DSC), intrinsic viscosity, and proton NMR. The degree of post-sulfonation was difficult to control, but FTIR was useful to characterize the sulfonation content. The T_g value could (in some cases) be measured on DSC.

INTRODUCTION

Proton exchange membranes fuel cells (PEMFCs) are attractive alternative energy sources for transportation, stationary and portable power. A fuel cell is an electrochemical device that combines a fuel, such as hydrogen, and oxygen from air in the presence of a catalyst to generate electricity. The primary by-products of fuel cells are water and heat, making the technology very environmentally friendly. A single proton exchange membrane cell contains a polymeric membrane electrolyte sandwiched between anodic and cathodic electrodes. The membrane transports protons from the anode to cathode and must prevent significant diffusion of fuel and oxygen. Current is generated by applying a voltage across the cell causing molecules to dissociate into protons and electrons in the presence of a platinum catalyst. The hydrated polyelectrolyte films transport the protons to the cathode of the cell, while the electrons are transported to the currents collectors. The protons subsequently combine by reacting with either pure oxygen or air, in the presence of a catalyst at the cathode, to form water.

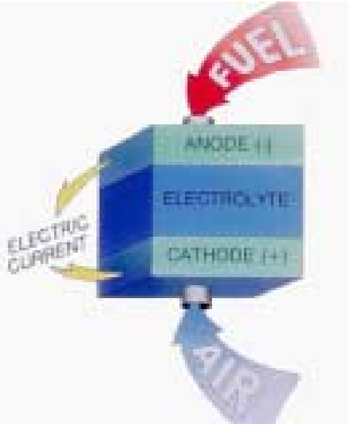

Figure 1. Schematic of a Single Proton Exchange Membrane Fuel Cell

Many common polymer membranes display poor properties in a fuel cell, but high performing perfluorinated polymers has emerged as the most widely used PEMs in fuel cells. Nafion, a poly (perfluorosulfonic acid) copolymer produced by Du Pont, is the current state-of-the-art polyelectrolyte membrane used for fuel cells. Although Nafion has many good chemical and physical properties for use in fuel cell applications, it has some drawbacks in terms of high cost, low conductivity at low humidity or high temperatures, as well as high methanol permeability, which decreases the cell efficiency.[3,4]

The challenge to find the ideal polymeric materials that will provide desired properties for use as a proton conductor in proton exchange membrane fuel cells (PEMFCs)[5] has been investigated ever since the use of ion exchange electrolytes for fuel cells was suggested in the 19th century.[6] Some of the desirable properties for a PEM include: (a) mechanically or functionally stable / durable film behavior in the cell operating environment with long life-times; (b) hydrophilicity for high proton conductivity, combined with water insolubility of the membrane; (c) reasonable production costs, compatible with application, etc.

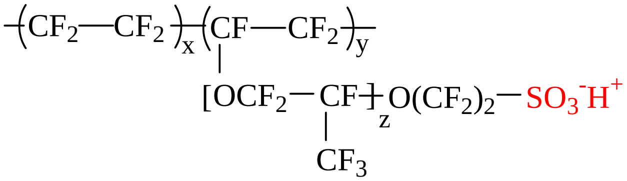

$$-(CF_2-CF_2)_x-(\underset{[OCF_2-\underset{CF_3}{CF}]_z-O(CF_2)_2-SO_3^-H^+}{CF}-CF_2)_y-$$

Figure 2. Nafion® perfluorosulfonic acid copolymer

Poly (arylene ether sulfone)s (PAES) are well known engineering thermoplastics that were first successfully prepared by R. Johnson, *et al* in 1967.[7] Their excellent mechanical properties, resistance to hydrolysis and oxidation, and high thermal stability have been well demonstrated. These characteristics allows for their usage in a variety of applications, such as adhesives, films, composite matrices and membranes. [8-10]

Nucleophilic aromatic substitution has been a successful technique to synthesizing PAES. Nucleophilic aromatic substitution involves the reaction a bisphenol and an activated dihalide in anhydrous aprotic, dipolar solvent such as N, N-dimethylacetamide (DMAC) or N-methyl 2-pyrrolidone (NMP). The reaction is carried out in the presence of a base (potassium carbonate) producing a reactive phenolate. This procedure generates high molecular weight amorphous polymers in less than 24h at temperatures ranging from 160-190°C depending on the reaction conditions.

Several researchers have examined modifications to PAES. The objective is to prepare advanced macromolecules for fuel cells by modifying PAES without sacrificing their excellent physical and other properties. The aromatic rings in the polymer backbone allow for facile electrophilic or nucleophilic reactions to modify the physical properties of the polymer. Sulfonation of the poly (arylene ether sulfone) s is one important modification that is being investigated. Sulfonated poly (arylene ether sulfone) s were investigated by Noshay and Robeson who used a relatively mild post-sulfonation procedure to chemically modify commercially available bisphenol-A based poly (ether sulfone).[11] Materials for desalination membranes for reverse osmosis and other water purification areas were also produced from this same method.

Studies show the post-sulfonation reactions on the polymer result in the placement of up to one sulfonic acid group per repeat unit ortho to the activated aromatic ether linkage. Sulfonic acids are introduced via electrophilic aromatic substitution using chlorosulfonic acid ($ClSO_3H$),[12] concentrated sulfuric acid,[13,14] pure or complexed sulfur trioxide,[15,16] and methanesulfonic acid.[17] In this research, chlorosulfonic acid was chosen as the sulfonating agent. Synthesis of sulfonated PAES first requires redissolving of the polymer in 1, 1, 2-trichloroethane (TCE)/ 1, 2-dicholorethane (DCE). The choice of solvents to maintain solubility depends on the type of PAES. Various mole percents of ClSO3H were diluted with 1,1,2 TCE and added slowly over a 30 minute interval to the polymer solution. The solution is allowed to stir over night and was precipitated out of methanol. The pendant sulfonate groups served as the proton exchange site in the PEMFC in a fuel cell.

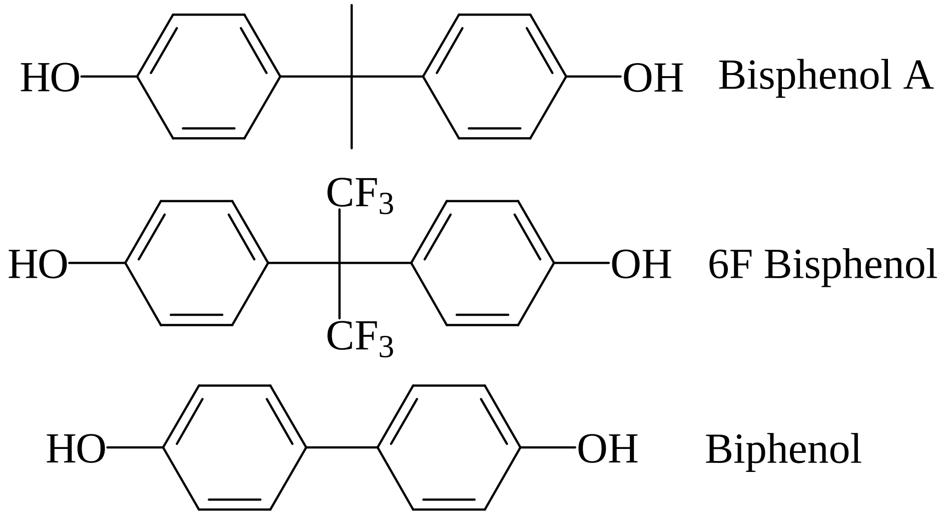

Figure 3. Investigated Bisphenol Structures

The objective of this research was to synthesize various sulfonated poly (arylene ether sulfone) s via step-growth, condensation polymerizations and to subsequent conduct post-sulfonation. The research utilized structurally different bisphenols and 4,4’-dichlorodiphenyl sulfone. Statistical or random copolymers area also being synthesized via using different molar ratios of sulfonated- and unsulfonated dihalide sulfone. The bisphenols investigated are shown below (Figure 3).

The selected bisphenols, shown in Fig.3 have been chosen on the basis of anticipated thermal and thermal-oxidative considerations, hydrophobicity characteristics and morphology, e.g. amorphous and rigidity. The structure-property relationship of the sulfonated poly (ether sulfone) s will be examined by the synthesis and characterization of a series of homopolymers and sulfonated analogues.

EXPERIMENTAL

Materials

Bisphenol A and 4,4- dichlorodiphenylsulfone (DCDPS) were obtained from BP-Amoco, and 4,4-biphenol (Eastman Chemical) were all monomer grade purity were dried and used as received. Hexafluorobisphenol A (6F-bis A) was received from Ciba and recrystallized from toluene. Potassium carbonate (Aldrich) was dried in vacuum oven at 130°C for twelve hours. Chlorosulfonic acid, chlorotrimethylsilane, and toluene were also obtained from Aldrich and used as received. The reaction solvents N-methyl-2-pyrrolidinone (NMP), dimethylacetamide (DMAC), 1, 2-dichloroethane (DCE), and 1, 1, 2-trichloroethane were purified by distillation from phosphorous pentoxide under vacuum and stored over molecular sieves.

Synthesis of Poly (aryl ether sulfone) s

For each respective bisphenol, the stoichiometric amount (1:1 molar ratio) of DCDPS is used. A sample polymerization is as follows: Bisphenol A 10g (0.044mol), DCDPS 12.648g (0.044mol), and potassium carbonate 7.003g (0.051mol, 15mol%) were dissolved in 65ml of distilled NMP in a 4-necked flask equipped with condenser, Dean Stark trap, nitrogen outlet and mechanical stirrer. The reaction mixture was heated at 145°C for 4 hours with refluxing toluene (30ml) as the azeotropic agent. The reaction temperature was slowly increased to 175°C, cooled by distillation and removal of toluene and allowed to react for 16-20 hours. The resulting viscous reaction mixture was diluted with dimethylacetamide (DMAc) and precipitated in vigorously stirring methanol and water mixture (9:1). The fibrous polymer was filtered and dried in a vacuum oven at temperatures up to 160°C.

Sulfonation of Poly (aryl ether sulfone)s

Sulfonation of 6F and biphenol based polymers did not utilize trimethylchlorosilane. Also due to solubility, biphenol based polymers were sulfonated in 1, 1, 2- trichloroethane. A typical reaction is as follows: Dissolve 3g of dried Bisphenol A polymer (0.0068mol) in 30ml 1,2-dichloroethane at room temperature for 1 hour in a 250ml 3-neck round bottom flask fitted with a mechanical stirrer, condenser, and a addition funnel with a nitrogen inlet. A mixture of chlorotrimethylsilane 0.7414g (0.0068mol) in 10ml of 1,2-dichloroethane (DCE) was added slowly over 15 minutes. Chlorosulfonic acid 0.7952g (0.0068mol) in 10ml of DCE was added dropwise over a 30-minute interval.[18] The reaction was allowed to stir overnight at 30° C. The reaction mixture is slowly added to methanol with vigorous stirring for 40 minutes. The precipitated polymer was washed with distilled water, then again in methanol and dried in vacuum oven overnight at temperatures up to 120°C.

Film Preparation

The dried sulfonated poly (aryl ether sulfone)s were redissolved in DMAc at 7 - 10% polymer concentration. Films were cast on glass plates under a nitrogen atmosphere and dried using infrared heating lamp.

CHARACTERIZATION

Fourier Transform Infrared (FTIR) Spectroscopy

FTIR spectroscopy was used to confirm the chemical composition of the sulfonated polymers. A Nicolet impact 400 FT-IR was used to record the FTIR spectra of the homogeneous, thin cast films.

Differential Scanning Calorimetry

The glass transition temperatures (*Tg*) were obtained on a Perkin-Elmer DSC-7 differential scanning calorimeter. Scans were conducted under nitrogen at a heating rate of 10^{o}C/min. Second heat *Tg* values are reported as the midpoint of the change in the slope of the baseline.

Thermogravimetric Analysis (TGA)

Dynamic TGA was employed to assess the thermal stability (weight loss) of the polymers using a Perkin-Elmer TGA-7 thermogravimetric analyzer. The hydrophilic copolymers were first vacuum dried and then kept in TGA furnace at 150^{o}C in nitrogen atmosphere for 30 minutes before TGA characterization. The typical heating rate was 10^{o}C/min in nitrogen.

Proton nuclear magnetic resonance (^{1}H NMR)

Proton nuclear magnetic resonance (^{1}H NMR) was conducted using a Varian 400 MHz instrument NMR Spectrometer. NMR spectroscopy was used to obtain chemical composition of the sulfonated and unsulfonated polymers used in the research. Homo- and sulfonated polymers NMR spectra were typically obtained from 10%(w/v) solutions dissolved in dimethylsulfoxide-d_6 (DMSO-d_6).

Intrinsic Viscosities and Solubility

Sulfonated polymer solubility was determined at a concentration of 10% (w/v) in a number of solvents, including NMP, DMAC, dimethylsulfoxide, and water. Intrinsic viscosities were determined at NMP at 25ºC using an Ubbelohde viscometer. Intrinsic viscosities were determined at NMP at 25^{o}C using an Ubbelohde viscometer.

RESULTS AND DISCUSSION

Successful synthesis of poly (arylene ether sulfone)s shown in Fig. 4 was achieved using bisphenol A, 6F bisphenol and biphenol, respectively, with dichlorodiphenyl sulfone with NMP as the polymerization solvent and toluene as an azeotropic agent in the presence of potassium carbonate. The desired sulfonated PAESs were synthesized from their homopolymers by dissolving in 1,2-dichloroethane or 1,1,2-trichloroethane and sulfonated using various molar ratios of chlorosulfonic acid. Chlorosulfonic acid and chlorotrimethylsilane were added to the polymeric solution respectively as a solution in 1, 2-DCE. It was discovered that chlorosulfonic acid was only temporarily miscible in 1,1,2-trichloroethane. For the biphenol series, in which

1,1,2-TCE was used the sulfonation solvent, a few reactions were attempted in which the chlorosulfonic acid was diluted with the DCE and added to the polymer solution. In these experiments no appreciable sulfonation was observed. The resulting compound was precipitated with methanol/water filtered and allowed to dry overnight in the vacuum oven without heat and then at 60- 100°C for 1 day.

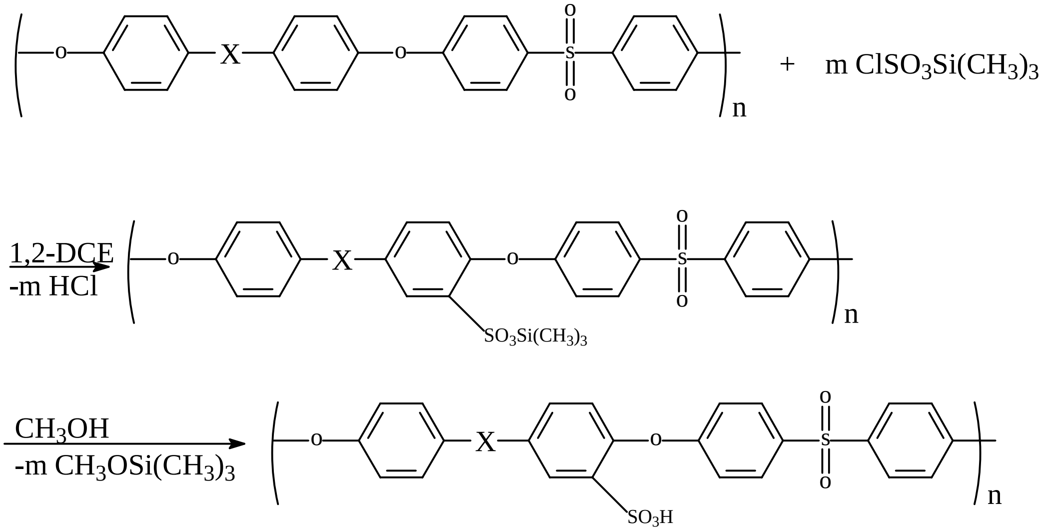

Figure 4. Synthesis of Sulfonated Poly (aryl ether sulfone)s

Tough, ductile films were obtained from DMAc solutions. FTIR spectra of the sulfonated polymers display the characteristic signal at 1025 cm^{-1} for the pendant sulfonic acid group. The relative increase in the intensity of the sulfonate group provides qualitative degrees of sulfonation. Figure 5 shows the FTIR series of sulfonated bisphenol A-based poly (aryl ether sulfone)s (BA-PAESs).

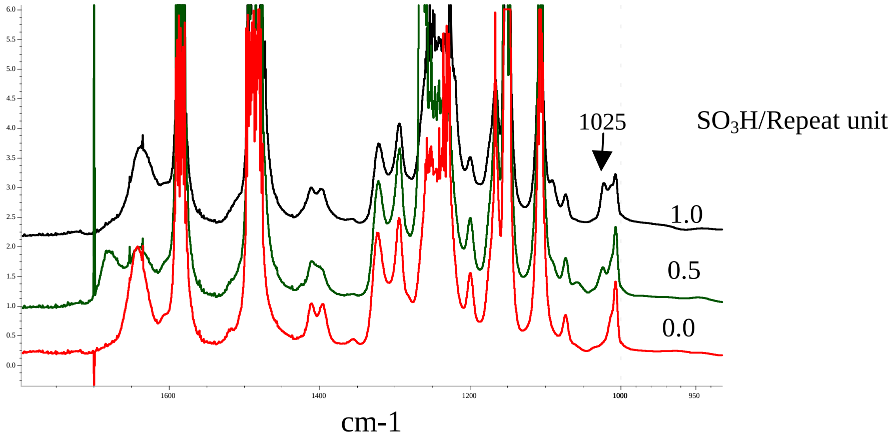

Figure 5. FTIR Spectra of Sulfonated Bisphenol A-PAESs

Proton NMR spectra were obtained for all the sulfonated polymers to confirm chemical composition. By taking the ratio of the integrated hydrogen adjacent to the sulfonated group to another known proton on the polymer chain one can determine the degree of sulfonation. Figure 4 shows an example of the sulfonated 1:1 biphenol A. As seen, each peak on the spectra can be assigned to protons along the polymer backbone. Integration of the hydrogen peak adjacent to the sulfonated group showed that there was only a 75% degree of sulfonation.

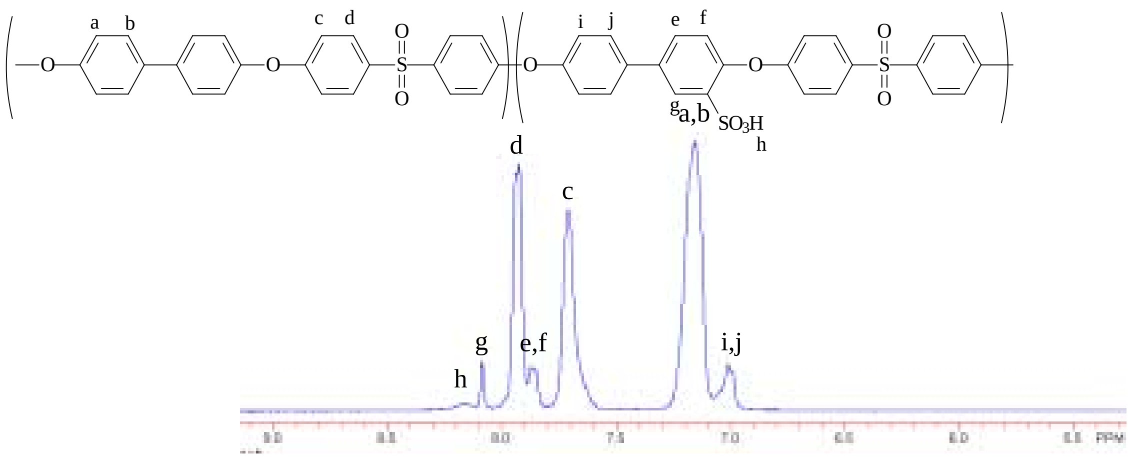

Figure 6. NMR Spectra of Sulfonated Biphenol-PAESs

Table 1 below demonstrates how different degrees of sulfonation affect the intrinsic viscosity of the polymers. The viscosity increase with higher degrees of sulfonation can be accredited to the association of the ionic sulfonate groups that is commonly observed in the case of ionomers.[19]

Table 1. Intrinsic Viscosity of Sulfonated PAESs

Polymer Type→ **Moles $ClSO_3H$↓**	**BA-PAES**	**BP-PAES**	**6F-PAES**
0	**0.52**	**0.50**	**0.50**
0.5	**0.67**	**0.52**	**0.56**
0.7	**0.86**	**0.51**	**-**
1.0	**2.8**	**0.86**	**0.69**
2.0	**1.21**	**0.60**	**1.78**

The effect of the degree of sulfonation on the glass transition temperature (T_g) was also investigated using DSC. The values found by DSC are presented in Table 2. These values confirmed, that the T_g did indeed increase as sulfonation increased. This might be due to the ionomer effect and bulky sulfonate groups restricting chain rotation. However, for the more highly sulfonated polymers no glass transition temperatures were observed. This can be attributed to the fact that some sulfonated ionomers have very broad transitions that are undetectable.

Table 2. DSC Glass Transitions Temperatures

Polymer Type	**0**	**0.5**	**0.7**	**1.0**	**2.0**
Bisphenol A	**188**	**200**	**-**	**undetected**	**undetected**
6F Bisphenol	**190**	**212**	**220**	**-**	**undetected**
Biphenol	**210**	**-**	**234**	**247**	**undetected**

Thermogravimetric analysis showed the thermal oxidative stability of the sulfonated polymers were different from that of the unsulfonated homopolymers. Figure 7 shows the thermal stability of bisphenol A homopolymers and its sulfonated analogue (1.0 SO_3H per repeat unit). The homopolymers shows high thermal stability to 460^{o}C while the sulfonated polymer displays distinct degradation beginning at 275^{o}C. This degradation is attributed to the lost of the pendant sulfonic acid group.

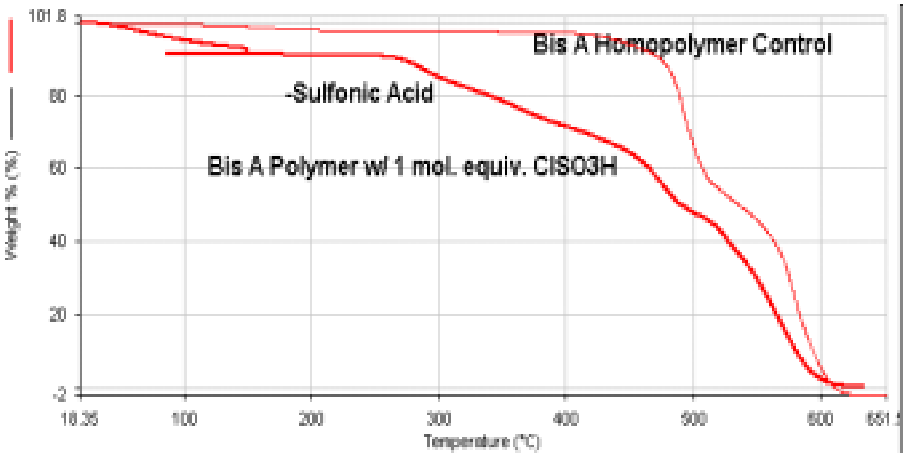

Figure 7. TGA Thermogram of Sulfonated and Unsulfonated Bisphenol A PAES

CONCLUSION

High molecular weight poly (arylene ether sulfone)s were synthesized. Various levels of sulfonation using chlorosulfonic acid were successfully achieved for the polymers. However, reproducibility of the desired level of sulfonation was difficult for all three polymer series; each degree of sulfonation were attempted in duplicate and/or triplicate with extreme variations in actual amount of substitution. Proton NMR and FTIR were effective tools used to verify the chemical composition of the unsulfonated and sulfonated PAES. Intrinsic viscosity and glass transition temperatures increased with increasing degrees of sulfonation**.** Thermal stability of the sulfonated polymers was less than that of the respective homopolymers due to the loss of the sulfonic acid group.

CURRENT AND FUTURE RESEARCH

Future syntheses of sulfonated poly (arylene ether sulfone)s will further complete, systematically, each polymer series and allow for further characterizations. Water sorption and other experiments will be conducted and used to draw possible correlations with conductivity, polymer -membrane swelling, etc. Potentiometric titration will also be carried out to determine the actual ion exchange capacity of the polymers. Careful analysis of all the data is also needed to identify any structure-property relationships as they pertain to bisphenol structure.

ACKNOWLEDGEMENTS

The authors of this paper would like to gratefully acknowledge the National Science Foundation for funding. Mr. Tom Glass of the Department of chemistry for his assistance with the proton NMR. Virginia Polytechnic Institute and State University, Department of Chemistry, Center for High Performance Polymer Adhesives and Composites without whom all this would not be possible.

REFERENCES

1) a) Applby, A.J., “The Electrochemical Engine for Vehicles”; b) Lloyd, A.C., “The Powerplant in Your Basement”; c) Dyer, C.K., “Replacing the Battery in Portable Electronics,” *Sci. American,* , 72-93 **(**July 1999).
2) “Fuel Cells are Heading for Sale,” *C&E News*, 31, (June 14, 1999).
3) Miyatake, K., Iyotani, H., Yamamoto, K., Tsuchida, E., *Macromolecules*, 29, 6969 (1996).
4) Zhang, Y., M., Savinell, R.F., Wainright, J.S., *ACS Div. Polym. Chem., Polym. Preprs*., 40(2), 480 (1999**)**.
5) Savadogo, J.O., *New Mat. Electrochem. System*, 1, 47 (1997**)**.
6) W.T. Grubb, *Proceedings of the 11th Annual Battery Research and Development Conference*, PSC Publications Committee, Red Band, NJ, p.5, (1957).
7) Johnson, R.N., Farnham, A.G., Clendinning, R.A., Hale, W.F., Merriam C.N., *J. Polym. Sci.:* A-1(5), 2399 (1967).
8) R.N. Johnson, Encyclopedia of Polymer Science and Technology, N.M. Bikales, Ed., Wiley, New York, (1969).
9) D.C. Clagett, Encyclopedia of Polymer Science and Engineering, Mark, H. F.; Bikales, N. M.; Overberger, C. G.; Menges, G., Ed., John Wiley & Sons: New York, , Vol. 6, 94 (1986**)**.
10) R.J. Cotter, Engineering Plastics: Handbook of Polyarylethers Gordan and Breach Publishers: Basel, Switzerland, (1995).
11) A Noshay; L.M. Robeson, *J. Appl. Polym. Sci.*, (1976) **20**, 1885; C.L. Brousse; R. Cheapurlet; J.P. Quentin, *Desalination*, (1976) **18**, 137; V. Deimede, G.A. Voyiatzis, J.K. Kallitsis, L. Qingfeng, N.J. Bjerrum,; *Macromolecules*., (2000) **33**, 7609.
12) J. Lee and C.S. Marvel, *J Polym. Sci., Polym. Chem. Ed*., **22**, 295 (1984).
13) L. Jia, X. Xu, H. Zhang, and J. Xu, *J. Appl. Polym. Chem*., **60**, 1231 (1996).
14) X. Jin, M.T. Bishop, T.S. Ellis, and F.E. Karasz, *Br. Polym. J*., **17**, 4 (1985).
15) M.I. Litter and S. Marvel, *J. Polym. Sci., Polym. Chem. Ed*., **23**, 2205 (1985).
16) T, Owaga and C.S. Marvel, *J. Polym. Sci., Polym. Chem. Ed*., **23**, 1231 (1985).

17) C. Bailly, D.J. Williams, F.E. Karasz, and W. J. MacKnight, *Polymer*, **28,** 1009 (1987).
18) R. Nolte; K. Ledjeff; M. Bauer: R. Mulhaupt, *J. Membr. Sci*., 83, 211, (1993**)**.
19) Tant, M.R., K.A., Wilkes, G.L. Eds. *Ionomers: Synthesis, Structure, Properties, and Application*; Blackie Academic and Professional (Chapman & Hall): New York, (1997).

Chemical Modification Of Silicon And Silicon Carbide Surfaces Via Plasma Treatment

Michael J. Bluemle*, David Xu, and John G. Dillard
Department of Chemistry
Virginia Polytechnic Institute and State University
Blacksburg VA, 24061-0212

* Department of Chemical Engineering, Case Western Reserve University, Cleveland, OH

ABSTRACT

The plasma treatments of silicon and silicon carbide surfaces with 3-aminopropyl-triethoxysilane (3-APS), vinyltriethoxysilane (VTES), 3- glycidoxypropyltrimethoxysilane (GPTMS), and acetylene/nitrogen plasmas were investigated to determine the surface chemistries created in these processes. Characterizations of these plasma treated surfaces were done using X-ray Photoelectron Spectroscopy (XPS) and Atomic Force Microscopy (AFM). Treatment of both substrates with a 3-APS plasma yielded a high silicon concentration (~ 36%), low nitrogen concentration (~ 5%) film or a high nitrogen (~ 35%), very low silicon concentration (~ 1%) film depending upon the gases used in pretreatment and post-treatment of the substrates. Plasma treatment of silicon and silicon carbide substrates with VTES created an SiO_2-like layer with little hydrocarbon chemistry (~ 5%). The GPTMS plasma treatment increased the oxygen concentration and decreased the carbon concentration of the substrate surfaces, but the mechanism for this process has not yet been determined. Lastly, the acetylene/nitrogen co-polymerization plasma created a hydrocarbon plasma polymer with the incorporation of ~ 7% nitrogen. The treatments with 3-APS and VTES plasmas had the effect of smoothing the silicon carbide substrate topography, whereas the GPTMS plasma slightly roughened the silicon carbide surface.

INTRODUCTION

Previous works [1-3] have documented the use of organosilanes as an adhesion promoter or coupling agent in a wide variety of systems including silicon surfaces. These processes usually involve aqueous or alcohol solutions, which forms a monolayer of the organosilane onto the substrate surface. The utilization of plasma treatments eliminates the need for solvents and is much a benign, environmentally friendly process. Plasma exists as a partially ionized gas containing positively and negatively charged particles and excited neutrals is considered the fourth state of matter. A plasma contains activated species that are able to initiate chemical and physical reactions at the surface of metals, glass fibers, polymers, and many other materials [4]. Polymerization, deposition and ablation can occur within the plasma depending upon the chemistry of the gases used.

The present paper reports results of research concerning the radio frequency (RF), low pressure plasma treatment of silicon and silicon carbide substrates with acetylene/nitrogen and organosilane monomers: (1) 3-aminopropyltriethoxysilane (3-APS), (2) vinyltriethoxysilane (VTES), and (3) 3-glycidoxypropyltrimethoxysilane (GPTMS). The chemical structures of these organosilanes being as follows:

(1) $NH_2(CH_2)_3–Si–(OCH_2CH_3)_3$; (2) $CH_2=CH–Si–(OCH_2CH_3)_3$;

(3)

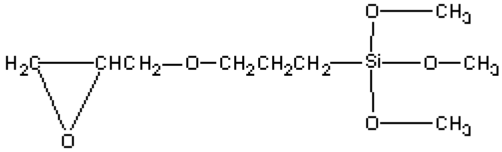

These organosilanes are similar in structure, but each has a different functional group at the end, which may enhance adhesion between the silicon or silicon carbide substrate and a polymeric coating. This type of bonding situation is common in a large number of microelectronic applications from pacemakers to cellular phones.

EXPERIMENTAL

Plasma treatment of substrates

The system for depositing the plasma films is shown in Figure 1. The apparatus is a Pyrex glass tube that is evacuated using a turbo and a rotary pump. The system has inlets for different gases to permit plasma treatments that could facilitate the preparation of co-polymerized coatings. Substrates were placed flat, with the face to be treated upwards, along the bottom of the reactor, ~ 15 cm (5.9 inches) away from the first RF coil. Prior to plasma treatment, the reactor pressure was reduced to less than 10 mTorr (measured with a Hastings-Raydist thermocouple gauge). In most cases the substrates were pretreated with a two-minute plasma to clean and activate the surface at a power setting of 50 W. In the case of organosilanes, the carrier gas was then introduced continuously through the organosilane in a bubbler cell attached to the reactor chamber. The gas flow was monitored by a Brooks Instruments 50 sccm mass flow controller (model 5850). Once the pressure in the plasma reactor was stable, the plasma was ignited and the power setting adjusted to 10 W. The inductive coil was tuned to match the source impedance to minimize the reflected power. Following the plasma treatment, the reaction chamber was purged for 10 minutes. This purge process removed any residual reactive radicals/species from the wafer surface. The samples were then removed from the reactor chamber and stored for characterization. The plasma reactor was cleaned with a 50 W oxygen plasma between each run.

The plasma polymerization experiments involved a combination of the following components:

pretreatment gas: argon, nitrogen, oxygen, and no treatment
plasma gas: 3-aminopropyltriethoxysilane (3-APS), vinyltriethoxysilane (VTES),
3-glycidoxypropyltrimethoxysilane (GPTMS), acetylene, acetonitrile
carrier gas: argon, nitrogen, acetylene, ammonia
post-treatment (purge) gas: argon, oxygen, acetylene, ammonia

The organosilanes were obtained from Aldrich Chemicals and shipped and packaged under nitrogen to prevent hydrolysis. The combination of pretreatment, plasma, carrier and purge gases was varied from run to run. The plasma treatment time was also varied, but a common preparation time of 15 minutes was used in most runs. The substrates used for plasma treatment were 15 mm square unpolished silicon and polished silicon carbide substrates.

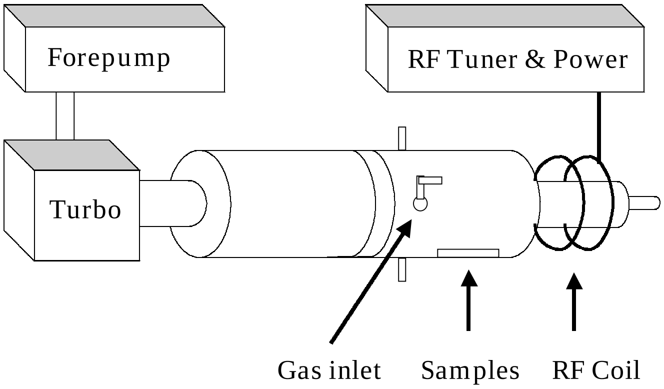

Figure 1. Schematic diagram of plasma reactor [5].

XPS characterization

All samples were characterized using a Perkin-Elmer Model 5400 XPS spectrometer equipped with a Mg K_α X-ray source (1253.6 eV), operated at 300 W and 14 kV DC, with an emission current of 25 mA. A 1.0 x 3.0 mm area was scanned by the spectrometer. Photoelectrons were analyzed in a hemispherical analyzer using a position-sensitive detector. The CC/CH carbon peak was calibrated to a binding energy of 285.0 eV. The atomic percentages were calculated by measuring the peak area of the respective photopeaks and correcting the measurement to account for ionization probability, analyzer transmission characteristics, and detector sensitivity.

AFM characterization

A Digital Instrument Atomic Force Microscope Dimension 3000 with a silicon cantilever and tip was used to characterize the topography of modified and unmodified silicon and silicon carbide surfaces. All AFM images were obtained using TappingMode AFM. 1 μm x 1 μm or 5 μm x 5 μm AFM scans were usually collected at a scan rate of 1.000 kHz.

RESULTS AND DISCUSSION

Plasma treatment with 3-APS

The plasma treated wafers were characterized using surface sensitive XPS and AFM. The surface chemistry of the untreated, as received, silicon carbide and silicon samples was characterized by carbon, oxygen, nitrogen, and silicon. The XPS surface characterization results for the 3-APS treated and untreated substrates are presented in Table 1. After plasma treatments using oxygen or argon as the pretreatment gas, with argon as the carrier gas, 3-APS as the plasma gas, and argon as the purge gas, the surface chemistry is altered in that the carbon concentration is reduced from about 40% to approximately 20%. The silicon concentration is lowered very slightly from ~ 30% to ~ 25-28%. Following these treatments, the oxygen and nitrogen concentrations increase to ~ 45% and ~ 5%. From the Si 2p binding energy results, silicon appears to be present in a form of SiO_2. An interpretation of these results suggests two different processes in the plasma treatment: 1) the initial surface is "cleaned" of contaminants as evidenced by the decrease in carbon and the increase in oxygen, or 2) the plasma induces the decomposition of 3-APS resulting in a coating containing nitrogen, oxygen, carbon, and silicon in some unidentified chemical functionality.

Table 1. Typical XPS results of SiC and Si substrates before and after 3-APS plasma treatments

Substrate	Pre-treatment	Plasma Treatment	Purge	Elemental Analysis			
				% C	**% O**	**% N**	**% Si**
SiC		Untreated		42.8	23.4	1.6	32.2
Si		Untreated		8.4	45.7	0.0	45.9
SiC	2 min Ar	15 min Ar thru 3-APS	10 min Ar	22.1	45.5	5.5	27.0
SiC	2 min O_2	30 min Ar thru 3-APS	10 min Ar thru 3-APS	21.3	44.8	5.6	28.3
Si	2 min Ar	15 min Ar thru 3-APS	10 min Ar	10.0	50.7	4.2	35.1
SiC	2 min O_2	15 min Ar thru 3-APS	10 min O_2	39.1	22.3	37.5	1.1
SiC	2 min Ar	15 min Ar thru 3-APS	10 min O_2	38.8	23.3	37.0	0.9
Si	None	15 min N_2 thru 3-APS	10 min N_2 thru 3-APS	41.8	21.1	37.1	0.0
Si	2 min Ar	15 min Ar thru 3-APS	10 min O_2	38.8	23.0	36.4	1.8

Plasma treatment of the silicon carbide or silicon wafers with 3-APS using other gas combinations results in the formation of a coating that contains little or no silicon and significant amounts of nitrogen. The approximate compositions for these coatings are: C = 40%, O = 20%, and N = 40%. It is apparent that the process using these gas compositions results in the formation of a coating that involves decomposition or fragmentation of the 3-APS reactant.

The elemental functionality of the coatings is also different for the two different coatings. For the samples exhibiting significant silicon, the surface includes silicon as SiO_2 and Si (elemental) in approximately equal concentrations. The chemistry associated with carbon includes the functionalities, CC/CH, C-O (carbon singly bonded to oxygen), and carbonate (CO_3^{2-}) and carboxyl (COO^-) carbon. On the other hand, for the specimens that contain little or no silicon, the carbon surface functionalities include CC/CH, C-O or C-N (carbon singly bonded to oxygen or nitrogen) and C=O or C=N or O=C-N groups. These differences are no doubt a result of the different reaction-deposition processes that occur in the plasma. At the moment it is not possible to offer a reaction scheme to account for the differences, although experiments are in progress hopefully to identify potential reaction processes.

Plasma treatment with VTES

The surfaces of specimens treated in a vinyltriethoxysilane plasma using various combinations of argon and nitrogen as the carrier gas show similar surface chemistries on the silicon and silicon carbide substrates as indicated in Table 2. The surfaces contain principally silicon and oxygen. Compared to the as received surface, carbon is present at a very low level (~ 5%) and nitrogen is detected at concentrations less than 1%. The specific chemistry is that silicon is present as an SiO_2 –like component and carbon occurs as CC/CH. The oxygen photopeak is characteristic of oxygen associated with silica or SiO_2. The plasma process results in an apparent "cleaning" of the wafer surface with little or no deposition of vinyl-containing components. It appears that the anticipated polymerization involving the vinyl group does not take place under the plasma conditions employed in this series of experiments.

Table 2. Typical XPS results of SiC and Si substrates after VTES plasma treatments

Substrate	**Pre-treatment**	**Plasma Treatment**	**Purge**	**Elemental Analysis**			
				% C	**% O**	**% N**	**% Si**
SiC		untreated		42.8	23.4	1.6	32.2
Si		untreated		8.4	45.7	0.0	45.9
SiC	2 min O_2	15 min Ar thru VTES	10 min O_2	3.8	64.8	0.2	31.1
SiC	2 min Ar	15 min Ar thru VTES	10 min Ar	5.9	63.2	0.8	30.1
SiC	2 min Ar	15 min Ar thru VTES	10 min O_2	3.7	65.6	0.8	29.8
SiC	2 min NH_3	15 min Ar thru VTES	10 min NH_3	3.6	65.8	0.8	29.8
SiC	2 min Ar	10 min Ar thru VTES	10 min Ar	4.4	64.9	0.0	30.7
SiC	2 min Ar	5 min Ar thru VTES	10 min Ar	7.1	62.4	0.2	30.4
Si	2 min O_2	15 min Ar thru VTES	10 min O_2	4.0	64.9	1.2	29.8
Si	2 min Ar	15 min Ar thru VTES	10 min Ar	3.7	65.1	1.0	30.2
Si	2 min Ar	15 min Ar thru VTES	10 min O_2	2.8	65.5	1.0	30.7
Si	2 min NH_3	15 min Ar thru VTES	10 min NH_3	3.2	65.3	0.9	30.6
Si	2 min Ar	10 min Ar thru VTES	10 min Ar	6.0	63.5	0.2	30.3
Si	2 min Ar	5 min Ar thru VTES	10 min Ar	4.6	62.9	0.1	32.4

SiC	2 min O_2	15 min Acet[1] thru VTES	10 min O_2	13.2	57.8	0.0	29.0
Si	2 min O_2	15 min Acet thru VTES	10 min O_2	7.5	59.6	0.5	32.4
SiC	None	5 min Acet/Ar thru VTES	10 min Acet	84.9	12.8	1.1	1.2
Si	None	5 min Acet/Ar thru VTES	10 min Acet	84.3	13.0	1.5	1.1

[1] Acet = acetylene

In two experiments involving acetylene as the carrier gas, films with an increased carbon content were obtained. For these films the silicon content remained about the same as for other conditions discussed above. The principal change occurred in the distribution of carbon-containing components. For these two samples evidence of oxidized carbon components was obtained. It is not possible, at this time to propose a process for the deposition of films under these conditions.

The chemical composition of films produced using a co-polymerization of the vinyltriethoxysilane and acetylene yield a film that contains significant carbon (~ 85%). For each of these films, the elemental composition includes carbon, oxygen, nitrogen, and silicon. The specific process taking place is unknown. The carbon chemistry is predominantly that associated with CC/CH functional groups and demonstrates that the plasma processes occurring are predominantly associated with acetylene rather than the vinyl-silane.

Plasma treatment with GPTMS

The results of silicon carbide and silicon surfaces treated with a 3-glycidoxypropyl-trimethoxysilane plasma using various carrier gases is shown in Table 3. With this treatment the similarities within the silicon or silicon carbide substrates is greater than between the two types of surfaces. Compared to the as received silicon carbide substrate surface, the carbon concentration decreases significantly from ~ 40% to ~ 15%, the oxygen concentration increases from ~ 23% to ~ 53%, and the silicon concentration remain approximately the same at ~ 30%. For the silicon substrates, the decrease in carbon concentration is less significant with a decrease of ~ 8% to ~ 6%. The changes in oxygen and silicon concentrations are also small with a ~ 10% increase in oxygen and a ~ 8% decrease in silicon for the silicon substrates. The nitrogen concentrations for all substrates are ~ 1% or less. The carbon chemistry includes CC/CH and C-O (carbon singly bonded to oxygen) functionality. Additional experiments will be conducted to examine what effect pre- and post-treatments have on the treatment of silicon carbide and silicon substrates with GPTMS plasmas.

Table 3. XPS results of SiC and Si substrates after GPTMS plasma treatment

Substrate	**Pre-treatment**	**Plasma Treatment**	**Purge**	**Elemental Analysis**			
				% C	**% O**	**% N**	**% Si**
SiC		untreated		42.8	23.4	1.6	32.2
Si		untreated		8.4	45.7	0.0	45.9

SiC	2 min O_2	15 min Ar thru GPTMS	10 min O_2	14.6	53.8	0.1	31.5
SiC	2 min O_2	15 min N_2 thru GPTMS	10 min O_2	17.0	53.6	0.0	29.3
SiC	2 min O_2	15 min Acet thru GPTMS	10 min O_2	16.3	52.5	0.9	30.3
Si	2 min O_2	15 min Ar thru GPTMS	10 min O_2	7.3	54.1	1.1	37.5
Si	2 min O_2	15 min N_2 thru GPTMS	10 min O_2	5.1	56.7	0.3	38.0
Si	2 min O_2	15 min Acet thru GPTMS	10 min O_2	6.0	56.8	0.4	36.9

Plasma treatment with acetylene/N_2

The results of silicon and silicon carbide surface treated with an acetylene/nitrogen plasma are shown in Table 4. Purges with nitrogen, acetylene and oxygen all yield similar concentrations of carbon, oxygen, nitrogen and silicon. Compared to the as received substrates, the carbon concentrations increase greatly to ~ 83% and the oxygen concentrations decrease greatly to ~ 8%. The silicon concentrations also decrease significantly to less than 1%. The small increase of nitrogen concentration (~ 7%) indicates some incorporation of nitrogen containing functionality to the plasma polymerized film. The carbon chemistry is predominantly that which is associated with CC/CH functional groups, but also exhibits some C-N (carbon singly bonded to nitrogen) functionality. This is agrees with the expected mechanism for acetylene/nitrogen plasma polymerization.

Table 4. XPS results of Si and SiC substrates after acetylene/nitrogen plasma treatment

Substrate	**Pre-treatment**	**Plasma Treatment**	**Purge**	**Elemental Analysis**			
				% C	**% O**	**% N**	**% Si**
SiC		untreated		42.8	23.4	1.6	32.2
Si		untreated		8.4	45.7	0.0	45.9
SiC	2 min O_2	5 min Acet/N_2	10 min N_2	81.2	10.3	7.7	0.8
Si	2 min O_2	5 min Acet/N_2	10 min Acet	84.8	7.0	8.2	0.0
Si	2 min O_2	5 min Acet/N_2	10 min O_2	85.3	8.0	6.7	0.0
Si	2 min O_2	10 min Acet/N_2	10 min O_2	85.4	7.3	7.3	0.0
Si	2 min O_2	20 min Acet/N_2	10 min O_2	82.6	10.7	6.7	0.0
Si	2 min O_2	5 min Acet/N_2	10 min N_2	82.0	9.6	7.8	0.6

AFM images of treated and untreated silicon carbide substrates

The AFM images of untreated and treated silicon carbide wafers are shown in Figure 2. The untreated surface (Figure 2a) is a very smooth surface with mostly low points and only occasional high points. In the subsequent images of the treated surfaces (Figures 2b, 2c, and 2d), there are an increased number of high points with the low points no longer visible. The 3-APS and VTES plasma treatments give a slightly smoother surface than the untreated substrate, whereas the GPTMS plasma treatment yields a rougher surface. It must be noted that all of the images have the same x- and y-scales, 1 μm x 1 μm, the z-scales are not all the same. In Figures 2a, 2b, and 2c, the maximum z value is 5 nm. In Figure 2d, the GPTMS treated substrate, the maximum z value is 10 nm. These AFM images are evidence that these plasma treatments have an effect on the surface topography of the silicon carbide substrates.

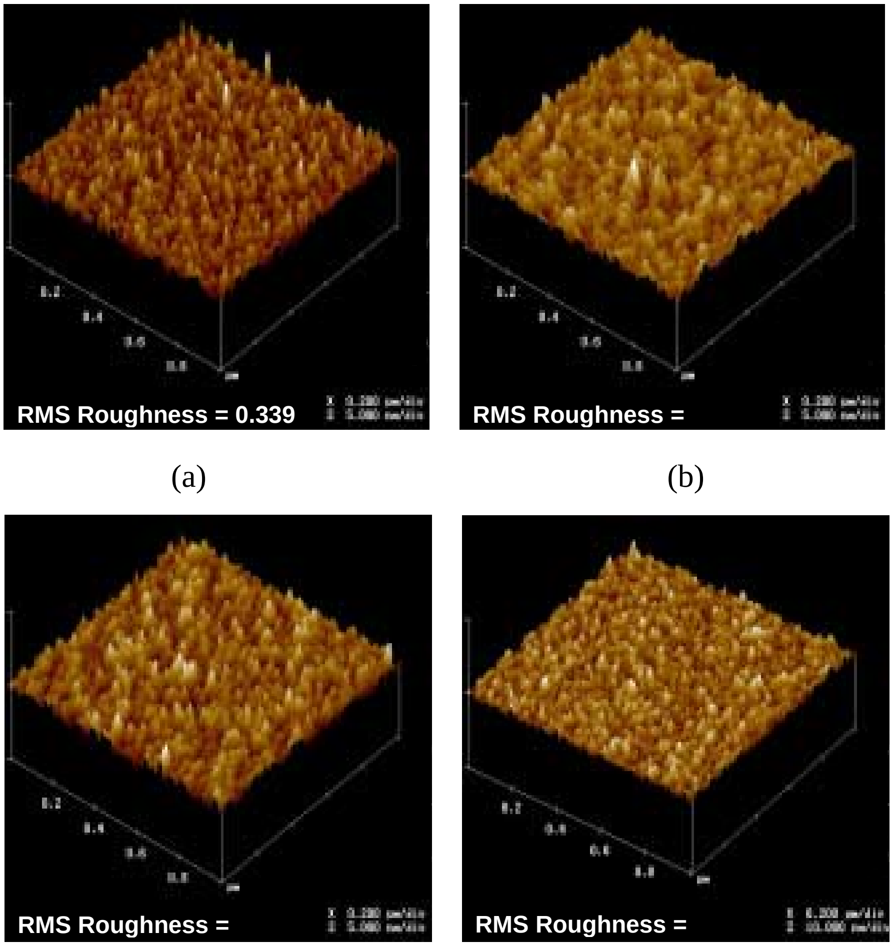

(a) (b)

(c) (d)

Figure 2. 1 μm x 1 μm AFM images of SiC substrate (a) untreated, (b) plasma-treated with 3-APS (2 min Ar pre, 15 min Ar→3-APS plasma, and 10 min O_2 purge), (c) plasma-treated with VTES (2 min Ar pre, 15 min Ar→VTES plasma, and 10 min O_2 purge), and (d) plasma-treated with GPTMS (2 min O_2 pre, 15 min N_2→GPTMS plasma, and 10 min O_2 purge).

CONCLUSIONS

The present research involving plasma treatments of organosilanes and acetylene/nitrogen has shown the following:

1. Treatment with a 3-aminopropyltriethoxysilane plasma yielded two very different films depending upon pretreatment and purge gases. Using oxygen or argon as the pretreatment gas, with argon as the carrier gas, and argon as the purge gas yielded a high concentration of silicon (~ 36%), low nitrogen concentration (~ 5%) film. Using other gas combinations created a high nitrogen (~ 35%), very low silicon concentration (~ 1%) film.
2. Plasma treatment with vinyltriethoxysilane yielded similar results for all combinations of gases. The plasma process resulted in an apparent "cleaning" of the wafer surface with little or no deposition of vinyl-containing components and deposition of an SiO_2-like layer.
3. Treatment with a 3-glycidoxypropyltrimethoxysilane plasma was also briefly studied. The functionality of the film created by this organosilane is unclear at this point and it is not yet known if the epoxide group was incorporated into the film.
4. The acetylene/nitrogen co-polymerization plasma successfully incorporated nitrogen containing functionality into an acetylene plasma polymer.

FUTURE WORK

The use of these plasma treatments as an adhesion promoting technique for the bonding of silicon and silicon carbide substrates to epoxies is still being evaluated. The effects of other plasma monomers, such as acetonitrile or additional organosilanes, on the surface chemistries of these substrates will be studied. Investigation of the effects of other plasma treatment process parameters on the surface chemistry of silicon and silicon carbide substrates will also be conducted.

ACKNOWLEDGEMENTS

The authors would like to thank the Hewlett-Packard Corporation for funding this research.

REFERENCES

1. D.E. Leyden, *Silanes Surfaces and Interfaces*, Gordon and Breach Science Publishers: New York, **1986.**
2. E.P. Plueddemann, *Silane Coupling Agents*, Plenum Press: New York, **1982.**
3. K.L. Mittal and A. Pizzi, *Adhesion Promotion Techniques*, Marcel Dekker, Inc.: New York, **1999.**
4. N. Inagaki, *Plasma Surface Modification and Plasma Polymerization*, Technomic Publishing Company: Lancaster, PA, **1996.**
5. R.A. DiFelice, Ph.D. Thesis, Virginia Tech, April 2001, Chapter 3.

Interactions Between Cationic Surfactants and Poly(Ethylene Oxide) Measured by Surfactant-Selective Electrodes

Kerry Campbell[a], William Lokar[b] and William Ducker[b]
[a] Department of Chemical Engineering, Kansas State University
[b]Department of Chemistry, Virginia Tech

ABSTRACTS

Interactions between poly(ethylene oxide) and the bromide and chloride salts of dodecyltrimmethyl ammonium ($C_{12}TA^+$) surfactants as well as dodecylammonium chloride (C_{12}ACl) were studied by electromotive force (EMF) measurements using ion-selective membrane electrodes. No detectable interaction was observed between PEO and C_{12}TAB and C_{12}TACl. Strange behavior was observed in the region around the cmc of C_{12}TACl, which was probably caused by impurities in the surfactant used. No conclusive data was obtained using the C_{12}ACl membrane electrode. This also may have been caused by impurities within the surfactant used to create the surfactant-selective membrane. Another possibility is that the physical properties of the C_{12}ACl membrane were not suitable to detect such ions.

Synthesis Of Bis(5-Carboxy-1,3-Phenylene)-14-Crown-4 And Its Polymerization With 4,4'-Oxybisaniline

Chin Ping Chng[a], Hong Wang, and Harry W. Gibson
Virginia Polytechnic Institute and State University
Department of Chemistry
Blacksburg, VA

[a] Department of Chemical Engineering, Florida Institute of Technology, Melbourne, FL

ABSTRACT

A novel rigid 14-membered diester crown ether, bis(5-carbomethoxy-1,3-phenylene)-14-crown-4 (**4**) has been synthesized using methyl 3,5-dihydroxybenzoate (**1**) and methyl 3,5-bis(2-chloroethoxy)benzoate (**3**) in the presence of sodium hydride in N,N-dimethylformamide (DMF). Several problems during the syntheses of precursors to the crown ether have been identified, and the best method for synthesizing methyl 3,5-bis(2-hydroxyethoxy)benzoate (**2**) was determined.

INTRODUCTION

A pseudorotaxane consists of a linear molecule that threads a cyclic molecule. These two species are linked mechanically but not covalently. In a pseudorotaxane, there are no bulky end groups on the linear molecule, so dethreading of the cyclic molecule is possible. In contrast, a rotaxane consists of bulky groups at the ends of the linear species that confine the cyclic ring at its position and prevent dethreading (Scheme 1).

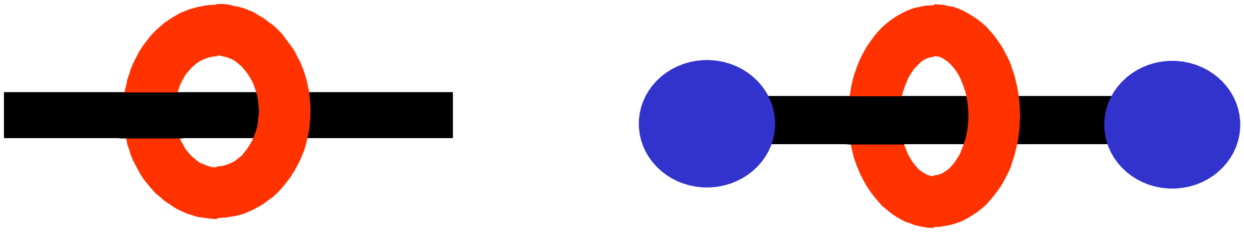

Scheme 1. Pseudorotaxane vs. Rotaxane

The structural requirement for the formation of pseudorotaxanes/rotaxanes is that the cavity size of the cyclic molecule has to be larger than the cross sectional area of the linear species to ensure that threading could occur. There are mainly four kinds of driving forces that could result in the formation of rotaxanes, including hydrogen bonding, π-π stacking, hydrophobic-hydrophilic interaction, and also electrostatic interaction.

Polypseudorotaxanes/polyrotaxanes consist of repeated units that contain pseudorotaxanes/rotaxanes. There are different architectures for the formation of polypseudorotaxanes/polyrotaxanes, both for the main chain and the side chain systems (Scheme 2).

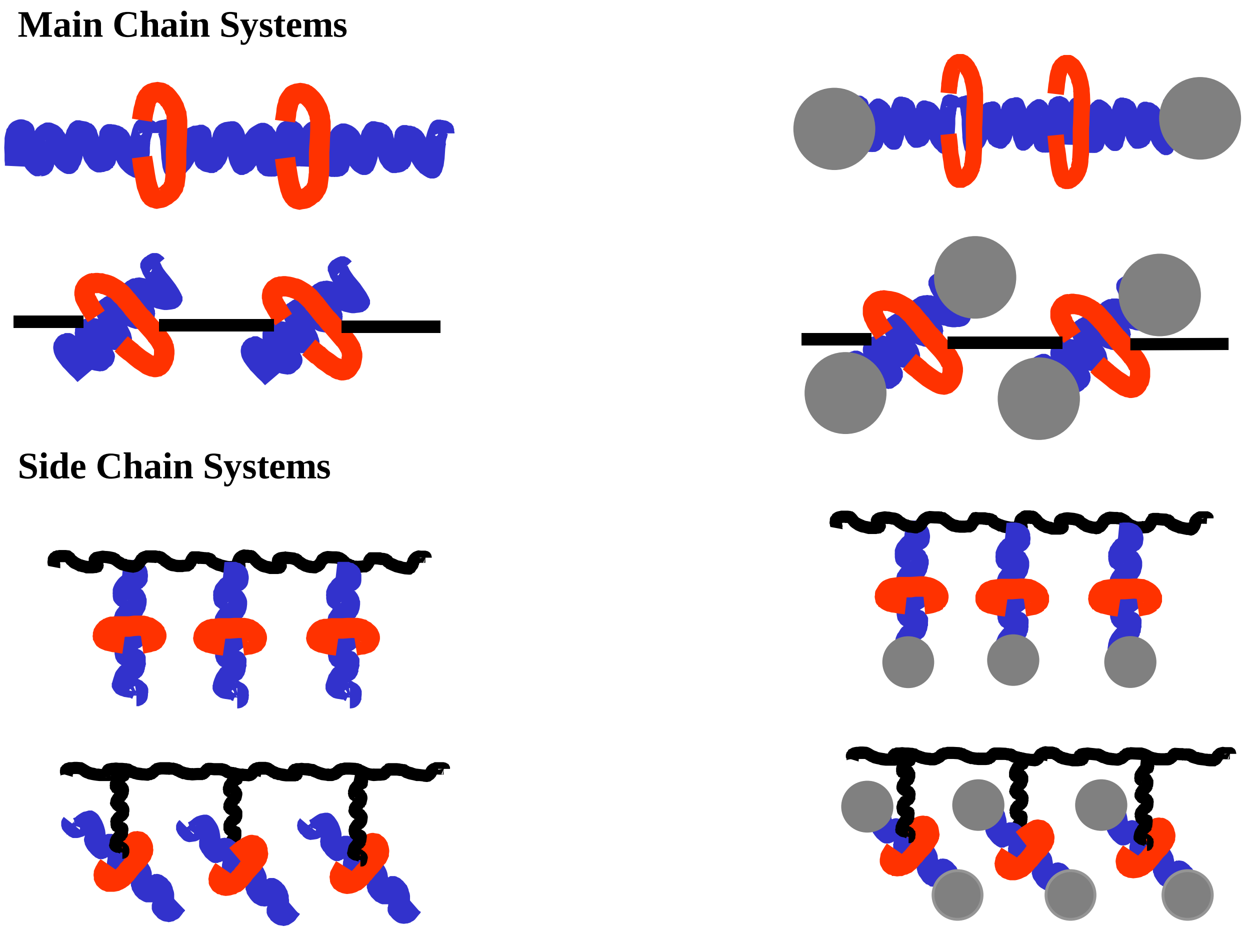

Scheme 2. Various Types of Polypseudorotaxane/polyrotaxane Architectures

Previous work on synthesizing the poly(amide crown ether)s had been carried out on bigger crown ethers. The 32-membered crown ether polyamide is insoluble in any solvents due to physical entanglements as a result of *in situ* treading of the macrocycles by the polyamide segments[1] (Scheme 3 and Table 1). For the 26-membered crown ether polyamide, although it is soluble in polar aprotic solvents, it gives a broad polydispersity of 5.24 due to two distinct molecular weight fractions. The high molecular weight fraction implies branching. This is also believed to be a result of the formation of polyrotaxanes during the polymerization process.[2] The smallest crown ether-containing polyamide synthesized in our group used a 20-membered macrocycle and it had a polydispersity of 5.78.[3] As the macrocycle size decreases, *in situ* threading should also decreases. The cavity size for the 14-membered crown ether is too small for threading to occur, and the polydispersity should approach the theoretical value of 2 for a step growth polymerization. Table 1 gives a summary of the gel permeation chromatograph (GPC) data for the various poly(amide crown ether)s.

In this project, a new polyamide containing 14-crown-4 ether in its backbone will be synthesized and its corresponding physical properties will be studied. The material properties studied will include molecular weight and polydispersity. Threading effects of crown ether lead to the formation of polyrotaxanes and crosslinking of the polymer. The small ring size of the 14-membered poly(amide crown ether) prohibits threading. Also, branching of polymers should not occur. Therefore, a theoretical polydispersity value of 2 should be obtained as the polymer undergoes step growth polymerization. Threading effects for larger crown ethers can also be deduced based on the molecular weights. If the molecular weights appear to be too high for linear polyamide step growth polymerization, this implies that branching and crosslinking of polymers have taken place, or perhaps ring opening of the crown ether has taken place.

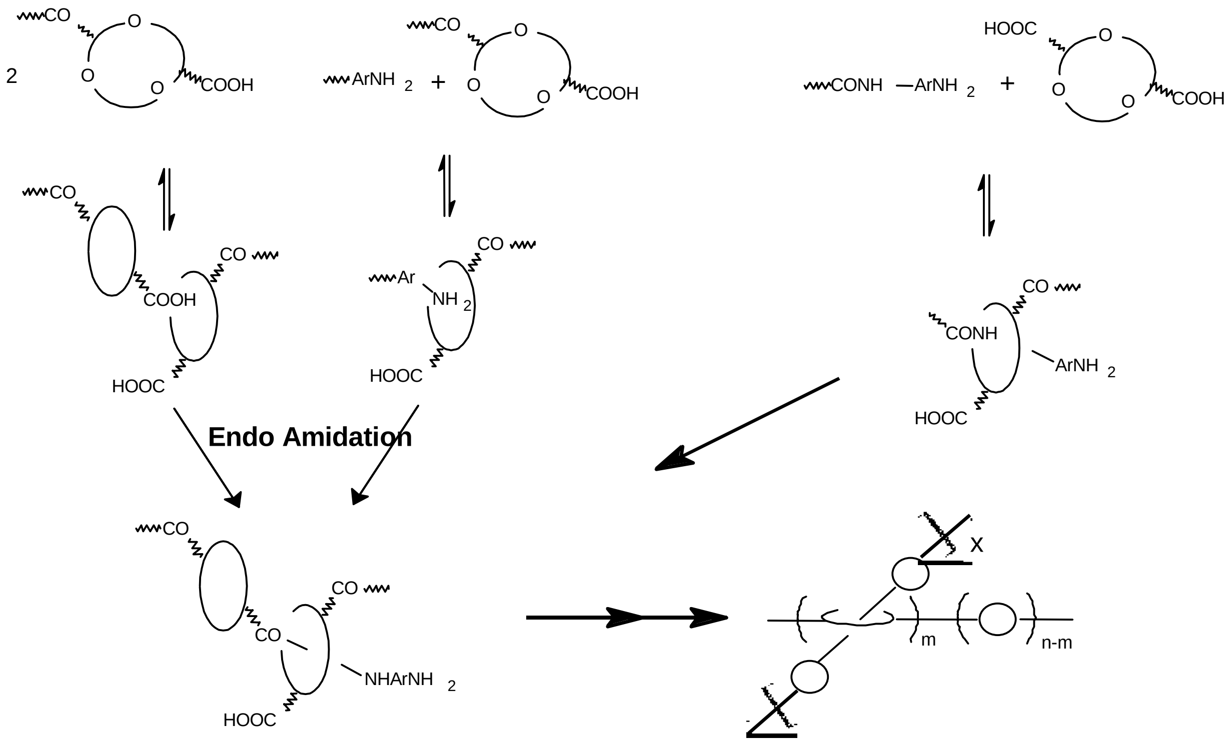

Scheme 3. Proposed Mechanism of Rotaxane Formation: Hydrogen Bonded Complexes of Crown Ether Moieties with Carboxylic, Amino and Amide Moieties.

EXPERIMENTAL SECTION

Materials. Reagent grade solvents and reactants were used as received from the chemical suppliers.

Measurements. Melting points were measured with a Mel-Temp II device. Thin layer chromatography (TLC) was done using Whatman PE SIL G/UV254. Preparative Thin layer chromatograph was done using TECHWARE SILICA GEL GF, 20x20 cm, 1000 microns. ^{1}H and ^{13}C Nuclear Magnetic Resonance (NMR) spectra were obtained at ambient temperature using a Varian Unity 400 MHz spectrometer with $CDCl_3$ as solvent with TMS (δ = 0.0 ppm) as internal standard unless stated otherwise. Fast atom bombardment (FAB) mass spectroscopy

(MS) was performed on a JEOL Model HX 110. Infrared spectra were recorded on a Midac FTIR Spectrometer.

Table 1. Comparison of data for Poly(amide crown ether)s

Poly(amide crown ether)s	M_n	M_w	Polydispersity	Solubility
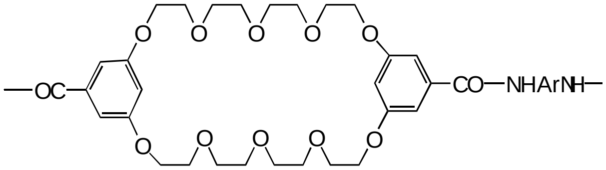	N/A	N/A	N/A	Insoluble in any solvents
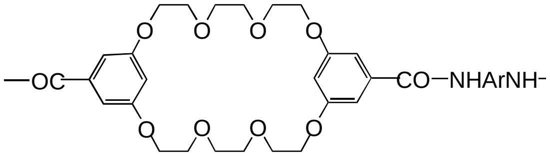	36.0	189	5.24	Soluble in DMF, NMP, DMSO
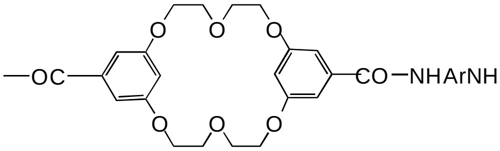	12.9	74.6	5.78	Soluble in DMF, NMP, DMSO
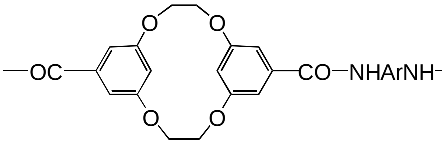	N/A	N/A	Predict to be closer to 2	Predict to be more soluble than the 20-membered polyamide

Synthesis

1. Methyl 3,5-Dihydroxybenzoate (1)[4]

3,5-Dihydroxybenzoic acid (100 g, 0.65 mol) was added to methanol (530 mL) and the mixture was stirred with a magnetic stir bar. Concentrated sulfuric acid (98%, 50 mL) was slowly added into the flask. The mixture was refluxed for 48 hours. The solution was cooled, and neutralized with sodium bicarbonate ($NaHCO_3$) to pH 7. It was then extracted with diethyl ether. The organic phase was dried over anhydrous sodium sulfate (Na_2SO_4) , and the solvent was removed by rotoevaporation to give an off white solid. The solid was recrystallized twice from water. Yield = 88.15 g (81%), mp = 167.5-170.5 ^oC (lit. mp[4] 167-169 ^oC). ^1H NMR (DMSO-d_6), δ (ppm): 9.65 (2 H, s), 6.80 (2 H, *J* = 2.2 Hz, d), 6.42 (1 H, *J* = 2.2 Hz, t), and 3.77 (3H, s).

2. Methyl 3,5-bis(2-hydroxyethoxy)benzoate (2)

4 different methods were used to synthesize this compound.

Method A[5]

K_2CO_3 (10.2 g, 74.1 mmol) and **1** (2.49 g, 14.6 mmol) were stirred in CH_3CN (75 mL) and refluxed for 4 hours. To the mixture was added dropwise 2-chloroethanol (2.41 g, 30 mmol) at 70^oC. After complete addition of 2-chloroethanol, the mixture was stirred for 140 hours at 70^oC. The mixture was cooled down to room temperature and vacuum filtered. The solvent was removed by rotoevaporation. A brown viscous oil was obtained. ^1H NMR showed multiple peaks.

Method B

1st Step—Synthesis of Protected Chloroethanol[6]

3,4-Dihydro-2H-pyran (200 mL, 2.2 mol) was cooled to 0^oC. To the flask were added 2-chloroethanol (147 mL, 2.19 mol) and 3 drops of concentrated hydrochloric acid. The mixture was stirred at 0^oC for 15 minutes. After that, the reaction mixture was stirred at room temperature for 3 hours. The protected chloroethanol was obtained via vacuum distillation of 4-5 torr at 88.5^oC (reported bp[6] = 52^oC, 0.5 torr). Yield = 218 g (60%). FTIR shows no OH absorption band.

2nd Step—Synthesis of Methyl 3,5-bis(2-hydroxyethoxy)benzoate

Acetonitrile (150 mL) was added to **1** (15.08 g, 89.66 mmol) and stirred until the ester dissolved. To the mixture was added K_2CO_3 (26.54 g, 192 mmol) and refluxed for 1 hour. To the mixture was added dropwise protected chloroethanol (33.44 g, 203.1 mmol). The mixture was refluxed for 3 days. The solvent was removed via rotoevaporation. H_2O and EtOAc were added to the residue. The solution was extracted with EtOAc (3x150 mL). Organic layers were combined, and washed with H_2O to pH 7, and subsequently washed with brine. The solution was dried over Na_2SO_4, and EtOAc was removed via rotoevaporation. ^1H NMR (DMSO-d_6) shows peaks of **1** instead of **2**.

Method C[7]

To 15 mL of DMF were added ethylene carbonate (22.9 g, 260 mmol), **1** (16.82g, 100 mmol), and n-Bu_4NI (8g). The mixture was stirred at 150^oC for 14 hours. The solvent was removed via rotoevaporation. Yellow liquid was extracted with EtOAc (3x150 mL). The EtOAc solution was washed with H_2O and brine. EtOAc was removed via rotoevaporation to give a yellow liquid. ^1H NMR does not show peaks of **2**.

Method D[8]

To a solution of **1** (15.08 g, 89.66 mmol) in 150 mL of DMF was added NaH (7.71 g, 192 mmol, 60% in mineral oil). The mixture was heated at 110^oC for 2 hours and cooled to 50^oC. The protected chloroethanol was added dropwise to the mixture while stirring. The mixture was stirred for 5 days and cooled to room temperature, filtered through Celite, and then concentrated via rotoevaporation. The brown oil was dissolved with methanol: dichloromethane (70:30, v/v, 375 mL) containing 30 mL of concentrated HCl. The solid precipitate was removed. The solvent was removed via rotoevaporation. The mixture was then diluted with 375 mL of H_2O, and was neutralized with saturated aqueous sodium carbonate to pH 7. The solution was extracted with EtOAc (3x150 mL). The organic layer was washed with H_2O and saturated aqueous sodium chloride. A brown viscous oil was obtained. TLC gave four spots. Crude yield = 15.66 g (68%). ^{1}H NMR, δ (ppm): 7.22 (2 H, J = 2.4 Hz, d), 6.71 (1 H, J = 2.4 Hz, t), 4.12 (4 H, J = 4.0 Hz, t), 3.98 (4 H, m), and 3.91 (3 H, s).

3. Methyl 3,5-bis(2-chloroethoxy)benzoate (3)[8]

A solution of **2** (30.02g, 117.15 mmol) in benzene (C_6H_6) (500 mL) was refluxed for 30 minutes using a Dean-Stark apparatus to remove water. The solution was cooled to room temperature. To the solution was added pyridine (18.86 mL, 234.4 mmol) and then thionyl chloride ($SOCl_2$) (17.05 mL, 234.5 mmol). Upon complete addition, the mixture was refluxed for 48 hours and cooled to room temperature. The salt was removed by decantation, and washed with C_6H_6. The organic layers were combined and washed with H_2O, diluted HCl, and brine. The organic layer was dried over anhydrous Na_2SO_4 and evaporated to give a yellow oil. TLC gave 1 spot. Yield = 5.31 g (70%), mp = 68.5-70.0 ^{o}C (lit. mp[8] = 68.2-69.4 ^{o}C). ^{1}H NMR, δ (ppm): 7.22 (2 H, J = 2.0 Hz, d), 6.71 (1 H, J = 2.0 Hz, t), 4.26 (4 H, J = 5.7 Hz, t), 3.91 (3H, s), and 3.83 (4 H, J = 5.7 Hz, t). MS Positive FAB $[M+H]^+$ = 293.03342, Calculated Exact Mass = 293.03474.

4. Bis(5-carboxymethoxy-1,3-phenylene)-14-crown-4 (4)[9]

To a suspension containing K_2CO_3 (6.2 g, 45 mmol) and n-Bu_4NI (0.01g) in DMF was added a solution of **1** (0.734g, 4.37 mmol) and **3** (1.28g, 4.37 mmol) via a syringe pump at 0.01mL/min at 110^{o}C. Upon complete addition, the mixture was stirred vigorously at 110^{o}C for 5 days. After the mixture was cooled, the solvent was removed via rotoevaporation. The residue was dissolved in dichloromethane and was filtered to remove salt. A silica gel column using ethyl ether: hexane (1:1, v/v) as eluent was used to purify the compound. Purification was unsuccessful. By using prep TLC plate with chloroform as eluent, product was purified. Yield is yet to be determined, mp = 240-241.5^{o}C. ^{1}H NMR, δ (ppm): 7.28 (4 H, J = 2.4 Hz, d), 5.81 (2 H, J = 2.4 Hz, t), 4.40 (8 H, s), and 3.92 (6H, s).^{13}C NMR, δ (ppm): 52.39, 67.57, 111.02, 111.68, 132.01, 158.64, and 166.53 (7 peaks as required).

RESULTS AND DISCUSSION

The synthesis of bis(5-carbomethoxy-1,3-phenylene)-14-crown-4 (**4**) involved 5 steps (Scheme 4). The first step was a Fisher esterification process to form methyl 3,5-dihydroxybenzoate (**1**) from 3,5-dihydroxybenzoic acid. Methanol (CH_3OH) was used as the reactant and also the solvent. Sulfuric acid acted as the catalyst to drive the equilibrium to the ester formation. The reaction was refluxed for two days. After the solvent was removed, the ester was recrystallized twice from water.

A Williamson ether synthesis was performed to obtain methyl 3,5-bis(2-hydroxyethoxy)benzoate (**2**). Four different methods were employed for this synthesis step. The first method (Method A) was done by adding 2-chloroethanol to **1**, with potassium carbonate (K_2CO_3) being the base and acetonitrile (CH_3CN) as the solvent. After stirring for 140 hours at 70°C, the salt was filtered and the CH_3CN was removed via rotoevaporation, producing a brown viscous oil. This method was not very effective as the 2-chloroethanol was unprotected, and was probably dehydrated during the reaction which resulted in a low yield.

The 2nd method (Method B) was done by synthesizing and then reacting a protected chloroethanol to prevent dehyration of the hydroxy group into an alkene group. K_2CO_3 was still used as the base, and the reaction was refluxed for three days. This reaction did not go to completion as the ^1H NMR shows the peaks of **1**, which were greater than the peaks for **2**. This may be due to incomplete reaction since the reaction was only run for three days.

Another method (Method C) was employed. Ethylene carbonate was used instead of the protected chloroethanol, with tetrabutylammonium iodide (n-Bu_4NI) being the catalyst and DMF as the solvent. The mixture was stirred at 150°C for 14 hours. The formation of product was low in this reaction, probably because the ethylene carbonate is not very reactive. The crude product obtained was a yellow liquid instead of a brown oil. Therefore purification was not performed as this already suggested a low yield, if any.

For Method D, sodium hydride (NaH) was used as the base as it is more reactive than K_2CO_3. After the protected chloroethanol was added, the mixture was stirred at 150°C for 140 hours. After removing the solvent, the resulting brown oil was purified using a silica column with 1:5 diethyl ether: chloroform (v/v) as eluent. However, purification was unsuccessful. This is probably due to the small differences in polarity between the product and byproducts. Therefore, to proceed on to obtain **3**, the crude product was used.

To synthesize **3**, a simple chlorination reaction was done. First of all, a Dean-Stark apparatus was used to remove any trace of water in the starting material and benzene. Thionyl chloride ($SOCl_2$) was added dropwise to the mixture. Pyridine was used to neutralize the hydrochloric acid which was formed when the reaction take place. After refluxing for 48 hours, the mixture was washed. The yellow oil obtained from the reaction mixture was purified using a silica gel column with chloroform as eluent. The purification of this product was very successful as the impurities from **2** was completely separated. This is most likely attributed to the differences in polarity. **3** is less polar in comparison to **2**, and most of the impurities from **2** have high polarities. Therefore, **3** can be easily purified from all the other impurities. A second attempt to synthesize **3** yielded a very pure product as depicted from the ^1H NMR spectra. Therefore, **3** was not purified through column but was used directly to proceed to the synthesis of **4**.

Bis(5-carbomethoxy-1,3-phenylene)-14-crown-4 (**4**) was synthesized by combining an equimolar mixture of **1** and **3**. Tetrabutylammonium iodide was used as a phase transfer catalyst because K_2CO_3 is insoluble in DMF. The importance of an equimolar mixture is to minimize the formation of byproducts. Also, high dilution conditions for the reaction were needed to maximize the ring closure reaction, rather than the formation of long chains. The reaction was stirred for five days at 110°C. After removal of solvent, a silica column with 1:1 hexane: ethyl ether (v/v) as eluent was used to purify the crude product. Purification was unsuccessful as more than one product came out from the column at the same time. Therefore, thick layer chromatograph was used to purify the crude product, with chloroform as the eluent. This purification method proved to be effective; however, it is not efficient for large amounts.

An interesting point regarding the ^{1}H NMR shifts of **4** is that the hydrogen (**b**) of the benzene ring was shifted upfield to δ=5.81 ppm (Figure 1) instead of the normal position between 6-7 ppm for bigger crown ethers . This is attributed to the fact that the small ring size causes the two benzene rings to be very close to each other, and therefore the hydrogens (**b**) are subjected to electron shielding from the opposite benzene rings which causes the chemical shift upfield.

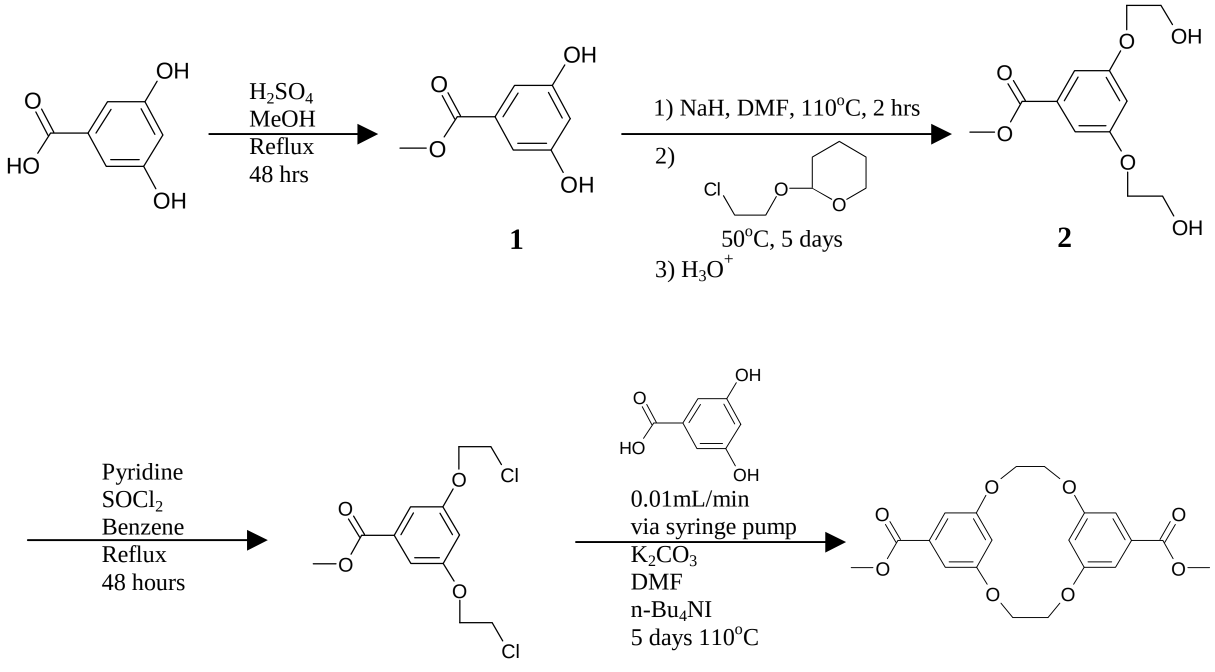

Scheme 4. Synthesis Roadmap for Bis(5-carbomethoxy-1,3-phenylene)-14-crown-4

A better purification method for **4** is needed. One possibility is to find an even less polar eluent for the silica gel column, or by using a very long column to ensure better separation. After that, hydrolysis of **4** needs to be done to obtain bis(5-carboxy-1,3-phenylene)-14-crown-4 (**5**) which will be used in the polymerization reaction with 4,4'-oxybisaniline (**6**) to yield the polyamide (**7**) (Scheme 5). Once the polyamide is formed, characterization of the polymer is needed. Several characterization techniques include ^{1}H NMR to confirm formation of polyamide, GPC to obtain the polydispersity value, and Differential Scanning Calorimeter (DSC) to obtain the glass transition temperature of the polyamide.

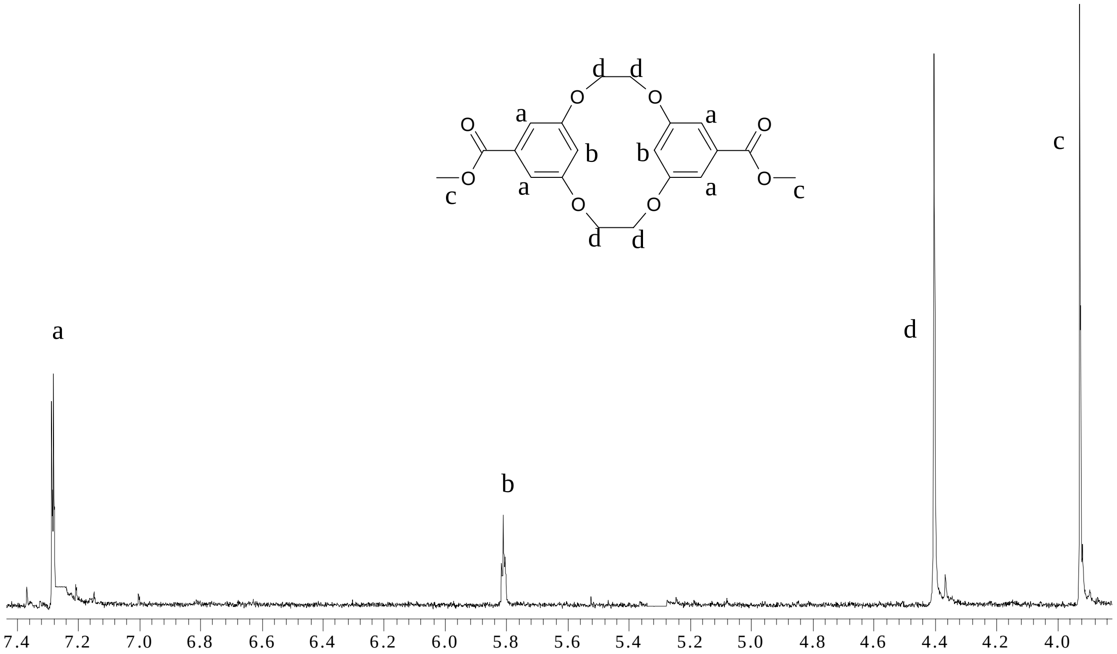

Figure 1. ^{1}H NMR of bis(5-carbomethoxy-1,3-phenylene)-14-crown-4 (4)

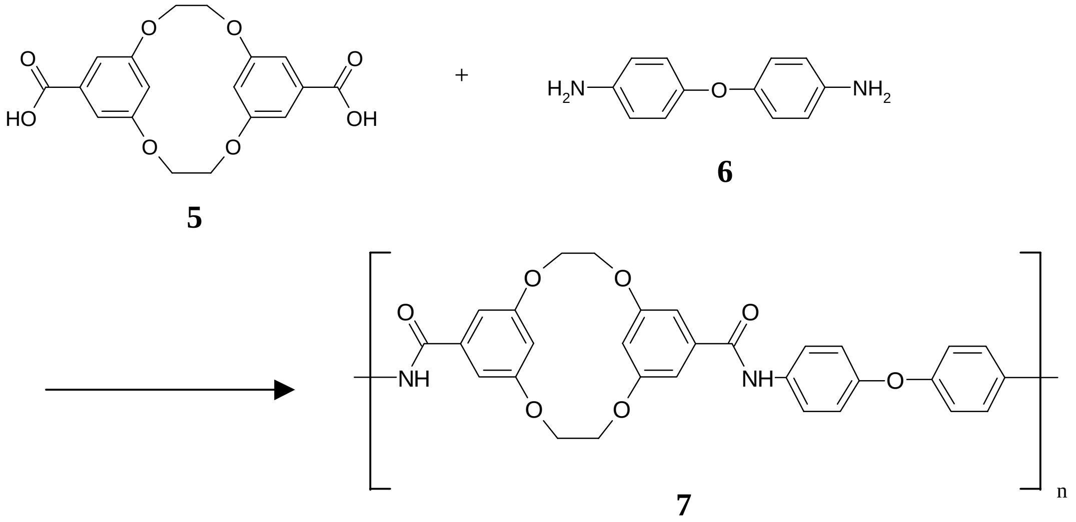

5

6

7

Scheme 5. Synthesis Roadmap for the Polyamide Formation

CONCLUSION

Several precursors that lead to the formation of the crown ether were successfully synthesized. For the synthesis of **2**, it can be concluded that NaH and the protected chloroethanol is the best method to use. A novel crown ether (**4**) was successfully synthesized. Column chromatograph with 1:1 hexane: ethyl ether (v/v) eluent is not suitable for purification of **4**.

ACKNOWLEDGEMENTS

I acknowledge Dr. Hong Wang for helping me with all the syntheses that I carried out, Dr. Harry Gibson for his advice on organic synthesis, and all members of the Gibson Group. Also, I would like to thank Virginia Tech Summer Undergraduate Research Program and all its organizers. Lastly I want to thank the National Science Foundation for providing funding.

REFERENCES

1. Delaviz, Y.; Gibson, H. W. *Macromolecules*. **25,** 4859-4862, 1992.
2. Gibson, H. W.; Nagvekar, D., Yamaguchi, N.; Bryant, W.S.; Bhattacharjee, S. *Polymer Preprints*. **38**, 64-65, 1997.
3. Bhattacharjee, S.; Gibson, H.W. Unpublished results.
4. Gibson, H. W.; Delaviz, Y. *Macromolecules*. **25**, 18-20, 1992.
5. Bryant, W.S., PhD Dissertation, Virginia Tech, 1999.
6. Bheda, M. C. PhD. Dissertation, Virginia Tech, 1992, p. 65.
7. Krakowiak, K E. *J. Heterocyclic Chem.*, **35**, 519-524, 1998.
8. Gibson, H. W.; Nagvekar, D. S.; Delaviz, Y.; Bryant, W. S. *Can. J. Chem.* **76**, 1429-1436, 1998.
9. Nagvekar, D. S.; Gibson, H. W. *Org. Prop. Proced. Int.*, **29**, 237-239, 1997.

Effect of Solvent Composition and Concentration on Aggregate Size in Polymer Dispersions for Fuel Cell Membrane Electrode Assembly

Curtis A Cleveland[a], Michael Hickner, and Dr. James E. McGrath
Virginia Polytechnic Institute and State University
Materials Research Institute
Department of Chemistry
Blacksburg, VA

[a] Department of Chemistry, Hampton University, Hampton, VA

ABSTRACT

The membrane electrode assembly (MEA) is the core of a polymer electrolyte membrane fuel cell (PEMFC). The MEA is composed a proton-conducting polymer membrane and electrodes containing the platinum electrocatalyst and a polymer binder. Sulfonated poly(arylene ether sulfone)s (BPSH-XX) are being developed as an alternative to Nafion. The electrodes must be easily fabricated, provide access of the reactant gases to the platinum catalytic sites, and have good adhesion to the polymer membrane substrate. A key component of MEA fabrication is the polymer dispersion or solution used to cast the electrodes.

This research involved the preparation, fabrication and characterization of BPSH-XX dispersions and comparison of these dispersions to commercially available Nafion analogs. Aqueous BPSH-XX prepared by addition of DMAc solution to 50:50 isopropanol: water mixture and Nafion dispersions were characterized using dynamic light scattering (DLS), Dilute Solution Viscosity, and Scanning Electron Microscopy (SEM). Results from the DLS show that hydrodynamic radius (R_H) is in the range of 17nm – 45nm and is dependent on solvent composition, polymer concentration, and ion exchange capacity. Results from the other two techniques showed that similar particle sizes are obtained for BPSH-XX as compared to commercial Nafion dispersions.

INTRODUCTION

A fuel cell is an electrochemical energy conversion device. It is two to three times more efficient in converting fuel to power than an internal combustion engine.[1] The core of a polymer electrolyte membrane fuel cell (PEMFC) is the membrane electrode assembly (MEA). The MEA is a proton-conducting polymer membrane positioned between two gas-permeable electrodes. A platinum catalyst supported on carbon black and bonded with polymer matrix is necessary for the electrochemical reactions to occur on the anode and cathode. This assembly usually consists of a Nafion® membrane and electrodes cast from a Nafion dispersion in a mixture of water and low molecular weight alcohols as the solvent.

Sulfonated poly(arylene ether sulfone)s (BPSH-XX) have shown desirable membrane properties such as high protonic conductivity and good thermal stability.[2] To take advantage of these properties in a fuel cell application, the polymer must be fabricated into an MEA. A critical step in MEA fabrication is forming a polymer dispersion that can be cast directly onto the proton exchange membrane without compromising membrane integrity. The electrodes must be porous to allow the reactant gasses to diffuse to the catalytic sites and adhere well to the membrane in the final assembly.

Sulfonated polymers can be dispersed in aqueous solutions due to their ampiphilic nature. The sulfonate groups (SO_3H) attached to the chain are hydrophilic while the unsulfonated backbone of the polymer remains hydrophobic. The polymer chains form micelles or aggregates as opposed to a true polymer solution where single chains exist separately in a good solvent. The size of the aggregate can be influenced by the concentration of sulfonate groups along the backbone and the quality of the solvent. Aggregate size in the polymer dispersions for electrode casting is essential to an efficient membrane electrode assembly (MEA).

To date, there has not been much research involving the characterization of these polymer dispersions even though they have been used in fuel cell technology for the past 20 years. Aqueous BPSH-XX dispersions will be characterized using Dynamic Light Scattering (DLS), Dilute Solution Viscosity, and Scanning Electron Microscopy (SEM). These three techniques probe the sizes of the aggregates in slightly different ways, but are complementary to one another. The dispersions will be compared to commercially available Nafion dispersions. In a separate project, the dispersions will then be used with BPSH-XX membranes to fabricate MEAs.

EXPERIMENTAL

Dispersion Fabrication

BPSH-XX polymer was dissolved in DMAC at high concentration (~20 wt %). Then 50:50 (by weight) Isopropanol alcohol (IPA): DI H2O was slowly added with stirring and heat until no solids remained. The final product was a clear, slightly yellow dispersion with low viscosity and no “gel” fraction or other solids remain. The final polymer concentration was determined using an evaporation method. The formula to find the percent polymer is Equation (1).

$$\%\ \text{Polymer} = \frac{(\text{dry wt} - \text{empty wt})}{(\text{wet wt} - \text{empty wt})} * 100 \qquad (1)$$

Dynamic Light Scattering (DLS)

The interaction of the light with matter can be used to obtain important information about structure and dynamics of matter. Study of this interaction is possible by light scattering experiments. A typical Light Scattering experiment is shown in the picture below.

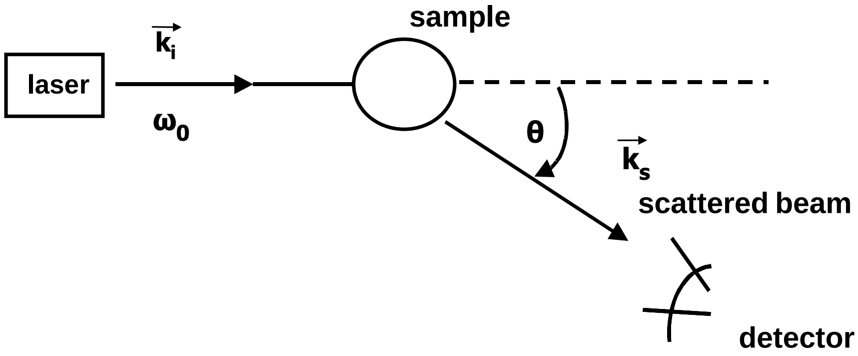

Figure1. Schematic of DLS experiment

When light is shined on matter it will scatter and the scattered light gives us information about molecular structure and motion in the material.

According to the semi-classical light scattering theory [*Berne and Pecora, "Dynamic Light scattering" John Wiley, 1975*], when light impinges on matter, the electric field of the light induces an oscillating polarization of electrons in the molecules. The molecules then serve as secondary source of light and subsequently radiate (scatter) light. The frequency shifts, and the angular distribution, polarization, and intensity of the scatter light are determined by the size, shape and molecular interactions in the scattering material. Information about the structure and molecular dynamics of the scattering medium should be possible to obtain form these characteristics, along with the aid of electrodynamics and theory of time dependent statistical mechanics.[3] Hydrodynamic radius was most important during this research (see Equation 2).

$$R_H = \frac{k_b T}{6\pi\eta D_T} \qquad (2)$$

The formula is called the Stokes-Einstein Equation (kb = Boltsman's constant, DT = Transnational Diffusion coefficient, η = Solvent viscosity). The light scattering instrument was a Dyna Pro 801-TC by Protein Solutions, Inc.

Polymer solutions were diluted with two different solvents and run in DLS experiments. The solvents used were de-ionized water and 50:50 (by weight) Isopropanol alcohol (IPA): DI H_2O. The percent polymer in each sample was calculated by weight. This calculation is required because the polymer concentration in each dispersion varied. This information was then used to calculate the concentration of each sample.

Scanning Electron Microscope (SEM)
Scanning Electron Microscopy works by bouncing an electron beam off a specimen. As the electrons hit the specimen, changes occur to the surface of the specimen, and the specimen emits its own electrons. The secondary electron detector measures these surface electrons and converts the electrons to a TV signal. The secondary electron gives information about the structure of objects.[4] A ISI SX 40 scanning electron microscope was used throughout this research.

Eight different samples were made using four polymers. The procedure used to prepare the SEM samples has been reported in the literature.[5] One drop of Nafion 950 (5%), Nafion 1100 (5%), BPS-40 (3.61%), and BPS-50 (3.61%) in both 200ml DI H2O and 200ml 50:50 IPA: DI H2O. One drop of polymer dispersion was pipetted in 200ml of DI H2O or 50:50 IPA: H2O. The diluted samples were stirred over night and three separate drops of each diluted sample were placed on clean glass slide. They were then evaporated in a vacuum for 48 hours and the slides were sputtered with gold and imaged. The scanning electron micrographs were collected and analyzed.

Dilute Solution Viscosity
Intrinsic viscosity, as does dilute solution viscosity, measures the flow time of a solution through a simple glass capillary and provides considerable physical insight. It is one of the simplest, cheapest and most precise measurements in polymer science. The actual viscosity measured in a capillary viscometer is obtained by taking the y-intersect of the inherent and the reduced viscosities extrapolated back to zero concentration.

The type of viscometer for used in determining intrinsic viscosity for this research was a "suspended level" or Ubbelohde viscometer (size 200), sketched below:

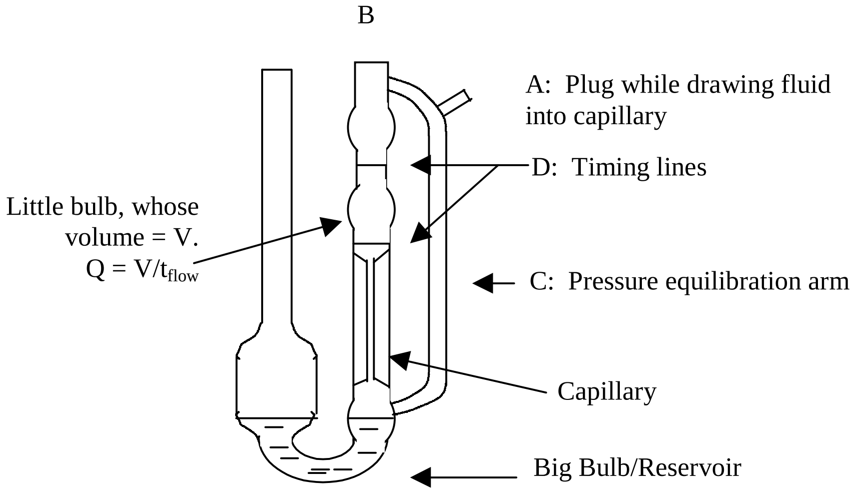

Figure 2. Schematic of Ubbelohde viscometer

The viscometer is called "suspended level" because the liquid initially drawn into the small upper bulb is not connected to the reservoir as it flows down the capillary during measurement. The capillary is suspended above the reservoir. In conjunction with the pressure-equalization tube, this ensures that the only pressure difference between the top of the bulb and the bottom of the capillary is that due to the hydrostatic pressure--i.e, the weight of the liquid.[6]

Samples for viscosity testing are made with 3.0g of the polymer solution and 25ml of a particular solvent. This results in a 6mg/ml final concentration for each polymer sample.

RESULTS AND DISCUSSION

Dispersion Fabrication

Sulfonated poly(arylene ether sulfone)s (BPSH-40 & BPSH-50) in DMAc solution (5%w/v) successfully dispersed by addition of 50:50 (by weight) isopropanol alcohol (IPA): deionized water. The solution was added drop by drop with rapid stirring and little heat for about 48 hours. The final product was a clear, slightly yellow dispersion with low viscosity and no visible gel fraction. The final polymer concentration ranged from 3-5 % by weight.

Dynamic Light Scattering (DLS)

The hydrodynamic radius (R_H) is affected by polymer concentration as shown in Figure 3 where 5% Nafion 950 solution was diluted with deionized water.

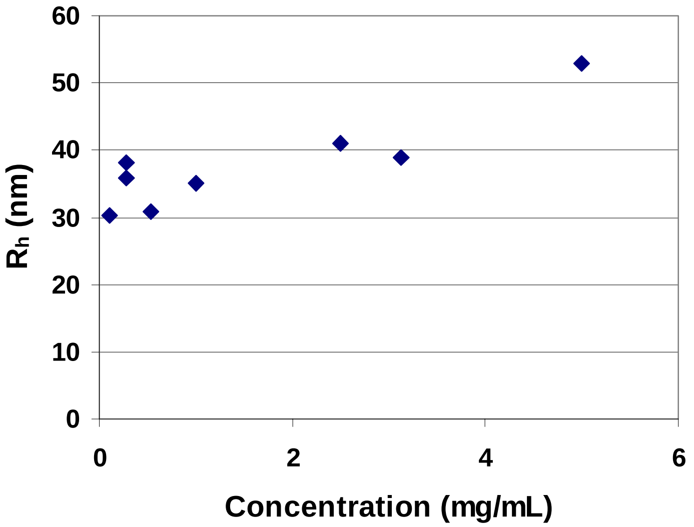

Figure 3. Plot of R_H Versus Concentration for Nafion 950 in Deionized Water

Figure 3 shows that the particle size of Nafion 950 in DI H2O increases as the polymer concentration is increased with particle sizes range between 30 and 50 nm. These sizes are clearly too large to be single molecules, so the dispersions must indeed be aggregates. This differs from a polymer in a good organic solvent where the hydrodynamic radius is expected to be about 1-3 nm.

Higher ion exchange capacity means there is a greater concentration of sulfonic acid groups along the polymer backbone. Polymers with a greater concentration of sulfonic acid groups along the backbone should swell more in an aqueous environment. This theory is supported by the data shown in Figure 4.

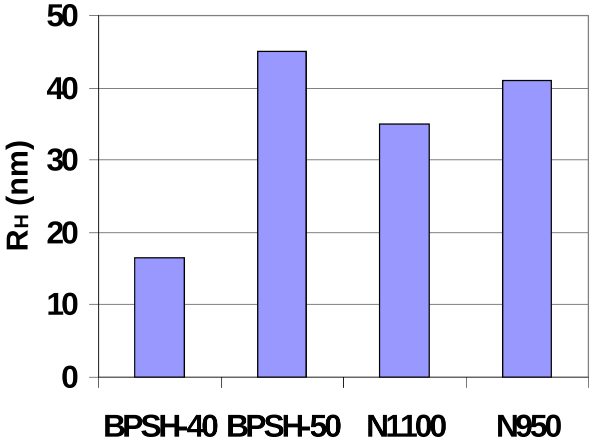

Figure 4. R_H for BPSH-40, BPSH-50, Nafion 1100, and Nafion 950 in Water

Figure 4 compares the R_H for Nafion and BPSH polymers of different ion exchange capacities (IEC). The aggregate size within a family of polymers increases as the ion exchange capacity increases. One can conclude that adding SO3H groups to the polymer backbone increase R_H in water.

Dilute Solution Viscosity

Chemical structure has an affect on viscosity and polymer solvent interactions. Nafion has flexible tetra-fluoroethylene-based backbone with the sulfonic acid groups located on side-chains. This structural make up allows the flexible molecules to rearrange in a 50:50 IPA: water solvent to maintain a low viscosity. BPSH has an aromatic ether backbone resulting in a stiffer polymer chain. The somewhat stiffer molecules cannot rearrange in a 50:50 IPA: water solvent resulting in a larger particle size. The results in Figure 5 support this idea.

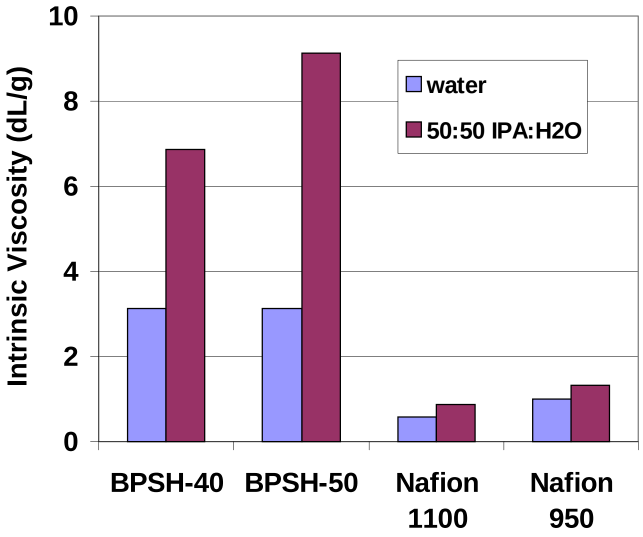

Figure 5. Effect of Polymer and Solvent on Dilute Solution Viscosity

An increase in viscosity for the 50:50 solutions may also be due to aggregation of smaller particles. This will be supported in the Scanning Electron Microscopy results presented in the next section.

Scanning Electron Microscopy
Images obtained from SEM experiments correlate well with the results from the dilute solution viscosity experiments. The increase in viscosity of BPSH can be seen in SEM photos, Figures 6 and 7.

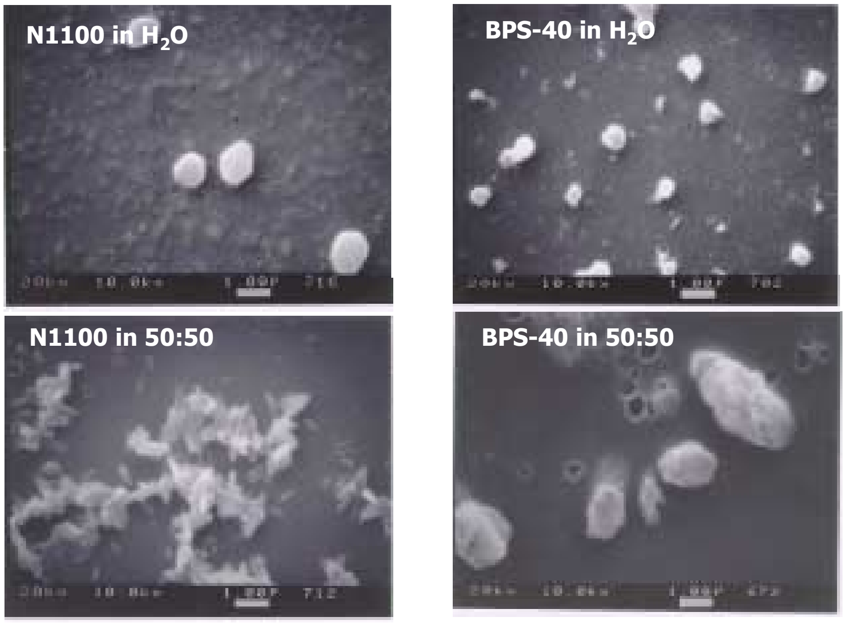

Figure 6. Scanning Electron Micrographs of Diluted and Dried N1100 and BPS-40 Dispersions

Nafion 1100 forms single particles of about 1µm in water while a somewhat continuous chain of single particles (with radius 0.5 µm) in 50:50 IPA: water. BPS-40 forms single particles with diameters of 0.5-0.75 µm in water. Large aggregates of 1.5µm - 3.5µm form in 50:50 IPA: water. These micrographs coincide with the larger viscosity values found in a 50:50 IPA: water solvent for both polymers in the dilute solution viscosity experiments.

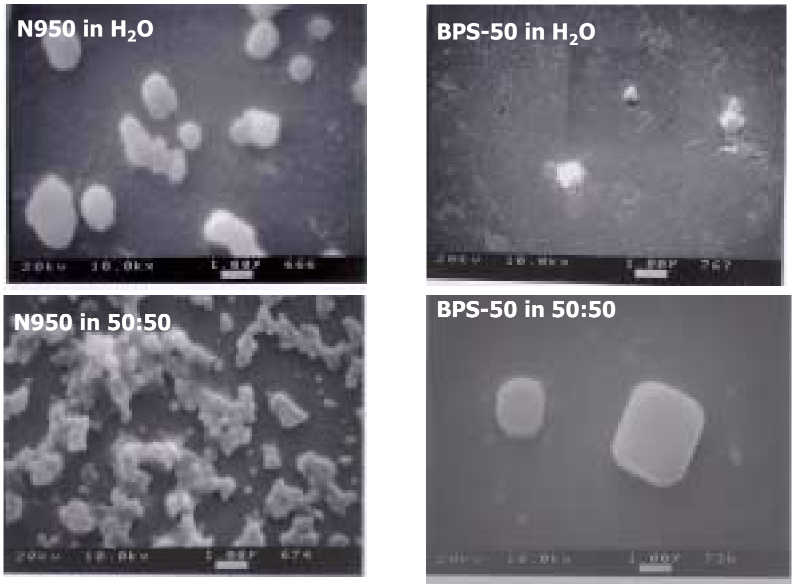

Figure 7. Scanning Electron Micrographs of Diluted and Dried N950 and BPS-50 Dispersions

As with Nafion 1100, Nafion 950 forms single particles of about 0.75µm - 2.5µm in water and a continuous particle, where in the single particles appear to be about 0.5µm - 1.0µm in 50:50 IPA: water. BPS-50 forms single particles with diameters approximately 0.25 - 0.5µm in water and large particles of about 2.0µm - 4.0µm in 50:50 IPA: water. This also is consistent with the larger viscosity values found in a 50:50 IPA: water solvent for both polymers in the dilute solution viscosity experiments.

All the micrographs above are of diluted and dried dispersions. The absolute values of the particle sizes do not match up between the SEM experiments and the DLS data but the trends support the same conclusions.

CONCLUSIONS

Sulfonated poly(arylene ether sulfone)s can be easily dispersed by addition of an aqueous/alcohol system to a polymer solution in DMAc. These dispersions can then be successfully used in the fabrication of a fuel cell membrane electrode assembly (MEA). Similar particle sizes (17nm – 45nm) were obtained with BPSH-XX polymer dispersions as compared to commercial Nafion dispersions. Hydrodynamic radius (R_H) of polymer dispersions is a function of solvent composition, polymer concentration, and ion exchange capacity.

Additional SO_3H groups on a polymer backbone increase R_H in water as demonstrated by DLS. Polymers with higher ion exchange capacities had a larger R_H within each family of polymers. Hydrodynamic radii for all polymers tested were between 17 and 45 nm.

IEC and solvent composition also have an effect on dilute solution viscosity. A larger increase in viscosity occurs in the BPSH-XX, due to the mobility of the chains in a poorer solvent. An increase in viscosity for the 50:50 solutions may also be due to aggregation of smaller particles in Nafion solutions as seen in the scanning electron microscopy. SEM pictures visually confirmed the dilute solution viscosity data that suggested similar trends are seen between Nafion and BPSH. Single particles were observed in water and changes that resulted in increasing viscosities occurred in 50:50 IPA: water by both polymers.

FUTURE WORK

In order to fabricate MEAs from different membranes being investigated, the dispersing characteristics of other families of sulfonated poly(arylene ethers), such as sulfonated ketones must be investigated. The chemical character of the polymer backbone is anticipated to play a role in dispersion fabrication.

One important variable that was not discussed in this research is the molecular weight of the polymers. The length of the chains would certainly have an effect on aggregate size. In the future it will be desirable to compare molecular weight effects on polymer dispersions.

ACKNOWLEDGEMENTS

The authors would like to gratefully acknowledge the National Science Foundation – Partnerships for Innovation for the financial support. Dr. Richey Davis, Jody Streeter, and Matt Guzy deserve recognition for assistance with the DLS. Also, we would like to thank Mr. Frank Cromer for assistance with the SEM, and Kerry O’Connor for assistance with dilute solution viscosity.

REFERENCES

1. Thomas S., Zaibowitz M., Fuel Cells - Green Power. *Los Alamos National Laboratory* 2000; www.education.lanl.gov/resources/fuelcells.
2. Wang F., Hickner M., Kim Y S., Zawodzinski T., McGrath J., Synthesis and Characterization of Sulfonated Poly(arylene ether sulfone) Random (Statistical) Copolymers Via Direct Polymerization: Candidates for New Proton Exchange Membranes. *Journal of Membrane Science* submitted 2000.
3. Finsy R., *Advances in Colloid and Interface Science* **1994**, 52, 79-143.
4. Wells O C., Scanning Electron Microscopy. McGraw-Hill. New York, NY. 1974.
5. Laporta, M. et al. *Macromol. Mater. Eng.* **2000**, 282.
6. Malkin A Ya., Experimental Methods of Polymer Physics: Measurement of Mechanical Properties, Viscosity, and Diffusion. Prentice-Hall. Englewood Cliffs, NJ. 1979.

Adhesion Between Epoxy and Glass Measured by the Shaft Loaded Blister Test

Kevin P. Doyle[a], Emmett P. O'Brien, and Dr. Thomas C. Ward
Department of Chemistry, Virginia Tech

[a] Departments of Chemistry and Chemical Engineering, Ohio University, Athens, Ohio

ABSTRACT

The shaft loaded blister test was used to investigate the strain energy release rate (G) of a model epoxy bonded to soda lime glass after exposure to environmental fluids at elevated temperatures. Strain energy release rate values were calculated from the relationships between the load (*P*), blister radius (*a*), and central shaft displacement (w_0). The model epoxy and the soda lime glass have significantly different coefficients of thermal expansion (CTE), causing residual stresses that may directly effect the calculated strain energy release rate value. Using the current sample preparation technique the calculated tensile rigidity (*Eh*) was inaccurate. Testing the dry samples, unexposed, resulted in film rupture. Film rupture, typical in thin films, was attributed to a small load bearing capacity of the film and *strong* adhesion between the epoxy and glass [1]. Samples exposed to water for as little as two hours weakened the bond enough such that a blister formed (G ~ 17 J/m^2); sample exposure to proprietary fluids for six hours also weakened the adhesion (G ~ 23 - 65 J/m^2). Silane-coupling agents having hydrocarbon tails were added to the soda lime glass surface to reduce sensitivity to water; however, after exposure to water for 24 hours, adhesion was significantly reduced such that the films lifted off effortlessly. Samples exposed to alcohols and alkyls also resulted in film rupture in this case.

INTRODUCTION

Background:

Epoxies are used to adhere silicon chips to printed circuit boards, and act as an encapsulant to protect the device from such things as vibrations, moisture, and heat. A typical adhesive-silicon wafer system is shown in Figure 1. This project focused on the effect of various environments on the adhesion of a model epoxy silicon interface. The silicon will be replaced by soda lime glass in this study.

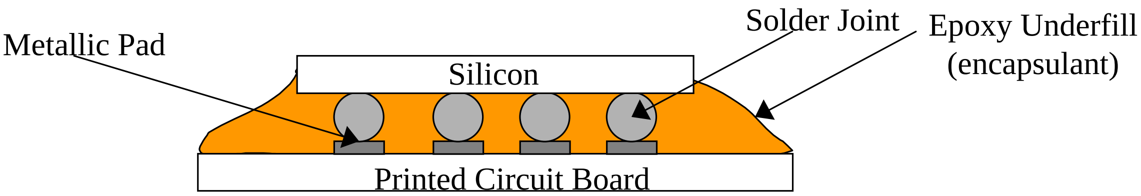

Figure 1. Schematic of a computer circuit

One way to characterize an adhesive bond is to find the energy required to debond, or the strain energy release rate (G). The strain energy release rate is the energy per unit surface area for critical crack growth to occur. The peel test, where a piece of tape is removed from a substrate, is a common method to measure strain energy release rates. One problem with the peel test is that when an environmental fluid, such as water, is applied, fluid exposure is not limited to just the crack front, as would be desired. During exposure the conditioning liquid may diffuse around the edges of the tape, which may result in an ambiguous strain energy release rate value. In contrast, an axisymmetric geometry, characteristic of the shaft loaded blister test, eliminates edge effects by directing the path of diffusion of the environmental fluid directly at the crack tip as seen in Figure 2.

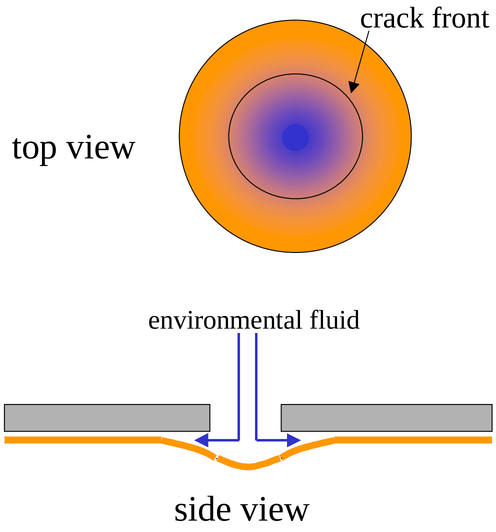

Figure 2. Schematic of axisymmetric fluid diffusion

A schematic of the shaft loaded blister test is shown in Figure 3. A hole is drilled in the center of a substrate (glass in this case), and a film is adhered to one side. A shaft applies a load (P), and the resulting shaft displacement (w_0) and blister radius (a) are measured as shown in figure 3.

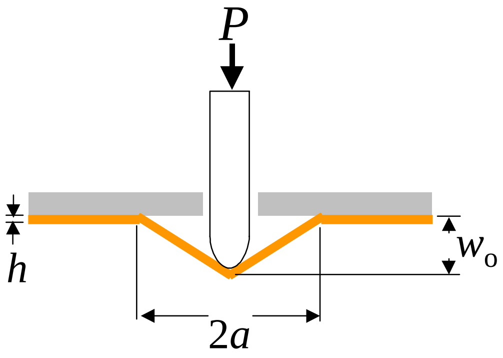

Figure 3. Schematic of shaft loaded blister test

A characteristic of either silicon or glass surfaces is their high surface energy and hydrophilic nature. One strategy to reduce the effects of environmental fluids, like water, is to use silane-coupling agents. Applying certain coupling agents having hydrophobic natures to a polar glass surface will cause the surface to become non-polar and reduce the affinity for water.

Theory:

K.T. Wan [2] originally presented the theory of the shaft loaded blister test for a pure stretching membrane. Based on what Wan proposed, equations 1, 2, or 3 can be used in determining the strain energy release rate:

$$G = \left(\frac{1}{16\pi^4 Eh}\right)^{1/3}\left(\frac{P}{a}\right)^{4/3} \qquad \text{(load-based equation) [1]}$$

$$G = \frac{1}{\pi^2 Eh}\left(\frac{P}{w_0}\right)^2 \qquad \text{(hybrid equation) [2]}$$

$$G = \frac{Eh}{16}\left(\frac{w_0}{a}\right)^4 \qquad \text{(displacement-based equation) [3]}$$

Where the variables are defined (seen in figure 3) as:

a	radius of blister
w_0	central shaft displacement
P	load
E	Young's tensile modulus
h	thickness of the backing

Examination of these three equations reveals that G calculated from equation 1 depends strongly on the measured load (P), and G calculated from equation 3 depends strongly on the measured displacement (w_0). The debond radius, a, is eliminated from equation 2, which is a hybrid form involving both load and displacement. As a consequence equations 1, 2, and 3 are referred to as the load-based, hybrid, and displacement-based equations, respectively. Theoretically, the strain energy release rate (G) calculated from the individual equations should agree; and if this is not the case, the results may provide valuable clues about the nature of the adhesive system. If the resulting strain energy release rates calculated from the three respective equations do not agree, information may be provided about the nature of the system.

The film tensile rigidity (Eh) is a common variable in all three equations. The film tensile rigidity can be determined from a stress-strain experiment or by using a volume fraction mixing rule. Using the SLBT, the film tensile rigidity also can be determined by applying the following relationship:

$$P \sim w_0^3 \qquad [4]$$

Thus, in the region where equation 4 applies, equation 5 can be used to calculate the film tensile rigidity (*Eh*), where a_0 is the initial radius of the blister:

$$P = \left(\frac{\pi (Eh)}{4 a_0^2} \right) w_0^3 \qquad [5]$$

Sample Preparation

The epoxy used was the Epon® 862, bisphenol F resin. Figure 4 shows the chemical structure of the model epoxy.

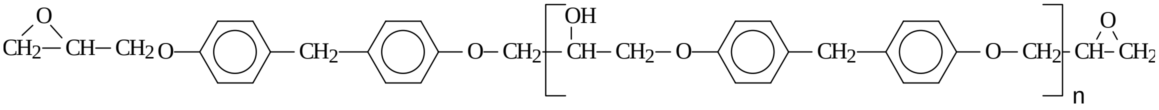

Figure 4. Model epoxy

The bisphenol F resin was selected versus the more common bisphenol A resin because of its lower viscosity. The curing agent used was 4-methyl-2-phenylimidazole, which was added at 3% by weight. A 10% by weight mixture of 1,4 butanediol was added to the epoxy to lower viscosity and promote adhesion. The epoxy was then cured at 130°C for one hour.

Figure 5 is a schematic of the typical test sample. Soda lime glass was used as the substrate rather than the actual silicon wafer. The glass was cut into 1.5" squares and had a hole 19/64" in diameter drilled in the center. The glass surface was then cleaned with acetone. A piece of Kapton® tape, 0.5" in diameter, was placed over the hole in the glass substrate to initiate a pre-crack.

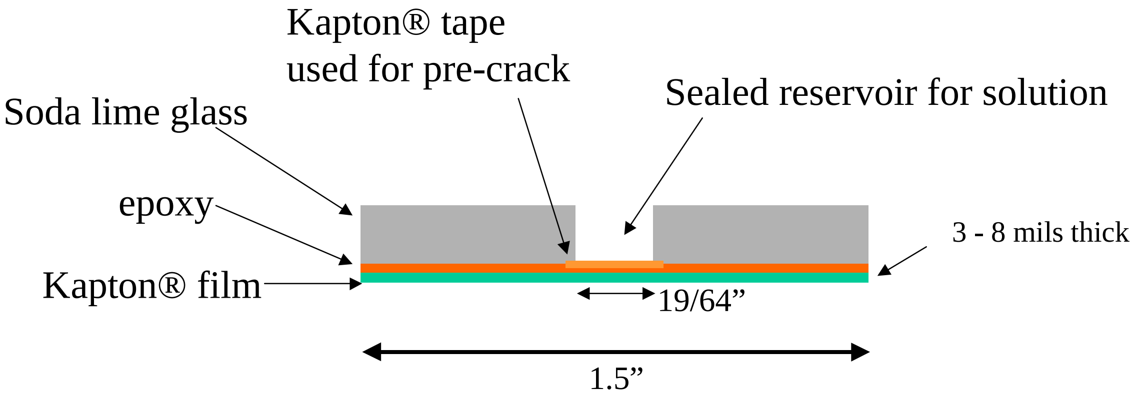

Figure 5. Test sample

A layer of epoxy (1-5 mils thick) was then applied to the glass substrate, and a piece of Kapton® film (2 mils thick) was placed on top of the epoxy to act as a reinforcement layer. The epoxy was then cured at 130°C for one hour.

Various environmental fluids (1-2 ml) were used as penetrants to debond the epoxy/glass interface. The liquids were pipetted in the solution reservoir and exposed at 40°C or 60°C for a predetermined amount of time. The solution reservoir was covered with a piece of Kapton® tape while the environmental fluids penetrated the epoxy-glass bond. Fluids used were water, various proprietary fluids (m1, m3, B, c1, and c2), three alcohols (methanol, ethanol, isopropanol), and three long chain alkyls (nonane, tridecane, heptadecane). In addition to the environmental fluids, three non-reactive silane-coupling agents (octadecyltrichlorosilane, octyltrichlorosilane, propyltrichlorosilane) were used to treat the glass substrate before the epoxy was applied.

Experimental Setup

A schematic of the experimental setup is shown in Figure 6. The test sample is placed on a stand with the film side facing down. A ball bearing 0.275" in diameter is placed on the end of a shaft, which is then used to apply a load on the sample film. An Instron model 1123 universal testing machine was used to deliver a constant shaft displacement of 0.078 in./min. With the aid of a mirror and a transparent ruler, the blister radius can be measured and recorded by a video camera. Because of the parallax error, a small correction of the blister radius is needed. The load (P) and shaft displacement (w_0) are recorded by the Instron. One criteria each sample must meet for the data analysis to succeed is that the debond must occur axisymmetrically.

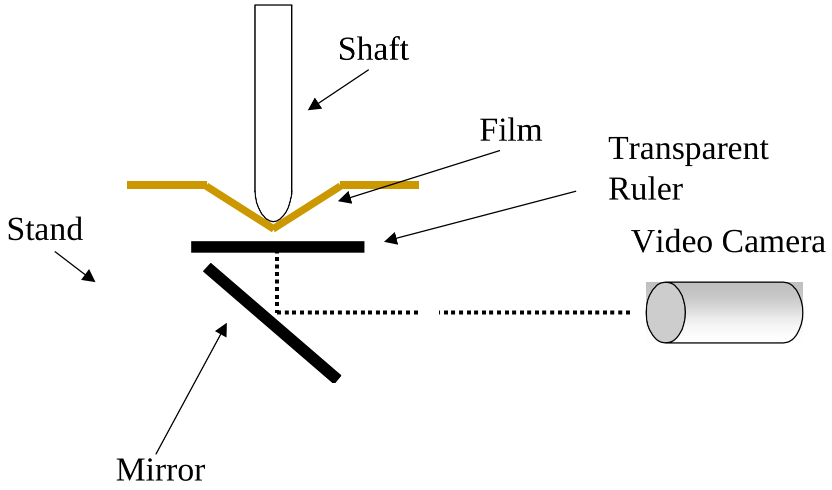

Figure 6. Experimental setup

RESULTS AND DISCUSSION

The typical load (P) versus displacement (w_0) curve obtained from the Instron is shown in figure 7. There are three regions of interest. Region 1 is where deformation of the sample film occurs prior to debonding. Region 2 is where the actual blister formation occurs. Region 3 is where the blister propagates. Of most interest is in region 3- the region where the slopes (P/w_0, P/a, w_0/a) are taken.

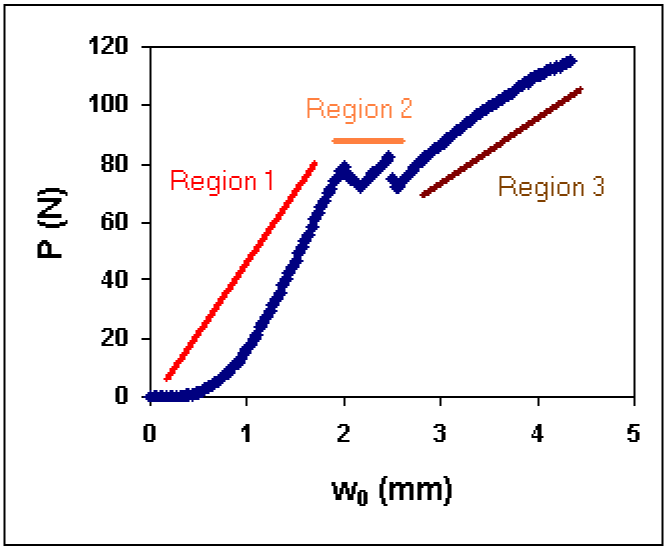

Figure 7. Load (*P*) versus displacement (w_0) curve obtained from the Instron

The film tensile rigidity (*Eh*) can be calculated by using region 1 and finding the specific region where *P* scales as w_0^3, as shown in figure 8. The slope of the *P* versus w_0^3 line can be substituted into equation 5 to determine the film tensile rigidity.

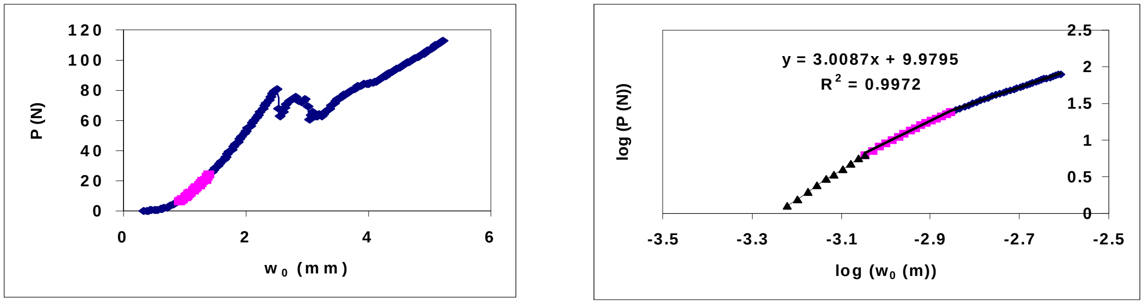

Figure 8. Curves used for determining tensile rigidity

Results from the samples exposed to the proprietary fluids (60^0C for 6 hours) are shown in Ttable 1. The most confidence can be placed in the strain energy release rates (G) obtained from the load-based equation, which is independent of the shaft displacement (w_0). Some uncertainty exist in the w_0 in the stretching membrane. The hybrid equation value is consistently higher relative to the load-based equation. The displacement-based equation value is consistently lower relative to the load-based equation. The shaft displacement (w_0) is believed to be underestimated due to residual stresses present in the test specimen, an effect illustrated in Figure 9.

Table 1. Strain energy release rates of proprietary fluids

Equation	Load-based	Hybrid	Displacement-Based
	G (P/a)	G (P/w_0)	G (w_0/a)
m1	45.4	93.5	14.9
c1	21.3	106.7	1.2
c2	54.6	428.8	0.8
c2	62.6	235	1.9
B	18.8	46.2	7
B	23.7	36.4	7.9

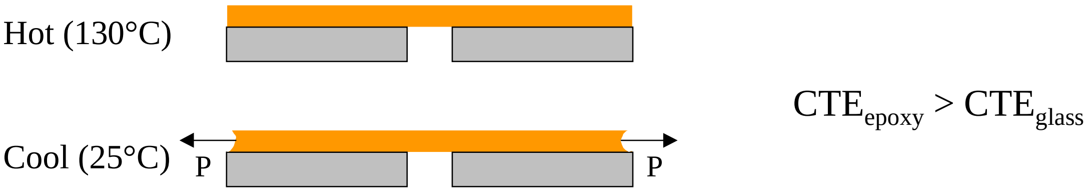

Figure 9. Residual stress

Residual stresses are formed when the epoxy cools from its curing temperature (130°C) to room temperature (~ 25°C). Since the epoxy has a lower coefficient of thermal expansion (CTE) than that of glass, it shrinks more than the glass after cooling thus imposing a tensile stress in the epoxy film. If the shaft displacement (w_0) were underestimated, this would explain why the measured hybrid equation G value is higher relative to the load-based equation G value. (Note the w_0 value is in the denominator of the hybrid equation.) Likewise, the displacement-based equation G value is lower relative to the load-based equation G value because the underestimated w_0 value (in the numerator of the its equation).

The epoxy/glass crack tip was exposed to alcohols and alkyl chains for 24 hours at 40^0C and 60^0C, respectively. The adhesion strength was not significantly degraded due to their presence and thus, the film ruptured other than debonding. Silane coupling agent treated surfaces exposed for 4 hours to 60°C water debonded effortlessly; and, as expected the octadecylchlorosilane showed weakest adhesion followed by octylchlorosilane and then propylchlorosilane. This result is presumably due to the increased surface coverage of the larger silane molecules.

The film tensile rigidity (*Eh*) calculated using equation 5 was an order of magnitude greater then that of the estimated (*Eh*) based on film thickness, relative volume fractions, and typical modulus values of the epoxy and Kapton® film. The Kapton® Tape used as the pre-crack initiator may cause this. During the test, as the sample is loaded and prior to crack propagation, the tensile rigidity of the Kapton® tape, the epoxy layer, and of the Kapton® backing are all measured, rather than the film of interest: the bimaterial epoxy/Kapton® backing.

FUTURE WORK

Future work will focus on improving the sample design, such that a more reasonable film tensile rigidity (*Eh*) value is calculated. Soda lime glass may have different surface chemistries depending on how it was manufactured. Quartz glass will be used in future sample preparation because of its controlled surface chemistry (approximately 99% SiO_2). The quartz glass surface will be treated with the reactive silane coupling agent aminopropyltrichlorosilane to improve adhesion by forming a covalent bond with the epoxy, which should improve environmental resistances. In addition, different pHs of water will be tested as environmental fluids.

CONCLUSION

The shaft loaded blister test was used to investigate the strain energy release rate between a model epoxy and soda lime glass. Exposing the system to different environmental fluids, a definite difference in adhesion was observed - a result of the different aggressiveness of the fluids. Water was the most aggressive fluid (G ~ 17 J/m^2), while the strain energy release rate of various proprietary fluids ranged anywhere from 23-65 J/m^2. Non-reactive silane coupling agents added to the soda lime glass resulted in a decrease in adhesion. Residual stress is thought to have a significant influence on the calculated strain energy release rate values. Also, the film tensile rigidity (*Eh*) may be more accurately calculated once the Kapton® tape, used for pre-cracking, is eliminated.

REFERENCES

1. Yeh-HungLai and David A. Dillard, *Journal of Adhesion* (1995), 59.
2. Kai-Tak Wan and Yiu-Wing Mai, *International Journal of Fracture* (1996), 181-197.

Immobilization and Hybridization of DNA on Polymer Surface.

by Abisake Feleke*, Sanjun Niu and Ravi Saraf
Department of Chemical Engineering, Virginia Tech,
Blacksburg, VA 24061

* Department of Chemistry, Florida Institute of Technology, Melbourne, FL

ABSTRACT

DNA chip has thousands of DNA (deoxyribonucleic acid) fragments arrayed at discrete sites on solid substrate. Hybridization of DNA sample to the chips allows us to measure the sequence of the DNA. The technology holds a great promise for identifying gene that predispose men to disease, gene regulation events involved in disease progression, and more-effective disease treatments.

A coated polymer chip is used for immobilization of specific complementary base and used for the detection of the DNA sequencing without the photoluminescent tagging. We have proven that the hybridized DNA can be detected without a tag. The chip is mainly used to identify the gene sequence.

Single DNA were immobilized on the polystyrene surface and hybridized to identify the complementary products. The samples were scanned with the light detector called fluorescents spectrophotometers. Fluorescence spectrophotometer is used to identify hybridization state of the DNA.

Currently, the majority of the microarrays are created by spotting aliquots of DNA on to a solid surface and supported by robotic technology. Photoluminescence is used to differentiate between single and double strand DNA. Photoluminescence is emission of light.

DNA chip is ten times faster than the regular gene chip and we can be benefited in various ways. It is used for drug designing, genetic mapping, personal identification as well as disease identification.

INTRODUCTION

DNA (Deoxyribonucleic acid) is a blueprint of life; that encoded the genetic information and determines heredity. Its also revels the transmission of characteristic from parent to offspring. DNA has the genetic blueprint in every living organism and each organism has a unique DNA signature. A person has more than 100, 000 genes, and many human diseases are associated with mistakes at the genetic levels significant of detection of DNA sequence. DNA sequence is the genetic instruction manual of an organism, although most of the genetic sequence is the same for all people. It is a combination of both parents. The genetic sequences of the mother and father are combinations as well from their parents. Making things even more difficult.

DNA has a double helix structure. The two strand DNA molecules are held together by hydrogen bone in the middle. Each strand contains a sequence of bases also called nucleotides. A base is one of four chemicals such as adenine, guanine, cytosine and Thymine. The base pair are only bond to other base pair. Adenine base on one strand will hybridized with Thymine base on the other hand and Guanine base will pair up with Guanine base. Each Individual has the same chemical structure but the only difference is the order of the base pair. Double strand DNA are read in a particular direction, from the top called the 5' or "five prime" end, to the bottom called the 3' or "three prime" end. In a double helix, the strands go opposite ways

DNA chip is a device used to detect gene sequencing. The term DNA chip is used by company called Affymetrix in California, invented this new tool to read the sequence book by book instead of reading it word by word. DNA consists only four letters rather than 26 English letters; therefore, the chip proved method to read the sequence chapter by chapter than word by word.

Currently the gene technology use DNA chip with tagging on the complementary base pair to detects the hybridized DNA. However our goal is to analyze the hybridized DNA without tagging the sample. Tag is a fluorescent dye that is used on the complementary DNA. The collected data resulted that DNA can be analyzed without the tag. This verifies our result.

The silicon chips were covalently grafted onto polystyrene surface. DNA molecules were bonded covalently onto the amine (NH_2) groups and immobilized to the solid surface at different locations. Immobilization can be obtained by passive adsorption, of UV light. It was confirmed that the DNA was bonded to the 5’ end, which has the phosphate groups. The ideal immobilization of the DNA onto solid surface is done by a single covalent bond.

After grafting DNA was hybridized onto polystyrene film. When two DNA strands hybridize perfectly, knowing the sequence of bases on one strand reveals the sequence on the other. DNA is a two-strand molecule and held together by hydrogen bond in the center. Two stranded DNA polymers have complementary base pairs that provide an inherent self-organization

Research believes that the DNA chip will enable the medical doctors to detect genetically based diseases and health conditions. If the doctor can determine whether the person is susceptible to a particular disease before it occurs, then a preventive measure can be taken to the path of the disease. The main function of the chips will be to analyze DNA and provide a speedy test for bacterial pathogens in tissues, blood, or other body parts. This can also be used to detect biological contaminants in water and food.

DNA Chips are compact in size, massively parallel and faster compared to the currently used gene sequencing method. At the present time the chip is very simple and less expensive compare to the currently used one.

EXPERIMENTAL

Reagent: DNA, oligonucleotide, Polystyrene, Toluene, Sulfuric acid (H_2SO_4), Hydrogen Peroxide (H_2O_2), EDC (1[3-Dimethylamino)propyl]3-ethlcarbodimide hydrochloride.), Hybridization buffer solutions, 0.75 M NaCl, 5mM Sodium Phosphate (pH 7.0), 5mM EDTA, 0.1% Tween 20, 50% formamide. Washing solution 5X SSC (standard saline citrate) + 0.25% SDS(dodecyl sulfate sodium salt) and 6X SSC, 0.1% SDS.

Preparing substrate of Polystyrene film: Clean silicon substrate with toluene because toluene is non-polar and will remove oil and unnecessary substance from silicone surface. Next, clean the substrate with piranha. Piranha is a mixture of sulfuric acid and hydrogen peroxide with the ratio of 1:3 peroxide and sulfuric acid. The purpose of piranha is to make the surface hydrophobic and then clean it with deionized water 3 times. Then treat silicon surface with hydrofluoric acid. The surface will be hydrophobic and dry it with Aragon air. Spin cast the silicon substrate alone and then spin cast 1% polystyrene in toluene on the silicon surface with speed of 3000 rmp. The polystyrene thin films will looks very smooth and shiny. After the procedure is done, place the substrate in the oven with the nitrogen atmosphere for 10 minute at 120 ^{0}C to remove the residue of solvent. As well as relaxing the molecules because nitrogen gas in an inert gas and will degenerate polystyrene at 120 ^{o}C.

Ammine group: Ammine groups are introduced on to the polystyrene film after the thinner film was dried with nitrogen gas. DNA covalently attached to ammine group. During the ammine attached to the polystyrene the surface become hydrophobic. Contact angle measurement is used to verify the result.

Grafting: Prepared 0.0767 gram with 2ml of distil water EDC (1[3-Dimethylamino)propyl]3-ethlcarbodimide hydrochloride) fresh for each experiment and added 50ul to each sample surface and place the single strand DNA onto the polystyrene surface. Then incubate for 5 hr at 50 ^{0}C. After incubation the chip is washed three times with washing solution to remove sample that doesn’t bind to the polystyrene surface. Washing solution: 0.1N NaOH + 0.25% SDS (Dodecyl Sulfate Sodium Salt) heated at 50 ^{0}C

Determination: After the chips washed, samples were run through a light detector called fluorescence spectrophotometer. This machine will detect whether the single strand was attached to the polystyrenes surface.

Hybridization: prior to the hybridization the surface was rinsed once with hybridization buffer which consist of 0.75NaCl, 5 mM Sodium phosphate (pH 7.0) 5mM EDTA (Ethylenediamine Tetraacetic Acid), 0.1% Tween 20, 50% formamide. The samples were incubated for overnight at 42 ^{0}C. After the incubation the sample was washed three times with washing solution 6X SSC (Standard Saline Citrate), 0.1% SDS at 60 ^{0}C. Rinsed it with deionized water and dried with air.

Determination: As it was mention above wash the sample with washing solution and run the sample in the florescence spectrophotometer again after hybridized process is completed.

Surface photoluminescence Measurement

Fluorescence spectrophotometer is used to detect hybridization of DNA. The sample is placed face down between the scanner holders and then scanned at the excitation wavelength of 265nm. A signal is measured using the intensity and the wavelength of the given sample. An image of the surface is obtained.
Repeating procedure: After the fluorescence signal is recoded, the sample was de-hybridized with 8.3M urea solutions at 37 °C for ten minutes to remove complement and then washed thoroughly with deionized water. The sample is used to hybridized again and the cycles can be done several time or repeatedly.

RESULTS

It was observed that when light impinges on the surface at least distinct processes occur, light scattering, light reflection, and absorption. The process of absorption followed by emission of light of different wavelengths is called photoluminescence. According to the result that as the intensity of reflection of light and the wavelength of the light increase, however the intensity of absorption will decrease. This signifies that the intensity of the light that passes through the sample depends on the amount of the light absorbed by the sample. The more the energy, the more light will be absorbed but will emitted the excess energy as photon.

Photoluminescence is used to characterize the electronic energy level of a surface. When an adequate amount of light incident on the surface, energy will be absorbed and electron excitation is produced. Ultimately, the excited electron relaxes and returns to the lower state and emitted energy as photon. This is a photoluminescence phenomena. (Refer figure 1) The emitted light is called a photoluminescence. Normally polystyrene does photoluminescence at 265nm-excited state and has the emission peak between 320 nm- 330nm. Refer to Figure 1.

The Incident input light reaching photoluminescent film =

$$I_{IN} = I_{Incident} - I_{absorption} - I_{scattering} - I_{reflection}$$

Output signal from the photoluminescent film =

$$I_{OUT} = K_1 I_{PL} = K_1 K_2 I_{IN}$$

K_1 = Photoluminescent Efficiency
K_2 = Detector Photoluminescent Efficiency

The single strand absorbs more light than the double strand. The difference between single and the double strand DNA is that the double strand DNA reflects more light than the single however the absorption is different. It was concluded that because double strand DNA, the nucleotide base will be stacked on top of each other such that the intensity (photon) will be longer wavelength however the absorption will decrease, while the intensity of the shorter wavelength absorption band will increase. The amount of the light reflected by the object is very dependent upon the texture of the surface. The light reflects with less concentration than with more concentration. This also refers to the thickness of the surface, the thicker the surface the less likely light will be reflected compare to the thinner surface. This signifies why we used 1% polystyrene.

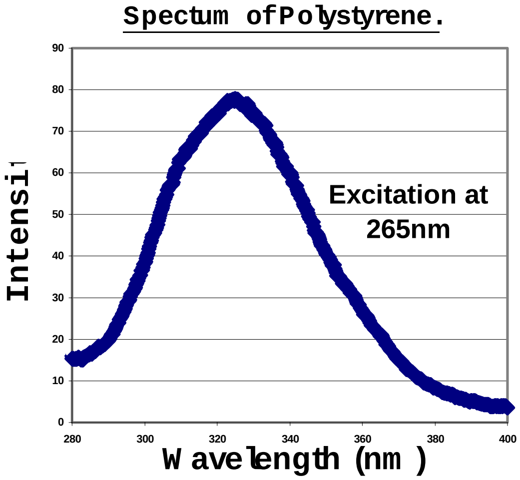

Figure 1, is Polystyrene excited at 265nm. The intenstiy measure by light sensitiviyt detector

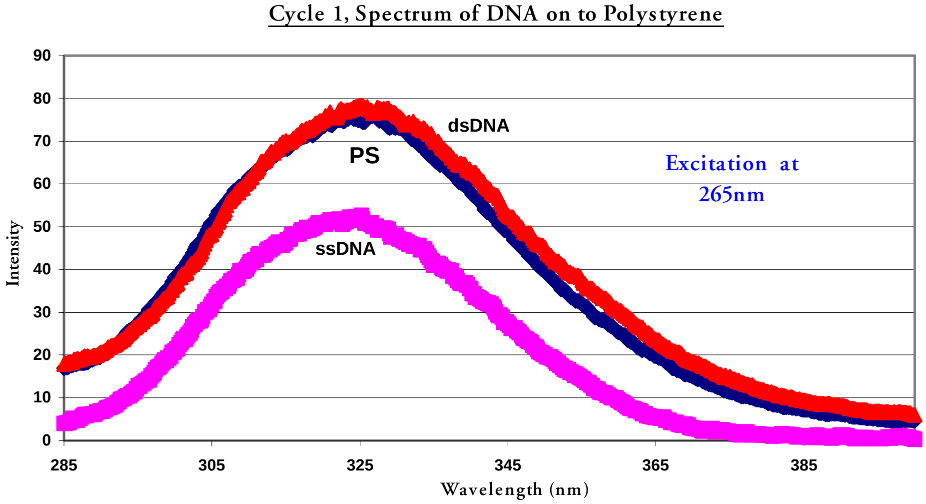

Figure 2. Illustrate the Polystyrene, ssDNA and dsDNA on the surface. The aim of this graph is to differentiate between ssDNA and dsDNA reflection of light by photoluminescence.

Figure 3 verifies that the sample can be repeatedly done in three cycles. It was de-hybridized and re-hybridized twice. The result is conformed that the de-hybridized one, which is a single strand, has lower peak than the re-hybridized DNA. When the sample is de-hybridized, it returns to the single strand DNA however re-hybridizing will de-bond the molecules and form double strand DNA. The cycle also show that the single strand DNA reflect less light than the double.

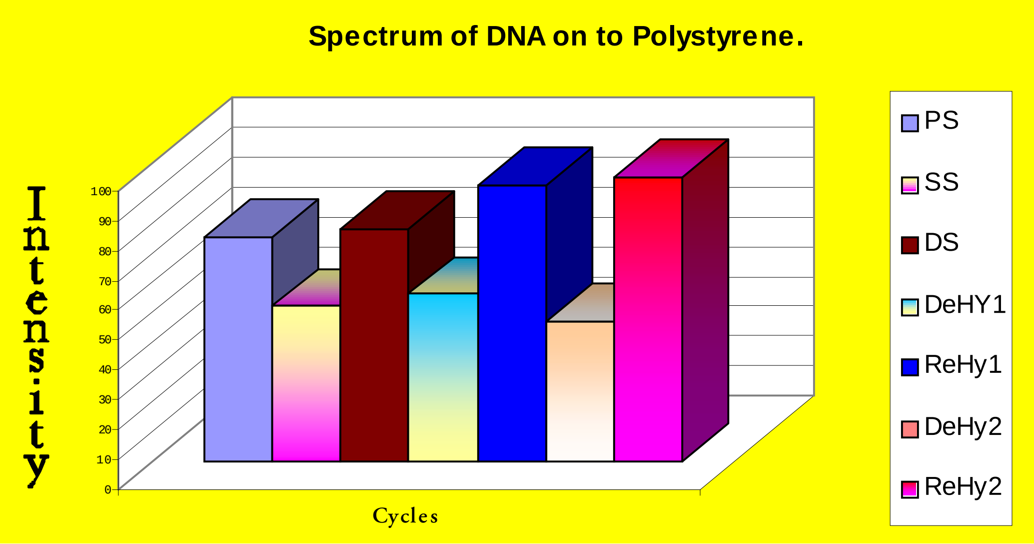

Figure 3. This is the repeated cycle of the single and double strand DNA.

DISCUSSION

So much of who we are eventually can be traced down to our gene and to our DNA that encode the genetic instruction. DNA chip does attracted everyone attention. It can be very useful mostly for medical reason. For instant, it is used for diagnostics purposes and drugs detection for HIV or Cancer.

Photoluminescence is very fast optical detector and the primary motivation for using the light detectors is to verify between single and double strand DNA.

Polystyrene photoluminescent at 265nm excited state, however, DNA strongly absorbed light at 260nm. Obviously it was conform that the pure double strand DNA can absorb less light than the single strand DNA. Our result challenge the significant of light reflect on the sample and suggest to that the photoluminescent might be inadequate technique. However, we have done more than one sample and the resulted are the same. (Refer to the figures) The result also changes, as optical thickness is change; When the concentration of the polystyrene was greater there was no DNA signal but with the less concentration we have emission peak.

Fluorescence spectrometer is used to conform the emission of photon light by DNA molecules, referring to the figure. Single strand DNA reflects less light compared to double strand DNA.

The absorption of the material will also depend on the energy of the incident light. Photon of a particular energy that was absorbed or emitted by the sample does provide the evidence of the difference of the electronic state. This indicates that hydrophobic interaction was the major driving force for absorption of individual DNA molecules.

CONCLUSION

We have shown that the concepts work of the chip. According to the result that was collected from the fluorescence spectrophotometer verified that the complementary DNA can be analyze without the fluorescent dye.

Polystyrene is also a good photoluminescence method for the measurement. (Figure1). We have also verified the absorption peak of the single and double strand DNA in figure 2. The emission peak rise up for the polystyrene and lower for the single strand DNA, however the emission goes up for the double strand DNA. Figure 3 also demonstrate the six cycles that was measured, and result, which show that the process can be repeatedly done.

In this paper, we explain the methods for binding of DNA molecules on to polystyrene surface as well as the hybridized process. Obviously, the hybridized of DNA molecules can be done without the tag. Tagging is also an extra step.

Although the DNA chips are now commercially available and today, more than two companies provide the products as well as the services. In the future we can all be benefited from this new technology and also can be able to detect any genetics base disease, which we inherited from our family.

REFERENCE:

1. Rasmussen, Soren R.; Larsen, Mette R.; Rasmussen, Svend E. *Covalently Immobilization of DNA onto Polystyrene Microwells: The Molecules are Only Bound at the 5' End*. **1991**, 138-141.
2. Cliff Henke**.** *DNA-chip technologies* IVD Technology Magazine. **Sep 1998.**
3. Michael Thompson and L. Michelle Furtado. *High Density oligonucleotide and DNA probe arrays for the analysis of target DNA***,** Analyst**, 1999,** 124, 1133-1136.
4. Timothy G. Gfroere, *Photoluminescence in Analysis of Surface and Interface*. Encyclopedia of Analytical Chemistry. **2000**, pp. 9209–9231

Creep Rupture of Semi-Structural Pressure Sensitive Adhesives

Joshua W. Grohs*, Dr. Don Ohanehi and Dr. David Dillard
Department of Engineering Science and Mechanics
Virginia Polytechnic Institute and State University
Blacksburg, VA 24061

*Department of Mechanical Engineering, Virginia Tech, Blacksburg, VA

ABSTRACT

Creep rupture tests were conducted under various stress levels and temperatures using adhesively bonded cylindrical aluminum specimens. The pressure sensitive adhesives used in this project were supplied by 3M Corporation Bonding Systems Division. Specimens were tested using a stepper motor creep frame, brought online during this summer project. From the tests, time to failure for the various stress levels, mode of failure for various test conditions, and strain as a function of time were recorded and analyzed to characterize the time dependent behavior of the test adhesives.

INTRODUCTION

A pressure sensitive adhesive is a very interesting viscoelastic material, which is permanently tacky at room temperature and requires brief moderate pressure for activation. Tacky requires that an adhesive be sufficiently soft to wet, or flow into, intimate contact with a substrate. Such adhesives are viscoelastic materials exhibiting characteristics of both an elastic solid and a viscous fluid, allowing elastic deformation like a solid as well as flow like a liquid. Creep rupture testing is one method of characterizing this time dependent behavior.

Certain concepts used for analysis of this project are introduced briefly in this section. Stress is defined as the force per unit area distributed over a given cross-section and shown mathematically in Equation 1-1.

$$\sigma = \frac{Force}{Area} \quad (1\text{-}1)$$

Figure 1-1 shows the stresses. Normal stress, which is the stress perpendicular to a given cross-sectional area, is represented by the Greek letter σ. Shearing stress, which is the stress parallel to a given cross-section, is represented by the Greek letter τ.

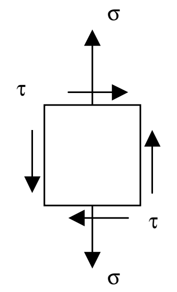

Figure 1-1: Normal and Shear Stresses

Strain is the change in length of a material over the original length. Equation 1-2 describes it mathematically, while Figure 1-2 represents it graphically.

$$\varepsilon = \frac{\lambda}{\Delta\lambda} \qquad (1\text{-}2)$$

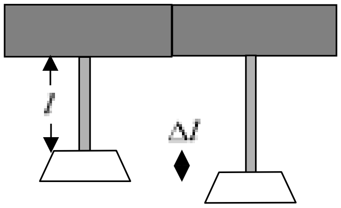

Figure 1-2: Normal and Shear Stresses

The stress levels calculated in this paper came from the applied load divided by the original cross sectional area of the adhesive. This load was always applied in the vertical direction and the test specimens were machined to get normal and shearing stresses. The creep tests performed in this project were conducted using stepper-motors in a control loop with load cells, which hold a set load level and move up or down in order to maintain this load. Equation 1-3 shows that this applied stress is defined by the magnitude of the creep stress, $\hat{\sigma}$, multiplied by the Heaviside or unit step function.

$$\sigma(t) = \hat{\sigma} \bullet H(t) \qquad (1\text{-}3)$$

The tests conducted during this project produced data useful for different analyses: creep analysis and creep rupture analysis. Creep analysis closely examines the time dependent behavior of strain and creep compliance of the adhesive. Equation 1-4 shows the creep compliance of viscoelastic materials calculation as the strain divided by the magnitude of the creep stress. This provides very important design information.

$$D(t) = \frac{\varepsilon(t)}{\hat{\sigma}} \qquad (1\text{-}4)$$

Creep rupture analyses focus on the time to failure results from the tests and allows for predictions of failure. This also produces important design information.

EXPERIMENTAL

Test Fixture:

In order to perform the creep rupture tests required for this project, a four-channel stepper motor creep frame had to be brought online. Previous experimenters purchased the stepper motors and environmental oven and built a homemade test frame at different times but they were unsuccessful in bringing all four channels online. Modifications were made to the fixtures including realignment of the oven, stepper motors, and test frame in order to have each component vertically aligned. From here the load train rods were machined to decrease the diameter to minimize contact interference where the load train passed through holes in the oven. End yokes were then purchased and modified to allow for some flexibility in the load train to maintain a vertical load. A 1000 N load cell was calibrated and placed on top of each of the stepper motors in order to input load into the data acquisition. A LabVIEW® programmer devised jog and creep test programs to perform the tests. With everything online, testing could then begin. Figure 2 displays a picture of the completed test fixture.

Specimens:

In this project three different tapes were used and tested at various load levels and temperatures. Testing was focused on tape A; tapes B and C were used for time to failure comparisons. All of the specimens were made of two pieces of one-inch diameter 6061-T6 aluminum bonded together. The outside ends were tapped for eyebolts that attached to the test fixture. For surface preparation the substrate was abraded by using Scotch-Brite® (3M trademark) in an orbital sander until a uniform surface was created. Then the specimen was wiped clean with 50/50 isopropyl alcohol/water solution until no visible contamination remained. A set of V-blocks was used in order to align the specimens for bonding. Figure 3-1 shows the pneumatic bonder that was used to apply a minimum of 15 psi (0.1 MPa) to the joint for 15 seconds. After bonding, each specimen was allowed to dwell and wet out at room temperature for a minimum of 72 hours prior to testing. After this dwell time the specimens were loading onto the test fixture and tested. Figure 3-2 shows a picture of a bonded specimen in the test fixture ready for testing.

Three temperature conditions were tested in this project: 25°, 45°, and 60°C. Three load levels were chosen for each test condition. The specimens were placed in the test fixture and allowed to thermally equilibrate before testing began. Test data was taken for every move of the stepper-motor, which has a resolution of 4724 steps per millimeter, recording three variables: time, displacement, and load.

Figure 2: Test Fixture

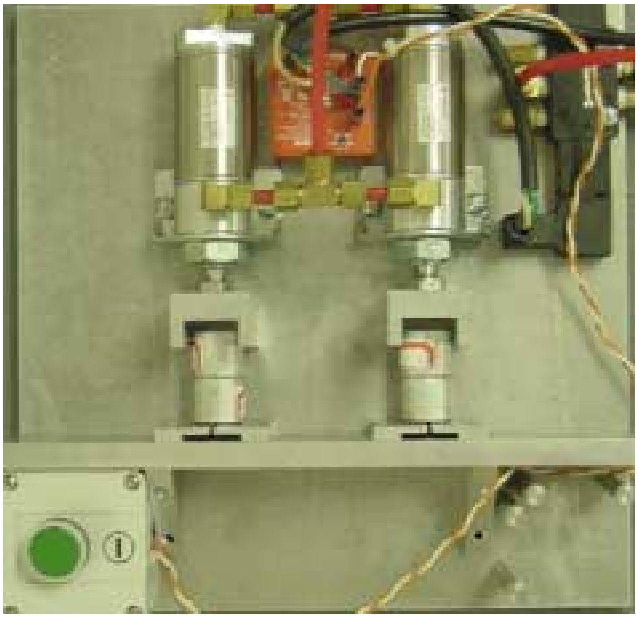

Figure 3-1: Bonding Fixture

Figure 3-2: Specimens in Fixture

RESULTS AND DISCUSSION

Creep Rupture Analysis:

A very important plot for creep rupture analysis is seen in Figure 4-1. This is the stress versus log time to failure for tape A of this experiment. This plot is a logarithmic regression in the form $\sigma = A\log(t) + B$, where A and B are constants. This regression allows a prediction of when failure will occur for various stresses. A designer finds this data important. For example, if a product's expected life is 5 years, then the designer can check the time to failure using this regression and feel confident his design will not fail in that 5-year span.

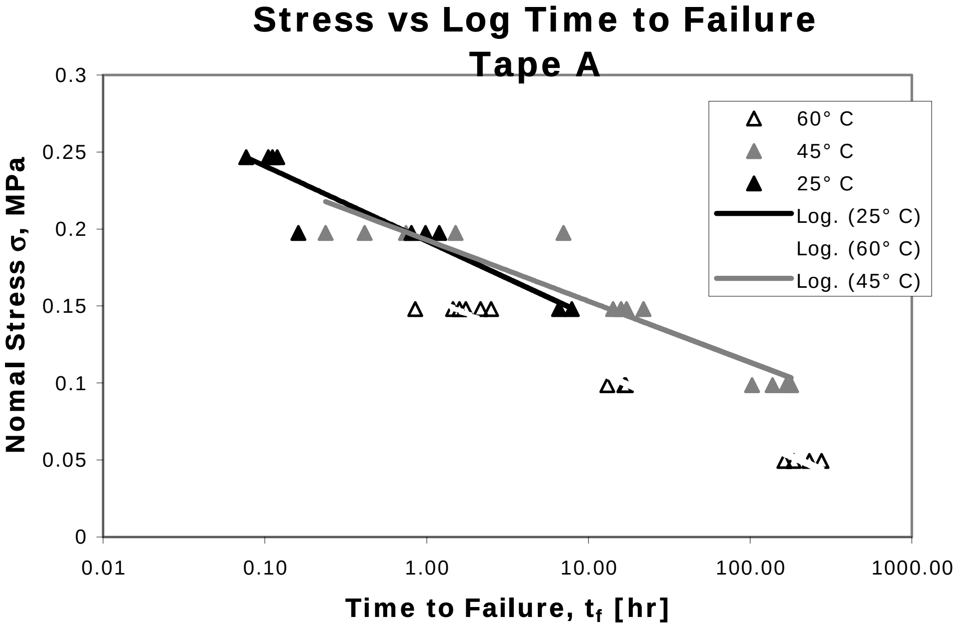

Figure 4-1: Normal Stress vs. Time to Failure

By closely examining this plot, it may first seem odd that the 25° C curve lay almost on top of the 45° C curve. One's intuition would expect that this curve should lay above the 45° C, following some pattern similar to the 60° and 45° curves. This may however be explained by the failure surfaces. Figures 4-2 show failure surfaces from the room temperature tests and the elevated temperature tests. From these one can see how the failure went from an adhesive layer failure, leaving a layer of adhesive on both sides, to the clean debond seen at the room temperature specimen. A change in failure mode is the current suspected driving force to the abnormality in Figure 4-1, and will be examined again in the creep analysis.

Elevated Temperature Specimen

Room Temperature Specimen

Figure 4-2: Failure Surface Comparison

Tape Comparison:

Figure 4-3 displays a Stress vs. Time to failure curve at 60° C for the three tapes in this experiment. From this plot we can compare the performance of the various tapes. Some discrepancies arouse with Tape B. Preliminary data from Tape B showed failure times similar to Tape A, however more recent data, taken at the two highest levels, approximately 0.15 and 0.1 MPa, shows a different behavior. Future work will include retesting Tape B for a better understanding. Tape C's failures at the high stress levels occurred before Tape A's failures. However the lower stress level tests indicate that the two tapes performed similarly. In order to have a full comparison, future testing of these other two tapes, Tapes A and C, is necessary.

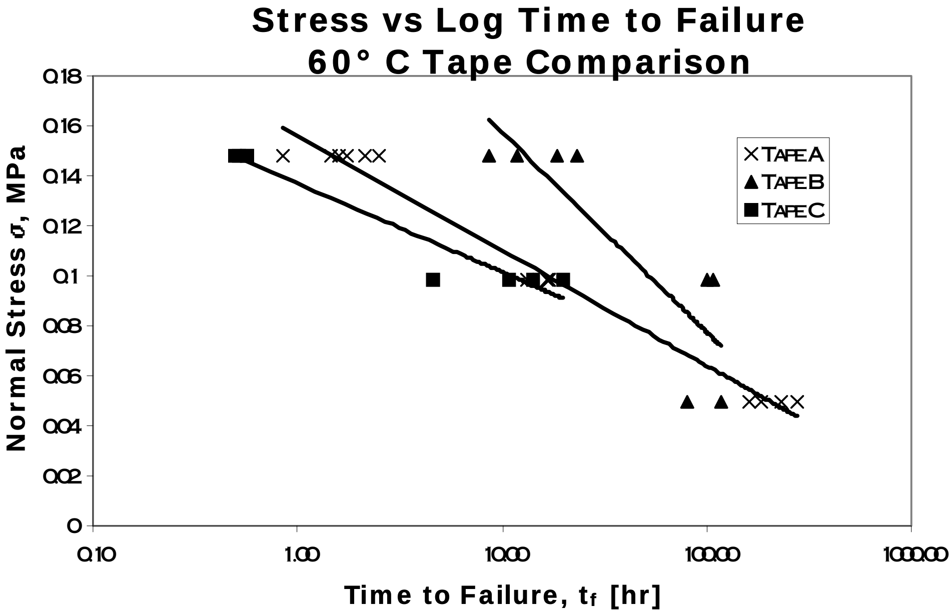

Figure 4-3: Tape Comparison at 60° C

Creep Analysis 60° C Tests:

Results are found in Figures 5-1 and 5-2, which display the strain as a log function of time and the creep compliance as a log function of time, respectively. From the strain vs. time curve, one can see that specimens at the lowest load, 25 N, spent the great majority of their life creeping very slowly until about 50% strain. At this point creep accelerates rapidly into a tertiary region leading up to rupture. Both of the other two load levels experience this shift into the tertiary region; however these increases in debond occur at approximately 100% strain. This is important to note when considering design criteria. Due to the accelerated creep in these tertiary regions, a designer would not want the adhesive to ever enter this region, and would therefore like to avoid exceeding these strain percentages. The other important plot for creep analysis is the creep compliance curve. As shown in equation 1-3, $D(t) = \frac{\varepsilon(t)}{\hat{\sigma}}$, the creep compliance relates the creep stress level to the strain as a function of time. From the creep compliance one can predict the strain as a function of time for any stress level at that test condition. This yields invaluable design information, since now the designer can empirically determine the time dependent behavior at various stress levels. Once temperature and humidity shift factors are determined one can calculate the strain as a function of time for any stress level and any temperature condition.

Creep Analysis 45° C Tests:

Results are found in Figures 6-1 and 6-2, which again display the strain, and creep compliance plots respectively. From the strain vs. time curve, one can see that specimens at the lowest load, 50 N, spent the great majority of their life creeping very slowly until about 100% strain. This is very different than with the other load levels for this temperature, which both crept rather rapidly in comparison. For this temperature and load level, a designer would want to stay under the 100% strain region in order to eliminate the accelerated creep that occurs after this strain level. Another thing to note from these strain plots is that all of the failures occur at approximately 700% strain. This is the same as the strain at failure for the 60° C tests. From this, one can speculate that the failure mode seen in both the 45° and the 60° C tests, is strain controlled and whenever the adhesive reaches this strain, rupture will occur. The creep compliance curve also gives valuable data for the 45° C tests. In this we see that the compliance is lower than that experienced at 60° C. A larger creep compliance means that the strain increases faster than a lower compliance's strain.

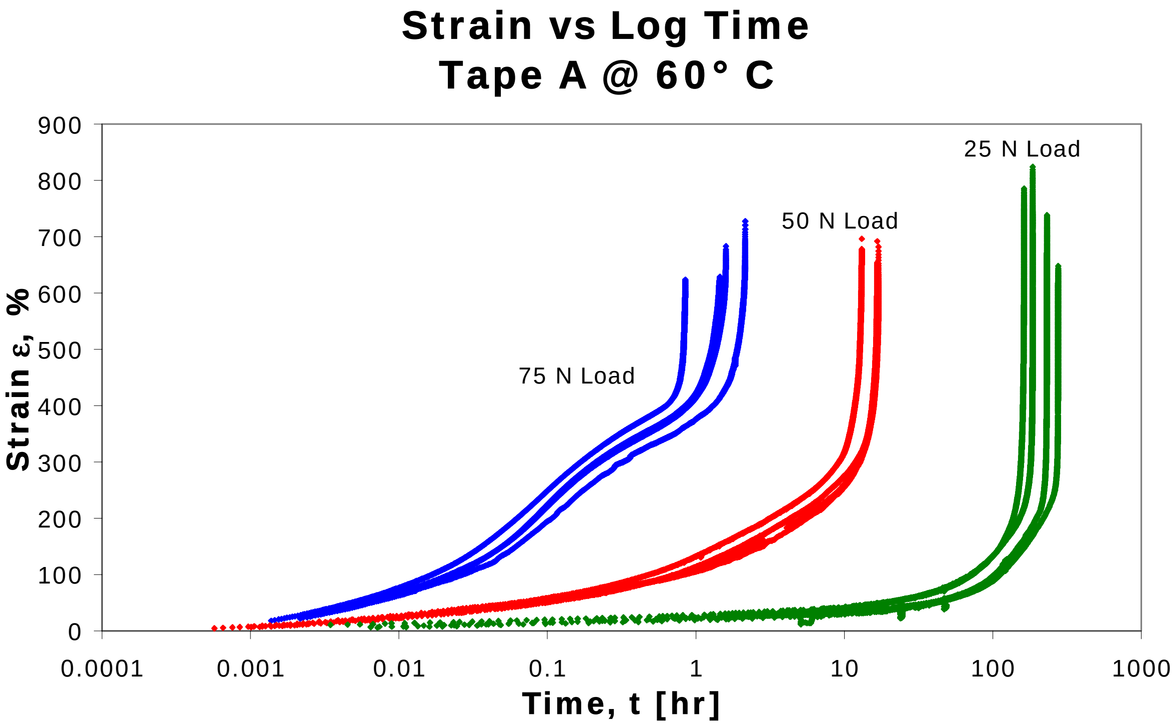

Figure 5-1: Strain vs. Log Time Plot

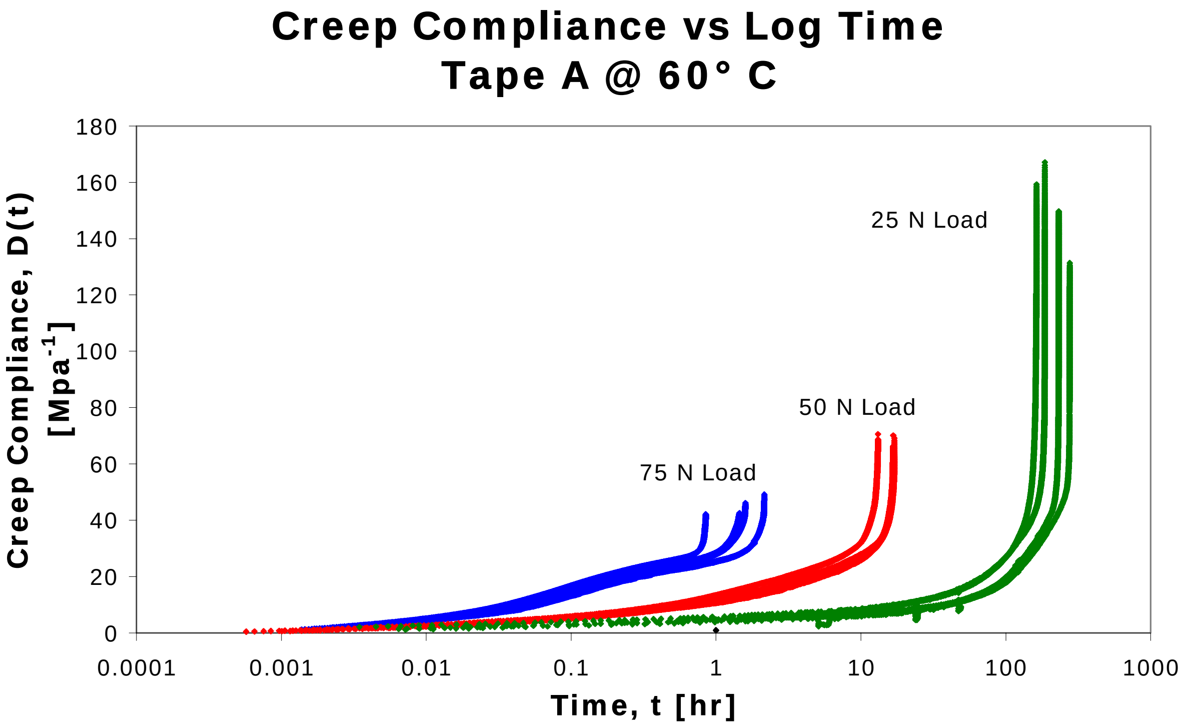

Figure 5-2: Creep Compliance vs. Log Time Plot

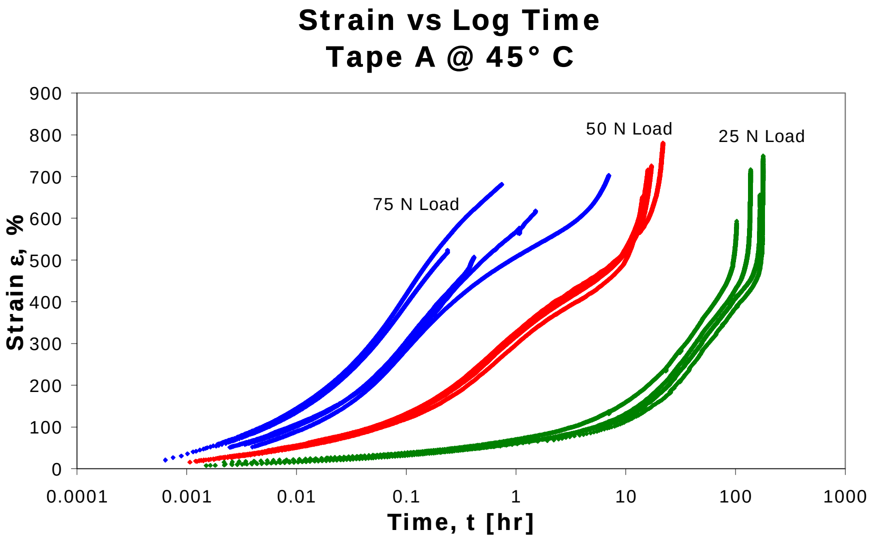

Figure 6-1: Strain vs. Log Time Plot

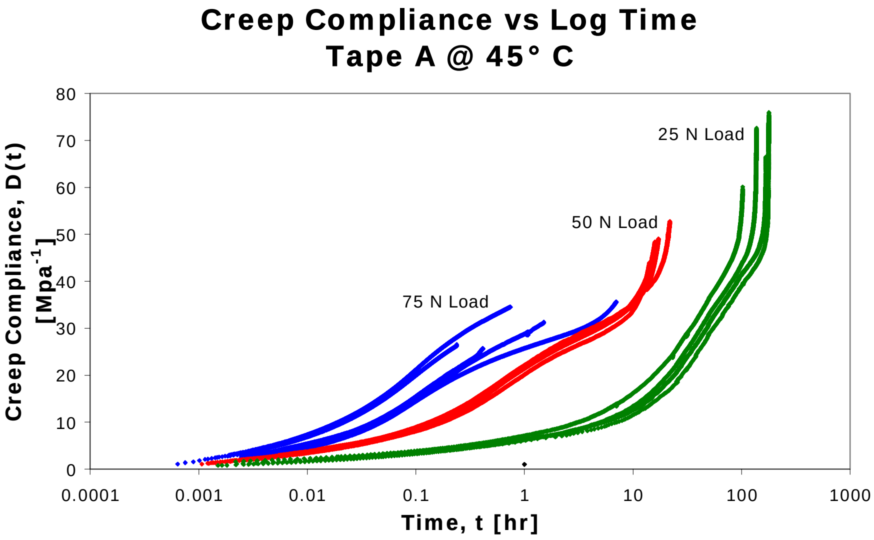

Figure 6-2: Creep Compliance vs. Log Time Plot

Creep Analysis 25° C Tests:

Results for the room temperature tests are found in Figures 7-1 and 7-2, which again display the strain and creep compliance plots respectively. The results from this temperature are very intriguing. The strain vs. time plot showed no real changes of creep rates, rather a steady creep until failure. All of the specimens failed much earlier than predicted. Creep compliances were much higher then expected due to this rapid creep. As described in the creep rupture analysis, a change in mode of failure was suspected to have occurred at this temperature, as first witnessed by a change in failure surface. This may be best described by Figure 7-3, showing the 75 N load curves for strain vs. time for all three temperatures. Analyzing the shapes of the two elevated temperature curves we see a similar knee; however this knee is not found in the room temperature curve. This knee seems to increase the life of the specimens and currently the suspected creep occurring in this knee is the beginning of a cohesive failure that causes rupture between the adhesive surface and the tape's core. This would account for the typical shadow, or adhesive residue, left on the failure surfaces at the elevated temperatures repeated here in Figure 4-2. With the room temperature curve being void of this knee, the specimens would be void of any adhesive residue on the failure specimens. This is exactly what was experienced.

Elevated Temperature Specimen

Room Temperature Specimen

Figure 4-2: Failure Surface Comparison

Further evidence that supports a mode of failure change occurred in the strains at failure. As described in the previous sections and seen in Figure 7-3, 45° and 60° C failed at approximately 700% strain, however at room temperature the failures all occurred around 500% strain. This again supports a different mechanism of failure.

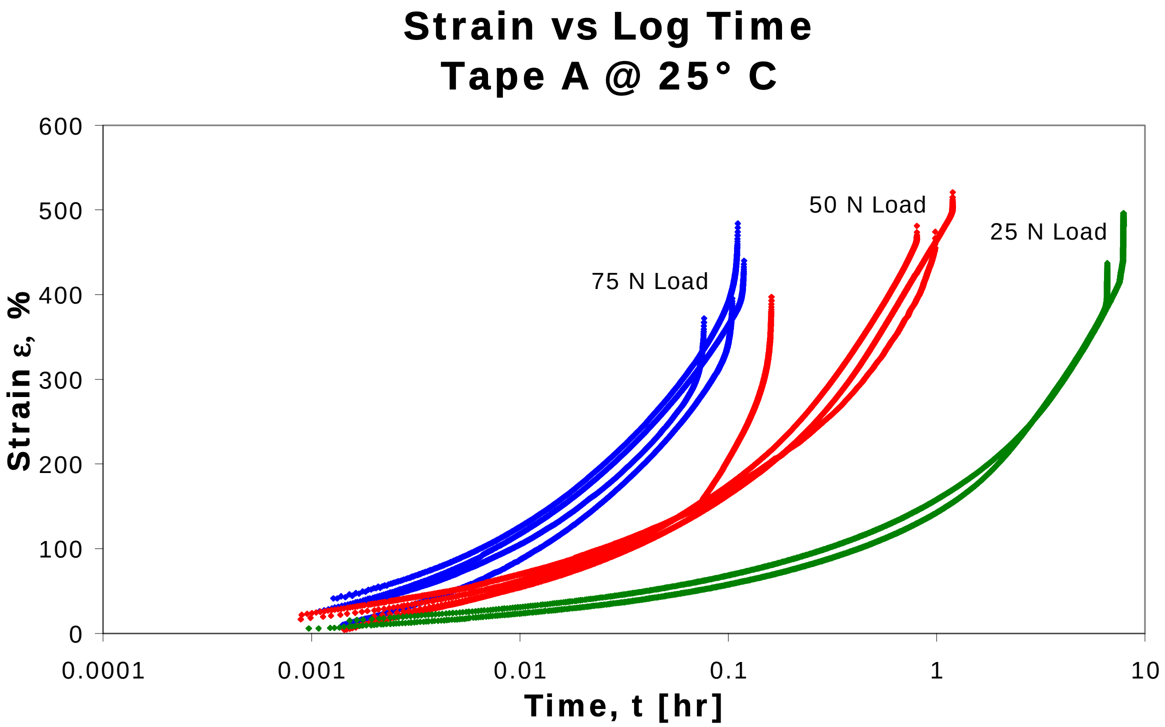

Figure 7-1: Strain vs. Log Time Plot

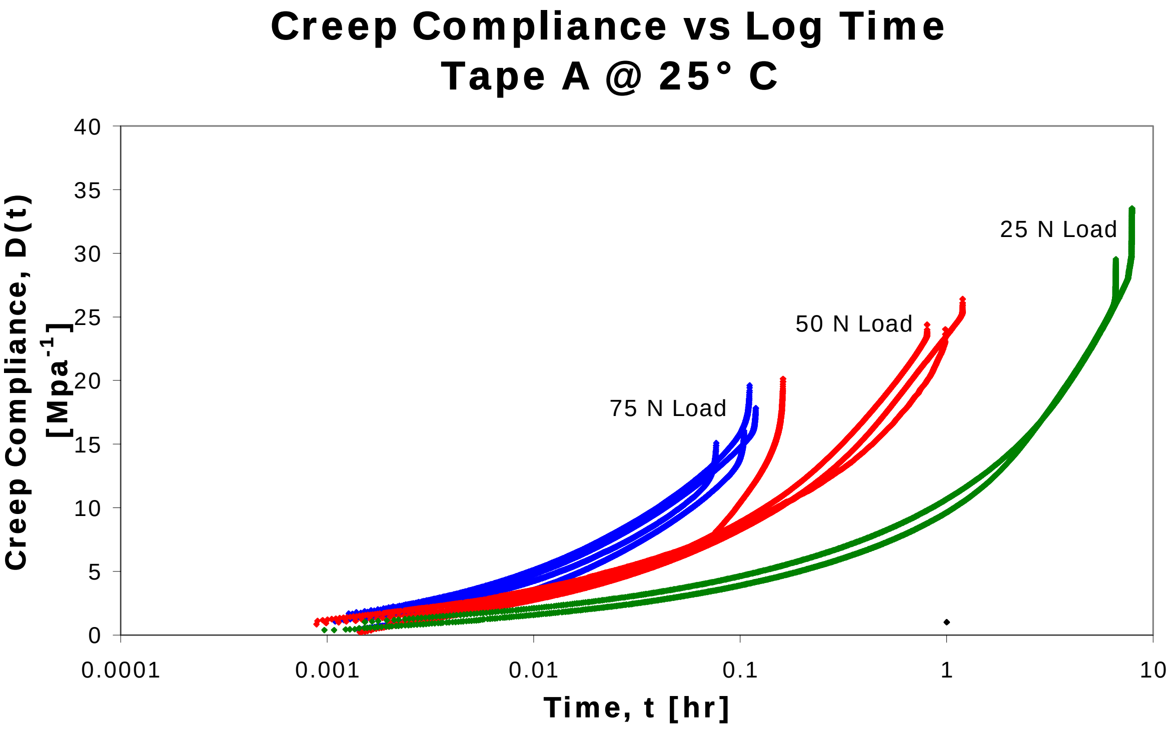

Figure 7-2: Creep Compliance vs. Log Time Plot

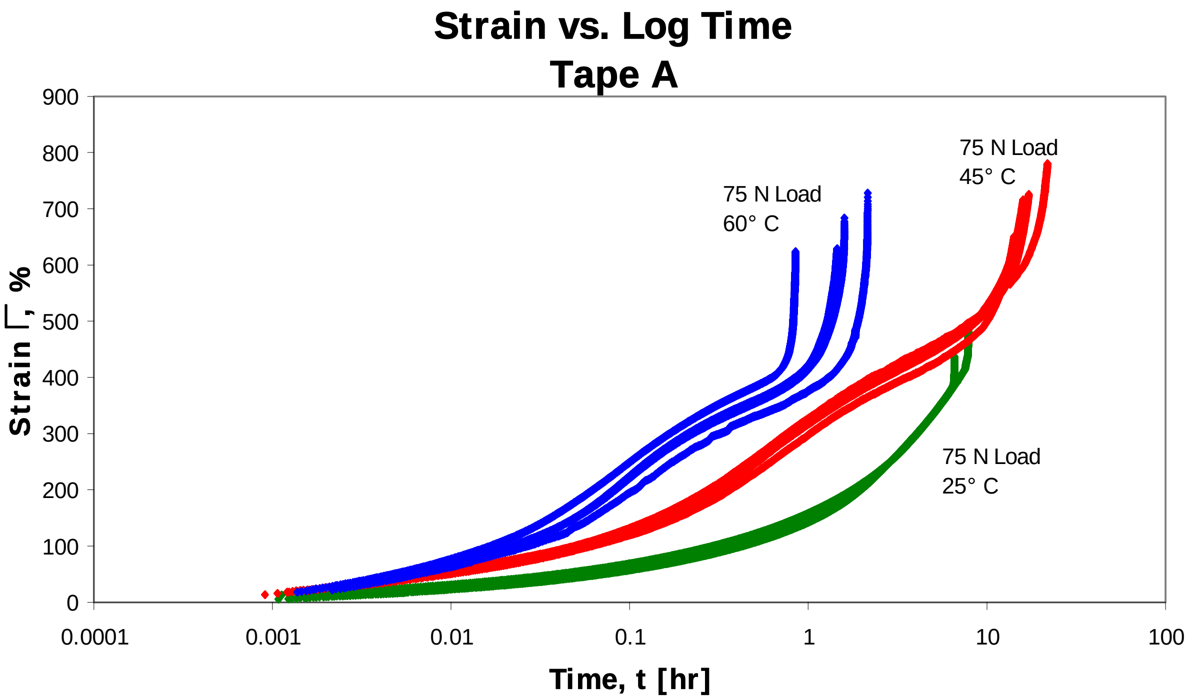

Figure 7-3: Temperature Comparison of Strain vs. Time Plot

Shear Creep Rupture Analysis:

Multiple angle testing began towards the end of the project and therefore the results are only briefly described here. Multiple angle tests were performed at the same load levels however with the varying cross sectional area of the adhesive joint the stress levels were not the same. Figure 8-1 shows a bonded shear specimen. Shear tests were completed for Tape A at 60° C before the completion of the summer project and creep rupture results are shown in Figure 8-2. From the preliminary data received from these tests, we see that Tape A has better resistance to normal creep than shear creep. When completed this curve will be very important for the designers since they can then predict shear creep rupture as well as normal creep rupture.

Figure 8-1: Shear Specimen

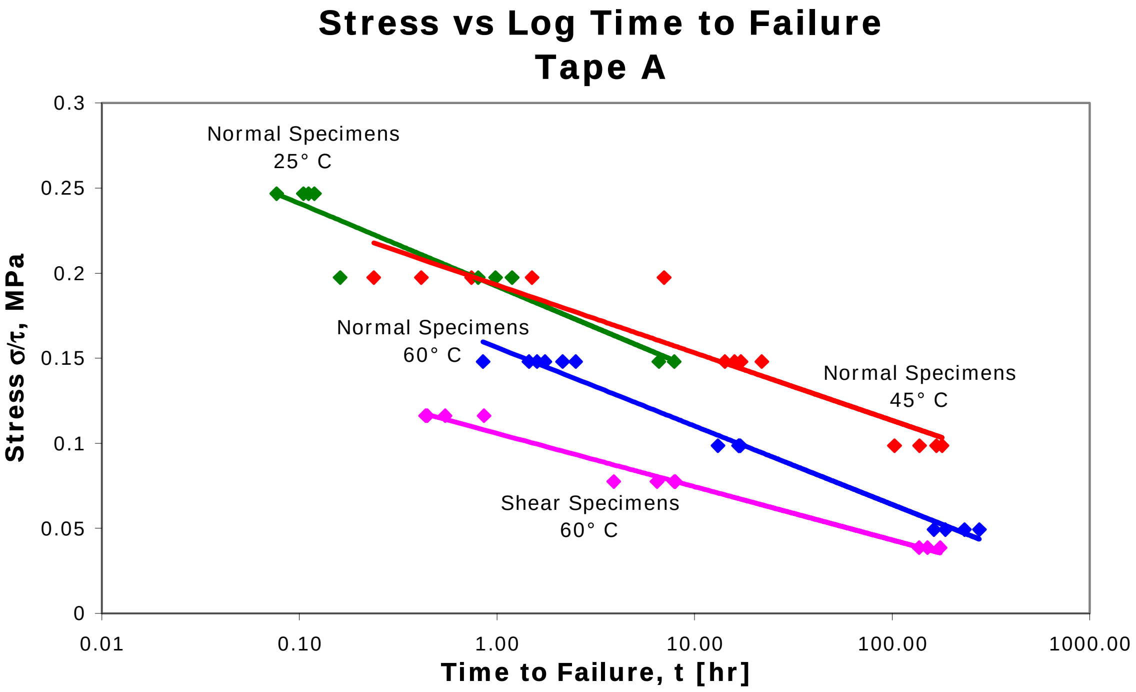

Figure 8-2: Shear Specimen Time to Failure

Conclusion:

Overall this project can be considered a success. The reconditioned stepper motor creep frame will prove useful in characterizing the time dependent phenomenon witnessed in viscoelastic materials. This creep frame allows for creep rupture tests will collected data that is crucial for design engineers and provided an understanding of the mechanisms happening with this particular pressure sensitive adhesive. Creep analysis allowed a characterization of the creep compliance and the strain as functions of time. Creep rupture analysis provided time to failure data for set load levels, which translates into time to failure predictions at various stress levels. Through the temperature comparisons a mode of failure change was witnessed and provided further insight for translating the strain vs. time curves into failure mechanism analysis. This project allowed for a better understanding of the time dependent phenomenon experienced by pressure sensitive adhesives.

Future Work:

Future work for this project should include the determination of the humidity shift factor by testing several different humilities as well as determining a temperature shift factor through future testing. From this, a design curve for humidity and temperature can be constructed and used for designing with tape A. Further work would also be the completion of tapes B and C for all temperatures and humilities to provide a broader comparison.

Future work for this project should include more repeated tests. Due to the low number of specimens there is limited statistical significance to the results; however it sets the framework for beginning to understand creep rupture of pressure sensitive adhesives.

Acknowledgments:

I would like to thank the National Science Foundation for the financial support and the opportunity to participate in this research program. I would also like to thank 3M Corporation Bonding Systems Division for supplying the adhesive tape used in these tests. For conceptual support and guidance, thanks goes to my mentors Dr. David Dillard and Dr. Don Ohanehi as well as Dr. Larry Mitchell. I would also like to thank Mr. Bob Simonds for his extensive help with programming in LabVIEW®.

Zirconium Phosphate/Sulfonated Poly(Arylene Ether Sulfone) Membranes for Elevated Temperature Fuel Cell Application

Melinda L. Hill*, Yu Seung Kim, and James E. McGrath
Department of Chemistry
Virginia Polytechnic Institute and State University
Blacksburg, VA

* Department of Chemistry, Bloomsburg University, Bloomsburg, PA

ABSTRACT

High temperature hydrogen and methanol based fuel cells are of increasing interest due to environmental concerns and of the availability of fossil fuels. The proton exchange membrane (PEM), a protonically conductive polymer film, is an integral component of the fuel cell. New polymer materials are needed for these membranes because of the high cost and low conductivity at high temperatures (> 80°C) of the membranes currently in use. Sulfonated poly(arylene ether sulfone)s (PBPSH) have good potential for use in fuel cells because of their excellent thermal stability, moderate water sorption, and sufficient conductivity at high temperatures. Addition of inorganic proton conductors to these membranes enhances the high-temperature conductivity as well as other important properties of the membranes. Zirconium phosphate has been added *in situ* to PBPSH membranes, and these films have been characterized by Fourier Transform Infrared spectroscopy (FTIR) , Nuclear Magnetic Resonance spectroscopy (NMR), Differential Scanning Calorimetry (DSC), Thermogravimetric Analysis (TGA), water uptake, microscopy, conductivity, and aging tests.

Addition of these inorganic materials at concentrations of 10-15% (after at least a six hour immersion in $ZrOCl_2$) was found to enhance the high-temperature (130°C) conductivity of these membranes significantly over the pure PBPSH membranes (up to 0.12 S/cm). Water uptake decreased slightly in the composites, and the excellent thermal stability of the base membranes was not affected.

INTRODUCTION

In view of the increasing financial and environmental disadvantages of fossil fuels, hydrogen and methanol fuel cells are an interesting prospect.[2] The basic unit of a fuel cell consists of a cathode and an anode, separated by a proton-conducting polymer membrane. The most common proton exchange membrane (PEM) currently in use is the perfluorinated copolymer Nafion®, made by DuPont. However, Nafion's® high cost, high rates of methanol crossover, and decreased conductivity at high temperatures have led to the search for new membranes. Sulfonated hydrocarbon polymers, such as sulfonated polyether ether ketones (SPEEK)[1] and sulfonated poly(arylene ether sulfone)s (PBPSH), are of particular interest because they are resistant to oxidation and are thermally and mechanically stable.[2]

It has been found that addition of inorganic conductors, such as zirconium phosphate or phosphotungstic acid, to PEMs enhances the water retention and electrochemical properties, and allows operation at elevated temperatures (>100°C).[3,4] Elevated temperature operation of fuel cells results in increased rates of methanol oxidation, which results in greater fuel cell efficiency. In particular, carbon monoxide poisoning of the expensive platinum catalyst can be significantly decreased by operation at elevated temperatures.

Our research involves the incorporation of zirconium based inorganic materials into a PBPSH matrix which contained varied percentages of disulfonation (0 to 50%). The thermally and mechanically stable polymer matrices are prepared from direct copolymerization of sulfonated monomers, rather than post-sulfonation reactions. This leads to increased stability at high temperatures because the sulfonic acid groups are positioned on the deactivated rings rather than on the activated rings, as with the post-sulfonation reactions.[1]

There are two methods by which inorganic conductors can be incorporated into the polymer.[4] One of these involves dispersing the inorganic material, in powder form, throughout an organic solution of the polymer. This method is considered to be less suitable than the *in situ* formation of conducting particles by ion exchange, as explained by Jones et. al.[4]

EXPERIMENTAL

Materials and preparation

Zirconyl chloride hydrate, zriconyl chloride 30% in HCl solution (12.8%), zirconium (IV) oxide, zirconium(IV) hydrogenphospate, and 85% phosphoric acid were obtained from Aldrich Chemical Company. Sulfuric acid was obtained from VWR Scientific Products and *N,N*-dimethyl acetamide (DMAc) was obtained from Fisher Scientific. All chemicals were used without purification.

Sulfonated biphenol based sulfone copolymers (PBPS) with degrees of disulfonation ranging from 0 to 50% were prepared in this laboratory and were received in the sodium form.[2] Figure 1 shows the structure of the repeating acid-form random copolymer (PBPSH).

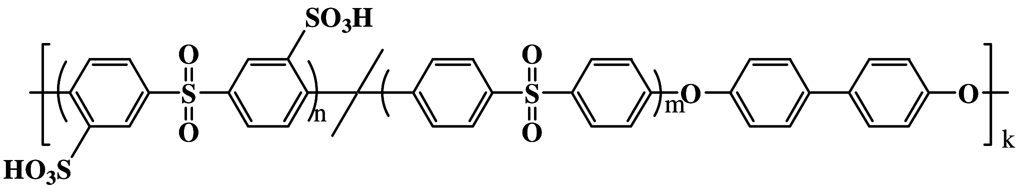

Figure 1: Structure of the PBPSH random copolymer.

Membranes were cast onto clean glass substrates from solutions in *N,N*-dimethyl acetamide of the sodium form of copolymers with different degrees of sulfonation (0-50%). The membranes were dried under a nitrogen atmosphere using an infrared lamp. They were then dried overnight in a vacuum oven at 80ºC. These cast membranes were converted from the sodium form to the acid form by boiling in 1M H_2SO_4 for 1.5 hours, and then in deionized water for 1.5 hours. The membranes were again dried overnight in a vacuum oven at 80ºC.

For ZrO_2/PBPSH composite membranes, PBPSH-40 membranes in the acid form were dissolved in DMAc and solid ZrO_2 was added to the solutions in polymer:ZrO_2 ratios of 1:1, 2:1, and 4:1. The solutions were then filtered and recast into opaque films. The solutions were filtered through a 0.45 µm syringe to remove large particles and impurities. Membranes were then recast using the previously stated procedure, which resulted in opaque films. Weight percent of incorporated ZrO_2 was calculated as weight gain after the films were dried.

For Zirconium phosphate (ZrP)/PBPSH composite membranes, the dried acid-form of PBPSH films were boiled in deionized water for one half hour and immediately immersed in solutions of $ZrOCl_2$ in 12.8% HCl at 80°C. They were then soaked for 1 to 24 hours in 1 molar H_3PO_4 at room temperature. The membranes were then thoroughly rinsed in deionized water to remove all traces of H_3PO_4 and HCl, and the transparent films were dried overnight in a vacuum oven at 80ºC. The reaction is shown in Scheme 1.

$$ZrOCl_2 + 2H_3PO_4 \longrightarrow Zr(HPO_4)_2{\bullet}H_2O + 2HCl$$

Scheme 1: Reaction of $ZrOCl_2$ and H_3PO_4 to form $Zr(HPO_4)_2{\bullet}H_2O$.

Weight percent of incorporated ZrP was calculated as weight gain after the films were dried, and confirmed by char yield from thermogravimetric analysis (TGA).

Characterization Methods

Fourier Transform Infrared (FTIR) Spectroscopy

FTIR spectroscopy was used to characterize the composite membranes and to evaluate water loss and membrane stability at increased temperatures. FTIR spectra were recorded on a Nicolet Impact 400 FTIR Spectrometer using thin films. A high-temperature cell was used to control the temperature of the film while inside the spectrometer. All spectra were measured at a resolution of 2 cm^{-1} and represent the average of 64 scans.

Nuclear Magnetic Resonance (NMR) Spectroscopy

Magic Angle Spinning (MAS) ^{31}P NMR were obtained on a Bruker MSL 300 instrument. The spectra were obtained using 128 scans per FID and a spinning rate of 7.5 kHz.

Differential Scanning Calorimetry (DSC) and Thermogravimetric Analysis (TGA)

Glass transition temperatures (T_g) of the membranes were measured using a Perkin-Elmer DSC-7 Differential Scanning Calorimeter. DSC measurements were made under a nitrogen atmosphere with a heating rate of 10ºC/minute. TGA was used to determine the thermal stability of the membranes and also to evaluate water loss and calculate the amount of inorganic residue in the membrane. TGA measurements were conducted on a Perkin-Elmer TGA-7 Thermogravimetric Analyzer. Measurements were taken under atmospheres of both nitrogen and air, and a heating rate of 10ºC/minute was used.

Water Uptake

For the water uptake experiment, the membranes were first dried in a vacuum oven at 80ºC overnight. They were quickly weighed and immersed in deionized water for one minute, after which time they were quickly blotted dry and weighed. The membranes were again immersed in deionized water and the weighing procedure was repeated at times of five minutes, 30 minutes, 2 hours, 5 hours, and 24 hours. After 24 hours, the films were dried in a vacuum oven at 80ºC for an additional 24 hours. The maximum water uptake for all membranes occurred within two hours, however, the 24 hour data is reported. The membranes were then weighed and this dry mass was used to calculate water uptake using the following formula:

$$\text{Water uptake} = \frac{W_{wet} - W_{dry}}{W_{dry}} \times 100\%,$$

where W_{wet} is the mass of the wet membrane and W_{dry} is the mass of the dry membrane.

Microscopy

Field emission scanning electron microscopy (FE-SEM, Gemini) was used for zirconium oxide/PBPSH composites.

Tapping mode atomic force microscopy (AFM) was performed with a Digital Instruments Dimension 3000, using micro-fabricated Si cantilevers with a force constant of approximately 40 N/m. All samples were fractured in cryogenic conditions and dried at 80 ^{o}C for 24 hr under vacuum conditions. The cross-sections of the samples were then imaged in relative humidity of about 35% at room temperature.

Conductivity

Conductivity at room temperature under full hydration conditions were performed using a Solatron 1260 Impedance/Gain-Phase Analyzer over a frequency range of 10-100,000 Hz. The cell geometry was chosen to ensure that the membrane resistance dominated the response of the system. The resistance of the film was taken at the frequency which produced the minimum imaginary response. High temperature conductivity measurements were conducted in saturated water vapor. The conductivity cell was placed above liquid water in the head space of a sealed vessel. This experimental setup allowed the membrane to equilibrate with saturated water vapor at the desired temperature. The temperature was controlled by a vessel resistance heater and feedback temperature controller.

Aging Tests

Aging tests under harsh conditions (saturated water vapor at 120°C) were performed to investigate long term stability of the composite membranes. Composite membranes were aged in a pressure vessel containing saturated water vapor at 120°C for 100 hours. FTIR, proton conductivity and weight loss of the aged sample were compared with unaged samples. The weight loss of the membranes was calculated with respect to the initial dry weight of the membranes and is reported as weight percent.

RESULTS AND DISCUSSION

ZrO_2/PBPSH-40 Composite Membrane

Because these membranes were prepared from solution dispersion technique and there is little interaction between particle and copolymer, ZrO_2 particles were uniformly dispersed in the membrane. The particle size was approximately 0.4 μm (Figure 2), producing an opaque film.

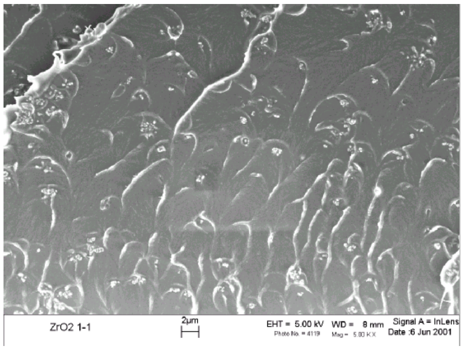

Figure 2: Representative FE-SEM Cross-Sectional Image of 2:1 PBPSH-40:ZrO_2 Composite Film.

The conductivities of these samples were found to be no higher than 0.04 Scm^{-1}, which is significantly lower than that of the pure polymer and the ZrP nanocomposites.

Incorporation of $Zr(HPO_4)_2$

Table 1 shows the influence of the preparation conditions on ZrP weight gain for ZrP nanocomposite membranes.

Table 1: Preparation Conditions and Weight Gain for ZrP Nanocomposites

Sample No.	Degree of Disulfonaion (%)	$ZrOCl_2$ Concent-ration (%)	Immersion Time in $ZrOCl_2$ (h)	Immersion Time in H_3PO_4 (h)	ZrP Content (%)	
					From Weight gain	From TGA char yield
1	30	30	6	24	27.3	-
2	30	0.3	6	24	0	-
3	40	1	6	24	14.6	-
4	40	2	6	24	12.6	-
5	40	3	6	24	31.2	-
6	40	10	3	24	33.2	5.7
7	40	30	1	24	36.4	31.5
8	40	30	3	24	38.0	43.0
9	40	30	6	24	40.5	43.6
10	40	30	6	1	33.8	-
11	40	30	6	6	32.0	-
12	40	30	9	24	41.2	-
13	50	30	6	24	45.4	-

The ZrP concentration increased with increasing degree of disulfonation of matrix copolymer, probably because the sulfonated copolymer with higher disulfonation has a higher water uptake, resulting in larger capacity of ZrP incorporation during the immersion process. Also, it was found that the ZrP concentration was increased with the $ZrOCl_2$ concentration in HCl solution while other factors such as immersion time in $ZrOCl_2$ or phosphoric acid have little influence on the final ZrP concentration of the nanocomposite.

Fourier Transform Infrared (FTIR) Spectroscopy

FTIR spectra were obtained from thin films of both pure PBPSH-40 and the ZrP/PBPSH-40 nanocomposites. In the spectra for the ZrP/PBPSH-40 nanocomposite, broad peak at the region from 900-1300 cm^{-1} were observed, as shown in Figure 3(a).

Using the standard aromatic C=C stretching signal at 1600 cm^{-1} as a reference, the two spectra were subtracted, and the result is shown in Figure 3(b) along with the IR spectra of pure ZrP. The spectra clearly shows the broad peak near 1050 cm^{-1} and PH stretching band at 1260 cm^{-1}. Based on the previous report[6], the broadness of this band led to the belief that more than one type of phosphate was present in the sample. From this spectrum the successful incorporation of ZrP into the PBPSH-40 films was confirmed. In addition, the subtracted FTIR spectrum was compared with pure ZrP spectrum obtained

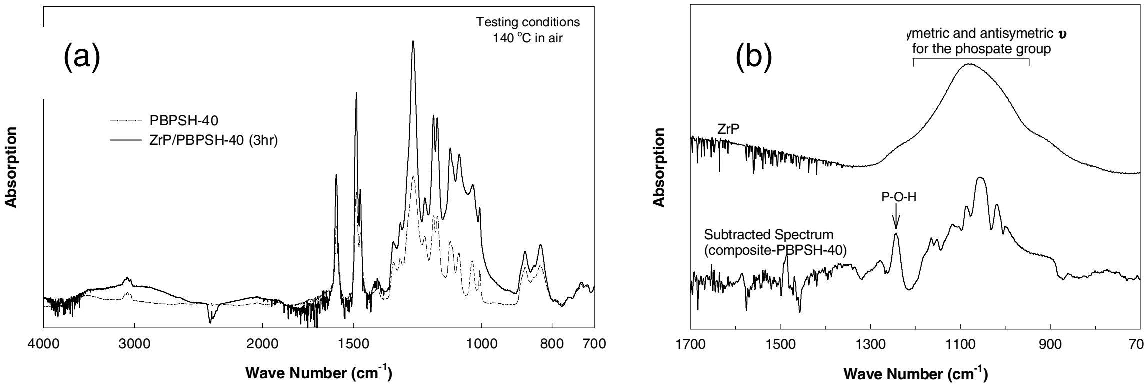

Figure 3: FTIR Spectra of (a) PBPSH-40 and ZrP/PBPSH-40 Nanocomposite and (b) Subtracted IR Data and Pure ZrP made from $ZrOCl_2$

from $ZnOCl_2$ solution. The symmetric and asymmetric stretching of the phosphate group can be seen at the same wavenumber for both the pure ZrP and the subtracted spectrum, which proves the ZrP that is incorporated into the PBPSH-40 membrane.

Nuclear Magnetic Resonance (NMR) Spectroscopy

^{31}P MAS-NMR, shown in Figure 4, confirmed that more than one type of phosphate was present in the sample. The intense signal at -22 ppm is associated with the □ form of ZrP, while the two smaller signals on either side of it, at -14 ppm and -28 ppm, are characteristic of the □ form. Also, weak signals at –6 ppm and 1 ppm were observed presumably due to the PH group and residual H_3PO_4, respectively. The spectrum in the insert shows the ^{31}P MAS-NMR of pure ZrP, which was made from solid $ZrOCl_2$ and 1M H_3PO_4. The peak assignments are the same, with the exception that there is no excess H_3PO_4 in the pure ZrP.

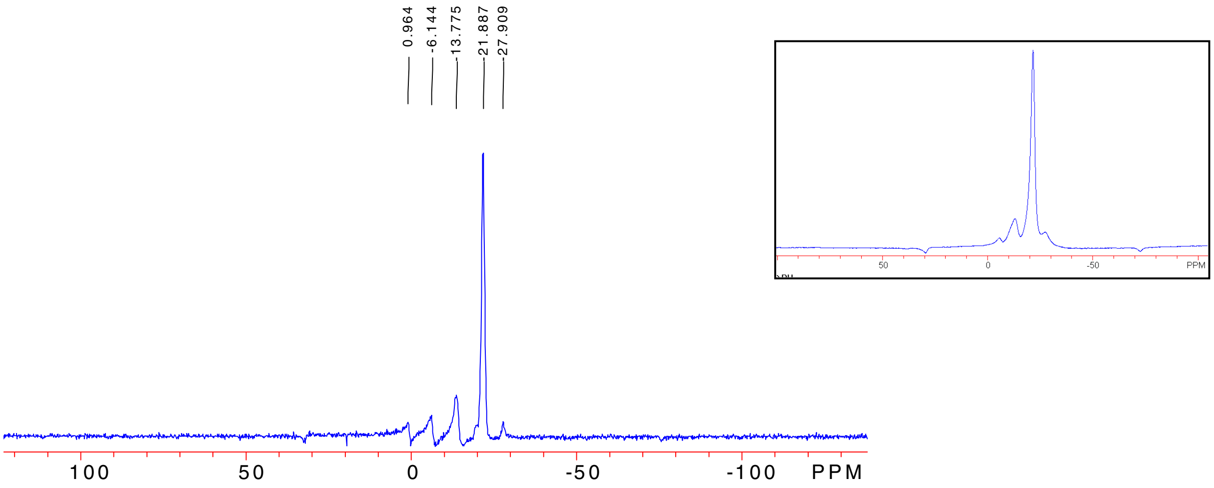

Figure 4: ^{31}P MAS-NMR of ZrP/PBPSH-40 (6h) nanocomposite film. Peak assignments are as follows: (*a*) H_3PO_4, (*b*) POH, (*c*) $H_2PO_4^-$, (*d*) HPO_4^{2-}, (*e*) PO_4^{3-}. Box: ^{31}P MAS-NMR of pure ZrP made from solid $ZrOCl_2$.

Morphology

Figure 5 shows the AFM cross sectional phase images of PBPSH-40 and composite membranes in terms of immersion time in $ZrOCl_2$ solution. PBPSH-40 copolymer membrane has a phase separated morphology due to the difference in surface modulus between hydrophilic and hydrophobic regions.

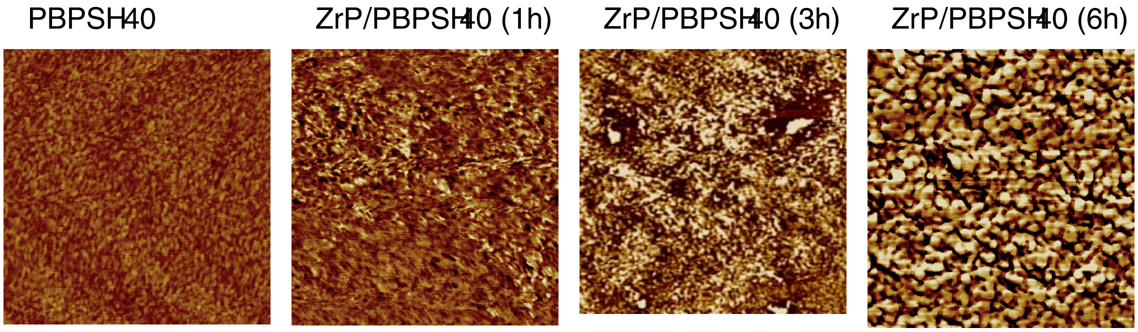

Figure 5: Effect of immersion time on cross-sectional AFM images of ZrP/PBPSH-40 nanocomposites in tapping mode with 10° phase angle and 1.00 □m scale.

The hydrophilic domains appear as uniformly distributed dark spots with an average size of approximately 15 nm. The morphology of ZrP/PBPSH-40 composites is strongly dependent upon the immersion time in $ZrOCl_2$ solution, in spite of the similar ZrP concentration (see Table 1). The irregularly shaped bright ZrP phase increased in size and the distribution became more uniform as the immersion time increased. These results indicate that the diffusion of $ZrOCl_2$ is a kinetic process, which reaches an equilibrium state after 6 hours under the experimental conditions.

Differential Scanning Calorimetry (DSC) and Thermogravimetric Analysis (TGA)

DSC was used to evaluate the T_g of the nanocomposite films and the pure PBPSH-40 films. The T_g of pure PBPSH-40 was found to be 258°C. The T_g for sample 4 (see Table 1) was found to be 249°C, slightly lower than that of pure PBPSH-40.

TGA measurements showed that the ZrP nanocomposite films maintain good thermal stability up to 300°C, as shown in Figure 6.

These nanocomposite films also showed a significantly higher char yield than the pure PBPSH copolymer, from which the amount of ZrP in the films was calculated. The ZrP compositions of several of the samples, as calculated from TGA data, are shown in Table 1. Table 2 shows the temperatures at which 5% of the mass was lost ($T_{5\%}$) and the char yields for the pure PBPSH-40 and several of the nanocomposite films.

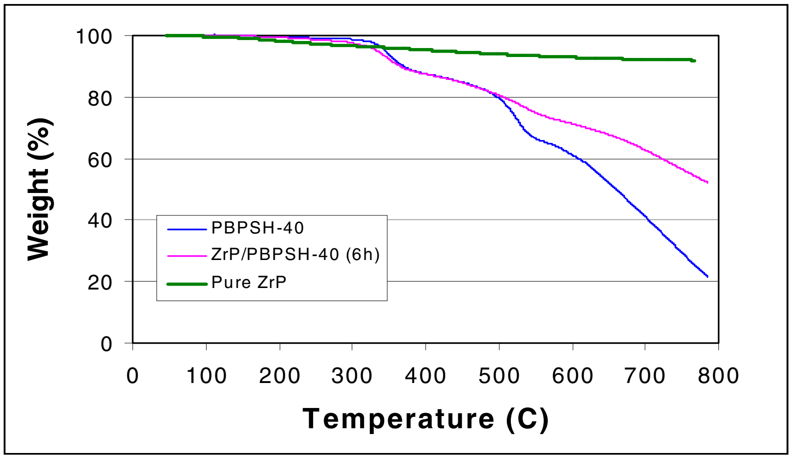

Figure 6: TGA data for pure ZrP (bottom), PBPSH-40 (top), and ZrP/PBPSH-40 (6h) nanocomposite (middle) with heating rate of 10°C/minute in nitrogen gas.

Table 2: Initial degradation temperature (5% weight loss), $T_{5\%}$, and Char Yield for PBPSH-40, 1h, 3h, and 6h nanocomposites, as calculated from TGA data with a heating rate of 10°C/minute under nitrogen.

	$T_{5\%}$, °C	Char Yield, %
PBPSH-40	346	-
ZrP/PBPSH-40 (1h)	340	31.5
ZrP/PBPSH-40 (3h)	349	43.0
ZrP/PBPSH-40 (6h)	336	43.6

Water Uptake

The pure matrix copolymer had a higher water uptake than the nanocomposite membranes, and water uptake decreased with increasing ZrP content. Lower water uptake is favorable for fuel cell applications because it leads to greater dimensional stability of the membrane at elevated temperatures. Weight loss after soaking and drying should also be minimal to ensure that the inorganic conducting material is not extracted in water. Table 3 shows 24 hour water uptake data for several of the membranes. The extraction was found to be 2.6%, with 1.8% being residual DMAc from casting, leaving only 0.8% extraction of the inorganic component.

Table 3: Water uptake for PBPSH-30, -40, and -50 pure copolymers and ZrP (6h) nanocomposites.

	Water Uptake (24 hours) (%)
PBPSH-30	33.5
ZrP/PBPSH-30 (6 hr)	34.1
PBPSH-40	57.0
ZrP/PBPSH-40 (6 hr)	36.2
PBPSH-50	160.0
ZrP/PBPSH-50 (6 hr)	102.0

Conductivity

The room temperature protonic conductivities of several of the ZrP/PBPSH nanocomposites are shown in Figure 7.

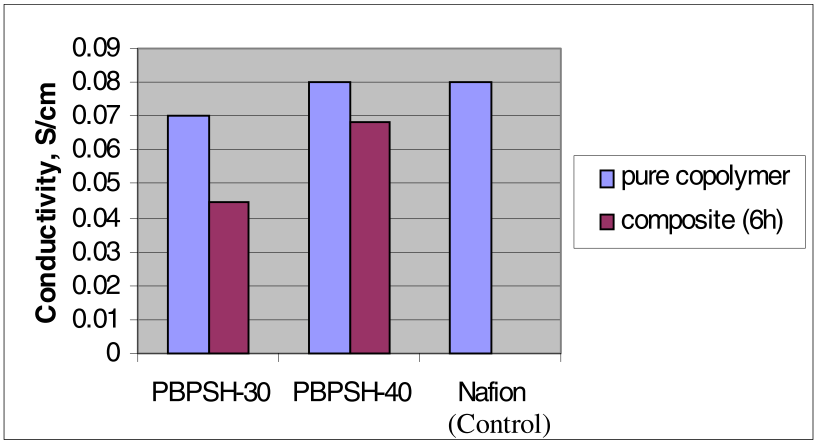

Figure 7: Room-temperature protonic conductivity data for several of the pure PBPSH copolymers, ZrP/PBPSH nanocomposites, and Nafion®.[7]

Even though these conductivities are slightly decreased with respect to those of the pure copolymers and Nafion®, the conductivities of the 3 hour and 6 hour ZrP/PBPSH-40 nanocomposites at elevated temperatures exhibit significant improvement, as shown in Figure 8.

These excellent high-temperature conductivities can be explained in terms of water retention at elevated temperatures. The FTIR data in Figure 9 shows that the ZrP/PBPSH-40 nanocomposites retain water at temperatures as high as 280°C.

Aging

After aging at 100% relative humidity and 120°C, the extraction for these nanocomposite membranes was very low, and was probably due mostly to residual traces of solvent. After aging for 100 hours, the high-temperature conductivity of the films was again tested, and the conductive properties of the membranes were not affected, as shown in Figure 10.

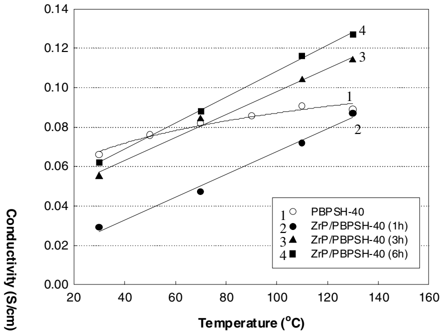

Activation Energy, E_a (kJ/mol)	
PBPSH-40	3.1
ZrP/PBPSH-40 (1h)	11.0
ZrP/PBPSH-40 (3h)	7.3
ZrP/PBPSH-40 (6h)	7.4

Figure 8: Elevated-temperature conductivity data for pure PBPSH-40 and 1, 3, and 6 hour ZrP/PBPSH-40 nanocomposites.

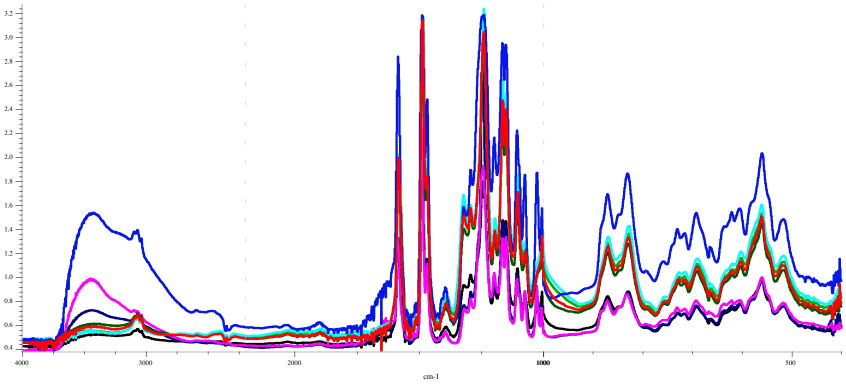

Figure 9: FTIR Spectra of ZrP/PBPSH-40 (1hour) sample. The top spectrum is at room temperature, and the temperature was increased gradually (10°C/minute) to 280°C, as shown in the bottom spectrum.

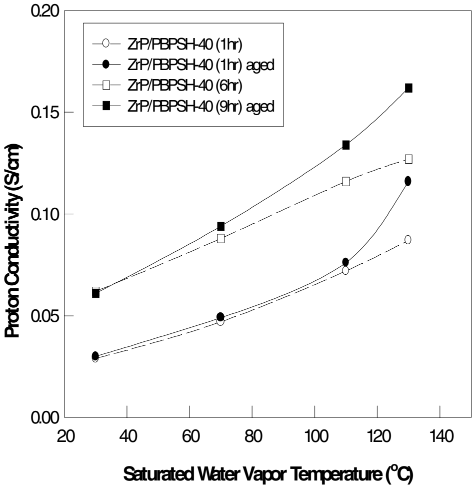

Figure 10: Elevated-temperature conductivity data for aged membranes (black dots) compared to unaged membranes (white dots).

CONCLUSIONS

Several $Zr(HPO_4)_2$•H_2O/PBPSH-40 nanocomposite films were prepared by *in situ* blending, and the results were confirmed by FTIR, ^{31}P MAS-NMR, DSC, TGA, AFM, and conductivity measurements. These films exhibited greatly improved conductivity at high temperatures and decreased water uptake, as well as minimal extraction and relatively long-term stability in harsh conditions.

Based on AFM images and conductivity measurements, it was determined that both the morphology and conductivity are directly dependent on immersion time in $ZrOCl_2$.

SUGGESTED FUTURE STUDIES

For practical use in fuel cells, the mechanical properties and long-term stability of the nanocomposites should be tested. It would also be interesting to investigate other zirconium compounds and compounds of other metals, such as cesium. Variation of the matrix polymer is also an interesting prospect for nanocomposite membranes. For all of these membranes, the optimum concentration of $Zr(HPO_4)_2$ should be determined in order to achieve maximum conductivity while maintaining good mechanical and thermal stability. Once a suitable membrane is found, fabrication of a membrane electrode assembly and testing in fuel cells is necessary.

ACKNOWLEDGMENT

The authors would like to thank the U.S. Department of Energy and the National Science Foundation for financial support of this research.

REFERENCES

[1] G. Alberti, M. Casciola, L. Massinelli, B. Bauer, *J. Membrane Sci.,* **185**, 73 (2001).

[2] F. Wang, M. Hickner, Y. S. Kim, T. A. Zawodzinski, and J. E. McGrath, *J. Membrane Sci.,* Submitted 2000.

[3] C. Yang, S. Srinivasan, A. S. Arico, P. Creti, V. Baglio, *Electrochemical and Solid State Letters*, **4**, A31 (2001).

[4] S.M.J. Zaidi, S.D. Mickailenko, G.P. Robertson, M.D. Guiver, S. Kaliaguine, *J.Membrane.Sci*. 173 (2000).

[5] D. Jones, J. Roziere, *J. Membrane Sci.*, **185**, 41 (2001).

[6] Clearfield, Ed., *New Inorganic Ion Exchangers*, CRC Press, Inc.: Boca Raton, FL, (1982).

[7] T. Zawodzinski, M. Neeman, L. Sillerud, S. Gottesfeld, *J. Physical Chem.*, **95,** 6040, (1991).

Design of a New Light-based Settling Characterization Device

D.L. Hoffman*, D. Brooks and B.J. Love
Department of Materials Science and Engineering, Virginia Polytechnic Institute and State University, Blacksburg, Virginia

* Department of Composite Materials Engineering, Winona State University, Winona, MN

ABSTRACT

Determination of settling characteristics is a task that is difficult for many reasons. Several devices and techniques are available, each with its own unique drawbacks. Existing manners of measuring settling are often dependent on visual boundaries or do not provide a complete and accurate measurement of the entire fluid sample. This settling characterization device overcomes these problems. This device maps all the expected settling regimes can be observed with out the use of a visible mud line. The overall settling behavior measured from the device matches documented settling behavior in previous tests. Measured settling velocities have a strong correlation with visible observations and expected results. The device provides useful, accurate and precise measurements in a simple, user-friendly manner.

INTRODUCTION

Settling is an important aspect of many natural and industrial systems. Natural settling systems include suspensions in lakes and waterways [1]. Sediment in this case affects water clarity, nutrient circulation and water depth. Water treatment is also heavily dependent on settling [2]. Resin systems containing small particulates are also influenced by settling.

The interaction of many particles while they are all falling through a fluid makes accurate modeling of settling particles a daunting prospect. Settling suspensions can be grouped into four categories [2]. Class-1 clarification is when particles in suspension settle with very little interaction. This is very similar to the behavior of just one particle in the fluid. Class-2 clarification results from flocculent particles settling. Both class-1 and class-2 clarification applies to dilute suspensions. If the suspension more concentrated interpretable forces can hold the particle close to each other. In this case, called zone settling, the particles seem to fall out of suspension as one solid mass, with a definite particles boundary called a mud line. Fluids with a very high concentration of particles act more like a porous medium through which the liquid matrix is further compressed by the particles' own weight. This category of settling is called compression. Figure 1 represents the relationship of each type of settling with particle properties.

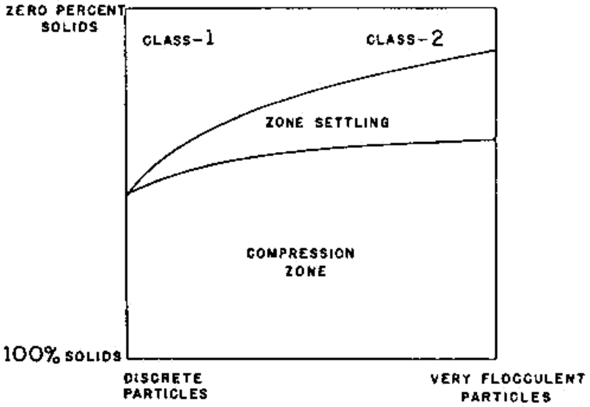

Figure 1. Relationship of settling type with particle properties.

Class-1 Clarification

Particles in class-1 clarification settle in the same manner as a single particle falling through the given fluid [2]. The final settling velocity in this case is identical to an object reaching terminal velocity as it falls through the air. At the point of terminal velocity the drag force on the object is equal to the force of gravity acting on the object. The force of gravity on a particle can be found with the following equation:

$$F_G = \rho V g$$

Because the particle is immersed in a fluid, buoyancy of the particle must be included so the equation becomes:

$$F_B = (\rho_p - \rho_l)Vg$$

The drag force on the particle is a function of the particle's Reynolds number [3]. The Reynolds number is a dimensionless number dependent on the particles density, geometry, speed and the fluid's viscosity. For spherical particles the Reynolds number is defined with the following equation:

$$Re = \rho V d/\mu$$

The drag force is made up of two components: friction drag and pressure drag [3]. The motion of fluid tangent to the particle causes friction drag. The frontal surface area of the particle causes pressure drag. The magnitude of the force is related to the drag coefficient. The drag coefficient on a sphere is shown in Figure 2.

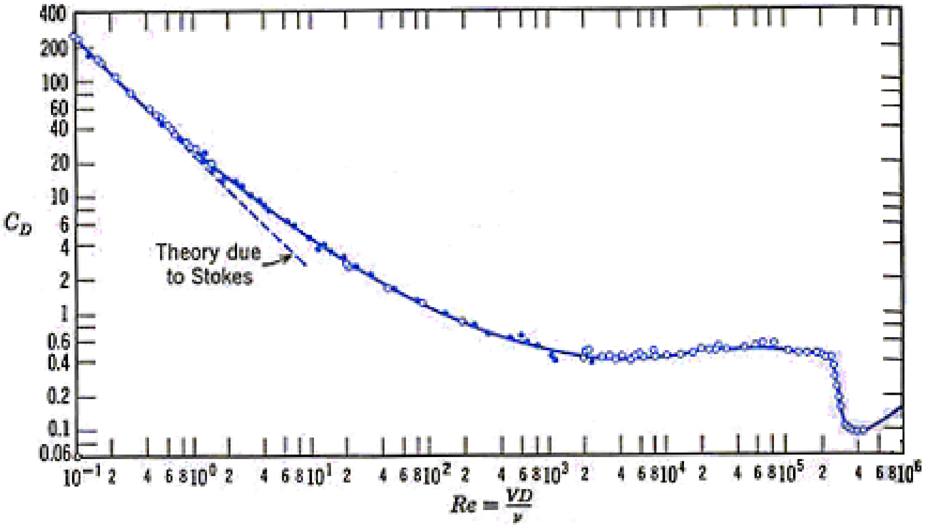

Figure 2. The drag coefficient on a sphere with various Reynolds numbers.

At low Reynolds numbers, the majority of the total drag force is caused by friction drag. Stokes has shown analytically for very low Reynolds numbers it can be said that the drag force on a sphere can be modeled with the following equation:

$$F_D = 3\pi \mu V d$$

The force caused by the acceleration of a falling object can be shown as:

$$F_A = m\,dv/dt = F_B - F_D$$

When a falling object stops accelerating it has reached its terminal velocity. This would require the following to be true:

$$0 = F_B - F_D = (\rho_p - \rho_l)Vg - 3\pi\mu Vd$$

The terminal velocity of a low-Reynolds number particle can then be expressed as:

$$V = ((\rho_p - \rho_l)Vg)/3\pi\mu d$$

After an initial acceleration period, the particle's height would be expected to drop linearly.

Class –2 Clarification

Class-2 clarification results from particles of different sizes overtaking one another as they fall out of suspension. This can result form the particles being different sizes or from individual particles flocculating to form larger particles which in turn agglomerate more particles [4]. The newly formed particle groups have less surface area per volume than the smaller initial particles and so have less drag force [2]. This causes the flocs to fall at a faster rate than the smaller particles and to grow in size as they overtake them. Because the size of the flocs depend on the length of time they have to overtake individual particles, class-2 clarification depends on the depth of the container. There is no satisfactory formulation to predict the flocculation effect of sediment in class-2 clarification [4]. Columns of suspensions can be sampled and isoconcentration lines can be measured. Figure 3 shows how such lines can be devolved.

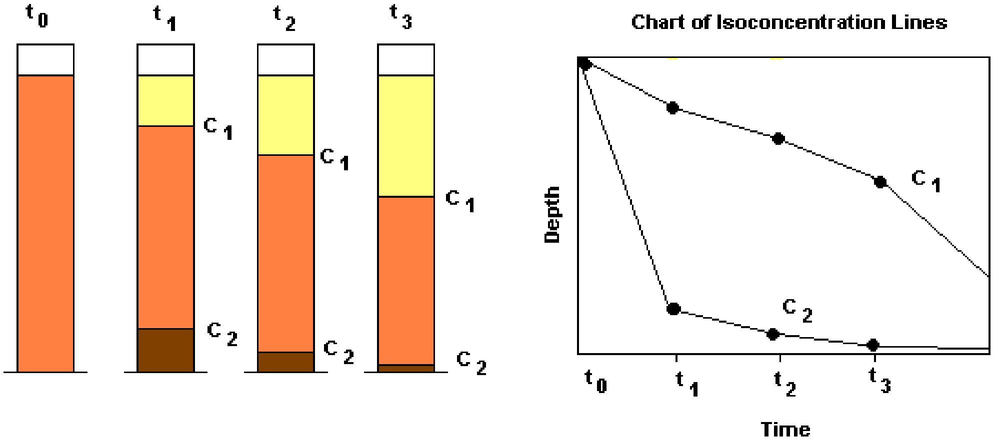

Figure 3. Construction of an isoconcentration chart.

Zone Settling

Once the majority of the falling particles have become a part of one group the settling is termed zone settling [2]. This group is seen as a solid mass with a definite boundary between it and the relatively clear liquid. This boundary, called a mud line can be tracked from formation till it reaches a point when it has reached a compression zone. Figure 4 illustrates the typical motion of this mud line.

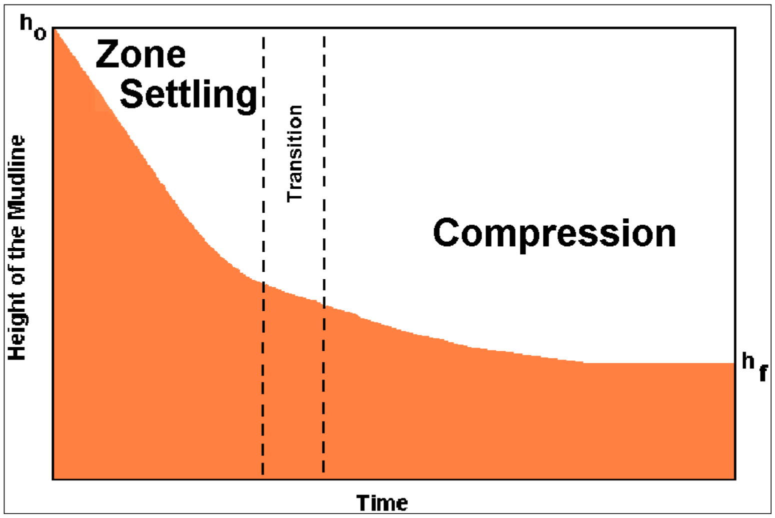

Figure 4. Mud line height as a function of time.

Compression

Compression occurs when the particle grouping has reached the bottom of the container. At this point the particle's mass force fluid out of the sludge bed, causing further drop in the mud line height. Compression and zone settling can be modeled with a first-order rate expression [2]:

$$-dh_z/dt = k(h_z-h_{zinf})$$

However, the final height of the particles and the rate constant must be measured experimentally.

Methods of Measuring Settling

The simplest way to measure settling in a column is to construct batch tests. This involves setting up several graduated cylinders of various heights and diameters. The settling mixture is allowed to settle and the mud line is tracked visually [4].

This procedure will only provide information about the mud line of the settling mixture. This procedure is also limited to mixtures where there is a clear mud line. The entire set-up requires that the mixture show visual signs of settling. In some cases the mud line is not an easily defined line and this can produce a lot of variability in the measurements.

A procedure that provides more information than just the mud line velocity is a sampling column [2]. A large column is filled with the settling mixture. At regular intervals along the depth of the column are sampling ports. Samples are obtained from these ports and particle concentration of each of these samples is determined. This is repeated until the experiment has ended.

This procedure requires a large amount of settling mixture if the experiment is to last any length of time. Each time a sample is taken a volume of the larger sample is removed. The sampling procedure disturbs the sample in the column, particularly if the sample fluid has a low viscosity.

Mahgerefteh and Kamugasha have published a design for an on-line sedimentation analyzer [5]. This device consists of a reed and plate submerged in the settling mixture column. As particles of the suspension settle out of the suspension, some collide with the reed and the plate. A connected detection apparatus analyzes the minute movements of the plate in the sample. Several reed apparati can be placed at various heights along the settling column.

Because no samples are removed from the column, this device provides good settling measurements with out disturbing the settling fluid. Measurements can only be taken at discrete points, where the reed apparatus is attached to the sample column.

Futterer, et al has patented a device to track the mud line of a sample [6]. This is a perfected version of the batch test. Instead of mud line height being determined by the naked eye, this device uses two light sensors to determine the location of the mud line. Input from the light sensors dictates where these sensors are moved and the location of the mud line.

This device provides a good measurement of the mud line. However, it provides no information about the particles in the rest of the settling column. In addition it only give quantitative measurements of the mud line height, not any information of the concentration gradient of the mud line interface.

In this study the design and testing of a light-based technique for mapping the settling dynamics of a sample. This machine overcomes the problems pointed out in the above techniques

The device makes used of the fact that with an increase in particle there will be an decrease in light detected through the sample. A map of the particle concentration can be created by measuring light transmittance across a sample's depth. The dynamic motion of these particle concentration levels can be tracked by continually re-mapping the sample.

Results validating the machine's abilities are presented. The tests include combinations of epoxy resin and a viscosity modifier mixed with either encapsulated imidazole particles or carborundum particles.

EXPERIMENTAL

Basic Device Layout

Figure 5 is a simple diagram of the device. A detailed design of the machine is included later.

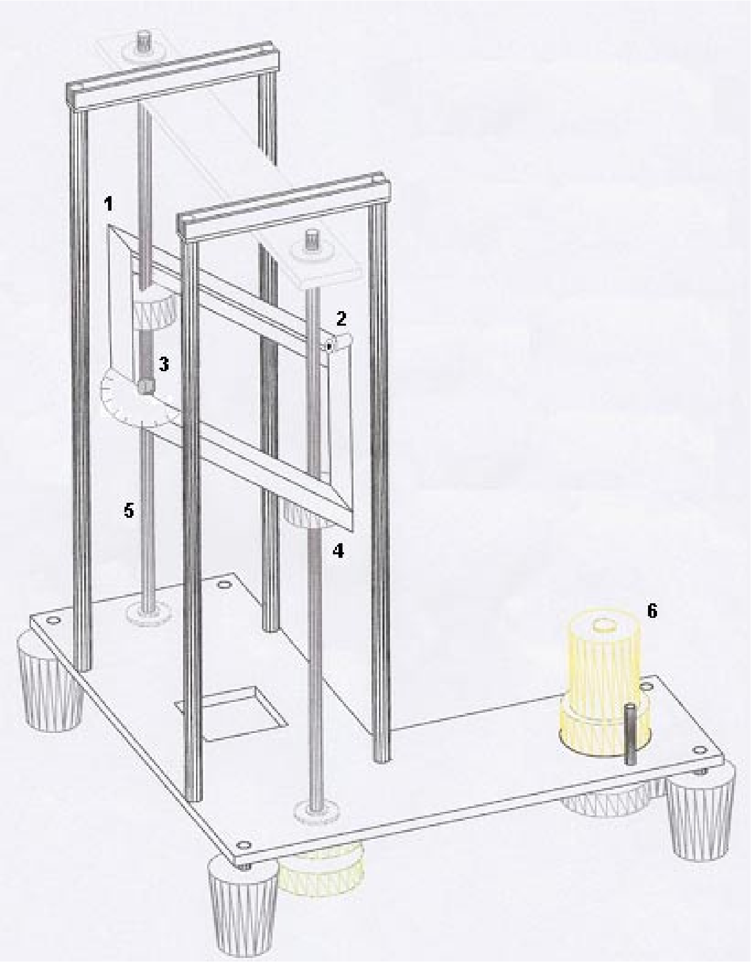

Figure 5. Layout of the settling characterization device.

The machine is comprised of a measurement platform (1), containing a laser (2), and a photodiode (3). The entire platform is mounted on a threaded machine nut (4) on a pair of threaded machine rods (5). A motor (6) turns these threaded machine rods to raise or lower the measurement platform along the height of the sample column.

Design Optimization

The machine relies on first an adequately strong light shining through the sample column. The machine then quickly records the intensity of the transmitted light. The machine therefore requires an optimal combination of these two components. The blue end of the spectrum was avoided, as that cures some light sensitive resins. The spectrum from 600 to 660 nm was explored. The transmittance through a suspension of the encapsulated imidazole particles did not vary significantly over this range. A commonly available laser wavelength of 635 nm was selected. A silicon photodiode was selected based on response time and precision.

Detailed Description of the Settling Characterization Device

The machine is built around a L-shaped aluminum platform. This platform supports the threaded machine rods by means of a pair of bearings. The motor is mounted on one end of the aluminum platform. The motor receives power from a 24-volt power supply. The circuit between the power supply and the motor is controlled by four solid-state relays. The motor's motion is transferred to a four inch radius gear. A series of belts transfers the motion to gears below the L-shaped aluminum platform attached to the threaded machine rods. The gears attached to the threaded machine rods have identical radii to provide identical rotational speeds. The threaded machine rods are supported at the top of the machine, attached by a pair of bearings. The top stabilizing bar is attached to the L-shaped aluminum platform by means of four quarter inch radius aluminum rods.

The identically rotating threaded machine rod's rotation motion is transferred to linear motion by a set of connected threaded machine nuts. The threaded machine nuts support the diamond-shaped measurement platform.

A 635 nm diode laser is mounted on the measurement platform. The laser is insulated from the aluminum machine. The computer controlling the machine supplies the five-volt power requirement for the laser.

The silicon photodiode is mounted on an adjustable protractor attached to the measurement platform. The photodiode can be turned to a prescribed angle to record scattered light. The photodiode records transmitted light intensity when it is directly pointed at the laser light source. The light intensity is reported to the controlling computer as an analog voltage signal.

A magnetic counter records the number of rotations the threaded machine rods make. The rods contain 12 threads per inch. This ratio makes it possible to measure the height of the measurement platform.

The entire apparatus is contained in housing to provide a dark environment. This ensures that all the detected light is from the laser. This also prevents errors from ambient light in the room.

Electronic System and Device Software

The polarity of the power, supplied to the motor, is controlled by four solid-state relays. Current is allowed through a relay when a five-volt digital signal is received. The computer provides this signal.

A sample height and time between scans is entered into the device software. The software waits till it is time to make a measurement. The correct collection of relays are signaled and the sample platform begins a scan. At the same time the laser turned on and height and voltage measurements are recorded. Once the prescribed sample height is reached the software signals the other relays and reverse the motor motion. When the measurement platform has reached its starting point the software turns off the laser and stops recording data. The software then waits until the next measurement event.

RESULTS AND DISCUSSIONS

Materials

All samples tested contained a mixture of EPON ® Resin 828 epoxy and HELOXY ® Modifier 107. Both chemicals are manufactured by Shell. The epoxy is a bisphenol A/epichlorohydrin based epoxy resin. This resin has a viscosity of about 20,000 cP and a density around 1.304 g/cm^3. The viscosity modifier is a diglycidylether of cyclohexane dimethanol. The modifier has a viscosity of about 60 cP and a density around 1.092 g/ cm^3. Both fluids are clear.

The encapsulated imidazole catalyst particles are Intelimer ® 7004. These white particles have a mean size of 10 microns and a density of approximately 0.308 g/cm^3. This means that the test containing catalyst particles will be settling upward in the fluid. The black carborundum particles have a mean size of 2 microns and a density of 2.297 g/cm^3.

Machine Tests

Four tests were run to demonstrate the machines abilities. The first test compares the machine's measurements with visible observed trends in an epoxy – carborundum mixture. The second test proves the device's ability to detect concentration changes were none are directly visible. This was done with an epoxy – catalyst particle mixture. Epoxy – carborudum mixes with various viscosities were then used to demonstrate the ability of the machine to measure a settling velocity. A final test implementing an epoxy- catalyst particle mixture was allowed to settle completely to demonstrate the machine's ability to measure all the settling regimes with out the use of a mud line.

Several samples of each particle/resin combination with known concentrations were measured. This provided a relation to translate observed voltage signals from the photodiode into concentration data.

Test Results

The results of the first test are shown in Figure 6. The sample was a 50/50 mix of EPON 828 and HELOXY 107. The sample was photographed at ten minute intervals. The machine started scans at the line placed on the photographs. The machine's measurements correspond very well to the observed sample.

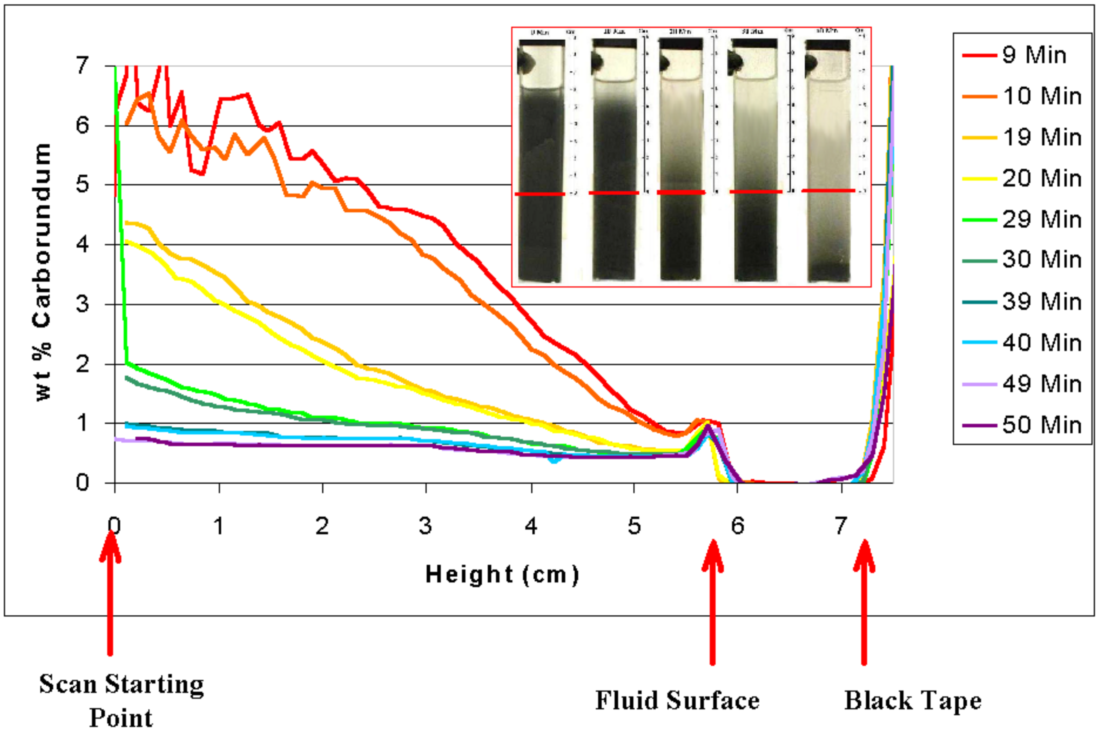

Figure 6. A comparison of the machine's data and visual observations.

The scan from the second test is aligned with a photograph of the sample used in Figure 7. The sample is a mixture of 10% EPON 828, 90% HELOXY 107, and catalyst particles. The scan shows an increase of particle concentration along the height. There is no sign of settling in the sample visible to the naked eye.

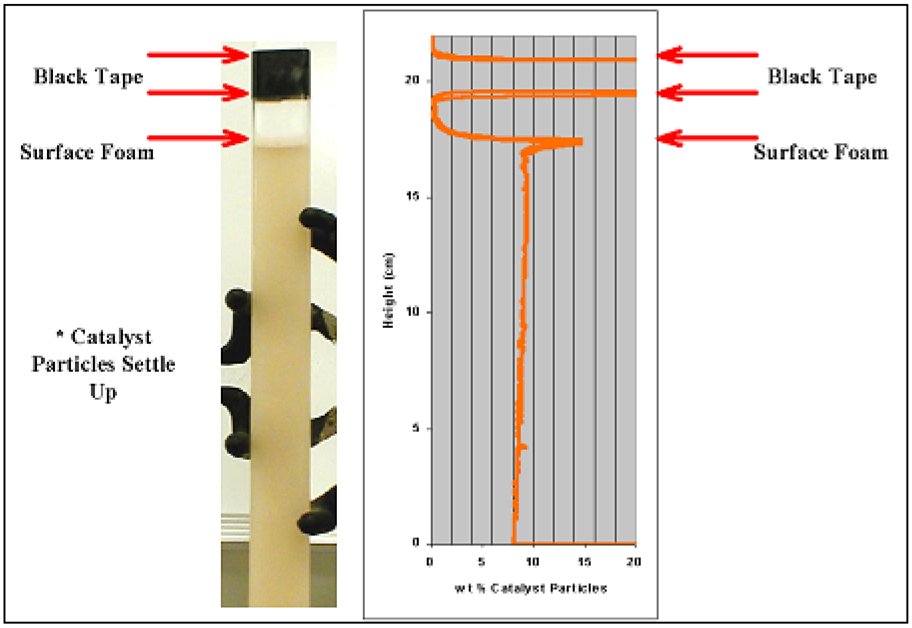

Figure 7. A scan of a sample were no settling is visible.

Three samples containing epoxy - catalyst particles mixtures of various viscosities were scanned a set concentration's height was charted verse time in Figure 8. The settling velocity increased with a decrease in viscosity.

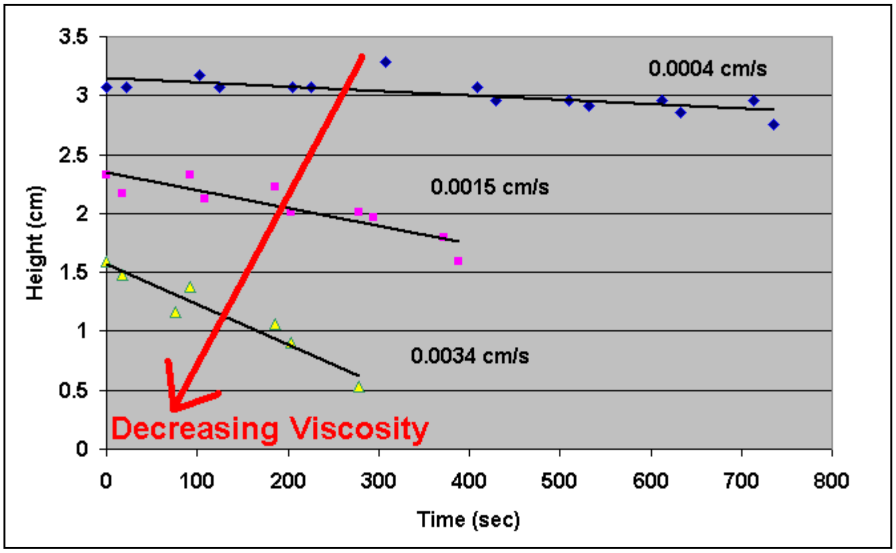

Figure 8. Velocities of 60, 108 and 384 cP samples.

The final epoxy – catalyst test mixture was scanned for approximately a week, allowing complete settling to occur. A scan of the sample is shown in Figure 9. Each line on the scan is separated by three hours.

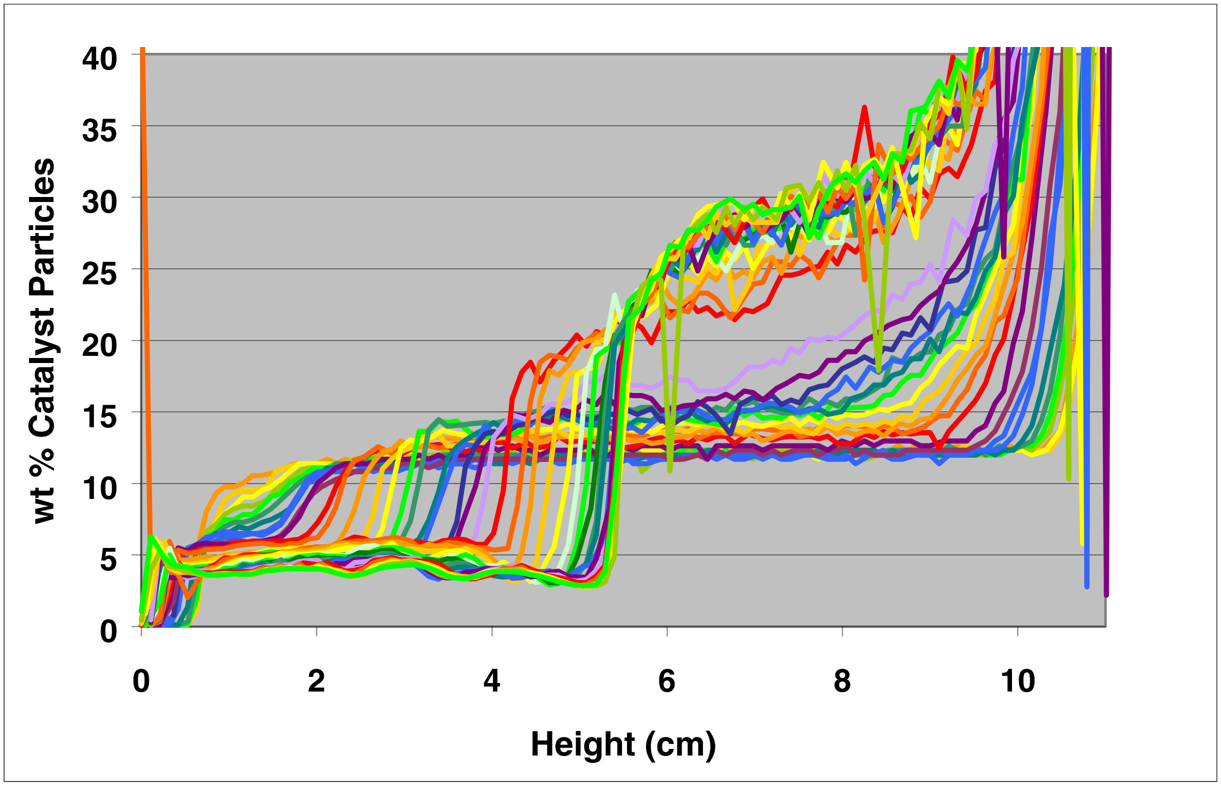

Figure 9. A compilation of scans taken at three hour intervals.

The 8% concentration level's height from the top of the sample was measured and charted verses time as shown in Figure 10. The resulting graph corresponds very well to results that can be expected from sample measured with a visible mud line.

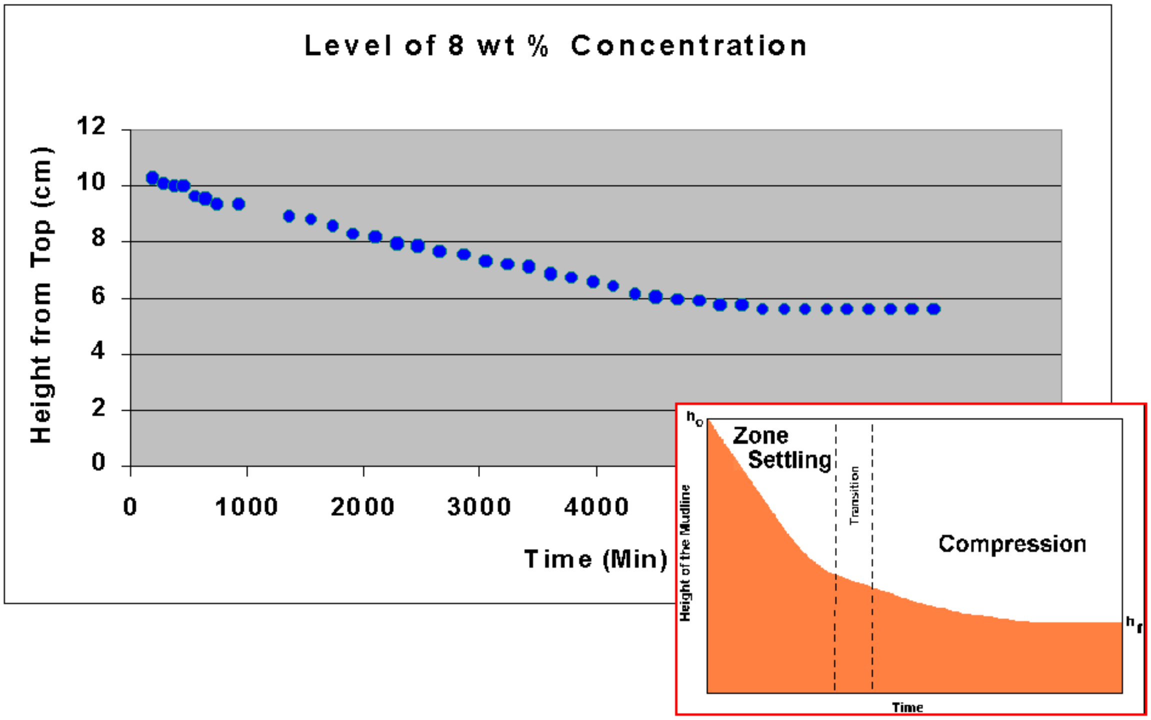

Figure 10. A comparison of measured results with expected trends observed in samples with clear mud lines.

CONCLUSION

This paper has reported the need for improved settling measurement techniques. The settling characterization device described overcomes many of the difficulties encountered with presently existing machines.

It has been successfully demonstrated that the settling characterization device is able to accurately measure the settling trends of a sample. The machine's measurements correspond very well to observable trends. In cases were settling has occurred the machine is able to observe trends were the naked eye cannot. From the machine's scans settling velocity can be derived. All the expected settling regimes can be observed from the machine's measurements with out the use of a visible mud line.

This machine provides a powerful tool to measure settling rates. The machine collects a wealth of accurate, precise empirical data. It is envisioned that the wealth of information that is collected by this machine will greatly improve understanding of settling.

ACKNOWLEDGEMENTS

The authors would like to thank Patricia Dolez and the Virginia Tech Photonics Dept. for their help and useful discussions. They also thank the National Science Foundation for financial support.

REFERENCES

1) Colomer, J.; Ross, J. A.; Casamitjana, X. Sediment entrapment in karast basins. Aquat. Sci. **1998**, 60, 338-358.
2) Weber, W. J. *Physicochemical Processes for Water Quality Control*; Wiley-Interscience: New York, NY, 1972, pp 111-138.
3) Fox, R. W.; McDonald, A. T. *Introduction to Fluid Mechanics*; John Wiley & Sons, Inc.; New York, NY, 1992, pp 437-449.
4) Papanicolaou, A. N. Settling Characteristics of Particles in a Suspension of Medium to High Solids Concentration. M.S. thesis, Virginia Polytechnic Institute and State University, Blacksburg, VIRGINIA, 1992.
5) Mahgereftech, H.; Kamugasha, D. Novel On-Line Sedimentation Analyzer. J. Colloid Interface Sci., **2000**, 228, 410-422.
6) Futterer, et al. Device and method for automatic detection of the height of sedimentation in a sedimentometer. U.S. Patent 5,531,104, 1996.

Synthesis and Characterization of Poly(Arylene Ether Ketone) Random (Statistical) Copolymers Via Direct Polymerization: Candidates for New Proton Exchange Membranes

Rachael Hopp*, Feng Wang, and James E. McGrath
Department of Chemistry
Materials Research Institute
Virginia Polytechnic Institute and State University
Blacksburg, VA 24061

* Department of Chemistry, University of Wisconsin, Stevens Point, WI

ABSTRACT

Environmental concern and energy source limitations have encouraged fuel cells as a promising alternative energy source for automobiles, portable power, and stationary power generation. Fuels cell use the chemical energy generated by the reaction of hydrogen and oxygen to create electrical energy with the only product being water. Currently Nafion® is being used as the proton exchange membrane in fuel cells, but efforts are under way to create more conductive, cost effective membranes. In the past, post sulfonation of both polysulfones and polyketones has been attempted, but these techniques produced brittle films with low molecular weight and low conductivity. Direct copolymerization of sulfonated poly(arylene ether sulfone)s has led to comparable membranes to that of Nafion and is of continuing interest. The next generation of proton exchange membranes involves the synthesis of sulfonated poly(arylene ether ketone) copolymers via direct polymerization and is the subject of this paper.

The pre-sulfonation route for synthesis of amorphous hexafluoro bisphenol-A based sulfonated poly(arylene ether ketone) copolymers was feasible using from 0% to 100% sulfonated monomer, with up to two sulfonate groups per repeating unit. High molecular weight copolymers allowed the casting of tough, flexible films from DMAc solutions. Acid form membranes were tested for conductivity, ion exchange capacity, and water uptake. The properties of the membranes compared well with Nafion 1100. The acid form membranes had proton conductivities of 0.09 and 0.10 S/cm for the PHFK-40 (IEC 1.14 meq/g) and PHFK-60 (IEC 1.67 meq/g), respectively, while the conductivity of Nafion 1100 (IEC 0.91 meq/g) was 0.12 S/cm under the same conditions. Ion exchange capacity results proved that SO_3Na and subsequently proton conductive groups, $-SO_3H$, were introduced into the copolymers via a sulfonated monomer without any side reactions, which are often observed in post sulfonation methods.

INTRODUCTION

With natural energy sources decreasing and automotive pollution on the rise, fuel cells have become a promising alternative energy source for automobiles and stationary power generation. Fuel cells convert hydrogen and oxygen to electricity while only producing water. The key component of a fuel cell is the proton exchange membrane (PEM). Currently Nafion® is used as the PEM in fuel cells, but there are disadvantages to this material. The structure of Nafion is shown in Figure 1.

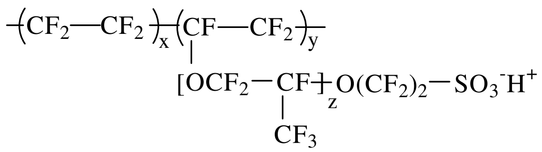

$$-\!\left(CF_2-CF_2\right)_x\!\left(\underset{\displaystyle [OCF_2-\underset{\displaystyle CF_3}{\overset{|}{CF}}\!+_z O(CF_2)_2-SO_3^-H^+}{\overset{}{CF}}-CF_2\right)_y\!-$$

Figure 1. Chemical Structure of Nafion

New materials are needed for PEM because Nafion is expensive, has low conductivity at high temperatures, has a high methanol permeability, and is difficult to process. Higher performance membranes are needed as fuel cells move towards commercialization. Post sulfonation of polysulfones and polyketones has been attempted.[1] The level of post sulfonation is difficult to control and side reactions often result. High electron density at the activated position leads to relatively easy desulfonation. Post-sulfonated polymers have low acidity and low stability due to the position of the sulfonic acid groups on the activated aryl ring. (Scheme 1)

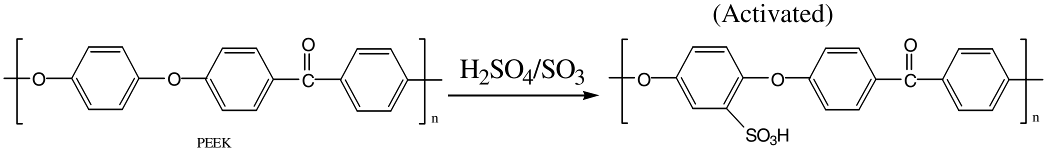

Scheme 1. Sulfonated PEEK in the activated position[2]

Previous efforts by McGrath et. al. have focused on direct copolymerization using sulfonated monomers.[3] These polymers have been based on poly(arylene ether sulfone) (PAES) backbones. Sulfonated PAES lead to comparable or better conductivity at higher temperatures than Nafion and post sulfonated polymers. These systems show promising properties due to the placement of the sulfonic acid moiety on the deactivated aryl ring and the control of the degree of sulfonation. The degree of sulfonation is controlled by adjusting the ratio of sulfonated to unsulfonated monomers at the start of the polymerization. Enhanced stability due low electron density can also be observed. Because the copolymers are formed through a step-growth mechanism with 99.9% pure monomers, the exact structure of the copolymer is known.

The next generation of membranes will be attempted by direct polymerization of appropriate monomers to produce sulfonated polyketone copolymers.[4] These polymers compare to previous efforts involving post sulfonated polyketones. However, as with the direct polymerization of sulfonated polysulfones, the sulfonic acid groups are located on the deactivated rings. (Figure 2) It is hypothesized that the directly polymerized sulfonated polyketones will have a higher acidity than post sulfonated polyketones and thus better performance as a PEM. The sulfonated poly (arylene ether ketone)s will be synthesized by copolycondensation of 5,5'-carbonylbis(2-fluorobenzenesulfonate), 4,4'-difluorobenzophenone, and hexafluoro bisphenol-A. The ratio of sulfonated to unsulfonated monomers will be varied as with the previous sulfonated polysulfones.

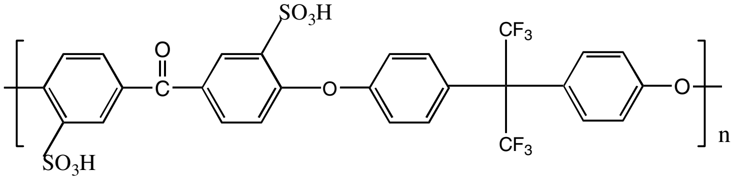

Figure 2. Copolymer containing a sulfonated ketone moiety in the deactivated position

EXPERIMENTAL

Materials:

Highly purified, commercially available, 4,4'-difluorobenzophenone and hexafluoro bisphenol-A were obtained from Aldrich and Ciba-Geigy, respectively. The reaction solvent *N*-methyl-2-pyrrolididone (NMP) was distilled over molecular sieves from calcium hydride under vacuum before use. Potassium carbonate was vacuum-dried prior to polymerization. All other reagents were obtained from Aldrich and used as received.

Synthesis of Sulfonated 4,4'-difluorobenzophenone (SDFK):

SDFK was synthesized according to a modified literature method.[5,6] To a 100-mL, three mecked flask equipped with a mechanical stirrer and a nitrogen inlet/outlet 30.0g of DFK was dissolved in 60mL 28% fuming sulfuric acid. The solution was then placed into an oil bath and raised to 150°C for 7 hours. At this point, the reaction mixture was cooled to room temperature, and poured into 450mL of ice-water. Next, 110.0g of NaCl was added which produced a white solid. The latter was filtered and re-dissolved in 300mL of deionized water. The solution was treated with 2*N* NaOH aqueous solution to a pH of 6~7. The solution was diluted with dionized water to 500mL. Next, 110.0g NaCl was added to salt out the sodium form sulfonated monomer. The crude product was filtered dried at 75°C overnight. Monomer grade sulfonated monomer was generated by recrystallization from a mixture of isopropyl alcohol and deionized water (3/1, in volume), producing white needle-like crystals.

Synthesis of Sulfonated Poly(arylene ether ketone)s (PHFK-00 ~ PHFK-100):

A typical polymerization for PHFK-40 (SDFK/DFK = 40/60, mole%) is described as follows: First, 5.0435g (15mmol) hexafluoro bisphenol-A, 1.9638g (9mmol) DFK, and 2.5337g (6mmol) SDFK were added to a 3-neck flask equipped with mechanical stirrer, nitrogen inlet, and a Dean Stark trap. Next, 1.15 equivalent of potassium carbonate and NMP were introduced to afford a 20% solids concentration. Toluene (NMP/Toluene = 2/1, v/v) was used as an azeotropic agent. The reaction mixture was refluxed at 150°C for 4 hours to dehydrate the system. Next, the temperature was raised slowly to 175°C and reacted for 7 hours. The solution became very viscous after this time and was subsequently cooled to room temperature and diluted with N,N-dimethyl acetamide (DMAc). The reaction product was allowed to sit overnight so the insoluble salts could settle out of solution. It was then isolated by addition to stirred deionized water. The precipitated fibrous copolymer was washed with deionized water several times to further remove salts and was dried at 75°C overnight. It was then vacuum dried at 120°C for 24 hours.

Membrane preparation:

Membranes were prepared by redissolving 1.0 g of copolymer in 20mL of DMAc. The solutions were filtered with 0.45μm syringe filters and cast onto clean glass substrates that were on a level hot plate set at 60°C. The films were allowed to dry overnight, after which the heat was increased to 100°C for two hours. The sodium form membranes were converted into the acid form by boiling in 2*N* H_2SO_4 for 1.5 hours, followed by boiling in deionized water for 0.5 hours. They were then vacuum dried at 85°C for 24 hours.

Characterization Techniques

Fourier Transform Infrared (FTIR) Spectroscopy:

FTIR spectroscopy was used to confirm the pendant functional groups on the copolymers. Measurements were recorded using a Nicolet Impact 400 FT-IR spectrometer with thin, homogeneous cast films.

Nuclear Magnetic Resonance (NMR) Spectroscopy:

NMR (^1H and ^{13}C) was conducted on a Varian UNITY 400 spectrometer. All spectra were obtained from a dimethylsulfoxide-d6 (DMSO) solution at room temperature. NMR was used primarily to determine monomer purity and to confirm molecular structure of the synthesized monomer.

Differential Scanning Calorimentry (DSC):

The glass transition temperatures (T_g) were obtained on a Perkin-Elmer DSC-7 differential scanning calorimeter. Scans were conducted under nitrogen at a heating rate of 10°C/min. Second heat T_g values were reported as the midpoint of the change in the slope of the baseline.

Intrinsic Viscosities:

Intrinsic viscosities were determined in NMP at 25°C using an Ubbelohde 200 viscometer.

Non-aqueous Potentiometric Titrations:

Non-aqueous potentiometric titrations were conducted using an MCI Automatic Titrator Modelo GT-05. The acid form membrane solutions in DMAc were titrated by a standard tetramethyl ammonium hydroxide solution. Titration was used to quantitatively determine sulfonic acid concentration in the copolymer, i.e. ion exchange capacity (IEC, meq/g).

Conductivity:

Conductivity measurements were performed on the acid form of the membranes using the cell shown in Figure 3. This cell geometry was chosen to ensure that the membrane resistance dominated the response of the system. An impedance spectrum was recorded from 10 MHz to 10 Hz using a Solatron 1260 Impedance/Gain-Phase Analyzer. The resistance of the film was taken at the frequency that produced the minimum imaginary response. All impedance measurements were performed at 30°C in liquid water.

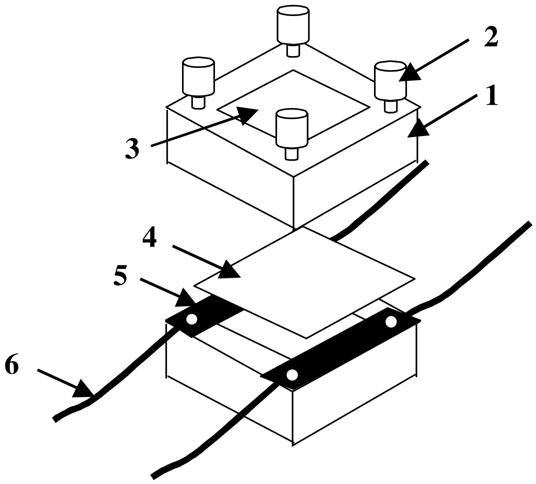

Legend
1. Teflon block
2. Thumbscrew
3. Open area to allow equilibration with environment
4. Membrane sample
5. Blackened Pt foil electrode
6. Pt lead

Figure 3. Conductivity Cell

Water Uptake of Membranes:

The membranes were vacuum dried at 85°C for 24h, weighed and immersed in deionized water at room temperature for 24h. The wet membranes were wiped dry and quickly weighed again. The water uptake of membranes are reported as weight percent as follows:

$$\text{Water uptake} = \frac{W_{wet} - W_{dry}}{W_{dry}} \times 100\%$$

Where W_{wet} and W_{dry} are the weights of the wet and dry membranes, respectively.

RESULTS AND DISCUSSION

Monomer synthesis:

The desired sulfonated monomer was prepared as shown in Scheme 2. Disodium 3,3'-disulfonate-4,4'-difluorobenzophenone was prepared by sulfonating 4,4'-difluorobenzophenone using fuming sulfuric acid (28%) at 150°C for 7 hours. The resulting acidic compound was neutralized first by sodium chloride and subsequently with sodium hydroxide at room temperature to ensure that the acid form compound was converted to the sodium form completely. (See experimental section) This electrophilic aromatic substitution provides derivatives that are meta to the ketone group and ortho to the fluorine group due to the electron withdrawing ketone group. Monomer grade sulfonated monomer was generated by recyrstallization from a mixture of isopropyl alcohol and deionized water. The chemical structure of the sulfonated monomer was confirmed by proton (Figure 4) and carbon (Figure 5) NMR. The anticipated structures were obtained at 80% yields.

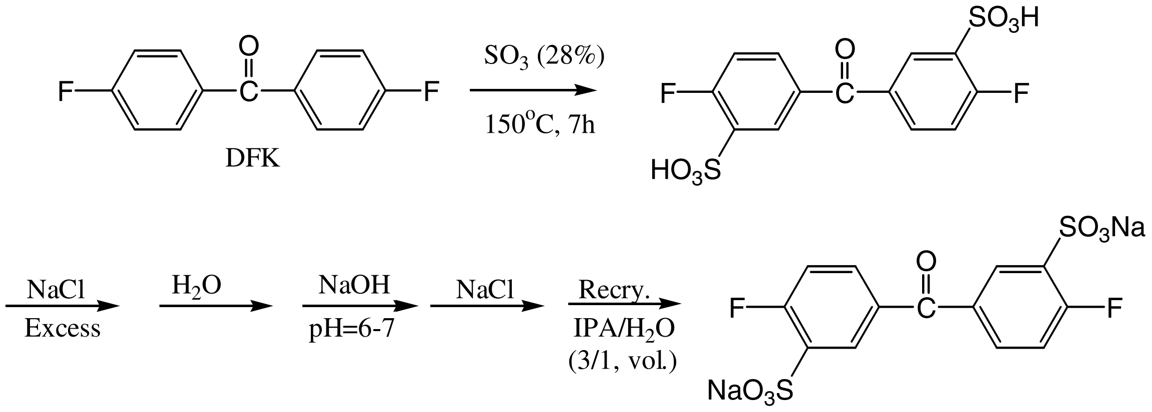

Scheme 2. Synthesis of SDFK

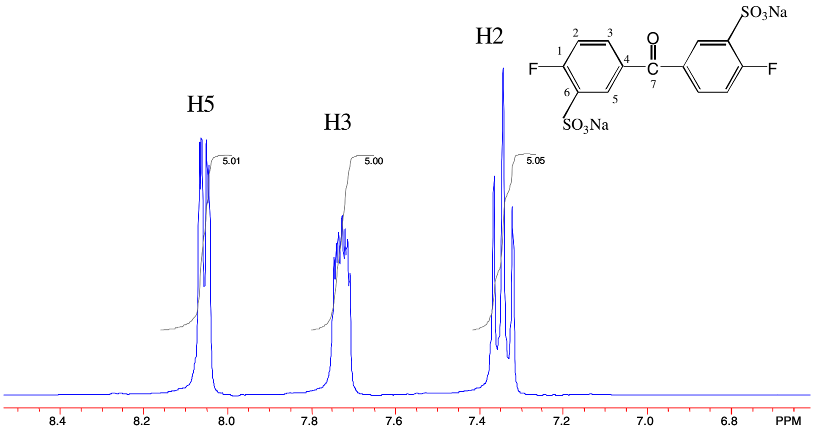

Figure 4. ^{1}H NMR of SDFK

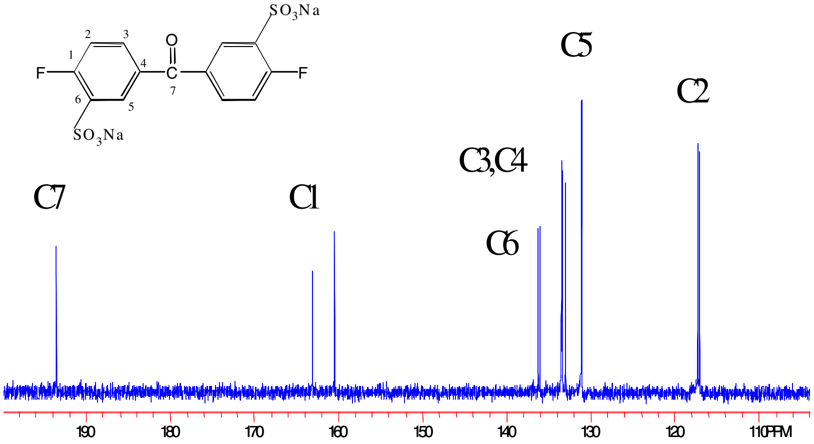

Figure 5. ^{13}C NMR of SDFK

Polymer synthesis and characterization:

Sulfonated poly(arylene ether ketone)s were successfully synthesized via nucleophilic aromatic substitution polycondensation of hexafluoro bisphenol-A, DFK, and SDFK using 0 to 60, 80, and 100 mole % of the SDFK. The polymer synthesis (Scheme 3) involved condensing a controlled amount of sulfonated activated halide, the 4,4'-difluorobenzophenone, and hexafluoro bisphenol-A in NMP, which contained toluene as an azeotropic agent. Homo and copolymers are expressed as PHFK-00 ~ PHFK-100, where the two or three digits represent the mole ratio of SDFK to the total dihalide monomers. The sulfonated poly(arylene ether ketone)s were prepared via a nucleophilic aromatic substitution reaction similar to the procedure used to synthesize sulfonated poly(arylene ether sulfone)s.[2] The rate of this reaction depends on both the basicity of the hexafluoro bisphenol-A salt and the electron-withdrawing power of the activating group of the dihalide. The substituted activated halide, SDFK, is less reactive than DFK, because the steric effect from the bulky sodium sulfonated group would be expected to hinder the nucleophilic attack of the phenolate. Less reactive monomers require higher temperatures to achieve high molecular weight polymers. Therefore, NMP, was the choice solvent for all the starting monomers because it has a relatively high boiling point allowing high molecular weight polymers to be synthesized. The polymerizations were conducted in the sodium salt form of SDFK to take advantage of the greatly enhanced stability of the sulfonic acid salt. Possible side reactions related to sulfonic acid groups generated via post sulfonation such as crosslinking and degradation were eliminated. However, since potassium carbonate was the base, some alkali sulfonate exchange probably occurred during polymerization. The recovered yields were quantitative and intrinsic viscosities determined in NMP at 25°C were high (Table 1). Of course, the intrinsic viscosities are influenced by the sulfonate groups, which is no doubt related to enhanced intramolecular stiffness and intermolecular associations. Polymers were prepared with up to 1.14 $-SO_3Na$ groups per repeating unit (40 mole% SDFK), while still allowing high molecular weight, tough, film-forming material to be obtained. Sodium form membranes (PFK) were converted to corresponding acid form (PHFK) using dilute sulfuric acid.

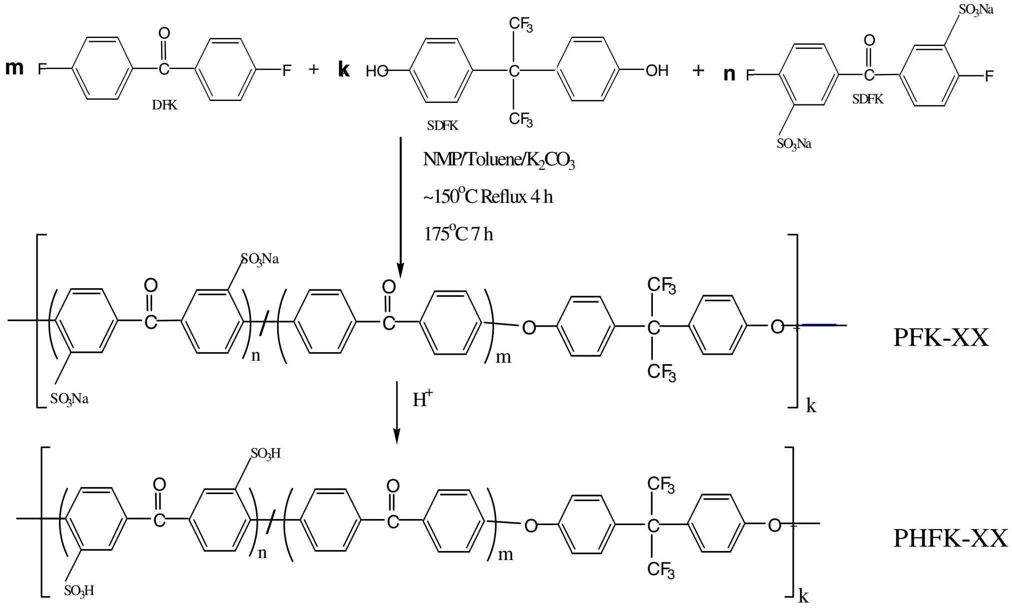

(n+m)/k = 1.00 (in mole); XX = 100n/(n+m)

Scheme 3. Synthesis of random sulfonated poly(arylene ether ketone) copolymers

Table 1. Influence of Hexafluoro Bisphenol-A Based Sulfonated Copolymer Compositions on Yield and Intrinsic Viscosity

Polymer	Monomer %		Yield	$[\eta]^{NMP}_{25^{\circ}C}$
	DFK	SDFK	(%)	dL/g
PFK-00	100	0	94	1.1
PFK-10	90	10	90	1.2
PFK-20	80	20	93	2.6
PFK-30	70	30	94	2.6
PFK-40	60	40	91	2.1
PFK-50	50	50	73	1.9
PFK-60	40	60	90	2.0
PFK-80	20	80	N/A	N/A
PFK-100	0	100	N/A	N/A

Characterization Techniques

Fourier Transform Infrared (FTIR) Spectroscopy:

FT-IR is a powerful and versatile tool to characterize individual chemical functionalities, especially for qualitative analysis, and has been used to analyze characteristic bands corresponding to the sulfonate groups in different polymers, eg. poly(arlyene ether sulfone)s[2] and poly(arylene ether ketone)s[3]. The successful introduction of the sodium sulfonate groups was confirmed by FT-IR spectra (Figure 6) where strong characteristic peaks at 1030 cm^{-1} and 1087 cm^{-1} assigned to symmetric and asymmetric stretchings of the sodium sulfonate groups were observed for all sulfonated copolymers from PHFK-00 to PHFK-60. The peak at 1511 cm^{-1} decreases due to the delocalization of the electrons around the aromatic ring with increasing sulfonation. The peak at 1596 cm^{-1} is consistent throughout the series and is due to the ketone bond in the polymer chain.

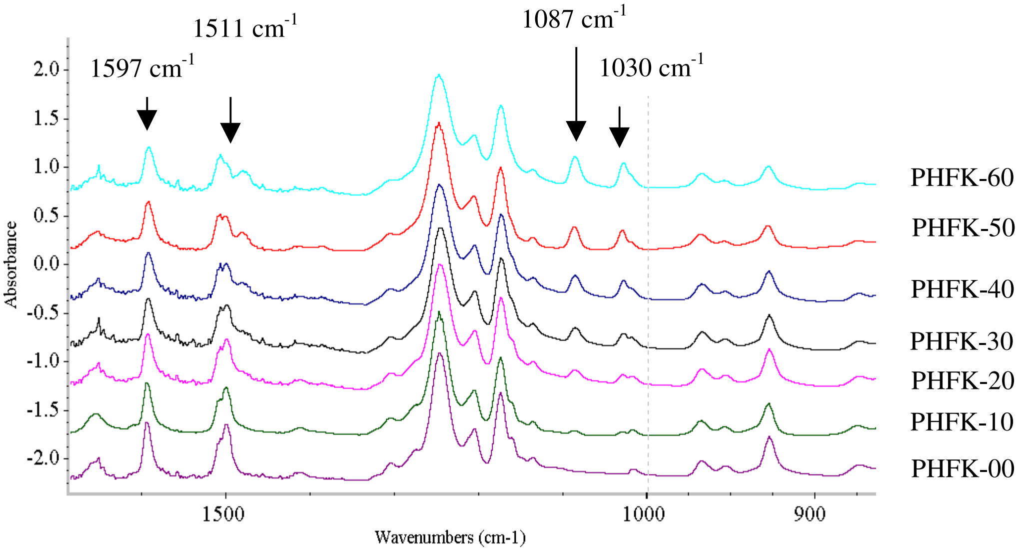

Figure 6. Influence of the Degree of Sulfonation on the FT-IR of Sulfonated Poly(arylene ether ketone) Copolymers

Differential Scanning Calorimetry (DSC):

The introduction of sulfonate groups has two effects on glass transition temperature: first, to produce increased molecular interaction by pendant ions, i.e. ionomer effect; and second, to increase molecular bulkiness. Both effects hinder internal rotation, leading to increased glass transition temperatures for sulfonated polymers. The DSC data showed a linear increase of T_g in the range from 0% to 60% acid sulfonate group as shown in Table 2.

Table 2: Glass Transition Temperatures of Sulfonated Copolymers

Films	% SDFK	T_g (°C)
PHFK-00	0	170
PHFK-10	10	170
PHFK-20	20	175
PHFK-30	30	180
PHFK-40	40	190
PHFK-50	50	195
PHFK-60	60	200

Ion Exchange Capacity:

Non-aqueous potentiometric titration was used to quantitatively determine the ion exchange capacities (IEC) of the polymers. The PHFK solutions in DMAC were titrated by standard tetramethyl ammonium hydroxide solution (~0.05 N, in isopropanol). One sharp endpoint was observed confirming the strong acid/base reaction. All the experimental IEC values listed in Table 3 are in good agreement with the theoretical IECs, assuming that all of the sulfonated monomer was incorporated into the copolymer. The above results prove again that SO_3Na and subsequently proton conductive groups, $-SO_3H$, could be introduced into the copolymers via a sulfonated monomer without any side reactions, which are often observed in post sulfonation methods.

Table 3. Influence of sulfonate or sulfonic acid groups on water uptake, Ion Exchange Capacity, and conductivity at 30°C

% SDFK	IEC (meq/g)			% Water	λ
	[a]Exp	[b]Calc	[c]σ (S cm^{-1})	Uptake	$H_2O/-SO_3H$
10	0.26	0.36	0.001	0.8	1.7
20	0.61	0.72	0.008	7.6	6.9
30	0.93	1.05	0.036	15.2	9.1
40	1.14	1.38	0.085	26.3	12.8
50	1.43	1.70	0.088	50.1	19.5
60	1.67	2.01	0.104	N/A	N/A
Nafion 1100	N/A	0.91	0.12	N/A	24

Conductivity:
The conductivity of membranes in liquid water at 30°C cover a range of disulfonation and are shown in Table 3. The acid form membranes had proton conductivities of 0.09 and 0.10 S/cm for the PHFK-40 (IEC 1.14 meq/g) and PHFK-60 (IEC 1.67 meq/g), respectively, while the conductivity of Nafion 1100 (IEC 0.91 meq/g) was 0.12 S/cm under the same conditions.

Greater ion exchange capacities are needed with sulfonated poly(arylene ethers) to achieve similar conductivities to perfluorosulfonic acid Nafion polymers, which is attributed to the strength of the acid group in each system. The acidity of the pendant perfluorosulfonic acid is much stronger than the aryl sulfonic acid, therefore, more acid moieties are needed in sulfonated poly(arylene ethers) to achieve the desired conductivity.

Water Uptake of Membranes:
Water uptake in weight percent and λ (the molar ratio of water molecules to sulfonic acid groups) are presented in Table 3. Water sorption increased with sulfonate content due to the strong hydrophilicity of the sulfonate groups. The acid form of the membranes has a modestly higher water uptake than the corresponding sodium membranes. (Figure 7)

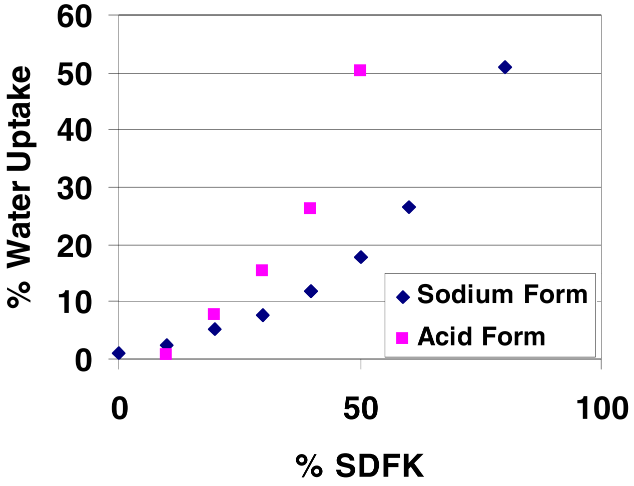

Figure 7. Comparison of water uptake for sodium and acid form membranes of poly(arylene ether ketone) copolymers

CONCLUSIONS

Successful synthesis of 3,3'-disulfonated 4,4'-difluorobenzophenone monomer was achieved with high purity. The structures were confirmed by both proton and carbon NMR. Using the pure monomers, polycondensation of poly(arylene ether ketone)s from 0% to 100% sulfonated monomer, with up to two sulfonate groups per repeating unit was successful. Increasing sulfonation of the polymer series was confirmed by FT-IR. The intrinsic viscosities of the polymer series increased with increasing sulfonation due to enhanced intramolecular stiffness and intermolecular associations. The high molecular weight copolymers were cast into tough, flexible films.

The sulfonated poly(arylene ether ketone)s (PHFK) were characterized by DSC, conductivity, and water uptake. Both conductivity and water uptake increased with increasing sulfonation. The acid form membranes had proton conductivities of 0.09 and 0.10 S/cm for the PHFK-40 (IEC 1.14 meq/g) and PHFK-60 (IEC 1.67 meq/g), respectively, while the conductivity of Nafion 1100 (IEC 0.91 meq/g) was 0.12 S/cm under the same conditions. Ion exchange capacity results proved that SO_3Na and subsequently proton conductive groups, $-SO_3H$, were introduced into the copolymers via a sulfonated monomer without any side reactions, which are often observed in post sulfonation methods.

FUTURE RESEARCH

Future research will include the synthesis and characterization of the sulfonated poly(arylene ether ketone)s based on other bisphenols. Also, end group analysis will be done on selected end capped systems for number average molecular weight determination. The durability of the membranes will be tested at 100°C in deionized water via Soxhlet extraction and compared to that of membranes cast from direct and post sulfonated poly(arylene ether sulfone)s and Nafion membranes. Ultimately, membrane electrode assemblies will be fabricated out of the membranes, and fuel cell tests will be conducted.

ACKNOWLEDGEMENTS

The authors would like to acknowledge the National Science Foundation – Partnerships for Innovation for financial support.

REFERENCES

[1] Nolte, R.; Ledjeff, K.; Bauer, M.; Mulhaupt R. Partially sulfonated poly (arylene ether sulfone) – A versatile proton conducting membrane material for modern conversion technologies. *J. Membrane Sci.* **1993**, *83*, 211-220.

[2] Jin, X.; Bishop, M.T.; Ellis, T.S.; Karasz, F.E. *Br. Polym. J.* **17**, 4 (1985)

[3] Wang, F.; Hickner, M.; Kim, Y.S.; Zawadzinski, T.A.; McGrath, J.E. Synthesis and Characterization of Sulfonated Poly(arylene ether sulfone) Random (Statistical) Copolymers Via Direct Polymerization: Candidates for New Proton Exchange Membranes. *J. Membrane Sci.* submitted 2001.

[4] Wang, F.; Chen, T.; Xu, J. Sodium sulfonate-functionalized poly(ether ether keone)s. *Macromol. Chem. Phys.* **1998**, *199*, 1421-1426.

[5] Robeson, L.M.; and Matzner, M. Flame Retardant Polyarylate Compositions, U.S. Patent 4,380,598 to Union Carbide, 1983.

---

[6] Ueda, M.; Toyota, H.; Ochi, T.; Sugiyama, J.; Yonetake, K.; Masuko, T.; and Teramoto, T. Synthesis and characterization of aromatic poly(ether sulfone)s containing pendant sodium-sulfonate groups, *J. Polym. Sci., Polym. Chem Ed.* **1993**,*31*,85.

Surface Chemistry Effects on Thin Film Stability

Holly C. Hudson* and Alan R. Esker
Department of Chemistry, Virginia Polytechnic Institute and State University, Blacksburg, VA 24061

* Department of Chemistry, Oswego University, Oswego, NY

ABSTRACT

Factors including deviations from bulk glass transition temperatures (T_g) and the dewetting of thin polymer films illustrate challenging problems facing the nanoscale fabrication of polymer based coatings in microelectronic and optical devices. To understand the role surface chemistry plays on dewetting, bilayer samples of poly(t-butyl acrylate) (PtBA) on cellulose ether coated silicon wafers have been prepared using the Langmuir-Blodgett (LB) technique. Upon annealing (80°C) above PtBA's T_g (≈40°C), PtBA dewets from the cellulose-coated substrate. By looking at dewetting as a function of time for different thicknesses and chemical compositions of the cellulose ether layer at a fixed PtBA thickness, information pertaining to the dewetting mechanism was obtained. Effects on hole radius, hole density, rupture time, and boundary conditions indicate that n-propyl->n-butyl->isopentylcellulose in terms of film stability for a fixed number of coating layers and that there is an increase in PtBA's instability as the thickness of the n-butyl- and isopentyl cellulose coating layer increases.

INTRODUCTION

Dewetting is the spontaneous formation of a hole on the surface of an unstable liquid film. Thin film stability can be controlled, by controlling the surface chemistry. As noted by Martin and Brochard-Wyart,[1] the stability of liquid films has several practical applications. In contact lenses, a stable thin film of water is necessary to prevent eye irritation, which results when water dewets from the contact lens causing it to adhere to the cornea. Tires on a wet road are another example, as it is necessary for the thin film of water to be squeezed out to maintain maximum grip.[1]

Dewetting occurs via two mechanisms: nucleation and growth, and spinodal dewetting. The nucleation and growth mechanism is observed when defects on the silicon substrate or "junk" sites in the film act as initiation sites. When heated above the glass transition temperature, T_g, films change from amorphous solids to viscous liquids. If the liquid polymer film is unstable, it pulls away from these initiation sites resulting in a thick rim of excess polymer around a hole. Spinodal dewetting occurs when capillary waves, present on the liquid surface arising from density fluctuations, attain an amplitude large enough to contact the substrate producing an initiation site. The film then pulls away from this site, resulting in a hole surrounded by a thick rim.

To understand thin film stability, the variables influencing dewetting must be examined. Factors such as molecular weight, temperature, chain topology, stereochemistry, and the Hamaker constant influence the stability of films and therefore dewetting.[2,3] Due to their large viscosities, polymers above T_g often serve as the dewetting liquid to facilitate studies of dewetting dynamics at convenient time scales. Surface chemistry also influences dewetting. Recent theoretical[4] and experimental[5] research shows how bilayer film samples, as depicted in Figure 1, can be used to probe thin film stability.

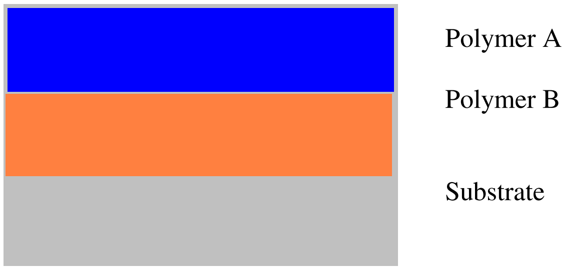

Figure 1. Schematic of a thin film set-up to alter dewetting using a second polymer.

Polymer B is a coating layer that alters polymer A's stability on the substrate. The composition and thickness of this coating layer can influence dewetting. To investigate the role of coating layers on film stability, samples were prepared with a film of poly(t-butyl acrylate) (PtBA, polymer A) on a silicon substrate coated with a cellulose ether (polymer B).

To prepare this system, the Langmuir-Blodgett (LB) technique was utilitzed.[6] LB prepares uniform films of a precise thickness at the molecular scale. PtBA (polymer A) and cellulose ethers (polymer B) are utilized since they are well known for their ability to make LB films.[7,8] Additionally, PtBA, a flexible coil polymer, will have limited miscibility with the rod-like cellulose derivatives.[10,11] The hairy-rod polymers form oriented molecular composites by LB. Alkylated cellulose derivatives according to Schaub et al.,[8] are consistent with the hairy rod concept.[9] As hairy-rod polymers, cellulose ethers are expected to have greater miscibility with PtBA and hence greater adhesion than non-derivatized rod-like cellulose.[11] Based on the notion that van der Waals forces are the most important forces in these films, as hair length decreases, miscibility should decrease, interfacial width should decrease, and dewetting should increase, therefore decreasing the stability of the film. As will be seen below, this hypothesis fails for the cellulose derivatives used in this study.

In addition to changes in the hole density, there are two important limits describing the rate at which the holes grow on coated substrates. These two extremes are: stick and slip boundary conditions. For slip boundary conditions, the substrate surface is perfectly smooth and passive. The surface velocity and the bulk velocity are equal, producing a uniform velocity gradient profile for the growing hole at all distances from the substrate. The polymer is expected to slip if the time dependence of the growing holes radius follows Equation 1.[12]

$$d \sim a \bullet t + t_o \tag{1}$$

In Equation 1, a ~ 1/k with k being the monomer/surface friction coefficient, d is the hole diameter, and t_o is the rupture time. For stick boundary conditions, the polymer sticks or partially grafts to the surface. The surface velocity of the growing hole is near zero, while the bulk velocity is not, resulting in a non-uniform velocity profile. Slippage of the polymer is suppressed with Equation 2 providing the limiting behavior.[12]

$$d \sim a \bullet (t + t_o)^{2/3} \qquad (2)$$

In Equation 2, a ~ 1/k[v(t)], which means the monomer/surface friction coefficient is velocity dependent. Slip and stick boundary conditions are an indirect measurement of interfacial width. Until enough of polymer B is present to allow the establishment of the entire interfacial width, the stick boundary limit is not observed. Using slip and stick boundary conditions, an estimate of the maximum interfacial width is obtained.

This optical microscopy study focuses on the preparation of bilayer films like those depicted in Figure 1 where polymer A is PtBA of fixed molar mass and thickness, and polymer B is comprised of variable thickness coating layers of isopentyl, n-butyl, or n-propyl cellulose.

EXPERIMENTAL

Synthesis and Characterization. Propyl Cellulose. General Procedure. 5.006 g of cellulose acetate (~4 mmol, Eastman) was dissolved in 50 mL of dried DMSO and the solution was degassed. After it dissolved for a 6 hour period at room temperature under nitrogen gas. 32.6759 g of sodium hydroxide solid (Malinckrodt) was placed in a coffee grinder, chopped, and added. 80 mL of 1-bromopropane (Acros) was added and the solution degassed. After it stirred for twelve hours an opaque white, very viscous solution resulted. 75 mL of water-free THF over sodium benzophenone was added, degassed, and stirred for 6 days. The resulting mixture was heterogeneous, white, and very viscous. The mixture was poured into 1600 mL of distilled water. The cellulose ether was isolated by dividing the aqueous solution into five fractions and extracting each fraction three times with 80 mL of dichloromethane (Burdick and Jackson). 200 mL of pure distilled water was added to every 240 mL of CH_2Cl_2 before it was placed on a rotary evaporator to remove the CH_2Cl_2, side product ester, and water. The polymers were reprecipitated twice from THF into water and four times from $CHCl_3$ into methanol. After each reprecipitation, the polymer was dried at 80°C in a vacuum over. The final precipitation yielded 0.87 g of n-propyl cellulose.

^1H NMR spectroscopy was ran to confirm the product. ^1H NMR for PrC (300 MHz, $CDCl_3$): δ 4.35 (s, 1H), 3~4 (m, 6H+2H*ds), 1.5 (s, 2H*ds), 0.9 (s, 3h*ds). GPC (THF, polystyrene standard) results were: M_w = 170 kg/mol, M_n = 552 kg/mol, M_w/M_n. = 3.09. Elemental analysis was also ran on the product. Observed 59.41% C, 9.25% H, calculated for propylcellulose with a degree of substitution (ds) of 2.28, with 59.78%C, 9.19%H.

A similar procedure was followed to prepare the isopentyl- and n-butylcellulose derivatives. The characteristics of these polymers areas follows. ^1H NMR for nBC (300 MHz, $CDCl_3$): δ 4.35 (d, 1H), 3~4 (m, 6H+2H*ds), 1.6~1.3 (d, 4H*ds), 0.9 (s, 3h*ds). GPC results were: 182456 M_w =

182 kg/mol, M_n = 68 kg/mol, M_w/M_n = 2.66. Elemental analysis was also ran on the product. Observed 61.92% C, 9.66% H, calculated for butylcellulose with a degree of substitution of 2.15 with 62.04 %C, 9.63% H. ^{1}H NMR for IPC (300 MHz, $CDCl_3$): δ 4.4 (s, br, 1H), 3.9-2.9 (m, br, 6H+2H*ds), 1.7 (m,br,2H), 1.5-1.3 (m,br,2H), 0.9 (dd,6H). GPC results were: M_w = 144 kg/mol, M_n = 49 kg/mol, and M_w/M_n 2.92. Elemental analysis was also ran on the product. Observed 66.30% C, 10.61% H, calculated for isopentylcellulose with a ds of 2.7 with 66.67% C, 10.54% H. Poly (t-butyl acrylate) was purchased from Polymer Source, Inc. The polymer has M_n = 25.4 kg/mol, M_w/M_n = 1.07, and a T_g = 38°C. These numbers were confirmed by GPC analysis and differential scanning calorimetry.

Silicon Wafer Preparation. Four-inch silicon wafers (100) were cut with a diamond-tipped cutting instrument. The pieces were treated with an oxygen plasma set at 40 W for ten minutes at a pressure of 0.6 Torr. The pieces were ultrasonificated in dichloromethane. The pieces were rinsed with 4 Millipore water (Gradient A10 System, Millipore Corp.). Next the pieces were boiled for 1.5 hours in a 1:1:5 by volume mixture of 28 wt% ammonium hydroxide, 35 wt% hydrogen peroxide, and deionized water. Each silicon piece was washed 15 times with 4 ppb organics water, and dried with nitrogen gas. The pieces were placed in a sealed container with 1,1,1,3,3,3-hexamethyldisilazane for at least 2 hours at 80°C.

Film Preparation. Films were prepared using the Langmuir-Blodgett Technique on a commercial trough (KSV 200, KSV Instruments, Inc.) at a temperature of 22.5°C. The trough was cleaned with chloroform, its barriers cleaned with isopropanol, the trough was washed with Millipore water. The trough was filled again, contaminates were removed from the surface by suction, and the polymer, dissolved in chloroform, was spread across the surface of the water to a pressure of approximately 8 mN/m. After evaporation, the polymer was oriented at the liquid gas interface. The barriers were compressed to a specific pressure, 17 mN/m for IPC, nBC, and PrC, and 19 mN/M for PtBA, and the polymer formed an ordered monolayer on the surface. The cleaned silicon wafer was dipped at a rate of 10 mm/min, and removed from the water at a rate of 8 mm/min. The thickness of a PtBA monolayer was approximately 9 Å,[7] and an IPC monolayer was approximately 9.5 Å[8] thick. The samples produced were: 4x IPC/20x PtBA, 8x IPC/20x PtBA, 8x PrC/20x PtBA, 8x nBC/20x PtBA, 16x IPC/20x PtBA, 16x PrC/20x PtBA, and 16x nBC/20x PtBA, where the numbers correspond to the number of transferred monolayers.

Microscopy. A Zeiss Optical Microscope equipped with a DAGE-MTI CCD100 camera was used for optical measurements. Light passed through the microscope and reflects back from the sample. A mechanism of contrast depicts the changes in the films; bright areas correspond to thin films while dark areas correspond to thicker films. The films were heated on a computer controlled Linkman LTS 350 heating stage. All pictures were taken with a 20x lens. Pictures were taken at varying rates using Scion Image software, and transferred to a paint program where they were printed out. Initially films were made with gradients of thickness on them. These samples were heated in a vacuum oven in order to determine the appropriate temperature at which dewetting should be measured. The ideal rate was for the most unstable film to dewet over a period of two hours. After testing several thicknesses and several temperatures the final temperature of 80°C was chosen. At this temperature IPC dewet over a period of approximately an hour. High resolution was necessary in order to make correct measurements on the printed out pictures, therefore short movies were taken to insure appropriate refocusing. Analysis of hole density, rupture time, and hole radius were made using these pictures. Hole density was determined by measuring the area of the picture, counting the number of holes and dividing them by the area. The rupture time is the time when the first hole formed and was recorded as the movie was produced. The hole radius was measured by selecting five holes and measuring and averaging half the largest axis of the anisotropic holes.

RESULTS AND DISCUSSION

The Effect of Coating Layer Composition. The first films examined were the 16x IPC/20x PtBA, 16x nBC/20x PtBA, and 16x PrC/20x PtBA. Each film was placed on the heating stage and monitored until the temperature of 80°C was reached. Movies were then produced until complete dewetting had occurred. Using specific pictures from the movies, holes were selected and monitored in order to measure the largest axis of the anisotropic holes, called the radius here, as a function of time.

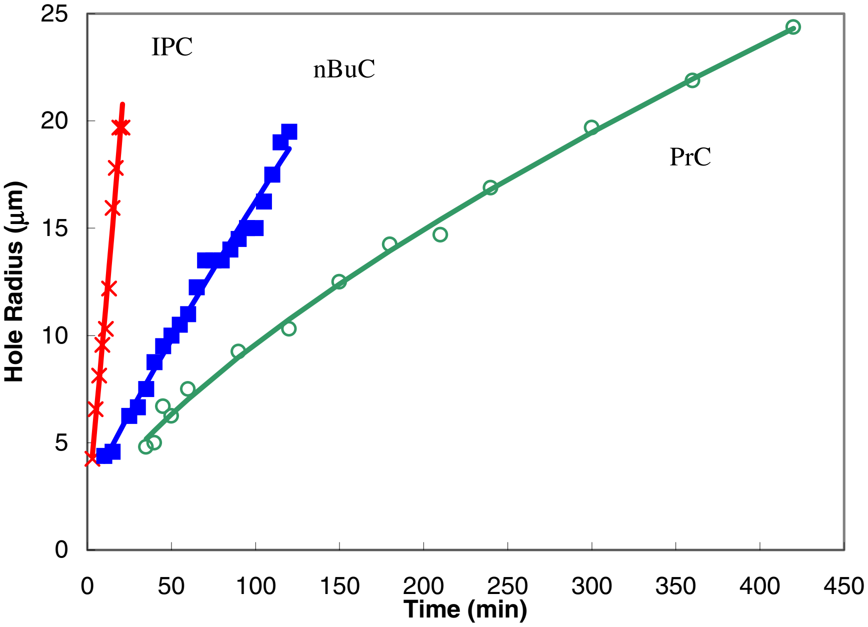

Figure 2. Hole radius vs. time for 16x IPC, BuC, PrC with 20x PtBA. The plot shows that PtBA demonstrates greater stability on propyl cellulose than n-butyl- and isopentyl cellulose, respectively.

As the chain length increased the rupture time decreases, as shown in Figure 2. The growth rate of the radii of the holes was faster as the chain length increased, also promoting faster dewetting In Figure 3, hole density increases as chain length increased. As chain length or hair size decreased, hole density decreased, holes grew at a slower rate, and rupture time increased; the shorter the chain length the more stable the film. The source of nucleation is likely due to both the nucleation and growth and spinodal dewetting mechanisms.

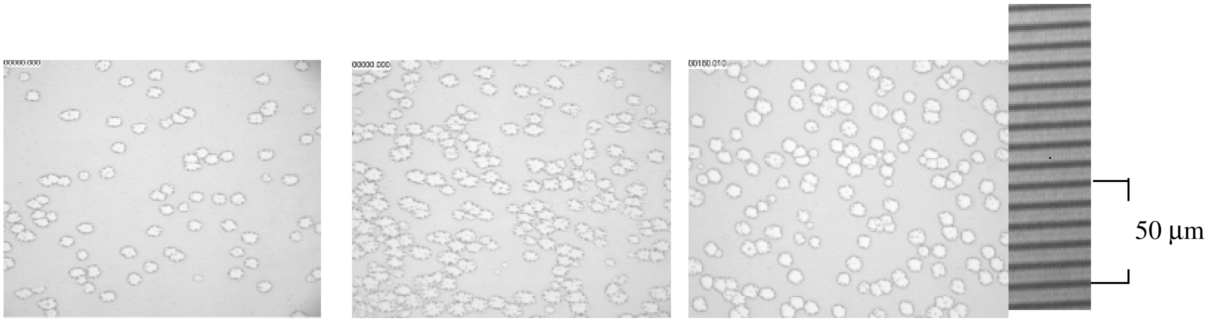

PrC
150 min

BuC
65 min

IPC
13 min

Figure 3. Pictures of Si/Cellulose Ether-16/PtBA-20/Air film annealed at 80°C, all with radii near 9μm and viewed with a 20x lens. The pictures show hole density increases, therefore stability decreases, as side-chain length increases.

Variable IPC Layer Thickness. 16x IPC/20x PtBA, 8x IPC/20x PtBA films were examined. Each film was annealed at 80°C and movies were produced until the films had completely dewet. Five holes were selected and monitored, and half their largest axis of the anisotropic holes, called the radius here, was measured as a function of time.

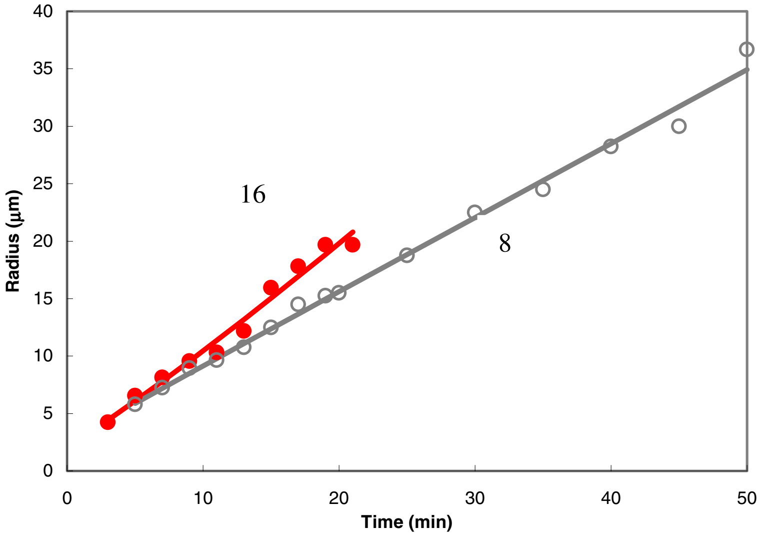

Figure 4. Hole radius vs. time for 16x, 8x IPC with 20x PtBA. The plot shows that PtBA demonstrates greater stability on eight layers than 16 layers of IPC.

As coating layer thickness increased the rupture time decreases as shown in Figure 4. The growth rate of the radii of the holes was faster as the coating layer thickness increased, also promoting faster dewetting. In Figure 5, hole density increases as film thickness increased. As thickness decreased, hole density decreased, holes grew at a slower rate, and rupture time increased; the thinner the layers of IPC the more stable the film. Thicker layers of IPC, such as the 16x coating layer appear to block the attraction from the substrate to the layers of PtBA therefore making the film less stable. The growth rate of the hole was carefully examined. 16x IPC/ 20x PtBA exhibited a slip boundary conditions; $r(t) \sim a\bullet(t + t_o)^{1.1 +/- 0.4}$. 8x IPC/ 20x PtBA also showed a slip boundary conditions; $r(t) \sim a\bullet(t + t_o)^{0.99 +/- 0.09}$.

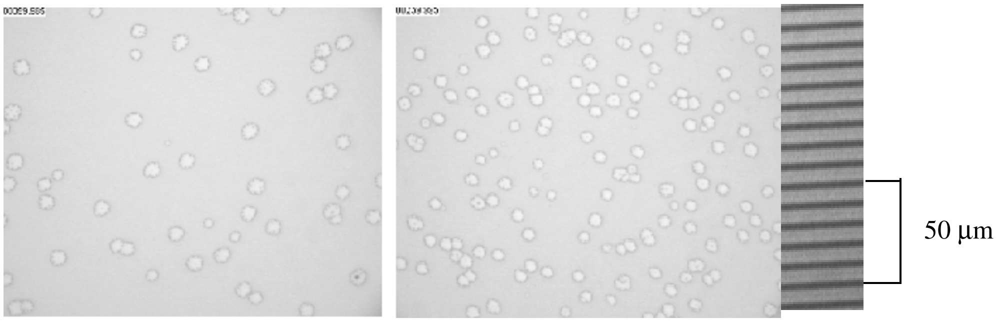

8
11 min

16
9 min

Figure 5. Pictures of Si/IPC/PtBA/Air films annealed at 80^{o}C, all with radii near 9µm and viewed with a 20x lens. The pictures show hole density increases, therefore stability decreases, as the number of IPC layers increase.

Variable BuC Layer Thickness. After annealing at 80^{o}C, 16x nBC/20x PtBA, 8x nBC/20x PtBA films were examined. Movies were made, and five holes were selected and monitored. Half the holes largest axis, called the radius again, was measured as a function of time.

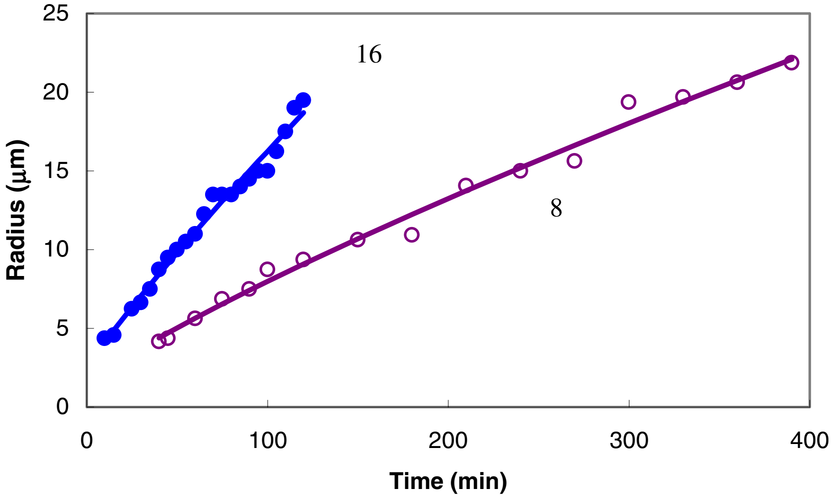

Figure 6. Hole radius vs. time for 16x, 8x nBC with 20x PtBA. The plot shows that PtBA demonstrates greater stability on eight layers than 16 layers of nBC.

As coating layer thickness increased the rupture time decreases, as shown in Figure 6. The growth rate of the radii of the holes increased with increasing thickness, increasing dewetting. In Figure 7, hole density increases as coating layer thickness increased. As BuC thickness decreased, hole density decreased, holes grew at a slower rate, and rupture time increased; the thinner the layers of nBC the more stable the film possible due to attraction between the substrate and the layer of PtBA. The growth rate of the hole was examined: 16x nBC/ 20x PtBA illustrated behavior intermediate between slip and stick boundary conditions; $r(t) \sim a\bullet(t + t_o)^{0.87 +/- 0.11}$. 8x IPC/ 20x PtBA also exhibited intermediate boundary conditions; $r(t) \sim a\bullet(t + t_o)^{0.81 +/- 0.10}$.

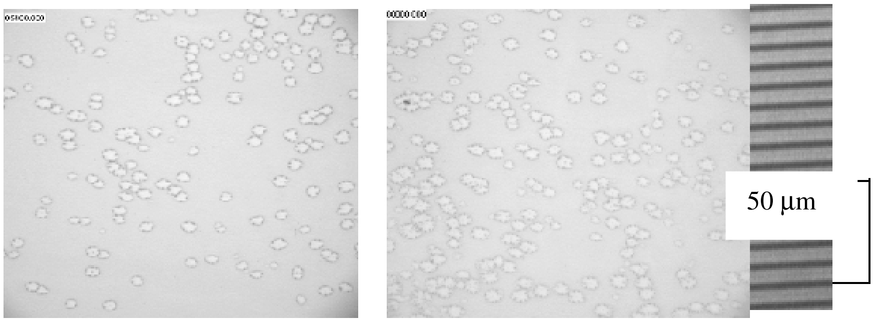

8
120 min

16
45 min

Figure 7. Pictures of Si/nBC/PtBA/Air films annealed at 80^{o}C, all with radii near 9µm and viewed with a 20x lens. The pictures show hole density increases, therefore stability decreases, as layers of nBC increase.

Variable PrC Layer Thickness. Finally, 16x PrC/20x PtBA, 8x PrcC/20x PtBA films were examined at 80^{o}C, and movies produced. Five holes were selected and monitored, half their largest axis, called the radius here, was measured as a function of time.

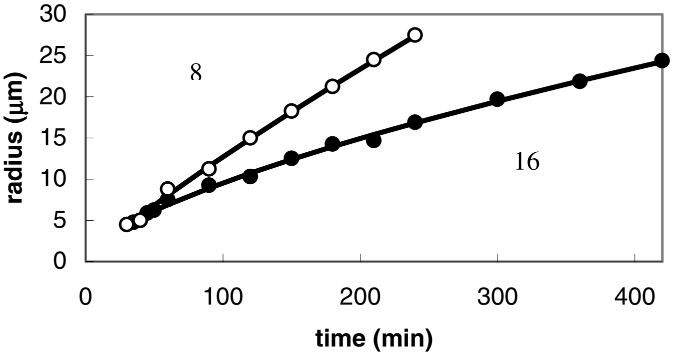

Figure 8. Hole radius vs. time for 16x, 8x PrC with 20x PtBA. The plot shows that PtBA demonstrates greater stability on 16 layers than eight layers of PrC.

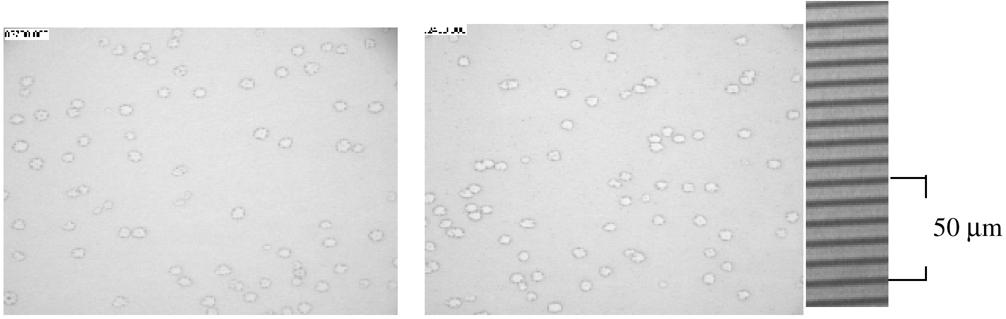

8
60 min

16
90 min

Figure 9. Pictures of Si/PrC/PtBA/Air films annealed at 80^{o}C, all with radii near 9µm and viewed with a 20x lens. The pictures show hole density remains near constant as layers of PrC increase.

As coating layer thickness increased the rupture time increases, as shown in Figure 8. The growth rate of the radii of the holes decreased with increasing PrC thickness, decreasing dewetting. In Figure 9, hole density remains near constant as film thickness increased. As thickness decreased, holes grew at a faster rate, and rupture time decreased; the thicker the layers of PrC the more stable the film. This observation is in stark contrast to both IPC and nBC. One possible explanation for this may lie in a cross-over from intermediate slip/stick boundary conditions to true stick boundary conditions. The growth rate of the hole was examined: For 16x nBC/ 20x PtBA, stick boundary conditions are observed; $r(t) \sim a\bullet(t + t_o)^{0.66 +/- 0.04.}$. In contrast, the 8x IPC/ 20x PtBA film exhibited behavior between slip and stick boundary conditions; $r(t) \sim a\bullet(t + t_o)^{0.86 +/-.06}$.

CONCLUSION

As film thickness increased for both butyl- and isopentyl cellulose, stability decreased; as the distances between the substrate and the polymer increases, the attractive forces between them decreased, promoting the formation of holes. However, with propyl cellulose, an increase in thickness stabilized the film, perhaps due to a crossover from intermediate slip/stick boundary conditions to true stick boundary condition achieved at 16x PrC/20x PtBA. An increase in chain length, or hair size, also had the effect of destabilizing the film. Although van der Waals forces are present, other stronger forces govern these films perhaps, causing them to dewet faster at longer chain lengths.

ACKNOWLEDGMENTS

The authors acknowledge the National Science Foundation, VT-Aspires and the Jeffress Memorial Trust for funding for this work. The authors additionally thank Lars Killian for his help with NMR, and GPC, Jianjun Deng for help with the optical microscope and heating stage, and Ana Pinto and Joe Polidan for assistance in wafer cleaning, and film preparation.

REFERENCES

[1] Martin, P.; Brochard-Wyart, F. Dewetting at Soft Interfaces. *Phys. Rev. Lett.* **1998**, *80*, 3296-3299.

[2] Kerle, T.; Yerushalmi-Rozen, R.; Klein, J.; Fetters, L.J. van der Waals stable thin liquid films: Correlated undulations and ultimate dewetting. *Europhys. Lett.* **1998**, *44,* 484-490.

[3] Brochard-Wyart, F.; Daillant, J. Drying of solids wetted by thin liquid films. *Can. J. Phys.* **1990,** *68,* 1084-1088.

[4] Khanna, R.; Jamell, A.T.; Sharma, A. Stability and Breakup of Thin Polar Films on Coated Substrates: Relationship to Macroscopic Parameters of Wetting. *Ind. Eng. Chem. Res.* **1996,** *35,* 3081-3092.

[5] Rengner, C.; Muller-Buschbaum, P.; Stamm, M.; Hinrichsen, G. Investigation and Retardation of the Dewetting on Top of Highly Viscuous Amorphous Substrates. *Macromolecules* **2000,** *33,* 8388-8398.

[6] Martin, P.; Szablewski, M. *Tensiometers and Langmuir-Blodgett Troughs,* 1999.

[7] Esker, A.R.; Mengel, C.; Wegner, G. Ultrathin Films of a Polyelectrolyte with Layered Architecture. *Science* **1998**, *280*, 892-895.

[8] Schaub, M.; Fakirov, C.; Schmidt, A.; Lieser, G.; Wenz, G.; Wegner, G.; Albouy, P.-A.; Wu, H., Foster, M. D.; Majrkzak, C.; Satija, S. Ultrathin Layers and Supramolecular Architecture of Isopentylcellulose. *Macromolecules* **1995,** *28,* 1221-1228.

[9] Wegner, G. Control of Moleucular and Supramolecular Architecture of Polymers, Polymersystems and Nanocomposites. *Mol. Cryst. Liq. Cryst.* **1993,** *235*, 1-34.

[10] Flory, P. J. "Statistical thermodynamics of mixtures of rodlike particles. 5. mixtures with random coils," *Macromolecules* **1978**, *11*, 1138-1141.

[11] Ballauff, M. "Compatibility of coils and rods bearing flexible side-chains," *J. Polym. Sci. Polym. Phys. Ed.* **1987**, *25*, 739-747.

[12] Brochard-Wyart, F.; Redon, C.; Brzoska, J.B. "Dewetting and Slippage of Microscopic Polymer Films", *Macromolecules* **1994,** *27*, 468-471.

Novel Methacrylate Copolymers: Photosensitive Adhesives and Hydrogels

Sheryl Kane*, Lars Kilian, Jeremy Lizotte, Vladimir Sinani, and Dr. Tim Long
Department of Chemistry, Virginia Polytechnic Institute and State University, Blacksburg, VA

* Department of Chemistry, Johns Hopkins University, Baltimore, MD

ABSTRACT

Photosensitive methacrylate copolymers were studied as candidates for biomaterials in the fields of hydrogel-based drug delivery and bioadhesives. An acid-labile hydrogel was synthesized and found to exhibit a 100-150% increase in water uptake in the presence of aqueous acid or a photoacid generator. A photocrosslinkable methacrylate adhesive was also synthesized, and peel testing determined that a time-dependent reduction in peel strength of up to 100% occurs upon irradiation with sunlight in the presence of a photoinitiation system.

INTRODUCTION

Acrylates and methacrylates have a wide variety of uses, ranging from artists' paint to fake nails. In addition, the biocompatibility of certain methacrylates, including 2-hydroxyethyl methacrylate (HEMA, Figure 1a) makes these monomers ideal for a number of medical applications. Currently found in contact lenses, bone cements, and dental composites, HEMA can also potentially be used in other biomaterials, including hydrogels for drug delivery[1] and adhesives for bandages and wound dressings[2].

Both fields require materials that do not irritate or poison the body, and that also possess specific mechanical properties—adhesives must be sticky and hydrogels must be absorb water well. Innovative materials in these areas exceed these basic requirements by providing additional characteristics beneficial to their applications. For example, an acceptable hydrogel would be any biocompatible material that absorbs water; an excellent hydrogel would be not only biocompatible and hydrophilic, but would also allow for controlled long-term drug release at a specific site within the body.

How can this be accomplished? Hydrogel-based drug delivery systems require very specific properties because of their application. First, the hydrogel should be biodegradable so that it will not require surgical removal[3]. Second, the hydrogel and all degradation byproducts must be biocompatible to prevent adverse reactions in the body. Third, the hydrogel must produce sustained, controlled drug release—sustained to make the system worth implementing, and controlled to prevent dose dumping and maintain drug concentration within the therapeutic window[1]. In addition, control over the location and initiation of drug release can also be important when localized drug delivery is preferable[4].

The composition and degree of crosslinking of a hydrogel, usually a copolymer of multiple biocompatible monomers, can be tailored to alter its release properties. For example, a study of lactoyl-functionalized poly(ethylene glycol) found that varying the molecular weight and number of lactoyl end groups resulted in different release profiles for the proteins studied[3]. The change in release profiles related directly to the calculated average mesh size of the hydrogels, the size of the holes or spaces formed by the network, which was controlled by the length of the polymer chains, the number of crosslinkable end groups, and the degree of swelling of the hydrogel. For mesh sizes much larger than the diameter of the protein being released, diffusion-controlled release was observed; however, for mesh sizes close to the diameter of the protein, the degree of swelling and network degradation strongly influenced protein release.

This clearly indicates that the mesh size of the hydrogel and its change over time with swelling and degradation are important in controlled drug release. One way to initiate release at a specific time and location within the body would therefore be to incorporate a pore-enlarging mechanism into the structure of the polymer, which could be accomplished easily by causing controlled degradation of the polymer.

Photoacid generation is one example of such a mechanism. Photosensitive compounds cause a variety of reactions upon exposure to light, including acid production and crosslinking, and many of these reactions can be used beneficially in biomedical applications. An acid-labile hydrogel that contains a photoacid generator (PAG) would begin to degrade and release drug upon exposure to light. This would be very beneficial in tumor treatment because the hydrogel could be implanted directly at the tumor site and then irradiated at the appropriate time to begin drug release. Local administration of the anti-tumor agent would ensure that the cancerous cells and surrounding tissue would receive the maximum possible dosage while systemic blood levels of the drug remained low, as most of the drug would remain close to the tumor site. Using such a hydrogel, higher doses of anti-cancer drugs could be administered with reduced systemic toxicity and side effects.

In this experiment, a HEMA-based methacrylate hydrogel with a novel crosslinking monomer was studied as a model drug delivery system to determine the effect of acid on degradation of the crosslinks. HEMA was chosen for its hydrophilicity, while the novel monomer, 2,5-dimethyl-2,5-hexanediol dimethacrylate (DHDMA, Figure 1b), was designed to possess two vinyl groups for crosslinking and two tertiary ester bonds that should be acid-degradable. As shown in Figure 2, the crosslinks formed by this monomer can be broken in the presence of acid—either from an external source, such as hydrochloric acid, or from a PAG such as diphenyliodonium nitrate (DPIN, λ_{max} = 226 nm, Figure 1c) impregnated into the hydrogel network itself; similar crosslinking agents have been shown to undergo the proposed degradation[5]. Upon degradation of the crosslinks, the mesh size of the hydrogel and mobility of the polymer chains should increase, leading to increased drug release. Network degradation also leads to increased water uptake and swelling as more space becomes available for water molecules to enter the system. Thus, water uptake can be used as an indicator of the relative degree of crosslinking of the hydrogel after exposure to acid.

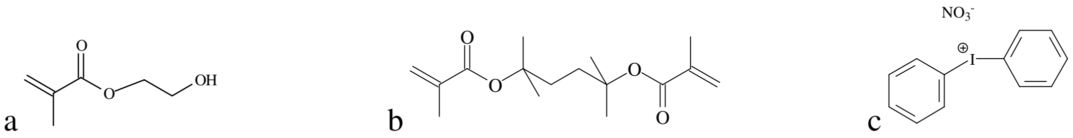

Figure 1: Structures of the hydrogel components: a) HEMA; b) DHDMA; c) DPIN.

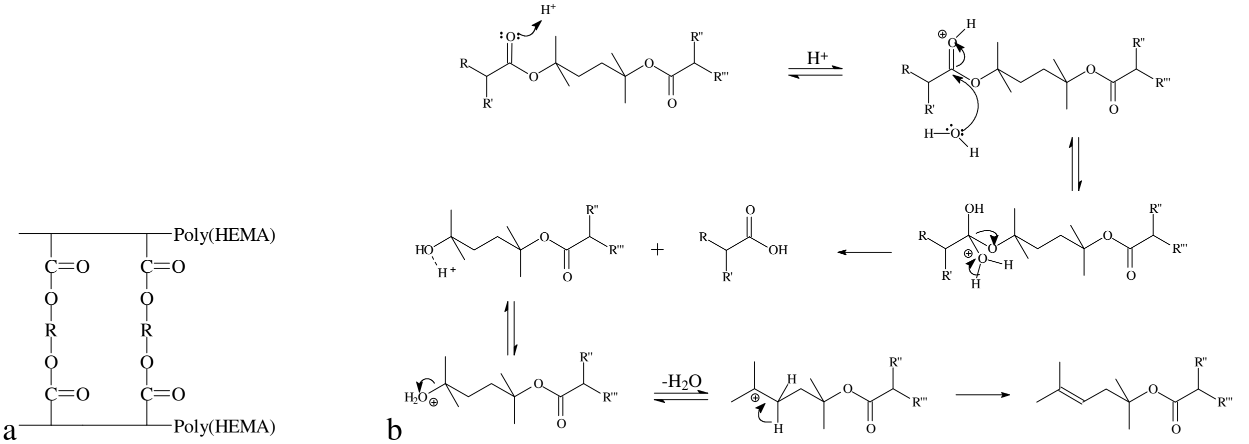

Figure 2: a) Schematic representation of the hydrogel; b) Proposed acid-catalyzed degradation mechanism of DHDMA. R, R', R'', and R''' represent chains of poly(HEMA) with other DHDMA crosslinks. The products of this reaction include a carboxylic acid, a tertiary alcohol or diol, and several vinyl or divinyl species, including 2,2',5,5'-tetramethyl-1,3-butadiene, a volatile conjugated hydrocarbon that should form favorably.

Another biomedical application of photosensitive polymers is the field of bioadhesives, compounds used to adhere bandages and wound dressings to human skin. An ideal pressure-sensitive adhesive (PSA) would be sticky for as long as the bandage was necessary, then "switch" to lose its tackiness just before removal. This type of PSA would eliminate the skin trauma now typically associated with bandage removal, particularly from patients with sensitive skin. One promising switching mechanism involves crosslinking polymers to raise their storage modulus above the Dahlquist Criterion, 10^5 Pa, the maximum storage modulus of an adhesive polymer[6]. Polymers with storage moduli below this value flow well and can wet substrates sufficiently to cause adhesion, but polymers with storage moduli above the Dahlquist Criterion are too stiff to be sticky.

Webster[2,7,8] takes advantage of this concept in his work on photoswitchable adhesives, specifically visible-light-initiated crosslinking of acrylate/methacrylate copolymers. Acrylates are widely used as adhesives in both medical and non-medical applications due to their inherent stickiness, good mechanical properties, and resistance to weathering[6]. Webster built upon these characteristics by incorporating pendant vinyl groups into the polymer structure, providing the potential to crosslink upon initiation. Using vinyl-functionalized copolymers of HEMA, *n*-butyl acrylate (BA, Figure 3a), itaconic anhydride, and 2-ethylhexyl methacrylate with Irgacure 784 as a visible photoinitiator, he has reported photoinduced adhesive switching of up to 86%, as calculated by the formula

$$\text{Percent switch} = [1-(P_e/P_u)]*100 \qquad (1)$$

where P_e represents the peel strength of a sample exposed to light and P_u represents the peel strength of an unexposed sample[2]. These results indicate that crosslinking acrylate/methacrylate copolymers can in fact significantly reduce the peel strength (tackiness) of the polymers, suggesting that the concept should be further explored.

This experiment aimed to do just that. Based on the same ideas, this study involved a simpler polymer, a different synthetic scheme, and a different photoinitiator. Again, the goal was to synthesize a high-molecular-weight, highly adhesive polymer containing pendant crosslinkable vinyl groups, but just two monomers were used: BA and HEMA. BA is a sticky and biocompatible monomer. As previously mentioned, HEMA is also biocompatible[9], and its bifunctionality makes it very versatile. The vinyl group allows for free radical polymerization, while the primary alcohol can be used as a nucleophile in a number of reactions, including esterification with acryloyl chloride (AC, Figure 3b)—the second step of the adhesive synthesis.

Like Webster's work, the photoinitiation system in this study involved a visible-light-active compound, but the components were chosen for other important characteristics as well. The photoinitiator, camphorquinone (CQ, Figure 3c), is currently widely used in dental applications, and its use within the body is FDA-approved. CQ requires a tertiary amine as a co-catalyst, and dimethylaminoethyl methacrylate (DMAEM, Figure 3d) was selected because it possesses both the tertiary amine and a vinyl group, which can be incorporated into the polymer backbone to avoid leaching into the body.

Figure 3: Structures of the adhesive a) comonomer, BA, and b) functionalization group, AC, and the photoinitiating system c) initiator, CQ, and d) co-catalyst, DMAEM.

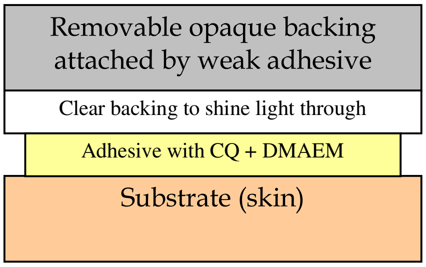

Figure 4: An ideal photoswitchable bandage.

The design of an ideal bandage incorporating the photosensitive polymer is shown in Figure 4. Though similar to current bandages, this dressing requires one additional component, which would have minimal contact with the patient's skin. To prevent switching before the desired removal time, an opaque top layer would completely cover the photosensitive adhesive. This layer, attached by a fairly weak adhesive (so that it could be peeled away without disturbing the rest of the bandage) would be pulled off just before the desired removal time, causing light exposure through the transparent backing.

EXPERIMENTAL

Materials

HEMA, BA, and DMAEM (all Aldrich) were purified by column chromatography to remove inhibitor and stored under N_2 at –5 °C. Triethylamine (TEA, Aldrich) was also stored under N_2 at –5 °C. AC, DPIN, CQ, 2,5-dimethyl-2,5-hexanediol, methacryloyl chloride and 2,2'-azobisisobutyronitrile (AIBN) were stored at –5 °C and used as received from Aldrich. HPLC-grade tetrahydrofuran (THF, Burdick & Jackson) was used as received for all free-radical polymerizations and distilled over sodium to remove water for all acid chloride reactions. 95% ethanol (EtOH, Aager) was used as received. Distilled H_2O was used for all precipitations.

Methods

Synthesis of acrylate-functionalized HEMA/BA (AFHB). The preparation of AFHB involved three steps, shown in Figure 5: 1) free-radical polymerization of 10 mol% HEMA/90 mol% BA; 2) reaction of the HEMA/BA with AC; and 3) purification of the product to remove excess acid chloride and TEA-HCl salt.

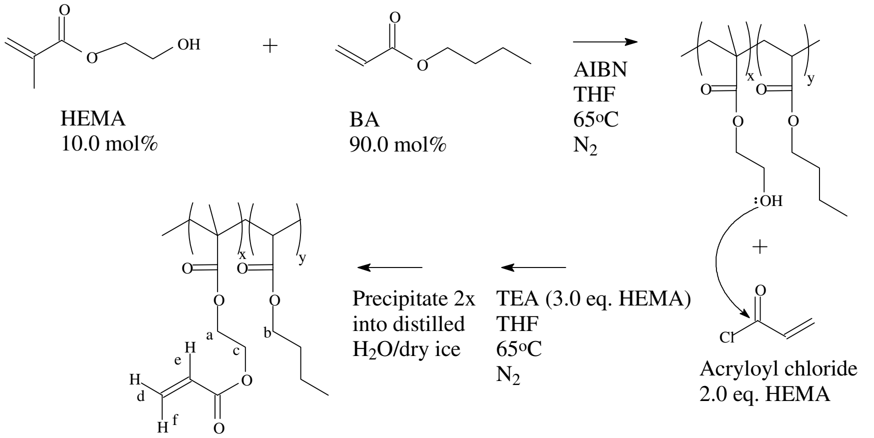

Figure 5: Synthesis and purification of AFHB. Lowercase letters a-f label protons used for NMR characterization.

First, 1.0 eq. HEMA and 9.0 eq. BA were syringed into a flask containing AIBN (0.5 wt% of monomers) and THF (50 wt% of total reaction). The mixture was sparged with N_2 for 5 minutes and heated to 65 °C for 24 hours with stirring. The product was carried on to the second step without purification or exposure to air. Additional THF (approximately four times the amount added in the first step) was added to decrease the viscosity of the solution, which was stirred to homogeneity. TEA (3.0 molar eq. of HEMA) was then syringed into to the reaction flask, which was placed into an ice bath. Finally, AC (2.0 molar eq. of HEMA) was syringed dropwise into the flask, and the mixture was allowed to react with stirring for 24 hours. To purify the product, it was precipitated into a beaker of distilled H_2O and dry ice, redissolved in THF, and reprecipitated into H_2O/dry ice, then dried in a vacuum oven for 24 hours.

NMR with a Varian Unity 400 produced peaks at δ4.0 and δ3.8 corresponding to the methylene protons a+b and c, respectively (see Figure 5 for labeling). These were used to determine the HEMA:BA molar ratio, 11:89. After functionalization, the c peak shifted from δ3.8 to δ4.2, and peaks from the vinyl protons d, e, and f appeared at δ5.8, δ6.2, and δ6.4, respectively. The average of the integration of the vinyl protons was used to calculate the conversion, 60-80%, of the HEMA alcohol to an ester.

Peel testing sample preparation. A stock solution of 0.0251 g CQ and 0.0275 mL DMAEM in 10.0 mL THF was prepared. 0.1 g AFHB was placed on one end of a glass microscope slide (VWR, 25 x 75 mm, polished with Kimwipes). For samples containing photoinitiator, 0.4 mL of CQ/DMAEM solution was syringed onto the end of the slide such that every slide contained 1.0 wt% each of CQ and DMAEM[10]. The samples were placed in chambers completely covered with aluminum foil to block out light and the THF was allowed to evaporate for 18 hours. A

Mylar strip (30 x 100 mm) was placed on each slide as shown in Figure 6, and 35 lbs. of weight were placed on the samples for 45 minutes.

Exposure to light. The samples were irradiated through their microscope slide backings by one of two methods. For 487 nm light, samples were placed 0.5" from the tip of an Oriel photoreactor with a mercury lamp source and a 487 nm light-pass filter and irradiated for 10, 20, or 30 minutes. For a broader spectrum, samples were exposed to direct sunlight with an intensity of 2.55-4.26 mW/cm^2, measured using an Oriel Instruments Goldilux UV-A Photometer (Model 70234) for 5, 10, or 20 minutes. Peel test results were obtained within two hours of exposure.

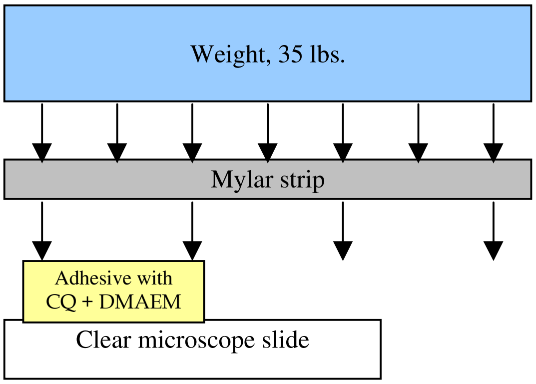

Figure 5: Preparation of peel testing samples.

Peel testing. An Instron 4411 Universal Testing Rig was used to perform an ASTM Method D903 180° peel test at a peel rate of 5"/minute at room temperature. Tests were performed in duplicate and the results are reported as an average of the data obtained.

DHDMA synthesis. 1.0 eq. 2,5-dimethyl-2,5-hexanediol was reacted with 2.0 eq. methacryloyl chloride in dichloromethane (Burdick & Jackson) at 0 ºC using TEA as an acid sponge. The product was purified three times by column chromatography.

Hydrogel coating preparation. 97.0 mol% HEMA (4.37 mL) was mixed with 3.0 mol% DHDMA (0.25 mL) and AIBN (0.0251 g, 0.5 wt% of monomers). Either 17.7 v/v% EtOH (1.0 mL) or DPIN (0.0501, 1.0 wt% of monomers) dissolved in 1.0 mL EtOH was added to the monomer mixture, which was then sparged for 5 minutes with N_2. To prepare coatings, pre-cleaned glass microscope slides were wiped with Kimwipes and placed in an airtight chamber fitted with a gas line and rubber septum. To remove oxygen, the chamber was purged with N_2 for 20 minutes, then filled with N_2 for 10 minutes. 0.5 mL monomer mixture was then syringed onto each slide and the chamber was placed in a water bath at 65 ºC for 4 hours. For slides containing DPIN, the entire chamber was wrapped in aluminum foil to prevent exposure to light. The coatings (attached to microscope slide backings) were dried in the vacuum oven at room temperature for 18 hours prior to use in water uptake studies.

Water uptake studies. The coatings were weighed upon removal from the drying oven to determine the dry weight (w_d) and, if applicable, exposed to unfiltered light from a mercury lamp source in the Oriel photoreactor. Each sample was placed in a 60-mL sample jar containing 50 mL of either distilled water or 1.0 M HCl. The sealed jars were immersed in a water bath at 60 ºC and weighed at regular intervals to determine the water uptake of the hydrogel. Before weighing, each coating and slide was patted dry with a Kimwipe[11]. The degree of swelling (DS) at a given time was determined by the equation

$$DS = (w_s - w_d)/w_d \tag{2}$$

where w_s represents the swollen weight of the hydrogel at that time[4]. In all cases, the wet and dry weights of the polymer itself were calculated by subtracting the total weight of the hydrogel and the slide minus the weight of the slide as determined before preparation of the hydrogel coating.

RESULTS AND DISCUSSION

As the crosslinks of a crosslinked polymer degrade, the polymer chains gain mobility and the entire network becomes more flexible. In the case of a hydrogel immersed in water, this should result in an increase in the ability of the hydrogel to absorb water due to increased space within the network for the water molecules. Thus, it would be expected that if the ester bonds in DHDMA are in fact acid labile, a HEMA/DHDMA coating exposed to acid would absorb more water and attain a greater equilibrium degree of swelling (DS_{eq}) than a coating exposed only to water.

Exposure to acid could occur through one of two methods: immersion in an acid solution (1.0 M HCl), which at any given time within the experiment would only expose the part of the hydrogel that had already taken up the acid solution, or impregnation with DPIN followed by exposure to light. In this case, assuming that the coating was thin enough to allow even exposure throughout the hydrogel, every bond in the hydrogel would be exposed to acid at the same time. The difference in exposure of internal ester bonds could result in a different method of degradation (bulk as opposed to surface), which could alter the kinetics of water uptake; however, regardless of the type of exposure, both acid-exposed hydrogels should exhibit a greater DS_{eq} than a coating exposed only to water. In addition, a hydrogel impregnated with DPIN but not exposed to light should exhibit identical a water uptake profile to that of the hydrogel without DPIN that was exposed only to water.

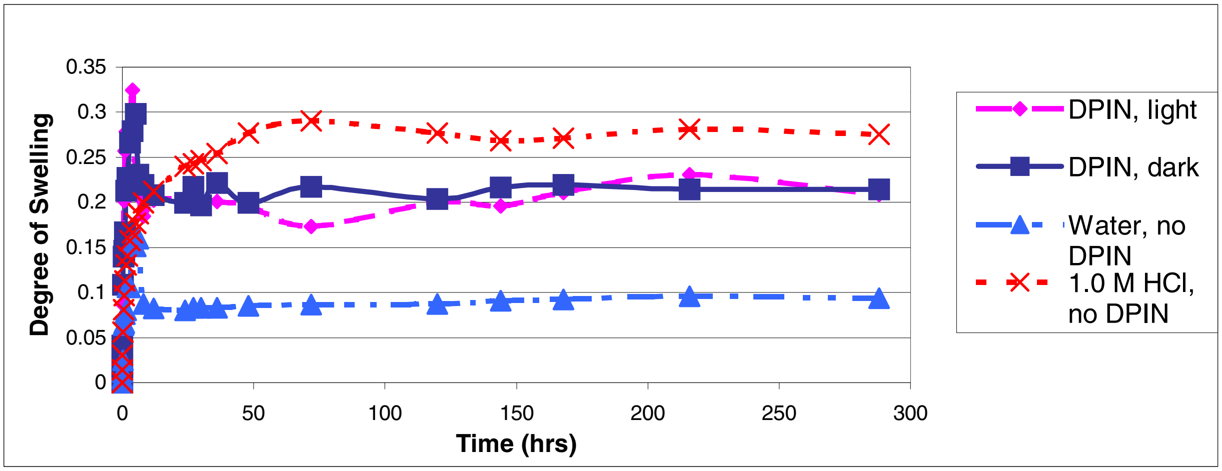

Figure 7: Hydrogel water uptake results as a function of time.

Figure 7 shows the results of the water uptake study, which was repeated three times with similar results (data not shown). A comparison of the water uptake of the hydrogel in water to the hydrogel in acid clearly the effect of the acid: DS_{eq} for the hydrogel in 1.0 M HCl is nearly three times that of DS_{eq} for the hydrogel in water. Similarly, DS_{eq} for the hydrogel with DPIN exposed to light is greater than twice that of DS_{eq} for the hydrogel in water. This strongly suggests that the ester bonds in DHDMA are indeed acid labile and can be broken under these conditions.

However, while the hydrogels exposed to acid did in fact attain a greater DS_{eq} than those exposed only to water, the DPIN-containing hydrogel kept in the dark exhibited water uptake kinetics nearly identical to those of the DPIN-containing hydrogel that was exposed to light. This result suggests one of three conclusions: first, the stock DPIN had already generated acid before synthesis of the coatings, such that acid was incorporated into the hydrogel network along with the DPIN; second, the DPIN-containing hydrogels meant to remain in the dark were inadvertently exposed to light; or third, a light-independent mechanism is responsible for the network degradation evidenced by the elevated DS_{eq} of the hydrogel left in the dark. If the third is true, then the light-independent mechanism was likely also responsible for the degradation of the hydrogel exposed to light, as the uptake profiles of the two are nearly identical.

Interestingly, all three of the samples in water reach equilibrium at nearly the same time, between eight and twelve hours into the study, and all three seem to uptake water to some sort of breaking point four to five hours after initial water exposure, then collapse and lose some water to reach equilibrium. Only the hydrogel in aqueous HCl exhibits different behavior, taking up water non-linearly until reaching equilibrium without collapse around 48 hours after exposure. This again suggests that DPIN does not act on the hydrogel by the same mechanism as HCl, or that there is a secondary mechanism at work, but the DPIN mechanism could not be determined in this study.

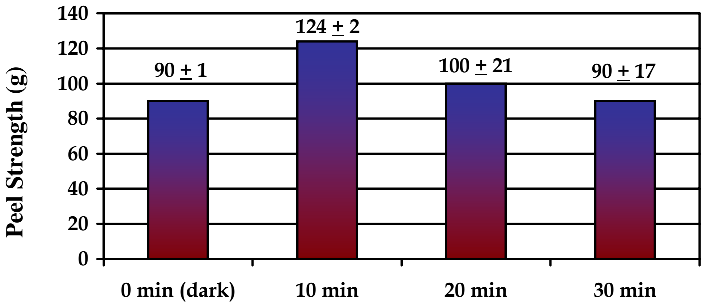

Figure 8: Peel strengths of adhesives exposed to 487-nm light.

The AFHB copolymer peel testing results are more conclusive, though likewise somewhat surprising. It was qualitatively observed that higher molecular weight polymers were stickier. Therefore, an AFHB with an M_w of 63,500 g/mol and M_w/M_n of 3.21 (determined by GPC with a Waters SEC using THF as a solvent and polystyrene standards) was used for all peel testing. In addition, this polymer exhibited a T_g of -43 ºC (quenched sample measured by DSC on a Perkin Elmer Pyris 1 instrument under helium at a heating rate of 20 ºC/min), which falls well within the range accepted for adhesive polymers.

As Figure 8 illustrates, exposing AFHB samples containing CQ and DMAEM to 487 nm light for 10-30 minutes did not substantially alter the peel strength of the copolymer, given the experimental error inherent to peel tests and the fact that only two data points were obtained for each exposure time. Since CQ is widely known react upon exposure to light around 470 nm, this result is unexpected. However, several factors could account for the observed lack of crosslinking. First, the light from the photoreactor may have been at slightly too high a wavelength—λ_{max} for CQ occurs at 468 nm, and 487-nm light was being used. Second, light from the photoreactor may not have been sufficiently intense, as the filter does block about 50%

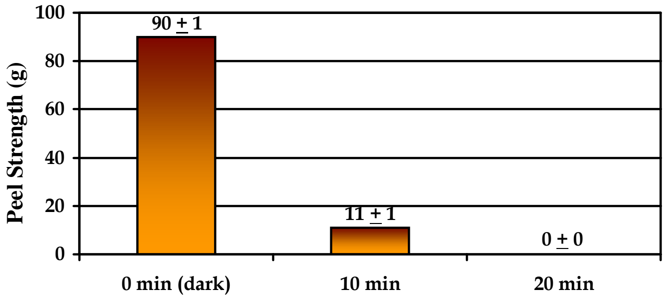

Figure 9: Peel Strengths of adhesives exposed to sunlight.

of the intensity. Lastly, irradiation occurred through the glass microscope slide, which may have also blocked some of the light.

The first or second option is more likely, as the results of exposure to sunlight, shown in Figure 9, indicate. P_u for AFHB containing CQ and DMAEM was 90 g; P_e after 10 minutes of exposure through the glass microscope slide, P_e dropped to 11 g, 88% switching. After 20 minutes, 100% switching was observed. Though further work must be performed to elucidate the switching kinetics and optimal conditions, particularly at body temperature, these preliminary results are reproducible and extremely encouraging.

CONCLUSIONS

The water uptake of a model hydrogel drug delivery system was studied and found to increase significantly upon exposure to acid as the result of network degradation from acid-catalyzed ester bond cleavage. The addition of a photoacid generator, DPIN, also resulted in a significant increase in water uptake by the hydrogel. However, since DPIN-containing hydrogels that were and were not exposed to light exhibited identical water uptake profiles that were significantly different from that of a hydrogel exposed to aqueous HCl, it is clear that the major mechanism of DPIN-induced degradation/water uptake does not occur via the expected light-induced pathway. Further studies must be performed to determine the cause of the unusual behavior observed.

Peel testing of 10:90 HEMA/BA functionalized with acryloyl chloride in the presence of a CQ/DMAEM photoinitiation system produced very encouraging results. Blue light exposure must be further examined using a 468-nm filter and a higher-intensity light source, with an appropriate instrument (such as the Oriel Instruments Goldilux Photometer, Model 70235) available to measure visible light intensity. However, sunlight caused 88% switching after 10 minutes and 100% switching—complete loss of adhesive properties—after 20 minutes of exposure, which fully meets the goals of the project. Clearly, photoinitiated crosslinking of an acrylate copolymer containing pendant vinyl groups is a viable method of significantly decreasing polymer peel strength.

ACKNOWLEDGEMENTS

Many thanks to the NSF Summer Undergraduate Research Program (SURP) for providing the opportunity and funding to perform this research. Many thanks as well to Dr. Timothy Long, Vicki Long, and all members of the Long research group for providing invaluable assistance. Thanks to the Virginia Polytechnic Institute and State University's Chemistry Department, Dr. Tom Ward, and Angie Flynn for hosting the SURP program and lending significant administrative aid.

REFERENCES:

[1] Meyvis, T.K.L.; De Smedt, S.C.; Demeester, J. Influence of the Degradation Mechanism of Hydrogels on Their Elastic and Swelling Properties during Degradation. *Macromolecules* **2000,** *33,* 4717-4725.

[2] Boyne, J.M.; Millan, E.J.; Webster, I. Peeling performance of a novel light switchable pressure-sensitive adhesive. *Int. J. Adh. Adh.* **2001,** *21,* 49-53.

[3] Lu, S.; Anseth, K.S. Release Behavior of High Molecular Weight Solutes from Poly(ethylene glycol)-Based Degradable Networks. *Macromolecules* **2000,** *33,* 2509-2515.

[4] Andreopoulos, F.M.; Beckman, E.J.; Russell, A.J. Light-induced tailoring of PEG-hydrogel properties. *Biomaterials* **1998,** *19,* 1343-1352.

[5] Ogino, K.; Chen, J.S.; Ober, C.K. Synthesis and Characterization of Thermally Degradable Polymer Networks. *Chem. Mater.* **1998,** *10,* 3833-3838.

[6] Pocius, Alphonsus V. *Adhesion and Adhesives Technology: An Introduction.* Hanser Gardner Publications, Inc., Cincinnati: 1997.

[7] Webster, I. The development of a pressure-sensitive adhesive for trauma-free removal. *Int. J. Adh. Adh.* **1999,** *19,* 29-34.

[8] Webster, I. Recent developments in pressure-sensitive adhesives for medical applications. *Int. J. Adh. Adh.* **1997,** *17,* 69-73.

[9] Kehe, K.; Reichl, F.X.; Durner, J.; Walther, U.; Hickel, R.; Forth, W. Cytotoxicity of dental composite components and mercury compounds in pulmonary cells. *Biomaterials* **2001,** *22,* 317-322.

[10] Svaldi Muggli, D.; Burkoth, A.K.; Keyser, S.A.; Lee, H.R.; Anseth, K.S. Reaction Behavior of Biodegradable, Photo-Crosslinkable Polyanhydrides. *Macromolecules* **1998,** *31,* 4120-4125.

[11] Monleon Pradas, M.; Gomez Ribelles, J.L.; Serrano Aroca, A.; Gallego Ferrer, G.; Suay Anton, J.; Pissis, P. Interaction between water and polymer chains in poly(hydroxyethyl acrylate) hydrogels. *Colloid Polym. Sci.* **2001,** *279,* 323-330.

Design, Fabrication, and Testing of Membrane Electrode Assemblies Containing Novel Ion Containing Copolymers

Jennifer A. Leeson*, Michael A. Hickner, and James E. McGrath
Virginia Polytechnic Institute and State University
Materials Research Institute
Department of Chemistry
Blacksburg, VA

* Department of Chemical Engineering, West Virginia University, Morgantown, WV

ABSTRACT

Sulfonated poly(arylene ether sulfone)s (BPSH) are high performance polymers that have been developed over the past several years at Virginia Tech.[1] These polymers are synthesized by direct copolymerization of a controlled concentration of sulfonated monomers. They are being investigated as proton exchange membrane (PEM) in fuel cells due to their excellent physical properties. Nafion® is currently the industry standard PEM, but these novel polymers have certain improved characteristics, including compatibility with higher temperature additives, lower methanol permeability and potentially lower cost.

The main objective of this research was to fabricate an entire membrane electrode assembly (MEA) from these novel ionic copolymers. In past fuel cell research, attempts have been made at using sulfonated poly(arylene ether sulfone)s (BPSH) for the ion exchange membrane with Nafion-based electrodes. Using dissimilar polymers in the membrane and electrode caused both poor adhesion and performance problems at the membrane-catalyst interface. By making the entire membrane electrode assembly out a single copolymer, these problems can be avoided. In this project, both the application of the electrode and fuel cell testing of the MEA were explored.

Catalyst “ink” was made by using prepared BPSH copolymer dispersions and a commercially available carbon supported platinum electro-catalyst. The dispersions consisted of the copolymer dispersed in a 50/50 IPA/H_2O mixture. The BPSH electrodes were applied using a cast electrode methodology. The membrane was held flat onto a vacuum plate and the electrode was then applied slowly, allowing it to air dry between coats. This provided consistent application across the active area and also created a robust electrode that survived subsequent boiling treatments.

Once the electrode was applied successfully to the membrane, the MEAs were tested in a fuel cell. The experiments were run at 75°C under atmospheric pressure with hydrogen and air. The polymer: catalyst ratio was varied in order to determine its effect on the performance of the cell. The highest performance was obtained with a 1: 2.5 weight ratio. By testing Nafion MEAs and the BPSH MEAs, it was found that BPSH performed comparably to Nafion. This study successfully demonstrated a viable MEA composed completely of BPSH polymers for the very first time.

INTRODUCTION

Economic and environmental issues are forcing industry to explore alternative energy sources for vehicles and electronic devices. Much effort is being put into fuel cell research because they hold the promise of high energy density, low environmental impact, and broad applicability.[2] As shown in Equation 1, hydrogen is the main source of fuel for high-performance applications with water being the only product.

$$H_2 + O_2 \Rightarrow H_2O + energy \tag{1}$$

These attributes make the hydrogen fuel cell a practical replacement for many power sources that are inefficient and environmentally unfriendly.

The basic functional unit of the fuel cell is the membrane electrode assembly (MEA). The MEA is the loci where the electrochemistry occurs to produce electricity from hydrogen and oxygen. The MEA consists of the polymer membrane (approximately 150µm thick) with an electrode (5-20 µm) adhered to either side. The electrode contains the platinum electro-catalyst dispersed on carbon black with a polymer binder. Several properties of the electrode such as porosity (transport) and adhesion (durability) to the membrane are critical to an efficient and durable fuel cell.

Very few polymers have been used extensively in fuel cell applications; the standard for the last thirty years has been Nafion®, a tetrafluoroethylene-based copolymer (see Structure 1).

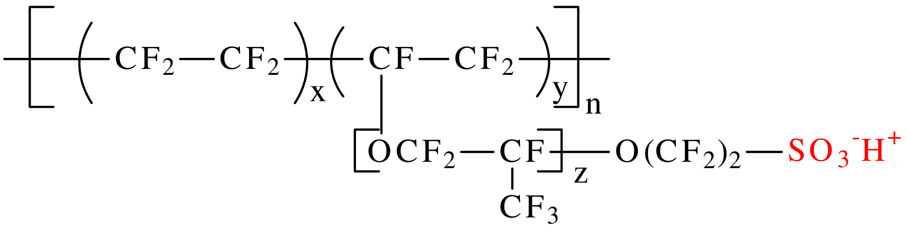

Structure 1: The Repeat Unit of Nafion®

As fuel cells become commercially important, new polymers are needed that are more cost effective and have better properties than Nafion. Recently, there has been renewed interest in developing new proton-exchange polymers. However, any promising new ionic polymer that displays desirable membrane properties must be adaptable to simple MEA fabrication using current techniques.

A new family of proton exchange polymers for use in fuel cells has been developed.[1] These polymers are based on the direct polymerization of monomers containing sulfonic ion conducting sites, which are required for proton exchange. Internally, these sulfonated poly(arylene ether sulfones) have been termed biphenol sulfones (BPSH-XX), where the XX represents the relative level of sulfonation. A generalized structure of the BPSH-XX copolymers is shown in Structure 2.

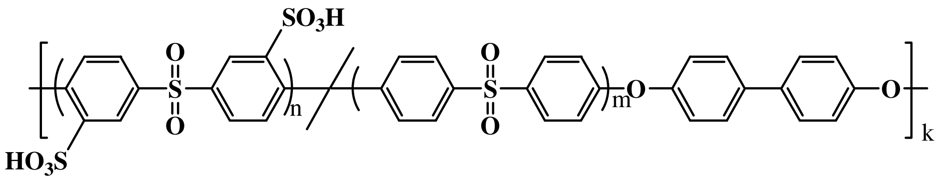

Structure 2: Structure of Novel BPSH-XX Copolymers

It has been determined that sulfonation levels between 30 and 60 percent are optimal for use in fuel cells. To take advantage of the promising physical properties displayed by the BPSH-XX membranes, they must be fabricated into MEAs for use in fuel cells. In past research attempts have been made to apply the sulfonated poly(arylene ether sulfone)s as the ion exchange membrane with Nafion electrodes. This approach did not work well. The electrodes did not adhere to the BPSH membrane which resulted in a fragile assembly.

It can be predicted from the chemical structures of the polymers that Nafion and BPSH-XX would most likely not be compatible. Nafion is a fluorine-based copolymer with the sulfonate groups located on flexible side chains, while BPSH has its sulfonate groups directly attached to an aromatic ether backbone.

This research focuses on the fabrication and testing of MEAs composed entirely of BPSH copolymers. A standardized procedure was developed for the fabrication of these MEAs. The electrodes were cast from catalyst ink, which was composed of a platinum electro-catalyst supported on carbon, the desired BPSH-XX dispersed in an alcohol/water solvent, and additional water. The platinum is necessary for the electrochemical reactions at the anode and cathode to oxidize H_2 to H^+ and reduce the O_2, as shown in Scheme 1. The polymer acts as a proton transport medium and binder. The electrodes were applied to the membrane using a painting technique.[3] It is important that the electrode be strongly adhered to the membrane without cracking on the electrode surface or damage to the membrane.

$$\begin{aligned} &Anode: && H_2 \Rightarrow 2H^+ + 2e^- \\ &Cathode: && \tfrac{1}{2}O_2 + 2H^+ + 2e^- \Rightarrow H_2O \end{aligned}$$

Scheme 1: Fuel Cell Electrochemical Reactions

Testing the performance of these membranes in a fuel cell is a very important step in verifying the feasibility of using new polymers in both the proton exchange membrane and the electrode. It is necessary to determine the effects of different BPSH-XX membranes and electrodes. Testing gives concrete evidence that the MEA behaves as predicted and the standardized procedure can then be used in further fuel cell studies.

EXPERIMENTAL

Dispersion

Approximately 0.50 g of acid form BPSH-XX was weighed into a clean, 20ml vial. Typically, 20% polymer solutions in N,N-dimethyl acetamide were utilized due to viscosity considerations. The solutions were allowed to stir overnight.

To form the polymer dispersion, a 50/50 mixture (by weight) of IPA/H_2O was added dropwise to the 20% BPSH-XX solution with rapid stirring and little heat until a homogenous dispersion was formed.[4] The dispersion was visually inspected for solids or discoloration. The final product was transparent yellow (the intensity depending on the concentration of BPSH-XX). After making the dispersion, the polymer concentration was determined. Three aluminum cups were weighed while empty and then three drops of dispersion was added to each. The foil cups were then weighed again and placed on a hot plate. They were heated until the polymer dried completely and then weighed a final time. The percentage polymer was calculated using Equation 2.

$$\%\ polymer = \frac{dry\ weight - empty\ weight}{wet\ weight - empty\ weight} \qquad (2)$$

Catalyst Ink

The catalyst ink contains three major components. They include deionized water, BPSH-XX polymer dispersion, and a carbon supported platinum electro-catalyst. The catalyst purchased from E-TEK (De Nora North America) is 20% platinum by weight on Vulcan XC-72R carbon black.

Both platinum loading per square centimeter and the electrode area were determined before the ink was mixed. From these two parameters, the amount of catalyst needed was calculated. A polymer: catalyst weight ratio was also chosen from 1:2.5 to 1:6. Using this ratio and the percentage of copolymer in the dispersion, the amount of polymer dispersion needed in the ink can also be calculated.

After calculating the ratio of components in the ink, they were weighed into a small vial. The catalyst was added first, including an extra 20% due to losses. Deionized water was added next, to avoid combustion of the catalyst. Although the amount of water added is not specific, it was enough to liquefy the mixture and facilitate painting. Next, the BPSH-XX polymer dispersion was added in the calculated amount. The ink was stirred for 10 minutes and sonicated for twenty before it was cast onto the polymer electrolyte membrane.

Electrode Application

The membrane was laid directly onto a vacuum plate, using a silicone rubber sheet to protect the polymer membrane and to seal the vacuum. The silicone sheet had a square hole cut in it, slightly larger than the size desired for the electrode, so that painting could be performed. The vacuum was maintained during the painting process so that the membrane was kept flat and an infrared (IR) lamp was used to gently dry the ink. The electrodes were painted slowly, with approximately five minutes drying time in between each coat. The direction of painting was alternated for each coat in order to assure even application across the entire electrode area. After the paint is applied, the membrane is allowed to dry completely under the IR lamp for 20 minutes. After drying, the membrane was turned over and the procedure was repeated. Once both electrodes were applied, the membrane was boiled in 1M H_2SO_4 for 1.5 hours. Then the MEA is boiled in deionized water for 1.5 hours to wash off any residual acid. This converts the membrane from the sodium form to the acid form. This boiling also serves as a qualitative adhesion test.

Fuel Cell Testing

Fuel cell tests were run at atmospheric pressure with a cell temperature of 75°C.[5] Hydrogen and air were humidified before entering the anode and cathode, respectively. The fuel cell hardware purchased from Fuel Cell Technologies employs a $5cm^2$ electrode active area with serpentine flow fields. The MEA was sealed in the hardware with a silicone gasket and gas diffusion backings on either side. Double sided ELAT v2.11 was used on the anode and single sided ELAT v2.22 was used on the cathode. The temperature was controlled at the hydrogen and air humidification points with typical temperatures for these being 95°C for hydrogen and 90°C for air. The temperature is also measured at the anode and cathode inlets, average values for these were 50°C for hydrogen and 82°C for air. Using a hydrogen stoichiometry of approximately 3 and an oxygen stoichiometry of 2, the flow rates used for all tests were 109 sccm for hydrogen and 192 sccm for oxygen. A voltage was applied across the cell to generate a current. This voltage was varied from 1 to 0 Volts and the current was measured in order to generate a polarization curve. This polarization curve was then used to characterize the performance of each MEA.

RESULTS AND DISCUSSION

MEA Fabrication

A $5cm^2$ active area and platinum loading of 1mg platinum/cm^2 was used in a typical MEA fabrication. Perhaps one of the most important variables in electrode fabrication is the ratio of catalyst to polymer in the electrode. This ratio was varied between 1: 2.5 and 1: 6. A higher concentration of polymer allows increased proton exchange, but may also block access to the platinum sites and impede gas diffusion. The opposing factor is too much catalyst, which causes a lack in proton exchange medium and also does not yield a continuous binder to adhere the electrode to the ion exchange membrane. It was found that 1: 6 had an overload of carbon and the electrode was very fragile due to poor adhesion while the 1: 2.5 applied and adhered better.

The addition of water to the ink proved to have an effect on how well it cast onto the membrane. With too little water, the ink was difficult to apply and usually cracked within the first few coats. With too much water, the ink was dilute and did not adhere to the surface of the membrane. It was important to find a moderate ratio of water: polymer in order for the ink to apply correctly. The average ratio was found to be 17mg of de-ionized water to 1mg of polymer in the dispersion. Notice this is water to polymer ratio, not polymer dispersion, so the percentage of polymer in the dispersion must be taken into account.

BPSH-40, 50, and 60 dispersions were all attempted with the corresponding BPSH-40, 50 and 60 membranes. Both BPSH-50 and 60 membranes swelled significantly more than BPSH-40 when the ink was applied. The swelling is due to their higher degree of sulfonation. This swelling causes the electrode to crack, therefore ruining the MEA. These highly sulfonated, swellable polymers require a slower application of the electrode to allow complete drying.

After applying both electrodes, the MEA is dried under an IR lamp for 20 minutes. Both the anode and the cathode are identical since they are cast using the same procedure and ink recipe. After the electrode is dried, the ion exchange membrane is converted from the sodium form to the acid form. In order to do this, the MEA is boiled first in H_2SO_4 for an hour and a half and then in de-ionized water for an hour and a half. Boiling also allows for the electrode to be checked for flaking or cracking. While being a quantitative test, inspection of the MEA during boiling is a good check for the durability of the MEA. Previous MEAs composed of BPSH-XX membranes and Nafion electrodes did not fair well during boiling. The electrodes delaminated almost immediately. All results reported in this research were generated from MEAs that survived the fabrication procedure without severe cracking or delamination.

Fuel Cell Testing

Once the MEAs were fabricated, it was necessary to test their performance in a fuel cell. The fuel cell tests were performed at atmospheric pressure and at a cell temperature of 75°C. Various cell temperatures were attempted, but it was found that the conditions were optimized at 75°C. Performance curves were generated for each MEA. The MEA that gave the best results was the BPSH-40 with 1.0 mg Pt/cm^2 loading and a polymer: catalyst ratio of 1: 2.5.

Figure 1 shows the effect of the polymer: catalyst ratio on the performance of the MEA. In this plot the two BPSH-40 MEAs are identical except for their polymer: catalyst ratio and the membrane thickness.

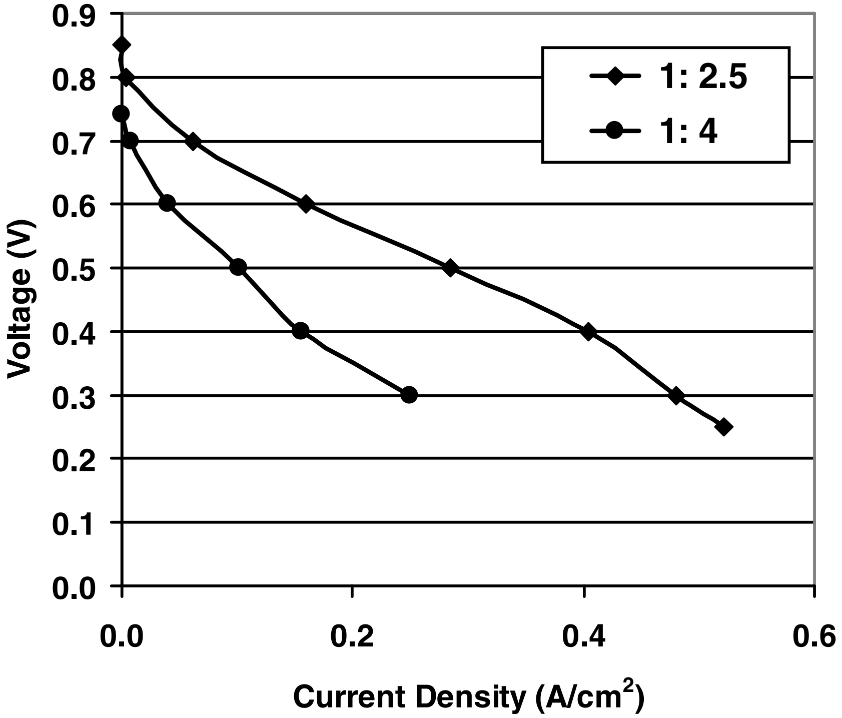

Figure 1: Effect of Polymer: Catalyst Ratio on MEA Performance

Both have a catalyst loading of 1.0mg Pt/cm^2 with the 1:2.5 membrane being 4.2 mils thick and the 1: 4 membrane being 2.9 mils thick. What is interesting about this result is that one would expect a thinner membrane to perform better than a thicker one (all other factors being equal) due to decreased resistance across the cell. Figure 1 makes it clear that the ratio of the catalyst and polymer has a larger effect on fuel cell performance than the membrane thickness and it is therefore important for us to study the optimization of the ratio in future research.

It was important to compare the performance of the BPSH-40 MEA to that of a standard Nafion MEA. Figure 2 shows this comparison. The Nafion MEA (prepared off-site using state-of-the-art technology) has a loading of 0.44mg Pt/cm^2, which is lower than the BPSH-40 loading of 1.0 mg Pt/cm^2. A BPS-40 membrane was fabricated with platinum loading of 0.44mg/cm^2 and in future studies, the effects of this lower loading on the BPSH electrodes will be studied. Some of the reasons that the BPSH-40 MEA shows a comparable performance to that of Nafion 1135, even with a greater platinum loading, are differences in the conductivity and thickness of the membranes. BPSH-40 has a conductivity of 0.08±0.01 S/cm while that of Nafion is 0.11±0.01 S/cm. Also, the BPSH-40 MEA is 4.2 mils thick and the Nafion is 3.5 mils. Both the decreased conductivity and thicker membrane increase the resistance across the cell and require higher platinum loading.

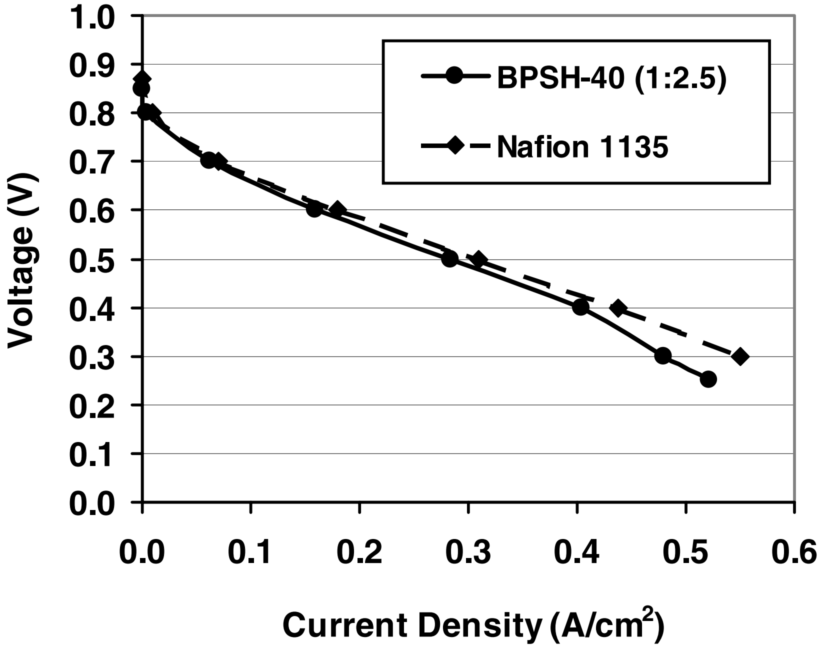

Figure 2: Polarization Curve Comparing BPSH-40 MEA and Nafion 1135 MEA

The power density (W/cm^2) of the two MEAs is also another method to compare their performances. Figure 3 shows that both MEAs have a peak power output at approximately 0.4 volts. At this voltage, the BPSH-40 MEA is producing approximately 0.16 W/cm^2 while the Nafion is producing 0.17 W/cm^2. This is a good way to show that the BPSH MEA performed quite comparably to the Nafion MEA fabricated using current methods.

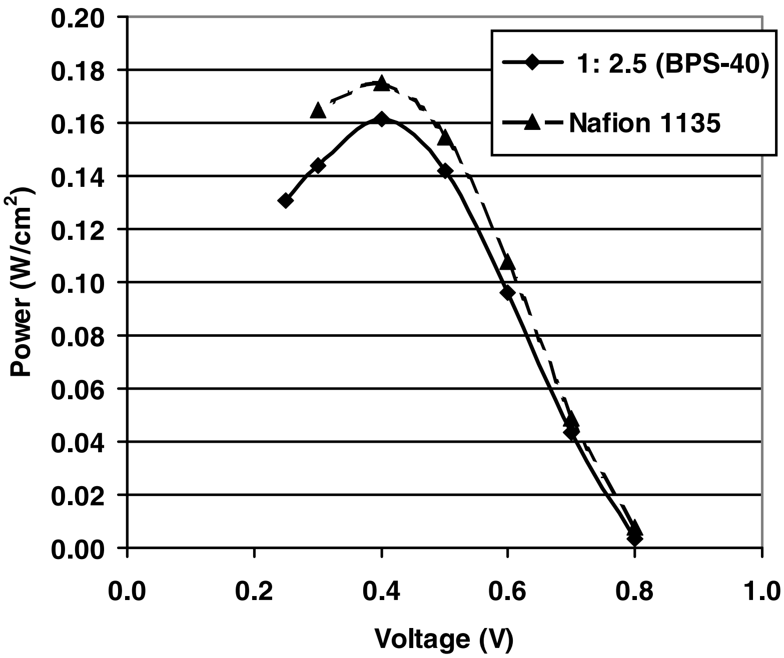

Figure 3: Power Density Comparison of BPSH-40 and Nafion 1135

CONCLUSIONS

A membrane electrode assembly was fabricated using novel copolymers in both the membrane and electrode for the first time. The initially prepared BPSH-40 MEA performed comparably to a Nafion MEA in atmospheric fuel cell tests at 75°C. It was found that the BPSH-40 MEA could be fabricated by applying the electrode using a previously established painting technique. A key component of this research was fabricating a polymer dispersion that could be painted on the membrane without compromising its integrity. The power produced by the new MEA was only 0.01 W/cm^2 (6%) lower than that of Nafion. When used for both the electrode and ion exchange membrane, these new sulfonated poly(arylene ether sulfone)s proved to be good candidates for use in a polymer electrolyte membrane fuel cells.

FUTURE WORK

First of all, the catalyst: polymer ratio was mentioned many times, and found to be important, but a detailed study needs to be conducted. In this work, it was found that a 1: 2.5 ratio was optimal, but that was the lowest ratio tested. In the future, 1: 2 and even lower ratios should be fabricated and characterized in a fuel cell. Also, the interface between the electrode and the ion exchange membrane requires a detailed study. Since this is where the electrochemistry takes place, it is a very important part of the MEA. Both adhesion and resistance are important properties that must be considered.

Currently, a painting technique is used to apply the electrodes. With Nafion, the electrodes are first painted onto a Teflon sheet and then hot-pressed onto the membrane. BPSH has a higher glass transition temperature and therefore, it may be harder to melt press onto the surface of the membrane. BPSH dispersions and ink also does not wet Teflon so a different transfer method needs to be found. The hot-press method is desirable because it provides a more uniform electrode and eliminates the swelling and cracking problems of the membrane during painting.

Most of the MEAs tested in this study were run for eight to nine hours in the fuel cell. In the future, life tests will be of interest. It is important that the MEA be run for hundreds or even thousands of hours in order to ensure its durability and performance. Also, the tests were run at ambient pressure and relatively low temperatures. In the future, high temperature testing will be done.

ACKNOWLEDGEMENTS

The authors would like to acknowledge the National Science Foundation for their financial support. Dr. von Spakovsky, Dr. Ellis, and John Evans deserve recognition for their help with the fuel cell test stand in the Mechanical Engineering Department at Virginia Tech.

REFERENCES

1. Wang F., Hickner M., Kin Y S., Zawodzinski T., McGrath J., Synthesis and Characterization of Sulfonated Poly(arylene ether sulfone) Random (Statistical) Copolymers Via Direct Polymerization: Candidates for New Proton Exchange Membranes. *Journal of Membrane Science* submitted 2000.

2. Thomas S., Zaibowitz M, Fuel Cells – Green Power. Los Alamos National Laboratory 2000; www.education.lanl.gov/resources/fuel cells.

3. Wilson M S., Membrane Catalyst Layer for Fuel Cells, U.S. Patent 05211984 to The Regents of the University of California, 1993.

4. Grot, Walther G., Process for Making Liquid Composition of Perfluorinated Ion Exchange Polymer, and Product Thereof, U.S. Patent 4433082, 1984

5. Davis, Mark W., Development and Evaluation of a Test Apparatus for Fuel Cells. Masters Thesis Virginia Tech, 2000.

Effects of Silica Inclusions on Plasticization in Permselective Polyimide Membranes

Morgan D. Mager*, Eva Marand, Rick Davis
Chemical Engineering Department, Virginia Polytechnic Institute & State University, Blacksburg, VA

* Department of Materials Science, Georgia Tech, Atlanta, GA

ABSTRACT

The permeation differences were examined between a pure polyimide membrane and one containing phenyltrimethoxysilane (PTMOS) regions. Tests were performed with methane and carbon dioxide at pressures of four, ten, twenty and forty atmospheres. Plasticization behavior was inhibited by the silica domains. A comparison was also made with a Dynamic Mechanical Thermal Analyzer (DMTA) between pure polyimide samples and those containing tetramethoxysilane (TMOS). Both materials were tested under atmospheric conditions and after being exposed to ten atmosphere nitrogen or carbon dioxide for 18 hours. The TMOS hybrid material was observed to be stiffer and have less pronounced transitions. Neither conditioned group exhibited changes in either alpha or beta transitions after the elevated pressure gas exposure.

INTRODUCTION

Until recently, the only effective methods of gas separation were costly processes such as cryogenic distillation and pressure swing adsorption [1,2]. A new option is emerging, however, in the form of permselective polymer mem-branes. The purity of gases obtained from a permselection process is generally lower than that from a traditional separation but this compromise is acceptable in many applications. One such application is CO_2/CH_4 separation for natural gas purification.

Low energy costs and a minimal initial cost for small point-of-extraction applications make membrane selection an attractive alternative for natural gas purification. Furthermore, since methane is the less permeable of the gas pair, it can be collected at the upstream pressure without the necessity of decompressing to atmospheric pressure and recompressing for transport. However, there are still problems to be overcome before this technology can become viable. One of the primary concerns is CO2-induced plasticization.

Natural gas sources can contain as much as 50% CO2 at pressures up to 60 atm [3]. Plasticization is believed to occur when penetrant molecules reach a high enough concentration in the membrane to force apart the chains and increase large-scale chain mobility. This increase can drastically affect the amount and distribution of the free volume within the membrane and consequently decrease the selectivity [4]. Plasticization is especially a problem with CO_2 since it has a quadrupole moment and is therefore more soluble in polar polymers [5].

For this study a pure 6FDA-FpDA-DABA polyimide membrane was compared to a hybrid membrane containing 22.5 wt% phenyltrimeth-oxysilane (PTMOS). It was hoped that the silica domains would add structural rigidity to the polymer and decrease the effects of plasticization. To test this hypothesis the membranes were subjected to permeation tests under conditions ranging from four to thirty atmospheres of methane and carbon dioxide. Samples of the pure polyimide and a hybrid membrane with 22.5 wt% tetra-methoxysilane (TMOS) were con-ditioned and investigated with a Dynamic Mechanical Thermal Analyzer (DMTA).

Theoretical

Permeability through a membrane is defined as the one dimensional flux normalized to thickness and feed pressure:

$$P = N/(p2-p1)/d \qquad (1)$$

where d is the thickness of the membrane and N is the steady-state Fickian flux.

Permeation is a two step process, relying on both solution and diffusion. Therefore, under the limiting assumptions of constant pressure and negligible downstream pressure, permeability is defined as the product of the solubility and diffusivity of a particular gas through a particular medium:

$$P = DS \qquad (2)$$

The equations presented so far imply that a linear increase in feed pres-sure should produce a corresponding linear increase in permeability. In fact, permea-bility is observed to decrease with increasing feed pressure. This observation can be explained through the dual mode sorption theory.

According to the Dual Mode theory gas can either sorb into a polymer via traditional Henry's Law type dissolution or it can sorb into microvoids that compose the polymer's free volume [6]. Consequently, the total gas concentration can be expressed as the sum of the Henry's Law mode and the Langmuir mode concentrations:

$$C = C_D + C_H = k_D p + (C'_H bp)/(1+bp) \qquad (3)$$

Since diffusion through the poly-meric free volume does not require the material to be in solution it is a much faster process. However, as the feed pressure increases the voids become saturated and additional gas can travel only through the slower Henrian method. Since permeability is normalized to pres-sure as shown in equation (1) this results in a net decrease in permeability in spite of the increase in gas flux.

Ideal selectivity is defined to be the ratio of the permeabilities of the gases, which are in turn the product of solubility and diffusivity as per equation (2) [7].

$$\alpha^* = P_A/P_B \qquad (4)$$

Although ideal selectivity does not exactly describe mixed gas behavior due to dual mode effects it is commonly accepted as a good approximation.

EXPERIMENTAL

Materials

The base polyimide used was 6FDA-6FpDA-DABA with 12.5 wt% diaminobenzoic acid (DABA. The structure of this copolymer is given in fig. 1. The samples used for DMTA study contained 22.5 wt% tetramethoxysilane (TMOS). The samples for permeation study contained 22.5 wt% PTMOS. The structures of these silica inclusions are also shown in fig. 1. All polymer membranes were synthesized by Chris Cornelius [8]. Carbon dioxide and methane were both obtained from Air Products with a purity greater than 99.99%.

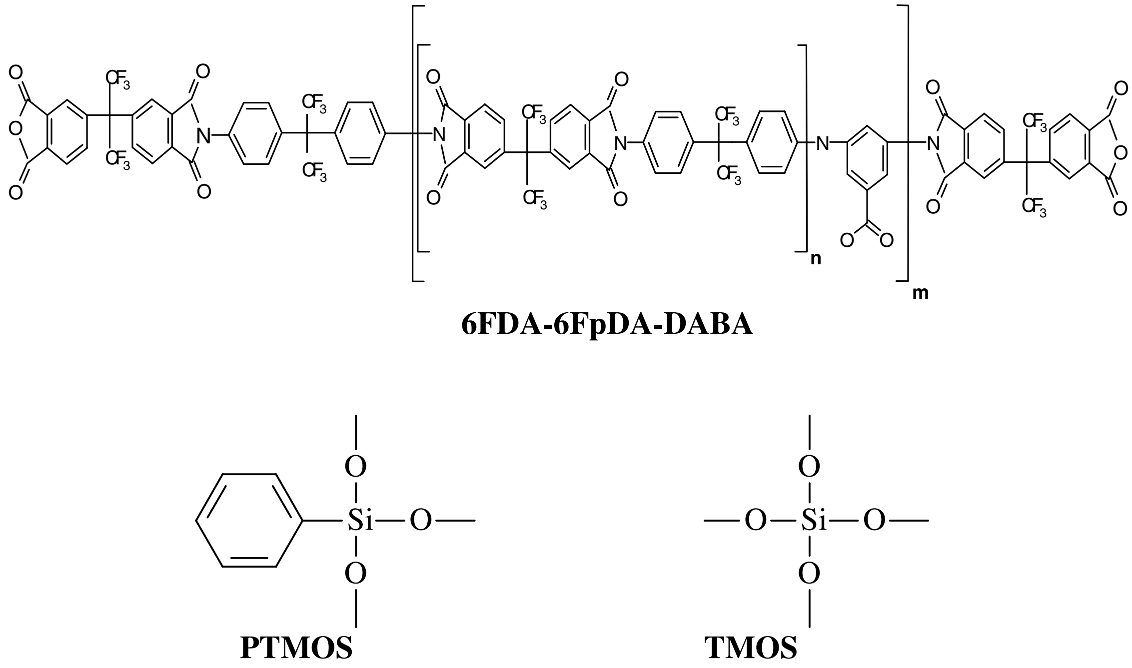

6FDA-6FpDA-DABA

PTMOS **TMOS**

Fig. 1. The structures of the base polyimide and the silica additives

DMTA Procedure

A Rheometric Scientific DMTA IV was used to perform the thermal analysis. All tests were performed as Dynamic Strain Sweep Tests with a tensile rectangular geometry. Sample dimensions were 12mm x 4mm x .07mm. The ratio of at least 3:1 length to width was chosen to decrease edge effects.

The DMTA is designed to produce plots of the storage modulus, loss modulus and tan delta. High temperature tests were performed to measure quantitative changes in the alpha transition (T_g) and qualitative changes in the beta transition. Low temperature tests were attempted to investigate the gamma transition. This transition is associated with smaller, more local chain movements than either the alpha or beta transitions. For this reason, the gamma transition is believed to have a closer correlation to permeation properties.

Run conditions were 0.01% strain rate, static prestress of 0.015N and a heating ramp rate of 2°C per minute. For the high-temperature tests the starting and ending temperatures were defined as 40 and 350°C respectively. Sub-ambient tests were attempted from 20 to -80°C but the instrument was proven unable to achieve temperatures below -25°C.

Both the pure polyimide and the TMOS samples were annealed at 220°C for 24 hr. The two material groups were then divided into three further groups. The first set was exposed only to atmospheric conditions. The other two sets were conditioned through exposure to ten atmo- sphere nitrogen and carbon dioxide respectively for 18 hours.

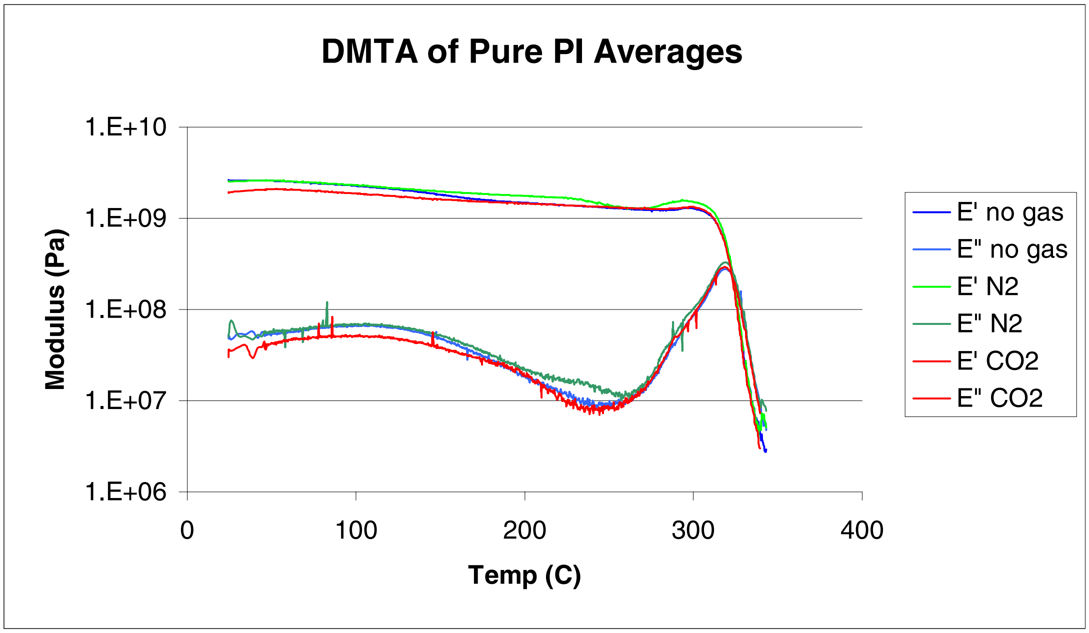

Fig. 2. High-temperature pure polyimide DMTA results

Permeation Procedure

All permeation measurements were performed using a custom permeation cell with an effective exposure area of 11.51cm^2. The cell was kept at a constant temperature of 35°C inside a GC 6000 oven.

Before and after exposure to methane, samples were pumped down for three hours. Samples exposed to carbon dioxide were pumped down for four hours. Vacuum pressure during pumpdown was maintained at or below 65mtorr as measured by a Televac II thermocouple Gauge.

Pressures for methane and carbon dioxide were varied between four and 30 atmospheres. Methane feed pressures were maintained by a US Gauge Model 210-1-350 regulator and carbon dioxide feed pressured were maintained by a Matheson 3020 regulator. Downstream pressure was measured by Televac 2A Thermocouple Transducer. Cell volume was calculated at the start of the experiment using the previously mentioned thermocouples and a known molar volume of gas.

RESULTS AND DISCUSSION

DMTA

As stated, the low temperature DMTA investigation failed to reveal the gamma transition due to an insufficiently low temperature range. Plots of E' and E" for each of the three exposure groups in pure polyimide are given in fig. 2. Each of the lines represents the average of three trials under the same conditions. Fig. 3 shows the average results for the sample containing 22.5 wt% TMOS.

For the pure polyimide samples, T_g stayed within one degree of 319°C regardless of preconditioning. The peak around 100°C that comprises the beta transition was depressed slightly in the samples conditioned with carbon dioxide. A small peak was observed just below T_g in the samples conditioned with nitrogen. The data from samples conditioned with carbon dioxide were observed to be noiser.However, this noise was cancelled out by averaging the three trials.

The moduli of the TMOS hybrid samples were significantly higher than those from the pure polyimide group. A comparison of the unconditioned samples from each material reveals that the TMOS samples have a storage modulus that is an average of 151 times higher than that of the corresponding pure polyimide samples. These measurements confirmed the fact that silica inclusions lend mechanical rigidity to a polyimide membrane.

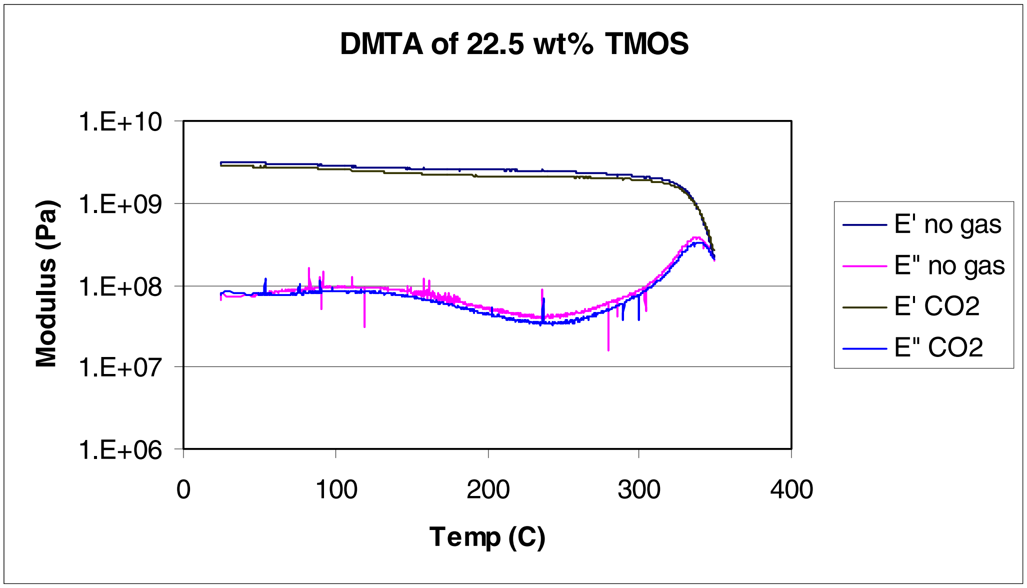

Fig. 3. High-temperature DMTA of 22.5 wt% TMOS hybrid samples

The addition of TMOS to the polyimide was also observed to hinder the alpha and beta relaxations. This is indicated by flatter curves with less pronounced peaks than those of the pure polyimide. T_g for the hybrid group was elevated to 337°C but again varied less than one degree with preconditioning within the material group. The depressed alpha and beta peaks were inhibited in the hybrid DMTA samples. These results indicated that macroscopic cooperative chain movements are inhibited by the addition of silica regions. No significant changes were seen in the hybrid material after conditioning with carbon dioxide.

A likely explanation for why no changes were observed in the transitions with conditioning is that the DMTA is a destructive test at elevated temperatures. During the two and a half hour run of a high-temperature DMTA experiment the sample is out of its conditioning environment. That is certainly enough time for the gas to desorb from the polymer matrix. If the effects of conditioning are reversible then they are unlikely to be observed under these conditions.

Permeation

Data from the permeation portion of the study are shown in fig. 4-7. Diffusivity, as shown in fig. 4, increases with increasing pressure for all gas/membrane combinations as would be expected. The increase in diffusivity with increasing feed pressure makes sense since the downstream pressure remained essentially zero. Thus, as the gap between upstream and downstream pressure increased, the driving force behind diffusion increased.

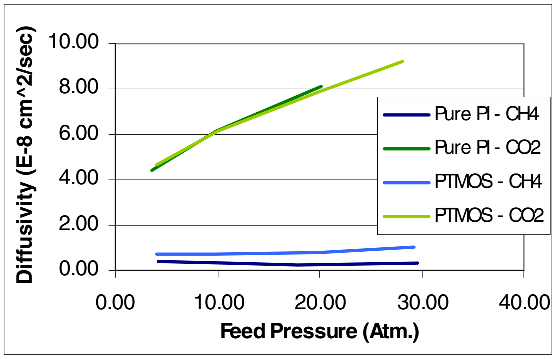

Fig. 4. Diffusivity coefficients

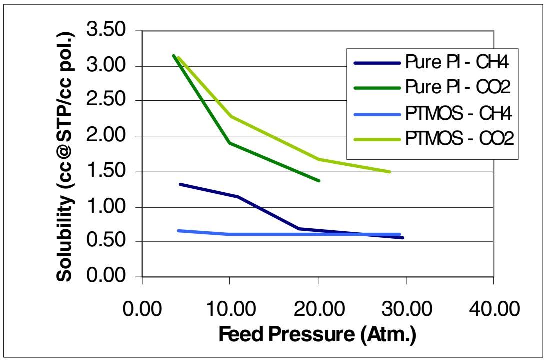

Fig. 5. Solubility Coefficients

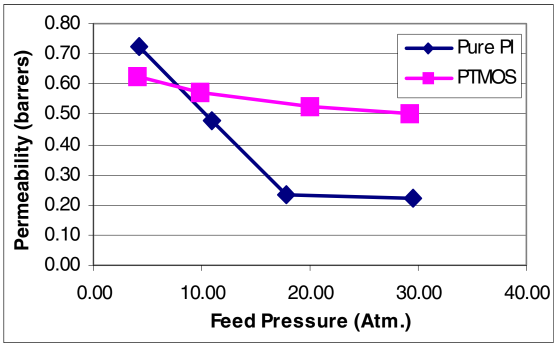

Fig. 6(a). CH4 Permeabilities

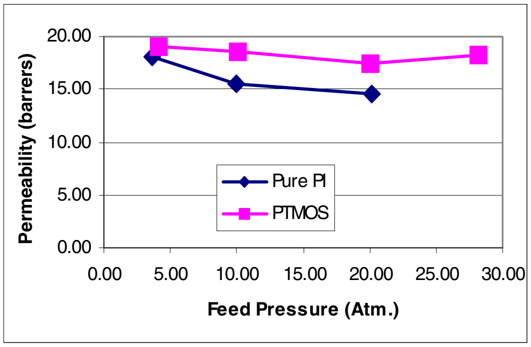

Fig. 6(b). CO2 Permeabilities

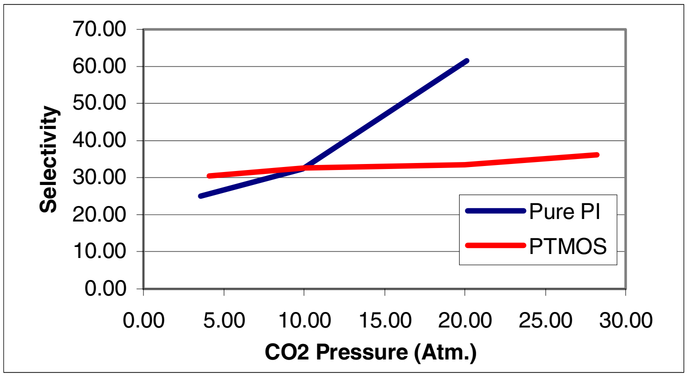

Fig. 7. Ideal selectivity coefficients for the pure polyimide sample versus the 22.5 wt% PTMOS hybrid

Solubility data, as shown in fig. 5, qualitatively agree with previously published dual sorption data for gas diffusion through a glassy polymer membrane [9]. The solubility coefficient decreased for every gas/membrane pair in this study. Solubility decreased more drastically for both gases in the pure polyimide membrane. The most drastic decrease in solubility was that of methane in the pure polyimide sample.

These results can be explained by taking a closer look at the Dual Sorption theory. The solubility factor of equation (2) is based on total gas sorbed into the matrix as shown in equation (3) and not just gas dissolved into the polymer. Therefore, this total includes gas in the Langmuir sites.

The second term of equation (3) represents the Langmuir mode of gas sorption. Since this term has pressure in the denominator as well as the numerator it can decrease with increasing pressure depending on the constants involved. Using the data from the pure polyimide permeation study a K_D value of 0.379 was calculated for methane and 1.26 for carbon dioxide. C_H values of 5.72 and 3.71 were calculated for methane and carbon dioxide. These results are consistent with data published for other polymer/gas systems [9,10].

The pure polyimide has a larger fractional free volume and therefore more Langmuir sites. Methane's large volume and lack of polarity keep it from sorbing into the polymer through Henrian mode, making Langmuir mode a proportionally larger component. The same decrease in solubility is noted for carbon dioxide in the pure polyimide matrix. However, the extent of this decrease is less severe for carbon dioxide because carbon dioxide has a quadrupole moment and thus sorbs more easily into the polymer itself.

The permeability of methane, as shown in fig. 6(a), dropped further in the pure polyimide than in the hybrid sample. This has been explained in terms of the Dual Mode drop in the solubility term. What is not clear is why the hybrid sample had a permeability comparable to that of the pure membrane at low feed pressures. The expectation would be that the silica domains would impede gas motion.

One possible explanation for this result is that the large phenyl group provides sufficient free volume in the silica for gas to diffuse through. Further studies would have to be performed to verify this explanation.

As expected, the permeability measurements for carbon dioxide, given in fig. 6(b), indicated plasticization at high feed pressures. The plasticization pressure for this polyimide is near 20 atmospheres for CO_2. As hoped, the hybrid sample showed an inhibited plasticization response, indicated that the mechanical strengthening of the silica did have beneficial results on permeation properties. This inhibition was due to both a lesser decrease in solubility and a slightly lesser increase in diffusivity.

Ideal selectivity measurements, as calculated by equation (4) show an increase in selectivity for both the pure polyimide and the hybrid samples. Part of this observation can be explained by the fact that these are ideal, not actual, selectivities. As plasticization occurs, the permeability of carbon dioxide increases without a corresponding increase in methane permeability since these were pure gas measurements. In reality, methane permeability would increase as well.

Plasticization effects were only one factor, though. The majority of the increase in ideal selectivity for the pure membrane can be attributed to the drastic drop in methane permeability with increasing feed pressure. This trend is opposite of that observed by Chern et al. for CO2/CH4 separation with Kapton® membranes [11]. Though solubility, diffusivity and permeability data are qualitatively similar between that study and this, the quantitative differences are sufficient to give a qualitatively different selectivity plot. No explanation other than basic material differences is available at this time. More investigation is warranted

CONCLUSIONS

Hybrid polyimide membranes fabricated with sol-gel chemistry have been demonstrated to have superior properties. Mechanical rigidity has been increased with a tolerable increase in brittleness. Long-range chain motion, as evidenced by alpha and beta transitions in DMTA study, has been inhibited. The glass transition temperature has been elevated by 18°C in the hybrid material.

Permeation properties have been stabilized over a wide range of pressures by the addition of silica domains. The solubility of methane in the hybrid membrane was essentially constant over the range tested. Carbon dioxide solubility decreased, but less than it did for the pure polyimide membrane. Diffusivity was minimally affected by the silica regions.

Changes in permeability with feed pressure were inhibited by the silica additions. In the case of CO_2 permeability, this inhibition indicates that the hybrid more effectively resists plasticization.

FUTURE WORK

Further low-temperature DMTA investigations of these materials is warranted. Establishing a direct correlation between gamma transition behavior and permeation properties would be a valuable investigative tool. High-temperature DMTA analysis of these membranes may also prove more useful in studying plasticization phenomena if an elevated pressure pure gas environment could be maintained during the experiment.

Future permeation studies should be performed over an even wider range of pressures to ascertain whether or not the gains observed for the hybrid sample are transient. More trials within the range already investigated would also be of use. With these data, the plasticization point could be more accurately described.

An investigation of the permeation properties of other hybrid membranes is advisable. Such tests would help determine whether nor not gases are able to permeate through certain types of silica domains and if so, what properties of the silica are needed to allow this behavior. Such knowledge would be invaluable for the custom design of membranes for specific applications.

Mixed gas permeation tests will also have to be performed at some point in the future. Though pure gas tests are an excellent initial tool, only mixed gas studies can accurately predict membrane performance under probable use conditions.

ACKNOWLEDGEMENTS

The author would like to thank Chris Cornelius for synthesizing and providing the membranes used in this study. He would also like to thank Chris Hibshman and Todd Pechar for their support in the lab and Rick Davis and Eva Marand for their theory contributions. Lastly, the author would like to thank Tom Ward, Virginia Tech and the National Science foundation for making this research possible.

REFERENCES

1. R. W. Spillman, *Chem. Eng. Prog*., **85**, 41 (1989).
2. K. Ghosal and B. D. Freeman, *Polym. for Adv. Tech*., **5**, 673 (1994)
3. C. Staudt-Bickel, W. J. Koros, *J. Membrane Sci.*, **155**, 145 (1999)
4. A. Bos, I.G.M. Pünt, M. Wessling and H. Strathmann, *J. Membrane Sci.*, **155**, 67 (1999)
5. G. J. van Amerongen, *J. Polym. Sci.,* **5**, 307 (1950)
6. Kumar, Gupta, *Fundamentals of Polymers*, McGraw-Hill (1997)
7. S. A. Stern and W. P. Walawender, *Separation Sci*., **4**, 129 (1969)
8. C.J. Cornelius, PhD Thesis, Virginia Polytechnic Institute, 2000
9. S. M. Jordan, W.J. Koros and G.K. Fleming, *J. Membrane Sci.*, **30**, 191 (1987)
10. T. Hirose, Y. Mi, A. Stern and K. St. Clair, *J. of Poly. Sci.*, **29**, 341 (1991)
11. R.T. Chern, W.J. Koros, B. Yui, H.B. Hopfenberg and V.T. Stannett, *J. of Poly. Sci.*, **22**, 1061 (1984)

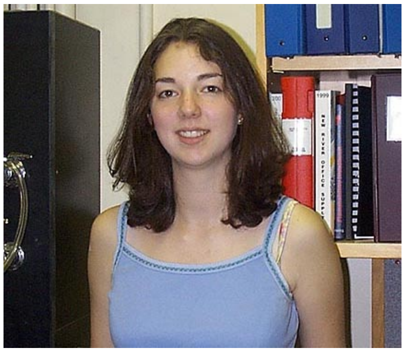

Synthesis of Poly(2-ethyl-2-oxazoline)-*b*-poly (dimethylsiloxane) for use in Silicone Magnetic Fluids

Heather M. Morrison*, Kristen S. Wilson, and Judy S. Riffle
Department of Chemistry
Virginia Polytechnic Institute and State University
Blacksburg, Virginia, 24061

*Department of Chemistry, James Madison University,
Harrisonburg, VA

ABSTRACT

The syntheses of poly(2-ethyl-2-oxazoline) (PEOX) and poly(dimethylsiloxane) (PDMS) homopolymers via living polymerization methods are discussed herein. The PEOX homopolymer was terminated with an allyl-containing endgroup. This endgroup will be hydrosilated with dimethylchlorosilane in the future, to obtain a chlorosilane terminus. This functionalized PEOX could then be used to couple to living PDMS homopolymer, to achieve poly(2-ethyl-2-oxazoline)-*b*-poly(dimethylsiloxane), and amphiphilic block copolymer. It is proposed that once this copolymer is synthesized, it could form micelles in nonpolar solvents, such as silicone, within which magnetic cobalt nanoparticles could be and stabilized.

INTRODUCTION

The synthesis of magnetic nanoparticles inside amphiphilic block copolymer micelles is a promising method for achieving stable magnetic fluids.[1,2] A well-designed amphiphilic block copolymer will form micelles in selective solvents. Nanoparticles can be stabilized within these micelles. It is proposed that the amphiphilic block copolymer micelles can serve as “nanoreactors” for the formation of nanoparticles. These copolymers stabilize the particles and may also lead to uniform nanoparticle size.

There are several examples of this type of nanoparticle synthesis in the literature. The synthesis of nonmagnetic, noble metal nanoparticles such as silver and gold, by the reduction of various metal salts has been carried out in amphiphilic block copolymer micelles by Antonietti, et al.[3,4,5] Magnetic cobalt nanoparticles have also been synthesized in a similar manner.[3] Antonietti et al. have reduced $CoCl_2$ in the presence of poly(styrene)-*b*-poly(4-vinylpyridine) micelles dissolved in toluene.[6] They found that this type of synthesis yielded magnetic cobalt nanoparticles that were 3-5 nm in diameter and exhibited superparamagnetic properties.[6] Cobalt nanoparticles can also be synthesized by thermal decomposition of $Co_2(CO)_8$.[6] In a similar study, Riffle et al. thermally decomposed $Co_2(CO)_8$ in the presence of poly[dimethylsiloxane-*b*-(3-cyanopropyl)methylsiloxane-*b*-dimethylsiloxane] micelles dissolved in toluene (Figure 1).[2] This synthesis produced magnetic cobalt nanoparticles that were 7-18 nm in diameter and were monodisperse for each individual reaction.[2]

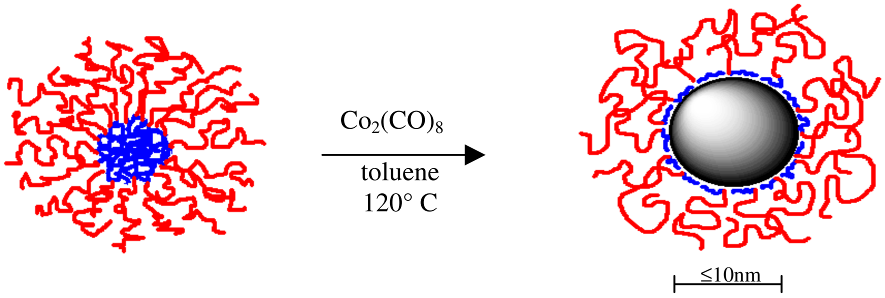

Figure 1. Synthesis of cobalt magnetic nanoparticles inside amphiphilic block copolymer micelles. [2]

The precise mechanism for this nanoparticle formation is unknown. However, it has been proposed that the metal reagents, when reduced or decomposed in the presence of these micelles, will diffuse into the micelles because of attraction to electron-donating groups in the hydrophilic micellar core. Once attracted to the core of the micelle, the metal reagents may react within the micelle to form nanoparticles. Also, further study of this synthesis is needed to determine how micelle core size (and hydrophilic block size) influences nanoparticle size. [2]

Synthesis of magnetic fluids for biological applications is of great interest, but many factors must be considered. For instance, biological applications require that each block of the copolymer is biologically compatible and nontoxic. Also, the magnetic cobalt nanoparticles must be stable to oxidation, so that they do not lose their magnetic properties. It is proposed that a thin layer of silica surrounding the nanoparticle could prevent the oxidation of the particle surface.

Poly(2-ethyl-2-oxazoline)-*b*-poly(dimethylsiloxane) (**1**) (Figure 2) appears to be a promising amphiphilic block copolymer for use in biocompatible magnetic fluid synthesis. The hydrophilic block of this copolymer is the poly(2-ethyl-2-oxazoline) (PEOX), and the hydrophobic block is the poly(dimethylsiloxane) (PDMS). Both blocks of this copolymer were chosen for their probable biocompatibility. The carbonyl group on the repeat unit of the PEOX block should interact well with the metal cobalt particles, stabilizing them with lone pairs of electrons. Also, the PEOX block of this copolymer is known to have a strong affinity for silica, which arises from the hydrogen bonding of the hydroxyl group on the silicon and the carbonyl group of the PEOX. It has been proposed that if PEOX is used as the hydrophilic block of the copolymer, a layer of silica could be synthesized around the cobalt nanoparticle to provide oxidative stability. The PDMS block is known to be biologically compatible, and is highly soluble in both toluene and silicone fluid, making it ideal for steric stabilization of the nanoparticles.

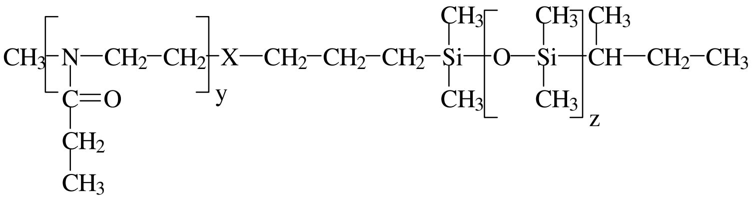

$$CH_3-\left[N(C(=O)CH_2CH_3)-CH_2-CH_2\right]_y-X-CH_2-CH_2-CH_2-Si(CH_3)_2-\left[O-Si(CH_3)_2\right]_z-CH(CH_3)-CH_2-CH_3$$

Figure 2. Poly(2-ethyl-2-oxazoline)-*b*-poly(dimethylsiloxane), an amphiphilic block copolymer. X represents the group that connects the two blocks.

(1)

The synthesis of (**1**) was investigated herein. Once the synthesis is optimized, this copolymer will be used in magnetic nanoparticle formation. The target molecular weights of this copolymer synthesis were a 2,000 g/mol PEOX block and a 15,000 g/mol PDMS block, with various groups connecting the two blocks. The relatively short PEOX block is an approximation of the length necessary to stabilize nanoparticles that are 1-10 nm in diameter. The longer PDMS block should provide sufficient steric stabilization for the nanoparticles, as it will be well solvated by nonpolar solvents.

The synthesis of (**1**) is outlined in three major synthetic steps (Scheme 1). PEOX homopolymer was first synthesized and terminated with an allyl-containing endgroup (**2**). This allyl group will be hydrosilated using dimethylchlorosilane in the presence of a platinum catalyst, to achieve a chlorosilane terminus on the PEOX (**3**). This chlorosilane terminated PEOX (**3**) will then be coupled to a living PDMS homopolymer (**4**) to achieve the block copolymer (**1**) (Scheme 1). The successful formation of both (**3**) and (**1**) are still pending. The syntheses of (**2**) and (**4**) are discussed here in detail.

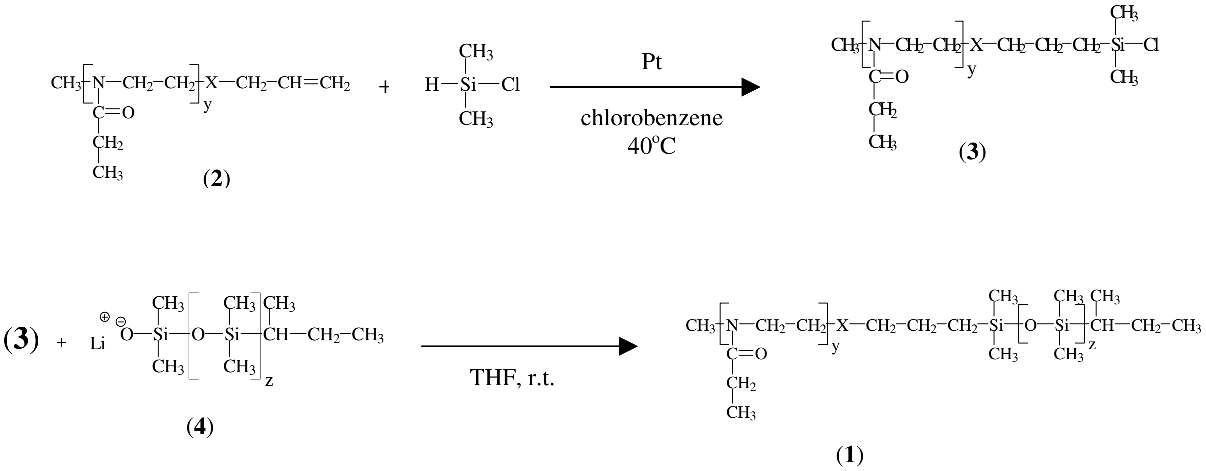

Scheme 1. General overview of block copolymer synthesis. X represents the groups that connect the PEOX to the allyl terminus.

The synthesis of (**2**) was carried out by living cationic polymerization initiated by methyl-*p*-toluenesulfonate.[7] Three different allyl-containing end-cappers were used in an attempt to terminate the polymer with an allyl group: sodium allyloxide (**5**), sodium allylthiolate (**6**), and sodium 2-allylphenolate (**7**) (Scheme 2). Each of these terminating agents were synthesized by modification of a literature procedure.[8]

A common solvent was needed for the PEOX and the PDMS, as these blocks are drastically different in polarity by design. PEOX and PDMS homopolymers are both soluble in THF. Because living PDMS homopolymer (**4**) will be added to chlorosilane functionalized PEOX (**3**) in the coupling reaction, it was necessary to synthesize the PDMS in THF. Normally, the PDMS synthesis is carried out in 80-90% cyclohexane with only 10-20% THF as a promoter. The synthesis of PDMS in THF was also investigated via modification of a literature procedure.[9]

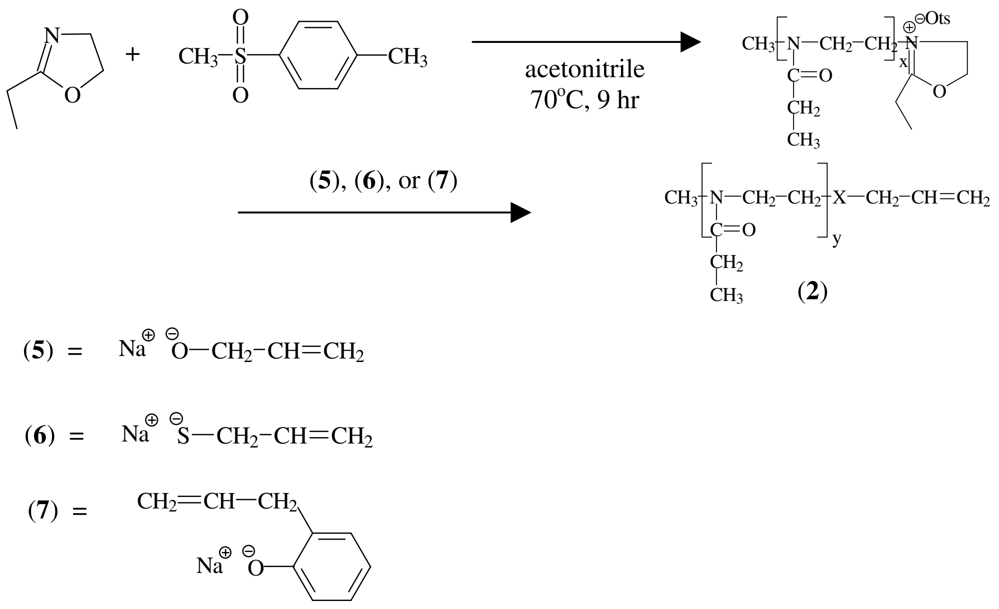

Scheme 2. Living cationic synthesis of (**2**) initiated by methyl-*p*-toluenesulfoneate and terminated with various allyl-containing endgroups.

EXPERIMENTAL

Materials.

Acetonitrile and 2-ethyl-2-oxazoline were dried over CaH_2 and distilled. Tetrahydrafuran (THF) was dried over CaH_2 and distilled, then dried over sodium metal/benzophenone and redistilled. Methyl-*p*-toluenesulfonate was distilled prior to use. Sodium hydride, allyl alcohol, allyl mercaptan (80%), 2-allylphenol, chloroform, diethylether, and $CDCl_3$ were all used as received without further purification. All ^{1}H NMR spectra were taken on a Varian Unity 400 MHz Spectrometer operating at 400MHz, and all samples were dissolved in $CDCl_3$.

*Synthesis of Sodium Allyloxide (**5**).*

Sodium hydride (0.060 g, 2.5 mmol, 1.7 eq. per 1 eq. living chain) was added to a dry 25 mL round bottom flask equipped with a Teflon-coated, magnetic stir bar and a septum. This flask was then gently flame-dried under argon. At 0°C, allyl alcohol (0.57 mL, 83.5 mmol) was slowly transferred via syringe into the reaction flask under argon. When the addition was complete, the reactants were stirred at room temperature until all of the sodium hydride had reacted, yielding a slightly hazy, yellow solution. This solution was then diluted with THF (5 mL), and was stirred at room temperature under argon pressure until use.

*Synthesis of Sodium Allylthiolate (**6**).*

Sodium hydride (0.12 g, 5.0 mmol, 2.0 eq. for 1 eq. of living chain) was added to a dry 100 mL round bottom flask equipped with a Teflon-coated, magnetic stir bar and a septum. This flask was then gently flame-dried under argon. At room temperature, a solution of allyl mercaptan (0.44 mL, 5.5 mmol) in THF (13 mL) was slowly added to the sodium hydride under argon. The final product was an opaque, white liquid. A second aliquot of allyl mercaptan (0.5 mL, 6.3 mmol) was transferred via syringe into the reaction flask. This mixture was stirred at room temperature under argon pressure until use.

*Synthesis of Sodium 2-allylphenolate (**7**).*

Sodium hydride (0.100 g, 4.17 mmol, 1.7 eq. for 1 eq. living chain) was added to a dry, 100 mL round bottom flask equipped with a Teflon-coated, magnetic stir bar and a septum, and was then gently flame-dried under argon. At room temperature, a solution of 2-allylphenol (0.544 mL, 4.17 mmol) in THF (15 mL) was transferred into the round bottom flask via syringe. The final product was a clear, yellow liquid. The mixture was stirred at room temperature under argon pressure until use.

*Synthesis and Termination of Poly(2-ethyl-2-oxazoline) (**2**).*

Representative procedure. To a clean, dry 50 mL round bottom flask equipped with a Teflon-coated, magnetic stir bar and septum, acetonitrile (17 mL), and 2-ethyl-2-oxazoline (5.0 mL, 50. mmol) were added under argon. At room temperature, the polymerization was initiated with methyl-*p*-toluenesulfonate (0.37 mL, 2.5 mmol). The reaction mixture was heated to 70°C , and was stirred until the desired conversion was reached. The polymerization was monitored by ^{1}H NMR spectroscopy by following the disappearance of the monomer peaks. After 9 hours (92% conversion), the reaction mixture was allowed to cool to room temperature. The polymerization was terminated by slowly transferring the living polymer solution via cannula to the solution of terminating agent (either (**5**), (**6**), or (**7**)). The terminating polymer solution was stirred at room temperature for 84 hrs as a closed system under argon pressure.

The terminated polymer solutions were then filtered, diluted with chloroform, and washed with deionized water (6x 30 mL). The organic phase was kept, and most of the solvent was then removed *in vacuo*. The polymer was precipitated in cold diethylether, and was allowed to stir for about 2 hrs. The ether was decanted, and the precipitated polymer was dried under vacuum at 70°C overnight. The product was a white solid. ^{1}H NMR ($CDCl_3$): $\delta = 3.45$ (*s*, CH_2N), 3.05 (*m*, CH_3N), 2.35 (*m*, pendant CH_2), 1.1 (*s*, pendant CH_3). Allyl peaks varied with terminating agent; see Results and Discussion section.

*Synthesis of Poly(dimethylsiloxane) (**4**).*

A solution of hexamethylcyclotrisiloxane (40.7 g, 174 mmol) in THF (60 mL) was added to a clean dry 500 mL round bottom flask equipped with a Teflon-coated, magnetic stir bar and a septum. Then, at room temperature, sec-butyllithium (1.52 mL, 2.71 mmol, 1.78 M in cyclohexane) was transferred into the reaction vessel via syringe under argon. The reaction mixture was stirred at room temperature as a closed system until the desired conversion was reached (5.5 hours, 95% conversion). This reaction was terminated when trimethylchlorosilane (0.4 mL, 3.15 mmol) was syringe-transferred into the reaction flask at room temperature. The polymer solution was stirred overnight under argon pressure. The polymer was precipitated into methanol (200 mL), and stirred for 0.5 hours. The viscous polymer was separated from the methanol using a separatory funnel, and was washed with deionized water (2x 100 mL). It was dried under vacuum overnight at 45°C.

RESULTS AND DISCUSSION

Results of Poly(2-ethyl-2-oxazoline) Polymerization and Termination.

Poly(2-ethyl-2-oxazoline) homopolymer (**2**) was successfully synthesized using methyl-*p*-toluenesulfonate as an initiator. The termination of this polymer with the allyl-containing thiolate (**6**) was also achieved. The ^{1}H NMR integration of the methyl end group at 3.05 ppm was compared to the integrations of the allyl endgroup peaks at 5.80 ppm, 5.15 ppm, and 3.18 ppm (Figure 3). The ratio of these integrals, when adjusted for the number of protons that they represent, was 1:1, indicating that there was an allyl terminus on every polymer chain.

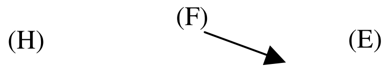

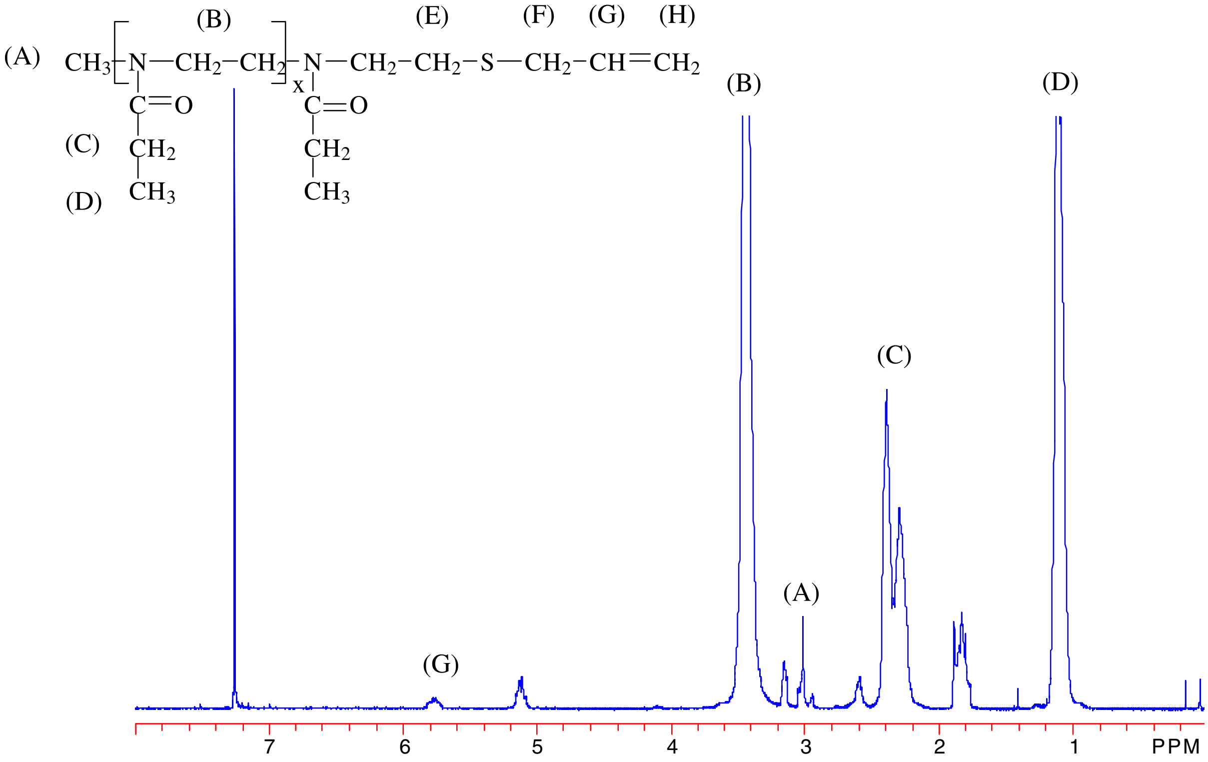

Figure 3. ^{1}H NMR spectrum of purified PEOX that is terminated with allyl thiolate.

The termination of the poly(2-ethyl-2-oxazoline) with the sodium 2-allylphenolate (**7**) was marginally successful, with about 8% of the polymer chains terminated with the allyl group as judged by ^{1}H NMR integrations. The degree of allyl termination was determined by comparing the methyl end group integration at 3.05 ppm to that of the ally protons at 6.0 ppm, 5.1 ppm, 5.0 ppm, and 4.2 ppm. The reason that this termination reaction did not go to completion may be that the delocalization of the electrons on the oxygen made it a poor nucleophile, and it was unable to ring-open the oxazolinium terminus. Also, there might be a steric problem with this reaction, as the nucleophile is ortho to the allyl group.

The termination of this polymer with sodium allyloxide (**5**) was unsuccessful, as there were no significant allyl peaks (expected at 6.0 ppm, 5.1 ppm, 5.3 ppm, or 4.1 ppm) in the ^{1}H NMR spectrum of the purified polymer. This apparent lack of allyloxide nucleophilicity may be due to interference of excess allyl alcohol. Hydrogen bonding with this small amount of alcohol may have prevented it from terminating the polymer. In the future, this termination may be attempted using stoichiometric amounts of allyl alcohol and sodium hydride to eliminate this possible complication.

Results of PDMS Synthesis in THF.

The synthesis of PDMS homopolymer in THF appears to have been successful, as the reaction had nearly gone to completion in just 3 hours. However, Gel Permeation Chromatography (GPC) results are still pending. It is not yet known if the faster reaction time had any negative effects on the polydispersity of the polymer. This information is necessary to determine if significant backbiting occurred during the polymerization.

CONCLUSIONS

Poly(2-ethyl-2-oxazoline) homopolymer was successfully synthesized via a living polymerization process that was initiated with methyl-*p*-toluenesulfonate. It was also quantitatively terminated with an allyl group when the living polymer solution was treated with sodium allylthiolate. Termination of the living PEOX was only marginally successful when using sodium 2-allylphenolate as the terminating agent, possibly due to steric factors or lack of sufficient nucleophilicity. Also, termination of the living PEOX was unsuccessful when using sodium allyloxide in excess allyl alcohol, possibly due to hydrogen bonding of the alcohol to the oxide, thus decreasing nucleophilicity.

Poly(dimethylsiloxane) appears to have been successfully synthesized using THF as the solvent, but GPC results are still pending to ensure that the speed of the reaction did not sacrifice the normally narrow polydispersity. Hydrosilation of the allyl-terminated PEOX, and its subsequent coupling to living PDMS are both still pending.

ACKNOWLEDGEMENTS.

We would like to thank the Chemistry Department at Virginia Polytechnic Institute and State University for the use of their facilities. We are also very grateful to the Summer Undergraduate Research Program and the National Science Foundation for their financial support, and the opportunity to do this research.

REFERENCES

1. Förster, S.; Antonietti, M. *Advanced Materials.* **1998**, *10(3)*, 195-217.
2. Stevenson, J.P.; Rutnakornpituk, M.; Vadala, M.; Esker, A.R.; Charles, S.W.; Wells, S.; Daily, J.P.; Riffle, J.S. *Journal of Magnetic Materials and Magnetism.* **2001,** *225*(1), 47-58.
3. Antonietti, M. et. al. *Macromolecules.* **1996**, *29*, 3800-3806.
4. Antonietti, M. et. al. *Colloid Polymer Science,* **1996**, *274*, 795-800.
5. Antonietti, M. et. al. *Advanced Materials*, **1995**, *7(12)*, 1000-1005.
6. Antonietti, M. et. al. *Colloid Polymer Science.* **1997**, *275*, 426-431.
7. Lee, S.C. et. al. *Macromolecules.* **1999**, *32*, 1847-1852.
8. Shimano, Y. et. al. *Journal of Polymer Science: Part A: Polymer Chemistry*, **1995**, *33*, 2715-2723.
9. Scibiorek, M. et. al. *Polymer Bulletin*, **2000**, *44*, 377-384.

Controlling Dewetting in Ultra-thin Films

Ana Maria Pinto*, Lars Kilian, Jianjun Deng and Alan Esker
Department of Chemistry, Virginia Tech,
Blacksburg, VA 24061
* Depts. of Aerospace and Mechanical Engineering, NC State University,
Raleigh, NC

ABSTRACT

Dewetting of ultra-thin poly(*t*-butyl acrylate) (PtBA) films on top of isopentylcellulose (IPC) has been observed due to film instability. IPC capping layer films can be used to control the stability by increasing the interpenetration between itself and PtBA, creating a Si//IPC//PtBA//IPC//air system. The dewetting behavior can be suppressed by increasing the number of capping layers on PtBA. As the thickness of the capping layer increases, hole radius growth rates and density decrease, rupture time increases, and a transition from slip toward stick boundary conditions are observed.

INTRODUCTION

Dewetting is the spontaneous formation of holes in unstable films. The dewetting of ultra-thin (<100 nm) films on nonwettable substrates are of scientific and technological interest in applications such as coatings, paints, adhesives, the production of ultra thin membranes with controlled pore sizes and thermal induced failure of multilayer micro-electronic and optical devices. Coatings are greatly affected by hole density and size, as hole density and size increase the holes begin to merge, thus degrading the coating. Hence, the control of hole size and density as well as developing mechanisms for suppressing dewetting will allow thin polymeric coatings to maintain their optical, mechanical and electrical properties at temperatures above the glass transition temperature (T_g). A number of factors influence the dewetting of polymer films, such as film thickness, polymer-surface interactions, viscosity, and surface tension.[1] In this study we are going to concentrate on the influence of thickness on the dewetting of thin polymer films.

A thin film of a non-volatile liquid which is forced to spread on a solid substrate may be stable, and preserve its initial shape, or it may be unstable and evolve by dewetting into an array of droplets.[2] There are two mechanisms known to account for dewetting: nucleation and growth (heterogeneous), and spinodal dewetting (homogenous). In the nucleation and growth mechanism an impurity in the film (e.g. dust or an air bubble) or on the substrate (e.g. scratch or other imperfections) acts as a nucleation site for the growth of a hole in the film.[3] In the spinodal dewetting case where the unstable film is heated above T_g into the liquid-like state, capillary waves form on the surface of the film due to fluctuations in the polymer's density. When the amplitude of one of these waves gets large enough to make contact with the underlying substrate, an initiation site for hole growth may occur. During the dewetting process, the film will pull

away from this contact site, where the substrate-air interface has been formed and start to grow.[3] The dewetting process is often characterized in terms of hole size and density
The understanding of the mobility of polymer chains near surfaces and interfaces impacts many technological areas where the properties of polymer thin films and polymers at interfaces are critical[4]**.** Slip and stick boundary conditions or slippage help us understand the limiting behavior for the growth rate of the holes. If a film sticks to a surface it will be more stable than a film that slips on a surface. When a film dewets, its radius grows with respect to time and this process can be described with good precision by a power law, which determines if the film expresses slip or stick boundary conditions. In an ideal condition the substrate's surface is perfectly smooth and the polymer is expected to slip on the surface. The power law that governs this slip condition is $R = a \cdot t + t_0$ (where $a \approx 1/k$ is related to the monomer-surface friction coefficient, t corresponds to time, and t_0 corresponds to the rupture time of the film)[5]. For a non-ideal condition the polymer sticks to the surface promoting stick boundary conditions and a hole growth rate is represented by the following equation: $R = a \cdot (t + t_0)^{2/3}$, where the monomer-surface friction coefficient is now velocity dependent, $a \approx 1/(k(v(t)))$.[5] In a semi-ideal condition there is a gradual transition from slip to slick boundary conditions where $R = a \cdot (t + t_0)^{2/3<x<1}$. Work by Grüll et al looked at polystyrene (PS) dewetting from cellulose coated surfaces (isopentylcellulose cinnamate, IPCC). The PS/IPCC system on silicon can be depicted as Si//IPCC//PS//air. The dewetting data shows slip boundary conditions for a 20Å IPCC coating layer and a 300Å PS film. In contrast the dewetting data for a 160Å IPCC coating layer and a 300Å PS film shows stick boundary conditions. The authors also performed neutron reflectivity experiments on a Si//800Å PS//400Å IPCC//air system, where the PS layer was deuterium labeled, to obtain the interfacial width between the incompatible polymers. When the coating layer is significantly less than twice the interfacial width (2σ) slip boundary conditions are observed. When the coating layer is greater than 2σ stick boundary conditions are observed. Hence observations of changing from slip to stick boundary conditions in dewetting experiments are indirect measurements of the evolution of adhesion arising from the interpenetration of polymer chains. Therefore if the coating is too thin the system does not develop the full interfacial width and slippage occurs.

Clarke and Esker previously demonstrated that IPCC can be used to control the stability of poly (*t*-butyl acrylate) (PtBA) films on silicon wafers prepared by the Langmuir-Blodgett (LB) film technique. The LB technique offers the possibility to fabricate highly ordered films with monolayer by monolayer control of thickness and low surface roughness.[6] There were three factors of interest from their findings regarding PtBA stability: 1) Placing IPCC between PtBA and silicon (Si//IPCC//PtBA//air) induces dewetting which worsens as the IPCC layer thickness increases; 2)Thicker PtBA layers on Si//IPCC//PtBA//air dewet more slowly; and 3) Placing as little as two monolayers of IPCC on top to from a trilayer arrangement of Si//IPCC//PtBA//IPCC//air substantially stabilizes the film.

To understand the mechanism by which capping layers suppress dewetting the combination of thicknesses for the trilayer arrangement of Si//isopentylcellulose (IPC)//PtBA//IPC//air will be optimized using the LB film technique. Optical microscopy will be used to investigate different dewetting properties in ultra-thin films such as hole density, rupture time, as well as slip and stick boundary conditions for the rate of role growth.

EXPERIMENTAL

Materials

The PtBA was obtained from Polymer Source, Inc. The hairy-rod IPC molecule was prepared by the method of Schaub.[7] The IPC structure consists of a rigid backbone, and flexible side-chain arms, where R = $CH_2CH_2CH(CH_3)_2$ (90%) and R = H (10%), which make the polymer amphiphilic and soluble in common organic solvents allowing IPC to forms spread monolayers on water. Because of its hairy-rod structure, IPC form very ordered polymer films facilitating LB-transfer to solid substrates, which are formed one molecular layer at a time. The specific characteristic and structures of these polymers are shown in Figure 1.

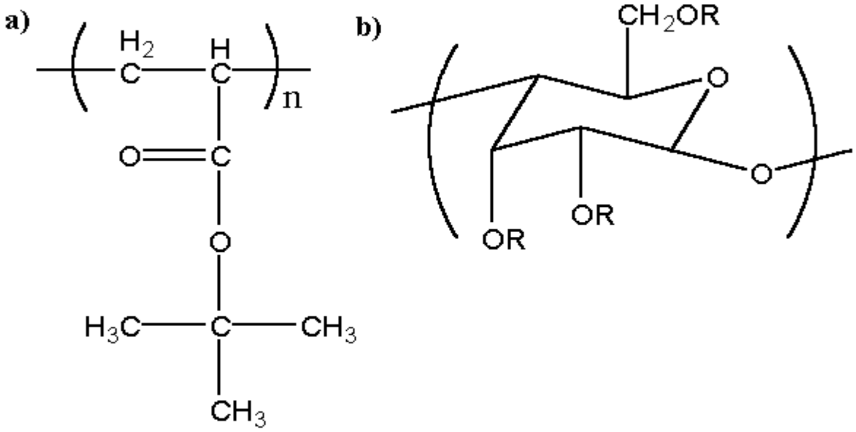

Fig. 1: a) PtBA (T_g = 38°C, M_n = 25.4 kg/mol, M_w/M_n = 1.07) b) IPC (M_n = 49 kg/mol, M_w/M_n = 2.92)

Wafer Preparation

The (100 mm in diameter; 500 μm thick) silicon wafers (TTI Silicon, Inc.) were first plasma treated (O_2, 40 W, 0.7 Torr, 10 min) to help remove residual griding paste and grow a uniform oxide layer. The wafers were then cut and cleaned via ultrasonication in dichloromethane solution for 15 minutes, to remove any organic contaminants on the surface. After drying the pieces and rinsing them with ultra-pure deionized water (Gradient A10 system, Millipore Corp.) they were boiled for two hours in an alkaline bath consisting of 28 wt % ammonium hydroxide, 35 wt % hydrogen peroxide and ultra-pure water (1:1:5 by volume). The wafers were then extensively rinsed with ultra-pure water and dried with nitrogen. Finally the wafers were placed in a sealed container, containing 1,1,1,3,3,3-hexamethyldisilazane (Aldrich) and set in an oven at 80°C for at least two hours. This process replaced the hydrophilic SiO_2 surface layer on the wafer with hydrophobic trimethylsilyl groups.

Film Preparation

The films made in this study were prepared by the Langmuir Blodgett (LB) film technique on a commercial trough (KSV 2000, KSV Instruments, Inc.). The LB film technique provides ultimate control over film thickness, where one molecule thick layers are added sequentially. After scrupulous cleaning the trough is filled with ultra-pure water, the polymer, dissolved in HPLC grade chloroform, is spread across the surface of the water until surface pressure reaches a range of 5-9 mN/m. After allowing the $CHCl_3$ to evaporate for 15 minutes the barriers are compressed at a rate of 2 mN/m/min until the surface pressure reaches a suitable value for y-type LB-film deposition (π = 17 mN/m for IPC and π = 17.5 mN/m for PtBA, at 22°C). Next the silicon wafer is dipped in the water at 10 mm/min and out of the water at 8 mm/min. The target pressure is maintained at a constant value during this process. A monolayer of polymer is transferred each time the wafer goes into the water or out of the water. The monolayer thickness for IPC is ~ 9.5 Å, [8] and for PtBA is ~9.1Å, [9]. This procedure has been used to make LB films with Si//IPC//PtBA//IPC//air configurations where there are 16 layers of IPC on the substrate, 20 layers of PtBA on top of the IPC and IPC capping layers of variable thickness (0 - 10 layers) on top of the PtBA.

Heating Stage Setup and Microscopy

After the films have been made, they are placed in a heating stage (LTS 350, Linkam Scientific Instruments, Ltd) at room temperature (25°C). The heating stage is setup under a fluorescence microscope operating in an optical reflection mode (Axiotech Vario, Carl Zeiss, Inc). The temperature is then increased at a rate of 30°C/min until it reaches 100 °C (the final temperature, which is maintained constant). As soon as temperature reaches 100°C the time is zeroed and film is observed under the microscope for rupture time. Pictures and movies of the films are then taken using Scion Image software. The pictures were then printed out so hole density and hole radii could be measured. Hole density was found by counting the number of holes from an area of the film under 20x magnification. Hole radii were found by measuring the radius of five holes at different times (1,2,3,4,5, and 10 min for no capping layer and 5, 10, 15, 30, 60, 90, 120 and 150 min for 0, 2, 4, 6, 8, and 10 capping layers) in an area of the film under 20x magnification and averaging out the values obtained at each time.

Fitting Equation

Once all the hole radius data is obtained we then use Igor Pro graphing software (WaveMetrics, Inc.) to fit our data to a power law equation with the following format: $R = A \cdot (t + B)^C$, which allows us to distinguish between slip and stick boundary conditions.

RESULTS AND DISCUSSION

Preliminary

In this experiment there was only one variable that was altered. The main objective of this experiment was to control dewetting in a purely organic system by adding capping layers, and analyze the capping layer thickness effects on film stability. This objective requires that an unstable Si//IPC//PtBA//air configuration is first obtained. As we know from the experiments done by Clark and Esker, if pure IPC is coated onto the silicon wafer and heated to 100°C no dewetting occurs. Similarly, a film of only PtBA is also stable upon heating to this temperature (which is above the value of T_g = 38°C for PtBA obtained by differential scanning calorimetry). A film is also stable if made with a bottom PtBA layer and a top layer of IPC. However; if the film Si//IPC//PtBA//air is made and heated to 100°C, it is unstable and will dewet.

When analyzing unstable films (Si//IPC//PtBA//air configuration) Clark and Esker showed that if the IPC thickness is varied and coated with a PtBA film of constant thickness, as the cellulose thickness increases the stability of the film will decrease by screening the attractive interactions between PtBA and silicon. If the IPC thickness is held constant and a variable thickness PtBA layer is placed on top, as the PtBA thickness increases the stability of the film increases as well. This result is expected based on the fact that the rupture time is strongly coupled to film thickness, $t_0 \sim d^5$.[10,11,12] According to the research done by Dalnoki-Veress, Nickel and Dutcher, showing how SiO_2 deposited capping layers inhibited the dewetting of freestanding PS films, we can expect that the film will be more stable as the number of capping layers in a Si//IPC//PtBA//IPC//air configuration increases.[13]

Zero Capping Layers

When analyzing the Si//16xIPC//20xPtBA//0xIPC//air configuration it is observed that the film rupture occurred even before the film reached 100°C**.** Even though the creation of holes first occur by nucleation and growth, film rupture is defined, in this experiment, as the time it takes for the first holes believed to be created by spinodal dewetting appear. Hole density and hole radius increased very fast as annealing time increased (Figure 2, 3 and 4). Complete dewetting occurred when the film was annealed for about 10 minutes at 100°C.

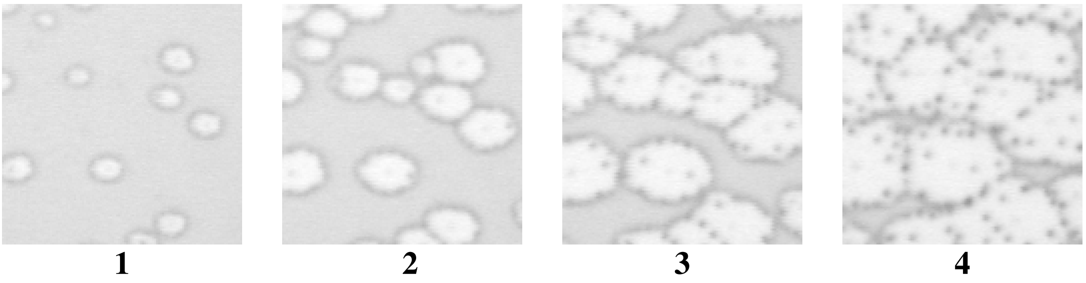

Annealing Time (min)

Fig. 2: Pictures taken of a Si//16IPC//20PtBA//0IPC//air film as a function of increasing annealing time at 100°C and view with the 20x lens**.** Pictures are 125X125 μm

Fig. 3: Hole radius of a Si//16IPC//20PtBA//0IPC//air film as a function of annealing time at 100°C.

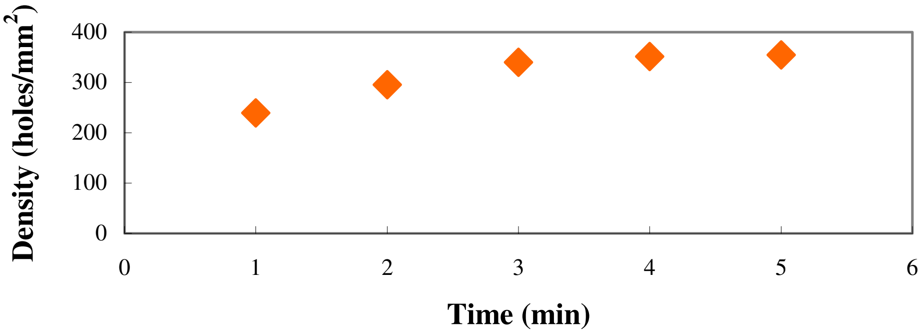

Fig. 4: Hole density of a Si//16IPC//20PtBA//0IPC//air film as a function of annealing time at 100°C.

When fitting the radius growth data with respect to time to the power law equation, $R(t) \sim A \cdot (t + B)^C$ we found that the system exhibits slip boundary conditions ($C=1.04 \pm 0.14$) and the rupture time was zero within experimental error ($B=-0.008 \pm 0.35$).

Two Capping Layers

When two capping layers of IPC are added to the 20 layers of PtBA (Si//16xIPC//20xPtBA//2xIPC/air configuration), a considerable suppression of dewetting is observed (Figure 5). Rupture occurred 2 minutes after film reached 100°C and complete dewetting took place when the film was annealed for 4 hours at 100°C. Hole radius and hole density increase more slowly with time than the film with no capping layers (Figure 5, 6 and 7).

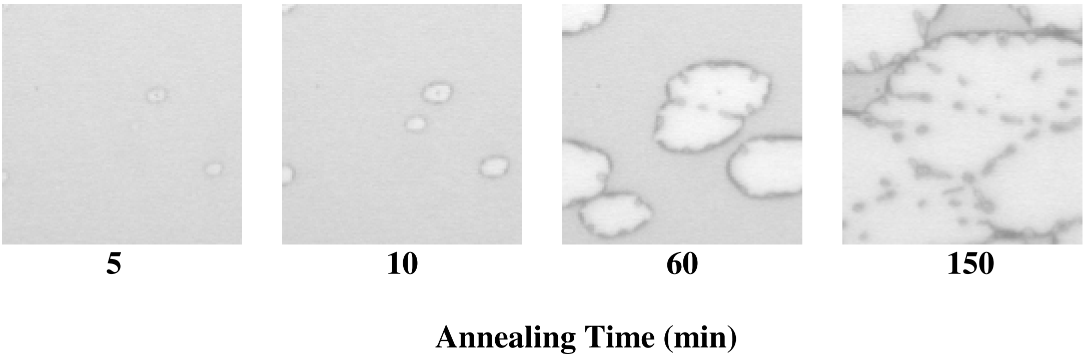

Fig. 5: Pictures taken of a Si//16IPC//20PtBA//2IPC//air film as a function of increasing annealing time at 100°C and view with the 20x lens**.** Pictures are 125X125 µm

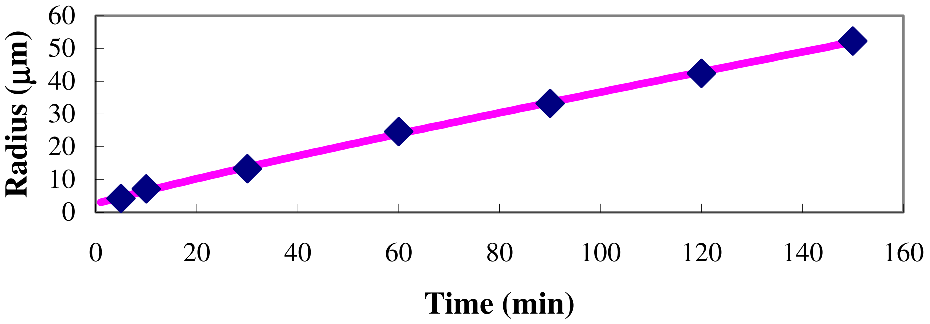

Fig. 6: Hole radius of a Si//16IPC//20PtBA//2IPC//air film as a function of annealing time at 100°C.

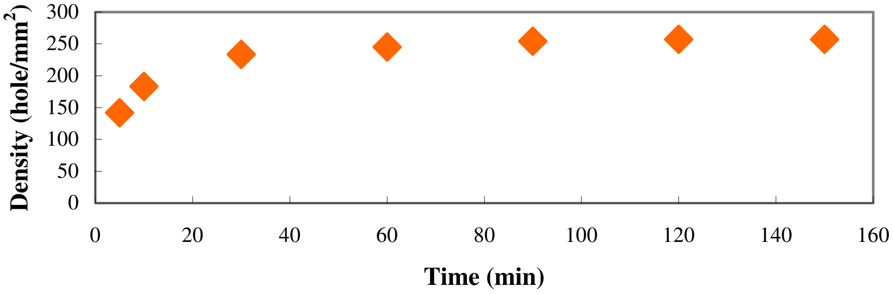

Fig. 7: Hole density of a Si//16IPC//20PtBA//2IPC//air film as a function of annealing time at 100°C.

A power law fit of the time dependence at of the hole growth shows deviation from slip boundary conditions (C=0.90 ± 0.04) and finite rupture time (t_0=B=5.4 ± 2.4 min). According to the power law equation there is a gradual transition from slip to stick boundary conditions since the exponent C of this equation has a value between 2/3 and 1. This behavior can be explained in terms of interfacial widths, where, as capping layer thickness increases, greater interpenetration between both polymers starts to develop until it reaches its full interfacial width.

Four Capping Layers and Six Capping Layers

The films with four capping layers and six capping layers demonstrated very similar dewetting behavior (figure 8, 9 and 10). Rupture times were 265 and 366 seconds for four and six capping layers respectively. Radii growth was severely hampered after films were annealed for 150 minutes**.** The films were removed from heating stage after annealing 5 hours at 100°C, as the hole radius and hole density were increasing very slowly with time, as a result, complete dewetting was not observed.

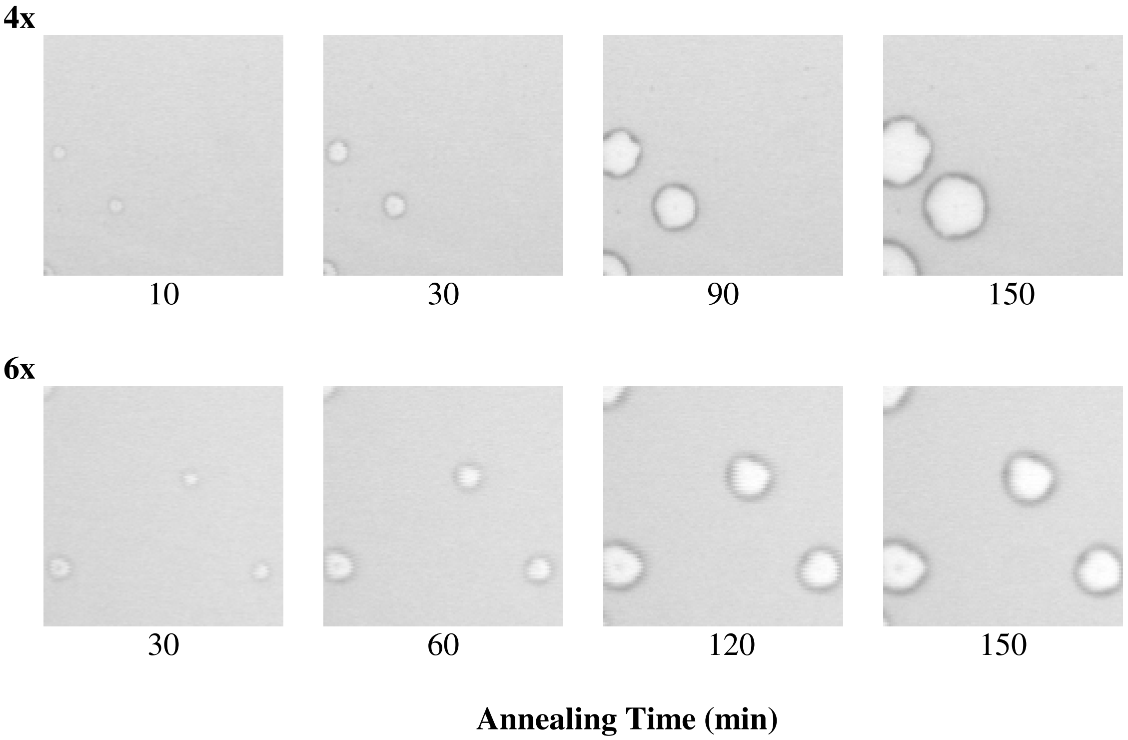

Fig. 8: Pictures taken of a Si//16IPC//20PtBA//4IPC//air and Si//16IPC//20PtBA//6IPC//air films as a function of increasing annealing time at 100°C and view with the 20x lens. Pictures are 125X125 µm

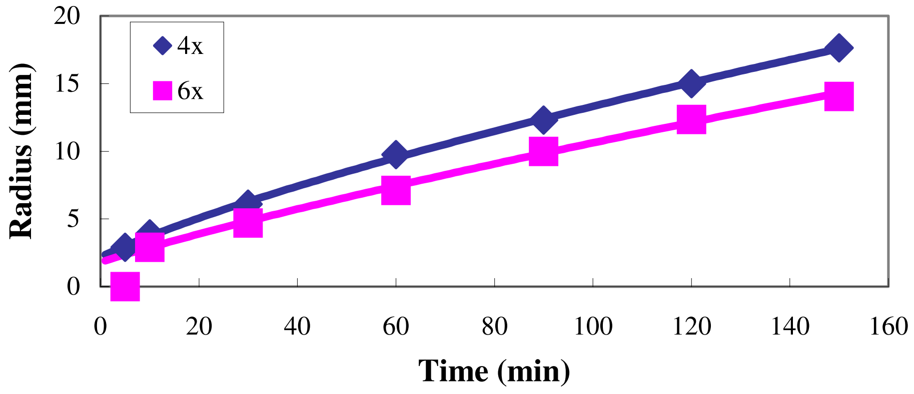

Fig. 9: Hole radius of a Si//16IPC//20PtBA//4IPC//air and Si//16IPC//20PtBA//6IPC//air film as a function of annealing time at 100°C.

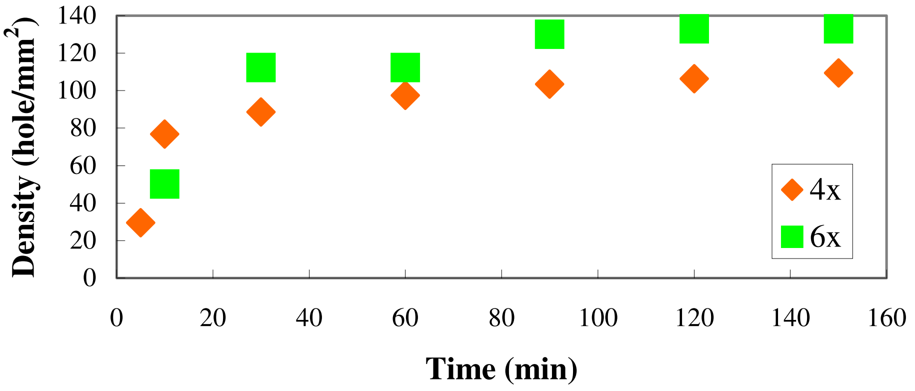

Fig. 10: Hole density of a Si//16IPC//20PtBA//4IPC//air and Si//16IPC//20PtBA//6IPC//air films as a function of annealing time at 100°C.

Just as noted above for the 2x capping layer system, both the 4x and 6x IPC capping layers exhibit intermediate behavior between the slip and stick limits. In contrast to the 2x capping layer, the deviation from slip boundary conditions is greater (4x, C=0.74 ± 0.04 and 6x, C=0.81 ± 0.09). As can be observed, when taking into account the margin of error, the exponents C for both equations are very similar to one another. Both C values lie between 2/3 and 1, which implies that the transition from slip to stick boundary conditions is not complete.

<u>Eight Capping Layers and Ten Capping Layers</u>

The films with eight capping layers and ten capping layers demonstrated very similar dewetting behavior (figure 11, 12 and 13). Rupture times were about 10 and 13 minutes for eight and ten capping layers respectively. Radii growth was severely hampered after films were annealed for 150 minutes**.** The films were removed from heating stage after annealing 15 hours at 100°C, as the hole radius and hole density were increasing very slowly with time, as a result, complete dewetting was not observed.

8x

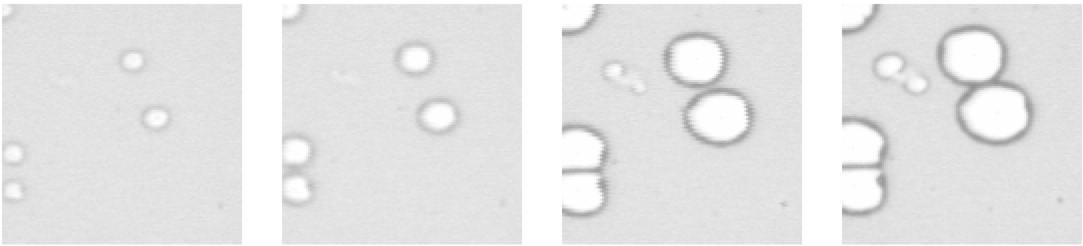

30 60 120 150

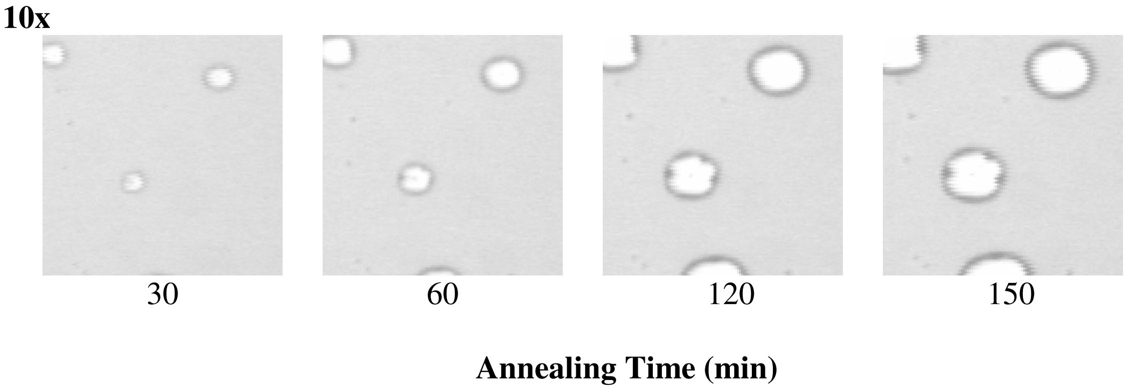

Fig. 11: Pictures taken of a Si//16IPC//20PtBA//8IPC//air and Si//16IPC//20PtBA//10IPC//air films as a function of increasing annealing time at 100°C and view with the 20x lens. Pictures are 125X125 µm

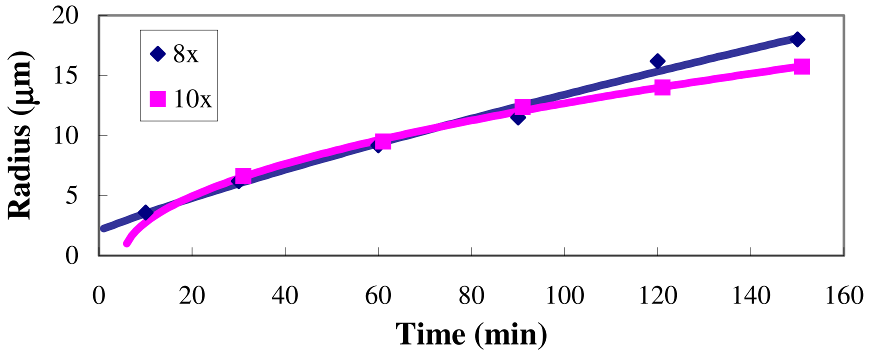

Fig. 12: Hole radius of a Si//16IPC//20PtBA//8IPC//air and Si//16IPC//20PtBA//10IPC//air film as a function of annealing time at 100°C.

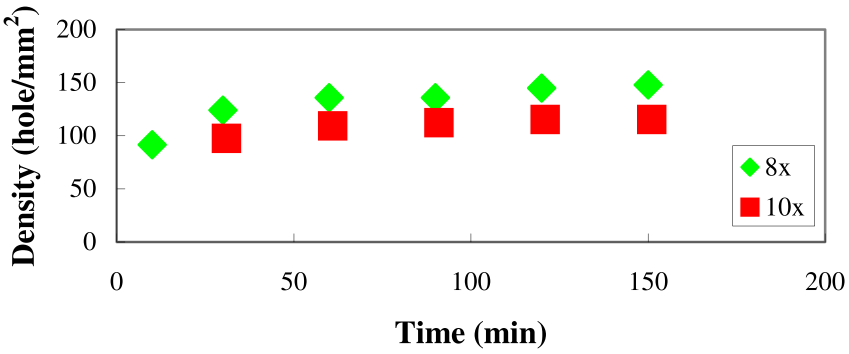

Fig. 13: Hole density of a Si//16IPC//20PtBA//8IPC//air and Si//16IPC//20PtBA//10IPC//air films as a function of annealing time at 100°C.

Just as noted above for the 8x and 10x capping layer system, both the 8x and 10x IPC capping layers exhibit intermediate behavior between the slip and stick limits. In contrast to the 2x capping layer, the deviation from slip boundary conditions is greater (8x, C=0.81 ± 1.05 and 10x, C=0.50 ± 0.0763). As can be observed, when taking into account the margin of error, the exponents C for both equations are very similar to one another. Both C values lie between 2/3 and 1, which implies that the transition from slip to stick boundary conditions is not complete.

CONCLUSION

The films made and observed in this experiment had a Si//16xIPC//20xPtBA// VariablexIPC //air configuration. Nucleation and growth and most likely spinodal dewetting were observed in all films, however; as the capping layer thickness increased dewetting was suppressed which leads us to conclude that film stability increases with increasing capping layer thickness. There was also a transition from slip to stick boundary conditions with the addition of capping layers. Hence observations of changing from slip to stick boundary conditions in dewetting experiments is an indirect measure of the evolution of adhesion arising from the interpenetration of polymer chains.

FUTURE WORK

In order to enrich the knowledge gained from this research it would be essential to perform neutron reflectivity experiments on Si//IPC//PtBA//IPC//Air conguration in order to measure interfacial widths. Even though we have observed in this experiment physical behavior that suggests changes in polymer mobility near surfaces and interfaces, there is not a clear understanding of the effects from the polymer/surface, polymer/polymer interactions. Neutron reflectivity provides a precise and nondestructive technique to measure the concentration profile between the different layers because of the large contrast to neutrons between the hydrogenated and deuterated species. Moreover, understanding how differences in capping layer chemistry and filler induced stabilization quantitatively affect the degree of thin film stabilization are natural extensions of this work.

ACKNOWLEDGEMENTS

The authors acknowledge the National Science Foundation, Jeffress Memorial Trust and Viginia Tech Aspires for funding this work. The authors would like to thank the SURP staff for all the administrative support, as well as Lars Kilian, and Jianjun Deng for all the explanations and discussions.

REFERENCES

[1] R. Xie, A. Karim, J.F. Douglas, C. C. Han, R. A. Weiss, *Phys. Rev. Lett.* **81**, 1251 (1998)
[2] T. Kerle, R. Yerushalmi-Rozen, J. Klein, L. J. Fetters, *Europhys. Lett.* **44**, 484 (1998)
[3] M. L. Clarke, A. R. Esker, Unpublished Work
[4] E. K. Lin, R. Kolb, S. K. Satija, W. Wu; *Macromolecules* **32**, 3753 (1999)

[5] Grüll, H.; Esker, A.R.; Yerushalmi-Rozen, R. (unpublished data)

[6] A. R. Esker, C. Mengel, G. Wegner, *Science*, **280**, 892 (1998)

[7] M. Schaub, thesis, University of Mainz, Germany (1993)

[8] M. Schaub, C. Fakirov, A. Schmidt, G. Lieser, G. Wenz, G. Wegner, P. -A. Albouy, H. Wu, M. D. Foster, C. Majrkzak, S. Satija, *Macromolecules*, **28**, 1221 (1995)

[9] A. R. Esker, C. Mengel, G. Wegner, *Science*, **280**, 892 (1998)

[10] T. Kerle, Yerushalmi-Rozen, R, J. Klein, L. J. Fetters, *EuroPhys. Lett.*, **44**, 484 (1998)

[11] Brochard-Wyart F., DIMeglio J. M., Quere D. *et al., Langmuir*, **7**, 335 (1991)

Probing Surface Effects in POSS Nanocomposites

Joe T. Polidan* and Alan R. Esker
Department of Chemistry
Virginia Polytechnic and State University
Blacksburg, VA

* Department of Aerospace and Ocean Engineering, Virginia Tech, Blacksburg, VA

ABSTRACT

Polyhedral oligomeric silsesquioxane (POSS) could play a very important role in the future of aerospace engineering. POSS can be used as a nanofiller to stabilize coatings while making them lighter and more efficient. The work contained three phases. First was the generation of Π-A isotherms. It was found that the different concentrations of POSS mix ideally with poly(t-butyl acrelate) (PtBA). Second, Brewster angle microscopy (BAM) was used to investigate the air/water interface of these mixtures. From BAM, the conclusion of ideal mixing obtained from the Π-A isotherms could be verified with images of the interface. These images provide further insight to the optimal transfer pressure for Langmuir-Blodgett (LB) film formation. In addition, it was found that POSS exhibited surfactant behavior and formed non-equilibrium dendritic domains at high surface pressures. Finally, films with various concentrations of POSS were prepared using the LB technique. The films were annealed and viewed with an optical microscope to measure differences (between various concentrations of POSS) in the dewetting properties. As the concentration of POSS increased to 10 wt% the films were stabilized but at higher concentrations (20 wt% POSS) the nanofiller lost its ability to stabilize the films.

INTRODUCTION

Currently, the cost of transporting one kilogram of mass into orbit is $10,000.[13] The aerospace industry is interested in materials that will reduce the mass of the vehicles hence making them less expensive to operate. Recent aerospace research focused on combining polyhedral oligomeric silsesquioxane (POSS) nanofillers with various polymers to decrease the payload's mass and improve fuel efficiency without sacrificing heat resistance. POSS nanofillers with large area-to-volume ratios are suspected to be more easily dispersed than other fillers, such as micron scale glass. Also POSS nanofillers should provide better adhesion with matrix materials in high performance composites. In addition, the aerospace industry is interested in POSS fillers acting as heat transfer agents, providing electromagnetic shielding, and controlling conductivity in electronic applications.[7]

Previous research has investigated several POSS / polymer blends and monitored their surface behavior via isotherm analysis and Brewster angle microscopy (BAM).[2] POSS was blended with poly(dimethylsiloxane) (PDMS) and poly(vinyl acetate) (PVAc). In these studies, the blended isotherms were studied on a standard Langmuir trough. Furthermore, the different aggregation behaviors at the air / water interface of these polymers were interpreted using BAM.

Another way to probe polymer-filler interactions is through dewetting studies. There is fundamental and practical interest in how the performance of the materials is effected by the wetting/dewetting characteristics of the blended polymers. To understand dewetting properties, films of POSS / polymer blends must be prepared on a hydrophobic Langmuir-Blodgett (LB) substrate, such as functionalized silicon. Amphiphilic poly(t-butylacrylate) (PtBA) will be combined with POSS nanofillers to form LB films for further analysis. Several techniques will be used to completely analyze POSS / PtBA blends. First, isotherm data for blends with specific POSS contents will be used to estimate target pressures that optimize polymer transfer as LB films. Next, BAM will be applied examine POSS / polymer aggregation at the air/water interface. Finally, optical microscopy will be used to determine how POSS alters PtBA dewetting on cellulose coated silicon wafers. scan the surface of these films and monitor the dewetting activity of the POSS blend.

EXPERIMENTAL

Materials. The PtBA was obtained from Polymer Source, Inc. It has a weight average molecular weight, M_w=25.7 kg/mol and a polydispersity of M_w/M_n=1.08. The PtBA sample has a glass transition temperature (T_g)=38°C. Isopentylcellulose (IPC) was prepared by the method of Schaub.[11] The IPC sample used has a degree of substitution D_s=2.7 isopentyl groups per repeat unit, M_w=144 kg/mol, and M_w/M_n=2.92. Isobutyltrisilanol POSS, or heptasubstituted -POSS, samples were provided by Dr. Brent Viers from Edwards Airforce Base.

The POSS molecules were synthesized through the hydrolysis of either a trichlorosilane or a trialkooxysilane.[2] POSS is an organic/inorganic hybrid about 1-2 nm in size.[2,12] It has a hard inorganic core and a soft organic corona. POSS molecules can be thought of as the smallest particles of silica possible. However unlike silica or modified clays, each POSS molecule contains covalently bonded reactive functionalities suitable for polymerization or grafting POSS monomers to polymer chains. Each POSS molecule contains nonreactive organic functionalities for solubility and compatibility of the POSS segments with the various polymer systems, such as PtBA. Isobutyltrisilanol also has very strong interactions with water which make compatible with the pure water subphase on the Langmuir trough. All polymer solutions were dissolved in chloroform in10mL volumetric flasks. Three to five milligrams of POSS and/or polymer were dissolved into the solutions.

Isotherms. Isotherms are plots of surface pressure vs. area per monomer. It is the two-dimensional analogue of a three-dimensional pressure vs. volume plot. From the plots, one can obtain the collapse pressure for any polymer system. This collapse pressure is the pressure where the molecules in the monolayer cannot squeeze any closer together. At this pressure the molecules begin to pile up onto one another forming domains which can be imaged with the Brewster angle microscope. At lower surface pressures the monolayer exhibits the properties of liquids and gasses. There is only one linear liquid condensed stage in the isotherms for these PtBA and POSS systems.

The first step for generating isotherms is to clean the commercial trough (NIMA) and its barriers with chloroform. After this, the trough is filled with water and suctioned off to remove any excess organic material. Then, the trough is refilled with deionized water to a level of 4-5 mm above the highest point on the trough. Next, the paper plate was attached to the balance and slowly lowered towards the subphase until initial contact. The balance measures surface pressure by a simple force balance on the Wilhelmy plate (see Figure 1).[9]

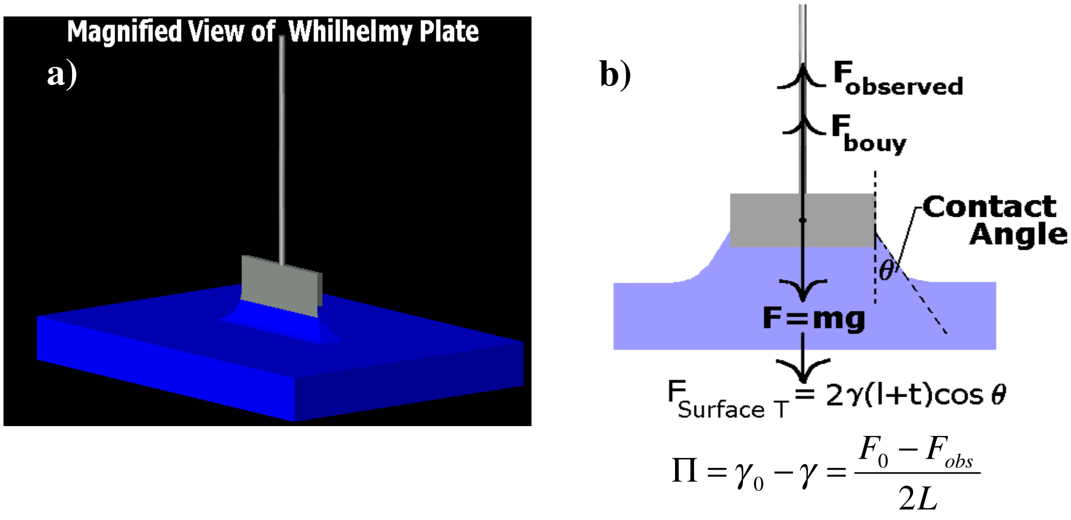

Figure 1. The balance measures surface pressure by using the Wilhelmy plate as seen in picture a). It starts with a simple derivation of Work = Force*Distance and ends with a force balance as seen in picture b). The contact angle is taken to be zero and the thickness is neglected.

After this, the barriers are compressed to a minimal area (without touching the Wilhelmy plate) and the surface of the water subphase is cleaned with a pipette that is attached to a vacuum pump. Subsequently, the barriers are opened. Next, the polymer was spread on the surface with a clean 100µL syringe (Hamilton). For every sample, 45 µL was spread. At this point fifteen minutes was allowed for the chloroform to evaporate from the monolayer. After evaporation, the balance was zeroed and the isotherm was obtained at a compression rate of 10 cm/min.

Brewster Angle Microscopy (BAM). The BAM was used to observe the air/water interface of the polymer systems as the surface pressure increases. The advantage of BAM over other techniques is that a Langmuir film can be studied *in situ* without chemical perturbation or deposition of a film onto a substrate.[2] The same technique of compression used in generating the Π-A isotherms was used here. With the BAM these Π-A curves can be physically verified with laser-imaged photographs.

First a black glass plate was placed on the commercial trough (NIMA) to reduce the amount of light scattering from the 30mW laser source. Then the laser arm was positioned 105 mm above the surface of the trough. Next, deionized water was added to the trough. Again the proper water level corresponds to a height of 4-5 mm above the trough. The BAM was adjusted until there is a minimum amount of light reflected into the objective (when the light on the monitor is a minimum). This condition corresponds Brewster's angle, the critical angle at which no reflection of the p-polarized light is observed. Brewster's Angle is defined as:

$$\tan \theta_b = n_1 / n_2 \qquad [1]$$

where n_1 and n_2 are the refractive indices of the upper and lower media, respectively. After the BAM was properly adjusted, the interface was cleaned and the sample was spread just like the isotherm studies. The polymer was added very slowly on top of the pure water subphase with a clean syringe. The addition of a film to the surface introduces some reflectivity that is dependant upon the films thickness and refractive index. The reflection caused by the monolayer will increase the intensity of the reflected light as film thickness and film index increase.[2,10]

45μL of POSS/PtBA mixtures were spread. The barrier speed was set at 10 cm/min (as in the isotherms). Following a 15 minute chloroform evaporation period, all of the lights in the room were turned off to reduce scattering and increase the contrast of the laser images. Also, the balance was zeroed. Then the monolayer was slowly compressed from a surface of 0 mN/m up to a target pressure of 25 mN/m. While the barriers were compressing, pictures were taken with the commercial BAM software (MiniBAM, NFT) while the corresponding surface pressures were noted from the NIMA software that was the same software responsible for the isotherm generation. This procedure was used for Pure PtBA up to pure POSS in intervals of 20 wt% POSS.

Wafer Preparation. Next, 4" Si (100) wafers were treated for 10 minutes in an oxygen plasma (40W,0.6 Torr). Subsequently, the wafers were cut into several pieces with a diamond edged razor and were ultrasonicated with dichloromethane for fifteen minutes. After removing the dichloromethane, the wastes were rinsed with ultra-pure deionized water (18.2 MΩ, 4ppb organics, Gradient A10 System, Millipore Corp). Following this, the wafer pieces were boiled for 1.5 hours 1:1:5 by volume mixture of concentrated ammonia: 30% hydrogen peroxide:water, respectively. After boiling in the basic solution the wafers were removed and rinsed repeatedly with the Millipore water. Following this, the wafers were dried with nitrogen and then placed into a sealed jar with 1,1,1,3,3,3-hexamethyldisilazane. The 1,1,1,3,3,3-hexamethyldisilazane made the wafers hydrophobic which is required to ensure that the amphiphilic polymers will transfer to the substrate from the air/water interface. The sealed jar was placed into an oven at 80°C for at least two hours before use.

Film Preparation. All of the films used in this research were prepared via the Langmuir Blodgett film technique on a commercial trough (KSV 2000, KSV Instruments, Inc.) filled with Millipore water. The temperature controller maintained a temperature of 22.5°C. The trough was filled such that 4-5 mm of water rose above the surface (made possible by the high surface tension of water and the hydrophobic Teflon® surface). Subsequently, a wet platinum Wilhelmy Plate was attached to the balance and positioned slightly above the subphase. The elevation of the plate was slowly decreased until the plate made contact with the water subphase. Next, the two barriers were closed and the surface was cleaned off (to ensure the correct value of surface tension for water) with a pipette attached to a vacuum. Then the two barriers were reopened and the plate was brought out the water subphase to verify that the surface tension of water was near 72 mN/m on the balance. Subsequently, the polymer films were spread on the surface with a clean 100μL syringe. Each drop was deposited very carefully ensuring that a surface pressure greater than 5-7 mN/m was not exceeded. After the film was spread, 15 minutes was allowed for the volatile chloroform to evaporate. Next, the barriers compressed the monolayer to the target pressure and maintained this pressure through out the entire procedure. Five minutes were allowed to assure the film was stable. After this, the dipping procedure was begun. The down speed of the dipper was set at 10 mm/min and the up speed was set at 8 mm/min. There was a two-minute delay before the process began to allow all vibrations to dampen. Also, there was a 15-second delay at the bottom of the dipping cycle to allow time for the meniscus to reorient on the film (flip direction) and a one minute delay at the top of the cycle to allow the film to dry. The Langmuir-Blodgett Technique allowed a thickness of about 10 Å on every dipping stroke (i.e. the thickness of the film is controlled to the thickness of a single molecule).[6] Films of various concentrations of POSS were prepared using this technique. The coating layer was identical in every film (16 layers of IPC) as was the thickness of second layer (20 layers). However the composition of the second layer was the controlled variable of interest. The composition of the second layer was PtBA blended with different amounts of POSS (see Figure 3).

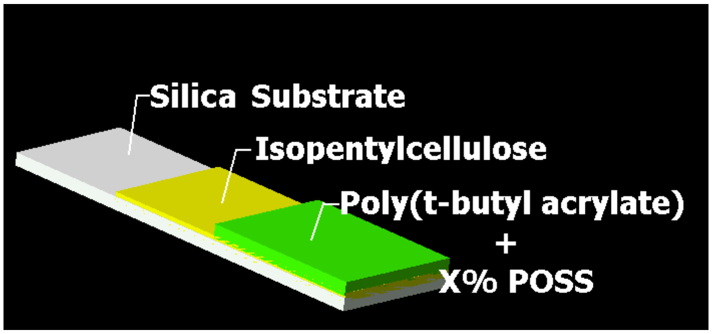

Fig.3: The controlled variable. The coating layer was the same for every film investigated (16 layers of IPC). The second layer had an identical thickness (20 layers) for every film but had variable concentrations of POSS.

Microscopy. All films were annealed on a heating stage and viewed with Scion imaging software to determine the dewetting properties (i.e. hole density and radius as a function of time). The samples were monitored using a 20x objective lens on a commercial fluorescence microscope operating in an optical reflection mode (Axiotech Vario, Carl Zeiss, Inc.). The dewetting temperature was controlled using a computer-controlled commercial heating stage.(LTS 350, Linkham)

RESULTS AND DISCUSSION

Isotherms. Π-A Isotherms were generated for the various POSS mixtures (Figure 4). These are the two-dimensional analogues to the three-dimensional pressure vs. volume plot. Up to the collapse pressure of POSS, these curves obey ideal mixing predicted by:

$$<A(\Pi)>=X_1A_1(\Pi) + X_2A_2(\Pi) \qquad [2]$$

In Equation 2, X_1 and X_2 are the mole fractions of the species one and two, $A_1(\Pi)$ and $A_2(\Pi)$ are the areas per monomer of the pure component at a given surface pressure and $<A(\Pi)>$ is the average area per monomer. The left-most curve in figure 4 is pure PtBA and the right-most curve is pure POSS. It could be seen that as the concentration of POSS increases, the curve shifts to the right as expected.

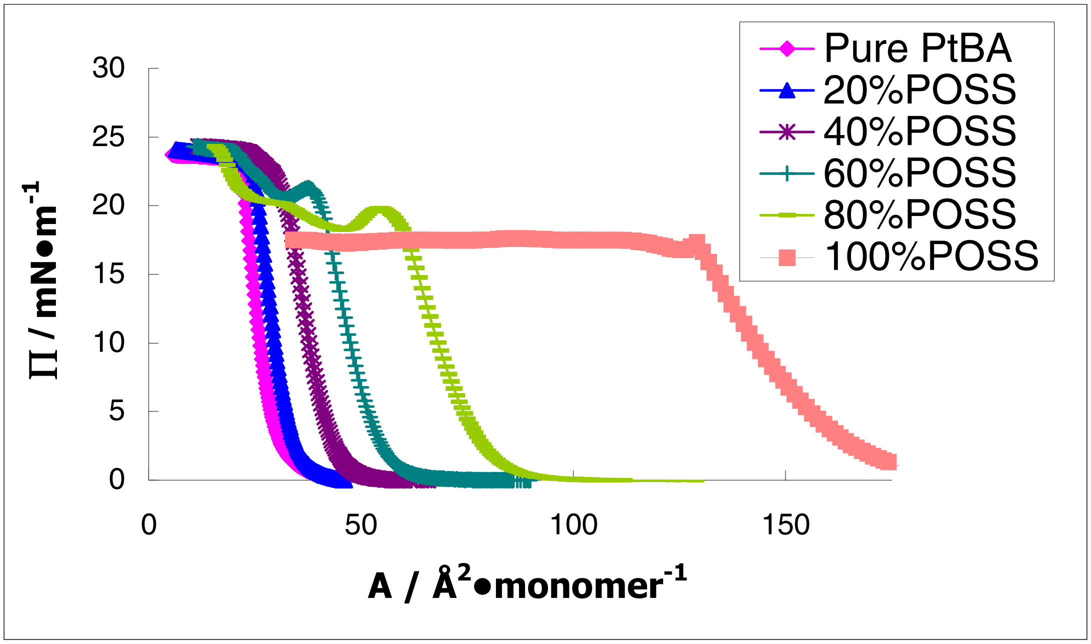

Figure 4. Π-A isotherms of PtBA/POSS blends from 0 wt% up to 100 wt% POSS. The curves obey ideal mixing predicted by Equation (1). As the concentration of POSS increases, the curves shift to the right.

The collapse pressures for the PtBA and POSS mixtures were read off these Π-A isotherms. This is the pressure at which the liquid phase can no longer be packed closer together. At higher pressures, the monolayer piles up on itself, or collapses. For example, take the 80 wt% curve. From an area of 150 to 100 Å^2•monomer^{-1}, the molecules of the monolayer were spread far apart. As the surface pressure increased and the area decreased, the 80 wt% POSS went through the liquid stage before the surface pressure increased to around 17 mN/m, where the monolayer collapsed. This information provided insight for the selection of surface pressure when using the Langmuir-Blodgett technique to make films. This graphical data was used to speculate about the surface behavior and make predictions about the morphology of the interface. This was verified by actually taking pictures of the air/water interface with the next facet of this study.

Brewster Angle Microscopy (BAM). BAM is a technique that investigates the morphology of monolayer systems at the air/water interface. It allows us to visualize what the ideal homogenous monolayers really look like and also provides insight to the specific geometry of the polymer domains in phase separated monolayers .

The first mixture of interest is 60 wt% POSS. This mixure displayed a uniform monolayer up to a surface pressure of about 18 mN/m where it starts to collapse. A pressure of 16 would be an ideal pressure to transfer at with the Langmuir Blodgett technique. In the early stages a very heterogeneous phase transition could be observed. White bands were strands of POSS attempting to form a type of dendritic structure. The dendritic structure could be seen more clearly as the mixtures approached that of pure POSS (see Figure 5-7).

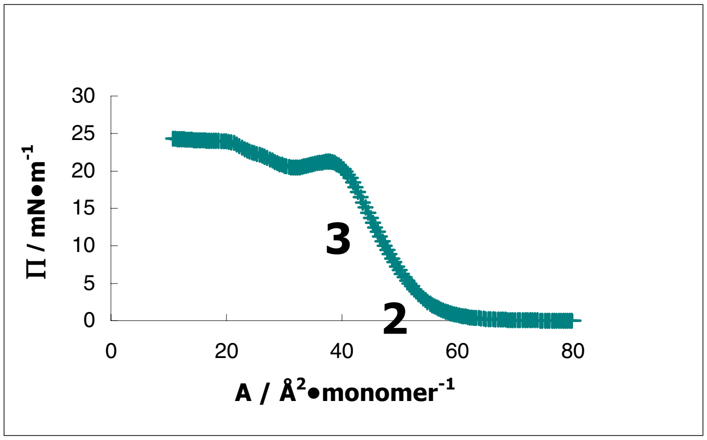

Figure 5. These pictures reveal what the air/water interface looks like. At a surface pressure of 19 mN/m the film begins to collapse. This pressure corresponds to picture 3. This would be an ideal surface pressureto transfer the monolayer using the LB technique. The heterogeneous phase separation is present in picture 4. The white bands are PtBA and the dense white dots are POSS domains. All bars on the pictures are 500 microns in length.

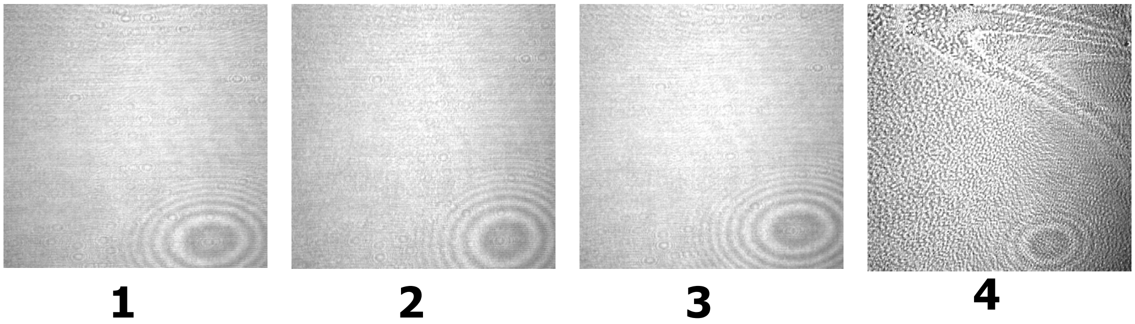

Next the behavior at the air/water interface of 80 wt% POSS was investigated via the BAM technique. The 80 wt% POSS exhibited similar behavior as the pure POSS. The dendritic domains were very well defined at surface concentrations above the collapse concentration. Also 80 wt % POSS blend with PtBA collapsed much earlier than the 60 wt% POSS blend. At very small areas per monomer, the 80 wt% POSS blend exhibited heterogeneous phase separation with the dendritic POSS domains encircling the dense PtBA spherical domains (see figure 6).[2]

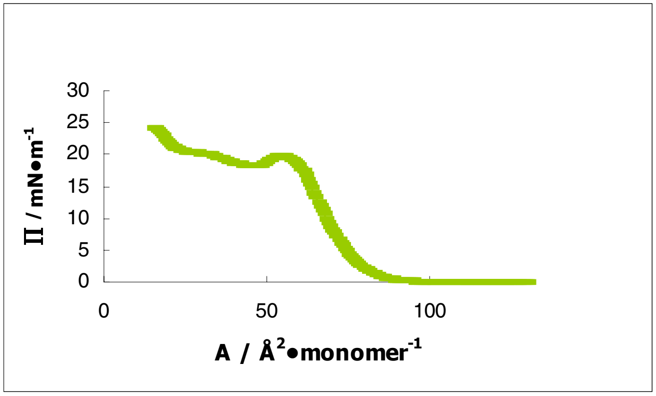

Figure 6. These pictures were taken at the air/water interface of an 80 wt% POSS blend with PtBA. In picture two, which was near the collapse pressure, the first domain separates out of the super-saturated monolayer. This measures about 80 microns across. Pictures 2 and 3 show the dendritic POSS domains very clearly. In picture 4, the high density of spherical domains was PtBA collapsing out of the monolayer. The scale measures 500 microns.

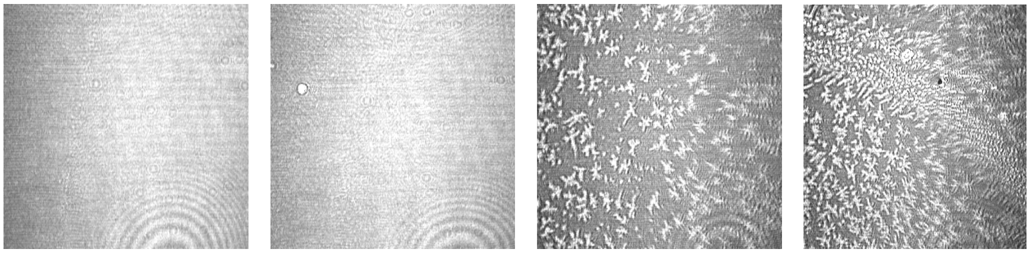

1 **2** **3** **4**

The last system that was studied with BAM was pure POSS. This exhibited the most interesting BAM. It clearly demonstrated the dendritic behavior of the domains for POSS derivatives. This type of surfactant behavior has never been observed before. Dendritic growth has only been reported for enantiomeric N-alkylaldonamide and for N-alkyl acid amide compounds.[8] An explanation for the formation of dendritic domains follows. We consider two ways to compress the monolayer on the Langmuir trough. It can be done by spreading a small amount with a syringe (45uL) and compressing at a certain barrier speed (around 10 cm/min), which seems slow but is actually fast relative to relaxation processes of the monomolecular film resulting in a nonequilibrium film. Alternatively, we could compress the film at a slow enough rate to allow equilibrium structures to form. For the POSS system, this require very slow compression rates that are not possible with our equipment.

As, noted above, the "quickly" compressed monolayer leads to nonequilibrium behavior and the monolayer becomes supersaturated around any initial domains (nucleation sites). Perhaps the molecule is unable to rotate in the subphase (this is a suspected cause in previous research with cis-double bonded fatty acids).[8] This would require the chains pack into 2-dimensional crystals with a dendritic shape as seen in Figure 7.

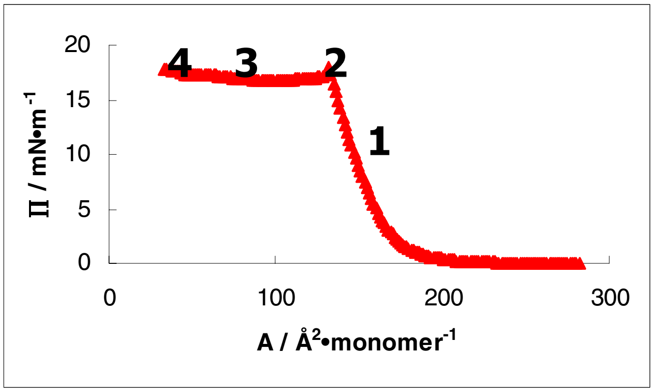

Figure 7. These pictures show the surfactant behavior of pure POSS. Picture 1 (at a pressure of 12 mN/m) may be an ideal dipping pressure for the LB-technique. The dendritic domains are clearly shown in pictures 3 and 4. If we wait a few hours were allowed after picture 4, the POSS monolayer would return to equilibrium conditions and dendritic structures will relax to spherical domains.

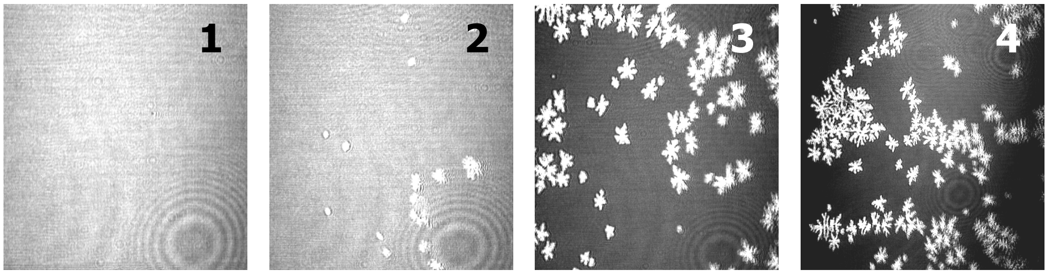

Filler Effects on PtBA Dewetting. The last aspect of this research project was the dewetting of thin films prepared by the Langmuir-Blodgett technique. Dewetting is the formation of holes by unstable liquid on a substrate. Due to convenient time scales, polymers above T_g are frequently used as the dewetting liquid on solid substrates like silicon or mica. Coating the substrate with a second polymer layer can modify van der Waals interactions between the top polymer and the substrate thereby altering film stability.[3] Hole formation is observed when the unstable trilayer (see Figure 8) system is annealed. Annealing causes capillary waves that propagate across the film. At a certain time and temperature, constructive interference occurs and the waves combine to form a wave with sufficient amplitude to reach the underlying substrate and spontaneously nucleate a hole down to the coating layer (IPC was used in this study).[5,7]

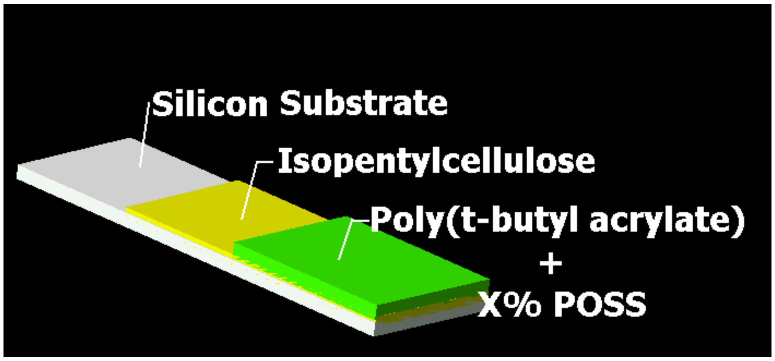

Figure 8. Silicon substrates coated with two materials as a bilayer: 1) 16 layers of IPC and 2) 20 layers of PtBA/POSS.

In this study, the composition of the second layer (on top of the coating layer) was varied. The idea was to increase the amount of POSS in the layer and see how the dewetting properties change. There are three important dewetting properties: rupture time, hole density, and hole radius as a function time. Rupture time is when the first holes begin to appear on the substrate, and the hole density is the number of holes on the film divided by the area upon which the holes are counted. POSS did stabilize the film up to a critical concentration. Pure PtBA was less stable than 5 wt% POSS which was less stable than 10 wt% POSS (see Figure 9). For mixtures above 20% POSS, the films dewet at least as fast as pure PtBA.

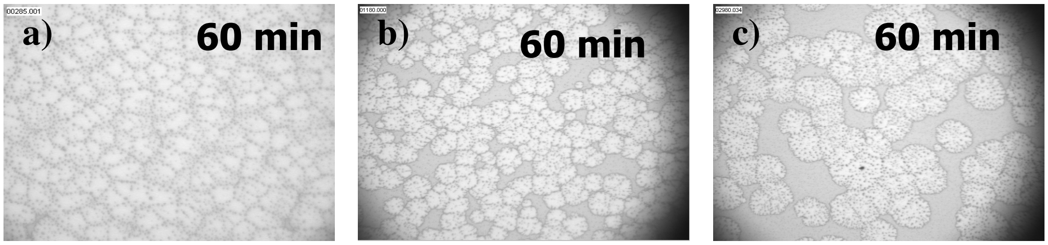

Figure 9. Dewetting pictures for Si // 16x IPC // 20x PtBA+POSS) // air: a) pure PtBA, b) 5 wt% POSS, and c) 10 wt% POSS. All samples were annealed at 80° C for 60 minutes. As the concentration of POSS increased up to 10 wt%, the hole radius and density decreased. This means the film was more stable as the concentration increased. However, if there was a picture of 20 wt% POSS, it would be completely dewet like the pure PtBA at 60 minutes.

CONCLUSIONS

This work was broken up into three elements: 1) isotherms, 2) Brewster angle microscopy, and 3) film dewetting. The isotherms of the various weight percents of POSS displayed ideal mixing. The images taken from the BAM are consistent with the interpretation of the Π-A isotherms. Pure POSS was discovered to display surfactant behavior and formed non-equilibrium dendritic domains near the collapse pressure. The dewetting of the thin films suggested that PtBA films could be stabilized on silicon wafers by the POSS up to a concentration of 10 wt% POSS. After that critical concentration, the POSS actually tends to further destabilize the films.

ACKNOWLEDGMENTS

The authors thank Edwards Air Force Base, Jeffress Memorial Trust, the National Science Foundation, and VT Aspires for funding this work. The authors also acknowledge Dr. Brent Viers (from Edwards Air Force Base) who assisted this project and provided the POSS samples. In addition, a special thanks goes out to Katie Farmer for her help with the Langmuir-Blodgett technique and Jianjun Deng for helpful discussions on the formation of POSS dendritic arms.

REFERENCES

[1] Martin P.; Szablewski, M., *Tensiometers and Langmuir-Blodgett Troughs,* 5th ed., Nima Technology, Ltd., Coventry, 1999.

[2] Farmer, C. E. “Surface Characterization of Siloxane, Silsesquioxane, and Maleic Anhydride Containing Polymers at Air-Liquid Interfaces,” Masters Thesis, VPI & SU, 2001.

[3] R. Khanna, A.T. Jameel, A. Sharma, *Ind. Eng. Chem. Res.* **35**, 3081 (1996)

[4] F. Brochard-Wyart, J. Daillant, *Can. J. Phys.* **68**, 1084 (1990)

[5] R. Xie, A. Karim, J.F. Douglas, C.C. Han, R. A. Weiss, *Phys. Rev. Lett.* **81**, 1251 (1998)

[6] A.R. Esker, C. Mengal, G. Wegner, *Science*, **280**, 892 (1998)

[7] Y. Yang, A.J. Heeger, *Nature*, **372**, 344 (1994)

[8] Iimora,K.-I.;etal, *Langmuir* **2001**, *17*, 4602

[9] Wilhelmy, J. *Annalen der Physik* **1863**, 119, 177

[10] Adamson, R.W.; Gast, A.P. *Physical Chemistry of Surfaces*, 1997

[11] M. Schaub, thesis, University of Mainz, Germany (1993)

[12] Zhu, B.; Katsoulis, D.E,; Keryk, J.R.; McGarry, F.J. *Polymer* **2000**, 41, 7559-7573.

[13] Halliday D., Resnick R., Walker J. *Fundamentals of Physics*, *5th Edition*, 1997